



Reichenbach, Judith (2017) *Structure and dynamics in ionic liquids and concentrated salt solutions: an ultrafast spectroscopy study*. PhD thesis.

<http://theses.gla.ac.uk/8571/>

Copyright and moral rights for this work are retained by the author

A copy can be downloaded for personal non-commercial research or study, without prior permission or charge

This work cannot be reproduced or quoted extensively from without first obtaining permission in writing from the author

The content must not be changed in any way or sold commercially in any format or medium without the formal permission of the author

When referring to this work, full bibliographic details including the author, title, awarding institution and date of the thesis must be given

Enlighten:Theses  
<http://theses.gla.ac.uk/>  
theses@gla.ac.uk

# **STRUCTURE AND DYNAMICS IN IONIC LIQUIDS AND CONCENTRATED SALT SOLUTIONS: AN ULTRAFAST SPECTROSCOPY STUDY**

**Judith Reichenbach**

Diplom-Chemikerin  
Karlsruhe Institute of Technology

Submitted in fulfilment of the requirements for the  
Degree of Doctor of Philosophy

School of Chemistry

College of Science and Engineering

University of Glasgow

November 2017



# Abstract

A combination of spectroscopic methods and symmetry considerations were used throughout the presented studies to investigate the terahertz spectra showing liquid dynamics in varied systems. Optical Kerr effect spectroscopy revealed clusters of different sizes in aqueous sodium thiosulfate solutions with non-Newtonian behaviour. In conjunction with terahertz infrared spectroscopy, optical Kerr effect spectroscopy showed the charge-ordered nature of butylammonium ionic liquids, which manifested through phonon modes in the terahertz spectra. In eutectic lithium thiocyanate solutions, a combination of mid-infrared spectroscopy, optical Kerr effect spectroscopy and X-ray scattering showed a separation into nanoscale water-rich and salt-rich domains at low temperatures. In summary, the use of terahertz spectroscopy on selected model system provides information on the dynamics governing the behaviour of liquids and solutions.



# Contents

<b>Abstract</b>	<b>i</b>
<b>Acknowledgements</b>	<b>xi</b>
<b>Author's declaration</b>	<b>xiii</b>
<b>1. Introduction</b>	<b>1</b>
1.1. Matter and Transitions . . . . .	1
1.1.1. Structure and Dynamics in Liquids . . . . .	5
1.1.2. Ionic liquids . . . . .	14
1.2. Measuring techniques . . . . .	19
1.2.1. Optical Kerr effect spectroscopy . . . . .	19
1.2.2. Infrared spectroscopy . . . . .	21
1.2.3. X-ray scattering . . . . .	23
1.3. Summary . . . . .	25
<b>2. Experimental</b>	<b>27</b>
2.1. OKE set-up . . . . .	27
2.1.1. Laser . . . . .	27
2.1.2. High time-resolution OKE set-up . . . . .	33
2.1.3. Long delay OKE set-up . . . . .	35
<b>3. Data analysis of terahertz spectra</b>	<b>39</b>
3.1. Correlation between OKE and IR terahertz spectra . . . . .	39
3.2. Fit functions . . . . .	42
3.2.1. Anti-symmetrised Gaussian . . . . .	43
3.2.2. Brownian Oscillator . . . . .	43
3.2.3. Havriliak-Negami function . . . . .	44
3.3. Curve fitting . . . . .	46
3.3.1. OKE and far-IR spectra . . . . .	46
3.3.2. OKE spectra . . . . .	50
<b>4. Low frequency spectra of ionic liquids</b>	<b>53</b>
4.1. Introduction . . . . .	53

4.2. Experimental details . . . . .	59
4.2.1. Samples . . . . .	59
4.2.2. Measurements . . . . .	60
4.2.3. Fitting procedure . . . . .	61
4.3. Results and discussion . . . . .	67
4.3.1. Tetrabutylammonium halides . . . . .	67
4.3.2. Tributylammonium halides . . . . .	70
4.3.3. Tributylmethylammonium halides . . . . .	73
4.3.4. Ethylammonium chlorides . . . . .	77
4.3.5. Cation calculations . . . . .	77
4.3.6. Discussion . . . . .	79
4.4. Conclusions . . . . .	86
<b>5. Structure and supercooled behaviour of eutectic salt solutions</b>	<b>89</b>
5.1. Introduction . . . . .	89
5.2. Experimental details . . . . .	94
5.2.1. Samples . . . . .	94
5.2.2. Measurements . . . . .	95
5.2.3. Fitting procedure . . . . .	97
5.3. Results and discussion . . . . .	100
5.3.1. OKE spectra of aqueous LiSCN solutions . . . . .	100
5.3.2. X-ray scattering of aqueous LiCl solutions . . . . .	105
5.3.3. X-ray scattering of aqueous LiSCN solutions . . . . .	110
5.3.4. IR spectroscopy of aqueous SCN-doped LiCl solutions . . . . .	114
5.3.5. Discussion . . . . .	119
5.4. Conclusions . . . . .	124
<b>6. Supersaturated sodium thiosulfate solutions and the hunt for pre-nucleation clusters</b>	<b>127</b>
6.1. Introduction . . . . .	127
6.2. Experimental details . . . . .	129
6.3. Results and discussion . . . . .	131
6.3.1. Crystal formation . . . . .	131
6.3.2. Water influence . . . . .	132
6.3.3. Sodium thiosulfate OKE spectrum . . . . .	135
6.4. Conclusions . . . . .	144
<b>Appendices</b>	<b>147</b>
A. Ionic liquids . . . . .	149
B. Eutectic salt solutions . . . . .	153
C. Supersaturated sodium thiosulfate solutions . . . . .	157
D. Water model . . . . .	163

# List of Tables

1.1. Distance dependence of intermolecular interaction potentials. . . . .	6
4.1. Butylammonium halides: melting points and measurement temperatures. . . . .	59
4.2. Ethylammonium halides: melting points. . . . .	60
4.3. Anti-symmetrised Gaussian function fit parameters. . . . .	65
4.4. Brownian Oscillator and Debye function fit parameters. . . . .	66
4.5. Polarisability values calculated for the ethylammonium cations. . . . .	78
5.1. Sigmoidal T-dependence of the <b>LiSCN:5.8H<sub>2</sub>O</b> OKE population fractions.	105
5.2. Halfway points of the T-dependence for <b>SCN_M</b> and <b>SCN_S</b> . . . . .	114
6.1. Vibrational modes of the thiocyanate ion below 20 THz. . . . .	135
6.2. Relaxation times and calculated volumes for <b>Na<sub>2</sub>S<sub>2</sub>O<sub>3</sub>:5H<sub>2</sub>O</b> . . . . .	140
6.3. Relaxation times and calculated volumes at 25 °C for <b>Na<sub>2</sub>S<sub>2</sub>O<sub>3</sub>:5H<sub>2</sub>O</b> and <b>Na<sub>2</sub>S<sub>2</sub>O<sub>3</sub>:32.7H<sub>2</sub>O</b> . . . . .	143
A.1. Averaged scans per IL. . . . .	149
B.1. Linear T-dependence of the <b>LiSCN:5.8H<sub>2</sub>O</b> OKE S population fraction. . . . .	153
B.2. Linear T-dependence of the <b>LiSCN:5.8H<sub>2</sub>O</b> OKE frequencies. . . . .	153
B.3. OKE fit parameters for the <b>LiSCN:12H<sub>2</sub>O</b> solution. . . . .	153
B.4. T-dependent anti-symmetrised Gaussian fit parameters for <b>LiSCN:5.8H<sub>2</sub>O</b> . . . . .	154
B.5. T-dependent Haviliak-Negami fit parameters for <b>LiSCN:5.8H<sub>2</sub>O</b> . . . . .	154
C.1. T-dependent fit parameters for <b>Na<sub>2</sub>S<sub>2</sub>O<sub>3</sub>:32.7H<sub>2</sub>O</b> . . . . .	159
C.2. T-dependent anti-symmetrised Gaussian and Brownian oscillator fit parameters for <b>Na<sub>2</sub>S<sub>2</sub>O<sub>3</sub>:5H<sub>2</sub>O</b> . . . . .	160
C.3. T-dependent Havriiliak-Negami fit parameters for <b>Na<sub>2</sub>S<sub>2</sub>O<sub>3</sub>:5H<sub>2</sub>O</b> . . . . .	161
D.1. Parameters for the OKE water model. . . . .	163



# List of Figures

1.1.	The basic states of matter. . . . .	2
1.2.	Possible paths when cooling a liquid. . . . .	3
1.3.	Critical radius needed for a nucleus to start crystallisation. . . . .	4
1.4.	Interaction potential from intermolecular forces. . . . .	5
1.5.	The intramolecular vibrations of water. . . . .	7
1.6.	The librational modes of water. . . . .	8
1.7.	Illustration of the translational diffusion. . . . .	9
1.8.	Illustration of the rotational diffusion. . . . .	10
1.9.	Generic terahertz spectrum. . . . .	10
1.10.	Transverse and longitudinal acoustic phonon. . . . .	11
1.11.	Transverse acoustic and optical phonon. . . . .	12
1.12.	Phonon dispersion relation. . . . .	13
1.13.	Charge ordering in ionic solids and liquids. . . . .	16
1.14.	A schematic of ion pairs and clusters in an ionic liquid. . . . .	16
1.15.	Schematic comparison between ion pairs in a solvent and an ionic liquid. . . . .	17
1.16.	Mesoscopic polar-apolar networks in ionic liquids. . . . .	18
1.17.	Kerr effect diagram. . . . .	20
1.18.	Schematic of a Michelson interferometer. . . . .	22
1.19.	Example of an interferogram. . . . .	22
1.20.	Scattering diagrams. . . . .	23
1.21.	Scattering Patterns. . . . .	24
2.1.	Diagram of the energy levels involved in a four level laser. . . . .	29
2.2.	Schematic laser cavity for a solid-state laser. . . . .	30
2.3.	Illustration of laser pulse dispersion. . . . .	31
2.4.	High time-resolution OKE set-up schematic. . . . .	33
2.5.	Long delay OKE set-up schematic. . . . .	36
2.6.	Attenuation of the amplified Legend Elite USX pulses. . . . .	37
3.1.	Anti-symmetrised Gaussian. . . . .	43
3.2.	Brownian Oscillator. . . . .	44
3.3.	Havriliak-Negami function. . . . .	44

3.4.	The influence of the rise modification on the shape of a Debye function. . . . .	45
3.5.	Illustration of possible reflections in an IR cell. . . . .	48
3.6.	Influence of the IR transformation on the Havriliak-Negami function. . . . .	49
3.7.	The influence of the decay modification on the shape of a Debye function. . . . .	51
4.1.	Structure of the tetrabutylammonium cation. . . . .	56
4.2.	Structure of the tributylmethylammonium cation. . . . .	57
4.3.	Structure of the tributylammonium cation. . . . .	57
4.4.	Background spectra of the IL far-IR measurements. . . . .	62
4.5.	Fitting process for the alkylammonium ILs. . . . .	64
4.6.	Terahertz spectra and fits of the liquid and crystalline tetrabutylammonium halides. . . . .	67
4.7.	X-ray powder scattering from tetrabutylammonium halides. . . . .	70
4.8.	Terahertz spectra and fits of the liquid and crystalline tributylammonium halides. . . . .	71
4.9.	Comparison of the OKE spectra for dry and wet tributylammonium chloride. . . . .	73
4.10.	Terahertz spectra and fits of the liquid and crystalline tributylmethylammonium halides. . . . .	74
4.11.	Terahertz spectra of the crystalline ethylammonium chlorides compared to their butylammonium chloride counterparts. . . . .	76
5.1.	Proposed phase diagram for non-crystalline water including the LLC. . . . .	91
5.2.	X-ray background subtraction for aqueous eutectic LiSCN solutions. . . . .	98
5.3.	Comparison of the OKE spectrum of $\text{LiSCN:12H}_2\text{O}$ with the calculated spectrum of the water fraction. . . . .	99
5.4.	OKE spectra of aqueous LiSCN solutions. . . . .	101
5.5.	T-dependence of the eutectic LiSCN fit. . . . .	102
5.6.	OKE spectrum analysis for an aqueous eutectic LiSCN solution. . . . .	104
5.7.	Fit for the X-ray scattering of $\text{LiCl:7H}_2\text{O}$ . . . . .	106
5.8.	T-dependent X-ray scattering of $\text{LiCl:7H}_2\text{O}$ . . . . .	107
5.9.	Temperature of the scans taken for $\text{LiCl:7H}_2\text{O}$ . . . . .	108
5.10.	Amplitudes of the X-ray scattering for an eutectic aqueous LiCl solution. . . . .	108
5.11.	Position and widths of the Gaussian lineshape functions in the LiCl X-ray scattering fit. . . . .	109
5.12.	T-dependent X-ray scattering of $\text{LiSCN:5.8H}_2\text{O}$ . . . . .	111
5.13.	Temperature of the scans taken for $\text{LiSCN:5.8H}_2\text{O}$ . . . . .	112
5.14.	Fit for the X-ray scattering of $\text{LiSCN:5.8H}_2\text{O}$ . . . . .	112
5.15.	T-dependent X-ray scattering amplitudes of $\text{LiSCN:5.8H}_2\text{O}$ . . . . .	113

5.16.	T-dependent X-ray scattering fit parameters of <b>LiSCN:5.8H<sub>2</sub>O</b> . . . . .	113
5.17.	The T-dependent IR spectrum of <b>LiCl-SCN:7H<sub>2</sub>O</b> . . . . .	114
5.18.	T-dependence of fit parameters for <b>LiCl-SCN:7H<sub>2</sub>O</b> . . . . .	115
5.19.	The T-dependence of the $\nu_{CN}$ asymmetric stretch in <b>LiCl-SCN:7H<sub>2</sub>O</b> . . . . .	116
5.20.	The T-dependent IR spectrum of <b>LiCl-SCN:9H<sub>2</sub>O</b> . . . . .	117
5.21.	Pump-probe IR spectra for <b>LiCl-SCN:7H<sub>2</sub>O</b> . . . . .	118
5.22.	Pump-probe vibrational lifetimes of the $\nu_{CN}$ stretch mode for <b>LiCl-SCN:7H<sub>2</sub>O</b> . . . . .	119
6.1.	T-dependent water OKE spectra. . . . .	132
6.2.	Space-filling three-dimensional model of the thiosulfate anion. . . . .	133
6.3.	Comparison of water and <b>Na<sub>2</sub>S<sub>2</sub>O<sub>3</sub></b> OKE spectra. . . . .	134
6.4.	OKE spectrum of <b>Na<sub>2</sub>S<sub>2</sub>O<sub>3</sub>:5H<sub>2</sub>O</b> at 25 °C. . . . .	135
6.5.	T-dependence of the <b>Na<sub>2</sub>S<sub>2</sub>O<sub>3</sub>:5H<sub>2</sub>O</b> OKE spectra. . . . .	137
6.6.	Change in the <b>Na<sub>2</sub>S<sub>2</sub>O<sub>3</sub>:5H<sub>2</sub>O</b> librations with temperature. . . . .	138
6.7.	Comparison of the <b>Na<sub>2</sub>S<sub>2</sub>O<sub>3</sub>:5H<sub>2</sub>O</b> and <b>Na<sub>2</sub>S<sub>2</sub>O<sub>3</sub>:32.7H<sub>2</sub>O</b> OKE fits. . . . .	141
A.1.	DSC measurement of tetraethylammonium chloride. . . . .	149
A.2.	OKE TD data for the butylammonium halides. . . . .	151
B.1.	OKE TD data for <b>LiSCN:5.8H<sub>2</sub>O</b> . . . . .	155
B.2.	OKE TD data for <b>LiSCN:12H<sub>2</sub>O</b> . . . . .	155
C.1.	Crystal structure for the <b>Na<sub>2</sub>S<sub>2</sub>O<sub>3</sub> · 1.25H<sub>2</sub>O</b> monoclinic prisms. . . . .	157
C.2.	Crystal structure for the <b>Na<sub>2</sub>S<sub>2</sub>O<sub>3</sub> · 2H<sub>2</sub>O</b> monoclinic rods. . . . .	158
C.3.	OKE TD data for <b>Na<sub>2</sub>S<sub>2</sub>O<sub>3</sub>:5H<sub>2</sub>O</b> . . . . .	162
C.4.	OKE TD data for <b>Na<sub>2</sub>S<sub>2</sub>O<sub>3</sub>:32.7H<sub>2</sub>O</b> . . . . .	162



# Acknowledgements

Here, I would like to thank all the people who helped me on my PhD journey. I was lucky enough to have a great supervisor in Prof. Klaas Wynne, whose vision, teaching, and support were crucial to the completion of this project. Next, I would like to thank the people in the Wynne group over the years. Chris, Gopa, Mario: Thank you for your perspective and guidance on being a PhD student. I enjoyed our discussions, both academical and about everything else. The same goes for my fellow PhD students, Asia, Finlay and Andrew. It was awesome to have a group which is so supportive and great company. Your company made it bearable when things did not work (again).

I would also like to thank my friends, who put up with my endless complaints and were still encouraging and supportive. Thanks for making sure I had a good time, regardless of how my studies were going at the moment. Special thanks go to Torjei, who was the best flatmate I could have asked for while writing this thesis.

Last but not least, I would like to thank my family for being there for me and always believing in me. For being understanding when I couldn't be around much because I did not want to leave my work. I am lucky to have you. In that vein, I want to dedicate this thesis to my grandpa Jean, who I hope would have been incredibly proud if he was still around.



## Author's declaration

“I declare that, except where explicit reference is made to the contribution of others, this dissertation is the result of my own work and has not been submitted for any other degree at the University of Glasgow or any other institution.”

Printed Name: Judith Reichenbach

Signature: \_\_\_\_\_

Chapter 4 was reproduced in part with permission from Reichenbach, J.; Rud-  
dell, S. A.; González-Jiménez, M.; Lemes, J.; Turton, D. A.; France, D. J.;  
Wynne, K. *J. Am. Chem. Soc.* **2017**, *139*, 7160. © 2017 American Chemical So-  
ciety.

This work was supported by the Engineering and Physicals Sciences Research  
Council [grant number EP/J009733/1, EP/J00975X/1, and EP/K034995/1] as well  
as a Chemistry Bank scholarship from the University of Glasgow.





# Abbreviations

AIMD	<i>ab initio</i> molecular dynamics
AUC	analytical ultracentrifugation
CIP	contact ion pair
CNT	classical nucleation theory
DFT	density functional theory
DRS	dielectric relaxation spectroscopy
DSC	differential scanning calorimetry
EAN	ethylammonium nitrate
ESI-MS	electrospray ionisation mass spectrometry
FT	Fourier transform
FTIR	Fourier transform infrared
FWHM	full width at half-maximum
HDA	high-density amorphous ice
HDL	high-density liquid water
IL	ionic liquid
IR	infrared
LA	longitudinal acoustical phonon
LDA	low-density amorphous ice
LDL	low-density liquid water
LiCl	lithium chloride
LiSCN	lithium thiocyanate
LLCP	liquid-liquid critical point
LO	longitudinal optical phonon
MS	mass spectrometry
MD	molecular dynamics
Na <sub>2</sub> S <sub>2</sub> O <sub>3</sub>	sodium thiosulfate
NMR	nuclear magnetic resonance
OKE	optical Kerr effect
PE	polyethylene
PNC	pre-nucleation cluster
PTFE	poly(1,1,2,2-tetrafluoroethylene)
SAXS	small-angle X-ray scattering
SED	Stokes-Einstein-Debye
SNR	signal-to-noise ratio
TA	transverse acoustical phonon
THz-TDS	terahertz time-domain
TO	transverse optical phonon
TPX	poly(4-methyl-1-pentene)
VdW	Van der Waals

# Nomenclature

$A(\omega)$	absorbance
$\alpha(\omega)$	absorption coefficient
$c$	speed of light
$\tilde{\epsilon}(\omega)$	complex dielectric function
$\gamma$	damping parameter
$n(\omega)$	refractive index
$\omega_0$	undamped oscillator angular frequency
$\omega$	angular frequency
$\tau$	relaxation time
$t$	time



# 1. Introduction

The aim of this thesis is to study the structures and dynamics of selected ionic liquids (ILs) and aqueous solutions using ultrafast spectroscopy techniques. Section 1.1 will introduce basic concepts concerning states of matter, their structures, and transitions. There, special attention will be given towards the structure, and resulting dynamics, in liquids. Furthermore, an overview of ILs will be given, as they tend to behave differently than molecular liquids, which are generally more well known. Section 1.2 will introduce the major techniques used to probe structure in these studies, which are optical Kerr effect (OKE) spectroscopy, far-infrared (IR) spectroscopy and X-ray scattering.

## 1.1. Matter and Transitions

Broadly, matter is classified into three states - gas, liquid and solid - which are illustrated in Fig. 1.1. Gases completely fill any container they are put into, liquids adjust their form, but not their volume, to the container while solids keep their form. This behaviour can be understood by looking at the structures associated with these states. Gases can be envisioned as randomly moving particles with only negligible interactions between them, such as in the noble gases. In solids, on the other hand, particles are assumed to be in a defined, nearly static position. Here, strong interactions between the particles result in the long range order which governs those positions, as exemplified in crystal lattices. Looking at these two extremes, it is easy to see the states of matter can be understood as a competition between disorder caused by movement and ordering due to particle interactions. As liquids are an intermediary between the solid and the gaseous state, even the simplified model is more complex than in either of the two other states. The classical picture for a liquid has interactions strong enough to cause local ordering, yet weak enough that, at longer distances, disorder is caused by the thermal movement of particles. These are, of course, rather simplified models, as glasses, liquid crystals, amorphous solids and viscoelastic materials are not classified in them.

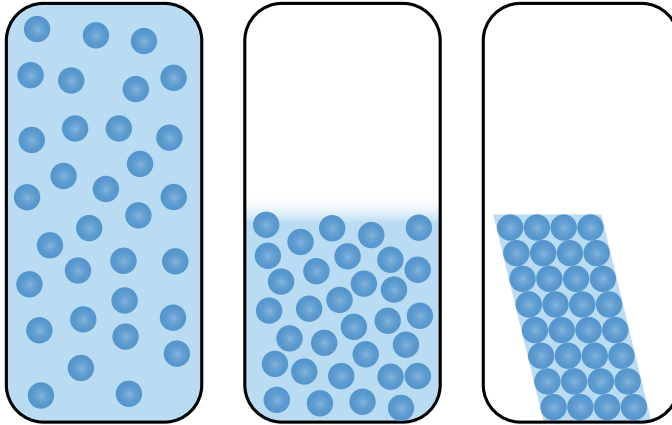


Figure 1.1.: The three basic states of matter: gas, liquid and solid (from left to right).

As said above, the difference between the solid, liquid and gaseous state can be understood in terms of the importance of the ordering due to particle interactions versus the disorder caused by particle movement. The particle movements, expressed as the average kinetic energy stored in the material, is directly related to the material's temperature. Therefore, the transition temperature between the states depend on the strength of the particle interactions which need to be overcome. Thermodynamically, this is described using the Gibbs free energy of the system,

$$G(p, T) = H - TS, \quad (1.1)$$

in which  $p$  is the pressure,  $T$  the temperature,  $H$  the enthalpy and  $S$  the entropy. If the interaction strength or the structure change during a transition, both the enthalpy and the entropy will change at the transition temperature, leading to a discontinuous slope  $\left(\frac{\partial G}{\partial T}\right)_p$ . Due to this the heat capacity,  $C_p = \left(\frac{\partial H}{\partial T}\right)_p$  will then show a singularity at the transition temperature. Usually, supplying heat to a material can be visualised as an increasing of the stored kinetic energy, which is equivalent to raising the temperature of the material. At the heat capacity singularity, however, the supplied energy is used up to break interactions and move particles, resulting in no temperature increase. Therefore, it appears as if the material can store infinite amounts of heat. Because the first partial derivative is discontinuous, this is called a “first-order phase transition”. In a second-order phase transition, on the other hand, the first derivative is continuous, while the second derivative is discontinuous. Therefore, the heat capacity does show a discontinuity at the transition temperature instead of the singularity observed in the first-order phase transition. Because the interaction energy, volume, and entropy cannot change during the transition, this implies a change in the symmetry of the structure as the cause of the transition. However, even though thermodynamically a transition is expected to occur if a different structure has a lesser free energy at a certain temperature, this does not always

happen immediately. A system can be metastable if it has a higher energy but is kinetically hindered, meaning that the movements necessary to change the structure cannot be performed. This can, for example, be seen when a liquid is supercooled. Because the movements necessary for the liquid to solidify are slow on experimental time scales, the liquid appears stable even when it is not.

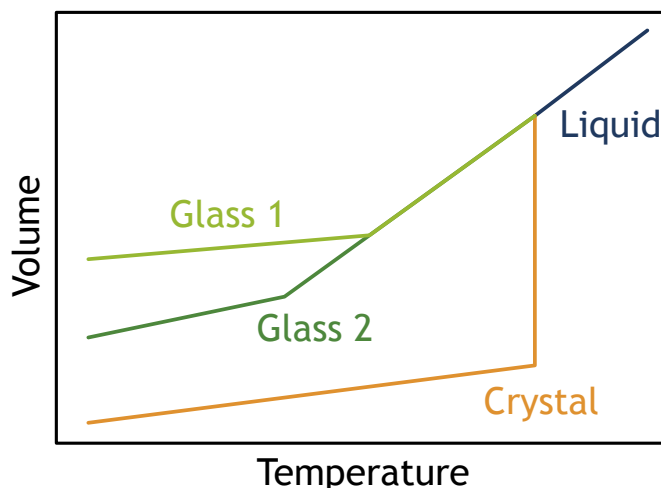


**Figure 1.2.:** Possible paths when cooling a liquid. The cooling speed determines whether the system will form a crystal or get arrested in a glassy state.

This is taken to the extreme in the formation of glasses, which macroscopically behave like solids but microscopically resemble the liquid structure. As the liquid structure is basically “frozen-in” in the glass, the transition is a kinetic rather than a thermodynamic one. This is achieved by lowering the temperature of the material fast enough to avoid crystallisation until the viscosity approaches infinity (see Fig. 1.2). However, this is only possible because crystallisation is not an instantaneous process. Crystallisation has been described for nearly a century by classical nucleation theory (CNT) since its formulation in the 1930s by Becker and Döring.<sup>[1]</sup> They, in turn, based their work on earlier nucleation treatments by Volmer and Weber,<sup>[2]</sup> as well as Farkas,<sup>[3]</sup> which were based on thermodynamical descriptions of droplet formation derived by Gibbs.<sup>[4]</sup>

Crystal growth in a solution is thermodynamically driven but tends to be kinetically hindered, rendering the solution metastable. In CNT, crystal growth starts once a nucleus above a critical size is formed. This critical size is determined by an interplay between the decrease in free energy from forming the thermodynamically favoured bulk phase versus the unfavourable increase in free energy caused by the interface between the liquid and the nucleus. Using the free energy of the bulk  $\Delta G_b$  and the interfacial energy  $\gamma_{sl}$ , the critical nucleus size can be calculated from<sup>[5]</sup>

$$\Delta G_n(r) = \frac{4}{3}\pi r^3 \Delta G_b + 4\pi r^2 \gamma_{sl}. \quad (1.2)$$

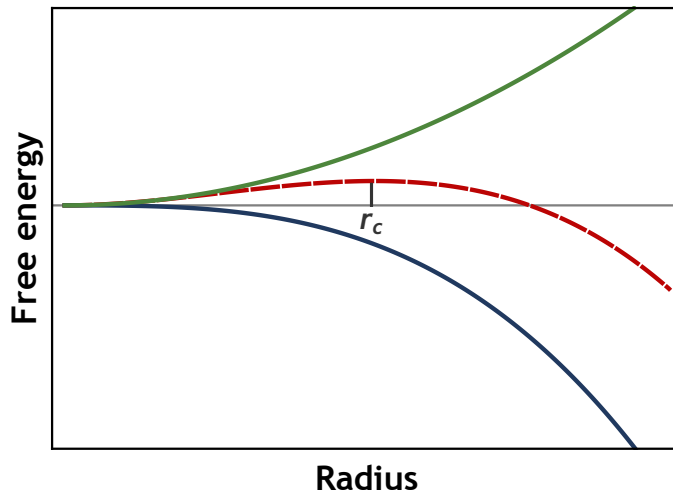


**Figure 1.3.:** Critical radius needed for a nucleus to start crystallisation. Shown are the destabilising surface term (green) and stabilising bulk term (blue), as well as the resulting free energy of a nucleus (red). The critical radius is defined as the radius at the maximum of the energy barrier.

The different radius dependencies of the competing terms, shown in Fig. 1.3, cause a maximum in the free energy which defines the critical nucleus size, after which growth will set in. However, the sign of the bulk free energy,  $\Delta G_b$ , is temperature-dependent, meaning that crystal growth will only occur if the crystal phase is thermodynamically favourable. In CNT, these nuclei are assumed to form through random density fluctuations, which aggregate the necessary amount of particles in the nucleus volume. Therefore, the chance that a nucleus of critical size forms is rather low and the probability  $P$  can be described by

$$\begin{aligned}
 P &\propto e^{-\Delta G^*/k_B T} \\
 &\propto e^{-1/T^3},
 \end{aligned}
 \tag{1.3}$$

with  $\Delta G^*$  denoting the height of the free energy barrier at the critical nucleus size.<sup>[5]</sup> Nuclei below the critical size are expected to be transient and dissolve again. Therefore monomers, or at most small aggregates like dimers, are expected in solution. The nucleus formation shown above is called *homogeneous* nucleation, as it only depends on density fluctuations in the liquid phase. However, the energy barrier can be changed by the presence of solid particles, on which the nucleus can form. This is because the interfacial energy  $\gamma_{ab}$  depends on the two phases,  $a$  and  $b$ , between which the interface is formed. If the solid-solid interface has a more favourable energy  $\gamma_{ss}$ , the energy barrier will be lowered and the probability that a critical nucleus forms will increase. This is called *heterogeneous* nucleation and is the primary cause of most observed crystallisation.<sup>[5]</sup>

### 1.1.1. Structure and Dynamics in Liquids

Previously, structures and intermolecular interactions were mentioned, but not specified. Here, more detail will be given on the interactions which cause structure, as well as the dynamics which arise. As the presented studies focus on liquids and solutions, all further discussion in this section will be done for the liquid state, unless specified otherwise.

#### Intermolecular Forces

Intermolecular forces define the interaction potential of particles, such as atoms, molecules, and ions, and each has a characteristic distance dependence found in Table 1.1. Many depend on transient or permanent multipoles present in the particles, but for simplicity, only dipoles will be considered in the following. Roughly speaking, a repulsive potential prevails when particles nearly overlap, while at longer distances attractive interactions dominate. These attractive interactions are caused by interacting dipoles or charges. Examples for this can be found in Fig. 1.4, which considers the Pauli repulsion, London dispersion, and an attractive Coulomb interaction. The Coulomb interaction is a special case in this regard, because the potential can be either attractive or repulsive depending on whether opposite or same sign charges are considered.

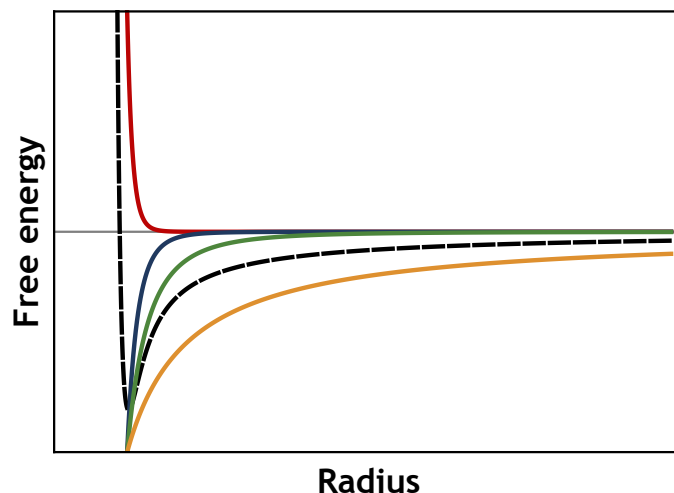


**Figure 1.4.:** Interaction potential from intermolecular forces. Plot of the distance dependence for the Pauli repulsion (red), London dispersion or Debye interaction (dark blue), Keesom interaction (green) and the attractive Coulomb interaction (orange). The resulting interaction potential is given by the black dashed line.

The repulsive interaction, also called Pauli repulsion, is based on the Pauli exclusion principle. It states that two fermions, such as electrons, cannot both occupy

Table 1.1.: Distance dependence of the intermolecular interaction potentials.

Interaction	Distance dependence
Pauli repulsion	$+R^{-12}$
induced dipole - induced dipole	$-R^{-6}$
dipole - induced dipole	$-R^{-6}$
dipole - dipole	$-R^{-3}$ to $-R^{-6}$
charge - charge	$-R^{-1}$

a state with exactly the same quantum numbers. This limits the space around a nucleus in which the electron clouds can overlap and, in a very simple picture, leads to the particles behaving like hard spheres. Deriving an exact mathematical expression for the Pauli repulsion is difficult and in practice empirical functions with an extremely steep slope are used, such as exponentials or high inverse powers. [5]

The interactions of induced and permanent dipoles with themselves and each other are often grouped together as Van der Waals (VdW) forces. [6] They can be further classified into the interactions between induced dipoles (London dispersion), between permanent and induced dipoles (Debye interaction), and between permanent dipoles (Keesom interaction). Of these, the London dispersion is the weakest but most ubiquitous force and is considered mainly between uncharged particles with no permanent dipole moment. It is based on transient dipole moments caused by electron density fluctuations, which induce further dipoles in the surrounding particles. These transient, induced dipoles then interact with each other, leading to a weak, attractive potential decaying with  $R^{-6}$  as shown in Fig. 1.4. [5,6] The Debye and Keesom interactions are more straightforward, as they are based on permanent dipole moments. In the Debye interactions, permanent dipole moments induce transient dipole moments in the surrounding particles and then interact with them, while in the Keesom interactions permanent dipole moments interact with each other. Their potentials can reach to longer distances, with an  $R^{-6}$  and  $R^{-3}$  to  $R^{-6}$  dependence, respectively (see Fig. 1.4). [6] Finally, the electrostatic forces between charges are described by the Coulomb interaction, which, with a distance dependence of  $R^{-1}$  (see Fig. 1.4), is stronger and more long-ranged than the other attractive forces covered above. [5]

Depending on the type of molecule, further interactions have to be taken into account. Most notable among these are hydrogen bonds and hydrophobic interactions. Hydrogen bonds are directional, partially covalent interactions between a partially positive hydrogen atom and the lone electron pair of an electronegative atom. [5,6] They are, for example, the main driving force behind the structure

which causes water to be liquid between 0 °C and 100 °C. Hydrophobic interactions, on the other hand, occur in solutions and are driven by the entropy of the solvent, which is often water.<sup>[5,6]</sup> When a solute is dissolved in a solvent, the solvent molecules will form a solvation shell around the solute. If the interaction between solute and solvent molecule is unfavourable, such as for a polar and an apolar molecule, the solvent will form tight cages around the solute molecules to minimise interaction with them, which decreases the entropy of the solvent. Solvent molecules can be released from this highly structured network, however, only if the surface area between solutes and solvent is reduced. This leads to the solute molecules aggregating together to minimise the solute-solvent surface and increase the total entropy.

## Dynamics

The ordering from intermolecular forces in liquids leads to different motions, which can be detected with spectroscopic techniques. Going from high to low frequencies, these are intramolecular vibrations, librations, cage rattling, cage diffusion and rotational diffusion. A more detailed description of these motions will be given below. In a molecule, each atom has three degrees of freedom to

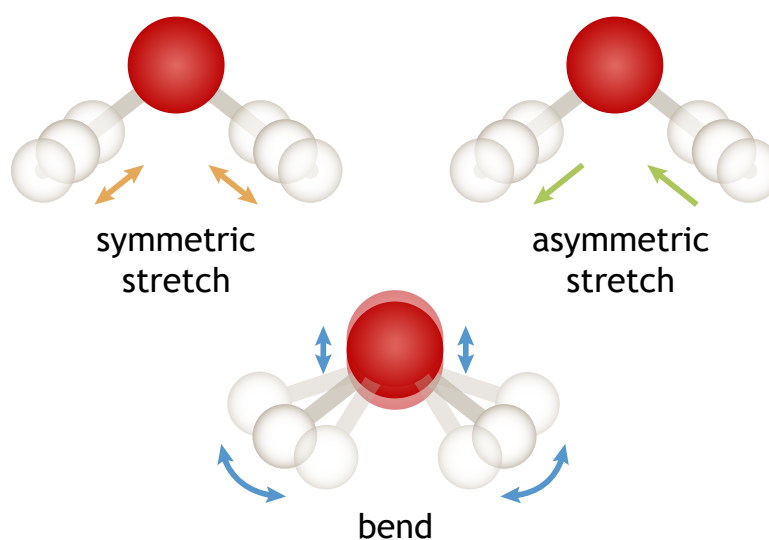


**Figure 1.5.:** The intramolecular vibrations of water. Shown are, from the top left in clockwise direction, the symmetric stretching mode, the asymmetric stretching mode and the bending mode.

move, leading to  $3N$  degrees of freedom in a molecule made out of  $N$  atoms. Out of these, three degrees of freedom are taken up by the translational movement of the molecule in the frame of reference. Furthermore, the molecule can rotate around its axes, taking up three more degrees of freedom, or two in a linear molecule. This leaves  $3N - 6$  degrees of freedom (or  $3N - 5$  for a linear

molecule) for motions in which the atoms move relative to each other, meaning intramolecular vibrations. These are illustrated for water, a non-linear molecule made out of three atoms, in Fig. 1.5. In the symmetric stretch, the hydrogen atoms move simultaneously in the same direction along their bonds, while they move in opposite directions in the asymmetric stretch. The bend, meanwhile, consists of a periodic change in the angle between the three atoms. The timescales, and therefore frequencies, of these motions depend on the weight of the atoms and how complex the motion is. Motions involving many atoms or heavy atoms tend to be slow and appear at low frequencies. An example of this are torsional motions in alkyl chains around 10 THz<sup>[7]</sup> which occur on a timescale of 100 fs. If few, or light, atoms are involved, the vibrations tend to be fast. This is seen in the stretch of the hydrogen molecule, found at 120 THz, meaning it occurs on a timescale of 8 fs.<sup>[8]</sup> Intramolecular vibrations in a liquid are usually similar to those found in isolated molecules in the gas phase. The interactions with surrounding molecules, however, generally lead to a broadening of the mode and, sometimes, to a shift of the centre frequency.

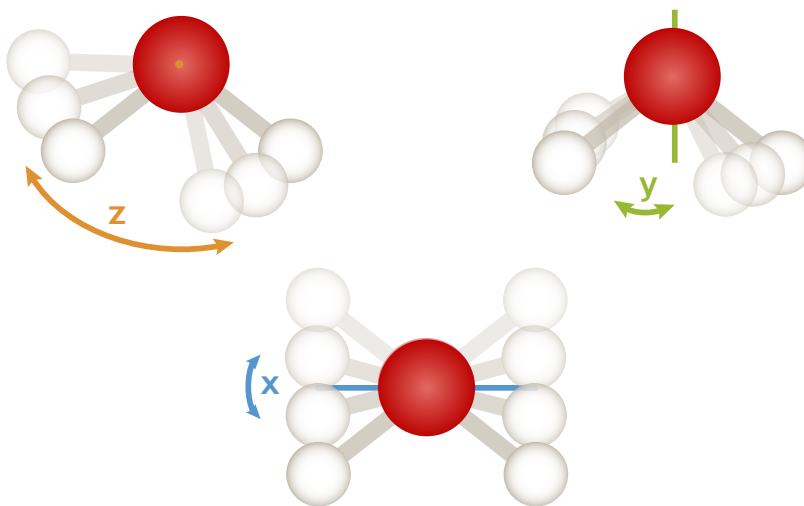


**Figure 1.6.:** The librational modes of water around its three perpendicular axes (x, y, z in anti-clockwise direction from the bottom).

At similar or lower frequencies, librational modes can be found. Librations, as shown in Fig. 1.6 for water, can be understood as hindered rotations in a cage. Because librations tend to occur on timescales of 100 fs to 1 ps (1-10 THz), the translational motions of the surrounding particles are assumed to be negligible. This means they are effectively “frozen” in their positions and therefore can be considered a static cage around the librating molecule. Because the structure in liquids is not ordered as strictly as in a crystal, a distribution of cage structures is expected. This leads to a broadening of the librational modes in the frequency domain. Furthermore, librations are rotational motions, meaning they depend on the moment of inertia of the molecule. Since the moment of inertia depends on

the rotation axis in non-spherical molecules, a molecule can have more than one librational frequency.

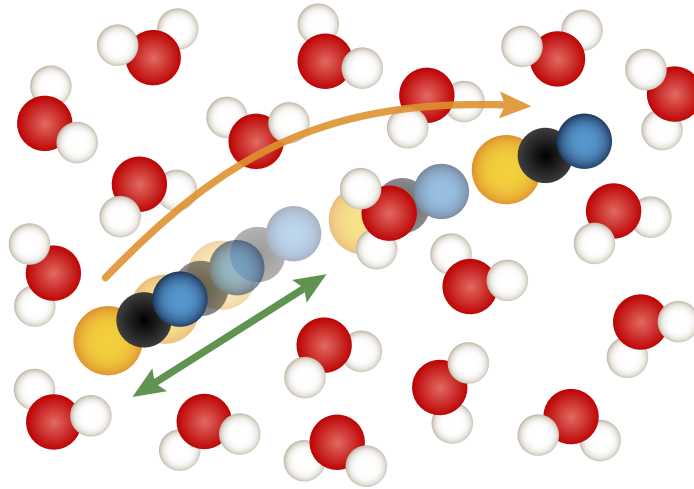


**Figure 1.7.:** Illustration of the translational diffusion, comprised of cage rattling (green arrow) and cage diffusion (orange arrow).

Of course, the molecule is not restricted to rotational motions inside the cage of surrounding molecules. The translational motion, illustrated in Fig. 1.7, is called cage rattling and has a timescale of 150 to 500 fs (2-6 THz). At longer times, the movement of the surrounding molecules is no longer negligible, allowing the trapped molecule to escape. This is called cage diffusion and is illustrated in Fig. 1.7. The timescales of this depend on the shear viscosity  $\eta$  of the bulk liquid as well as the size of the molecules, and are usually estimated from the Stokes-Einstein (SE) relation<sup>[6]</sup> for translational diffusion,

$$D_{trans} = \frac{k_B T}{6\pi\eta R}. \quad (1.4)$$

Here,  $D_{trans}$  denotes the translational diffusion coefficient and  $R$  the radius of the (spherical) particle. Practically, it can be hard to distinguish between the cage rattling and cage diffusion modes in a spectrum, and both processes end up being collectively described as the  $\beta$ -relaxation.

The slowest relaxation is, in general, the loss of orientation of the molecules by random tumbling, which is referred to as rotational diffusion or  $\alpha$ -relaxation (see Fig. 1.8). The timescales, and therefore frequencies, are often related<sup>[9]</sup> to the particle volume  $V$  and the shear viscosity  $\eta$  of the bulk liquid through the Stokes-Einstein-Debye (SED) relation

$$D_{rot} = \frac{k_B T}{6\eta V}, \quad (1.5)$$

where  $D_{rot}$  is the rotational diffusion coefficient. However, caution has to be applied when using the SE or SED relation because of the dependency on macroscopic bulk properties, such as the shear viscosity. The use of these implies that

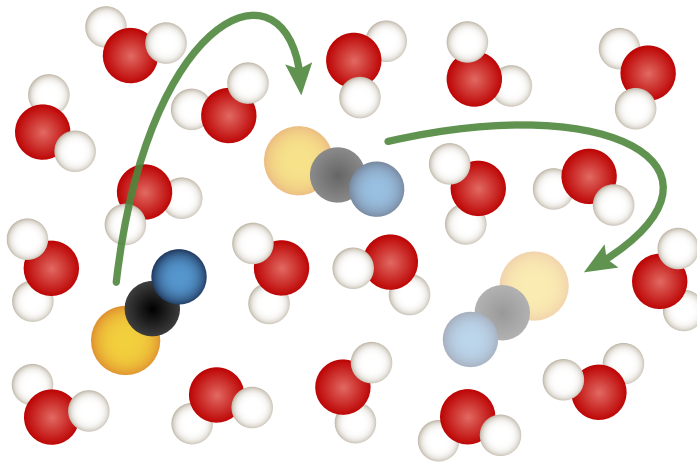


Figure 1.8.: Illustration of the rotational diffusion by random tumbling of the molecules.

the intermolecular interactions between the diffusing particle and the other molecules are negligible. <sup>[10]</sup>

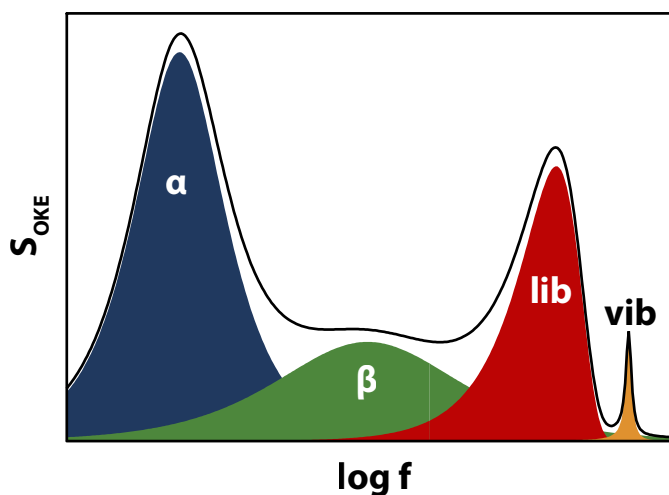
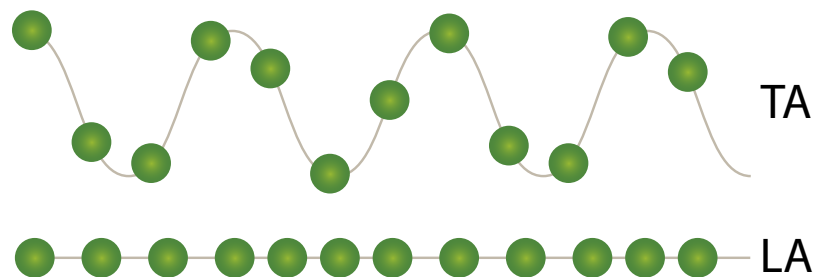


Figure 1.9.: A generic terahertz OKE spectrum plotted along a logarithmic frequency axis. From high to low frequency are intramolecular vibrations (orange), a librational mode (red), as well as relaxational modes. These are the translational  $\beta$ -relaxation (green), stemming from cage rattling and cage diffusion motions, and the rotational  $\alpha$ -relaxation (dark blue).

In the description above it is noticeable that higher frequency motions, except intramolecular vibrations, depend on structures which are destroyed in the slower relaxational processes. This idea is described as sequential relaxation and postulates that the start of a slower intermolecular motion signifies the end of the faster preceding one. The practical impact of this is discussed in Section 3.3.2, where modifications for fit functions are derived to account for sequential relaxation.

## Phonons

A different case of structure-dependent dynamics is phonons. Mostly visualised as crystal vibrations, the term phonon refers to the long-range collective motion of particles in a structured environment. Strictly speaking it is defined for (infinite) crystal lattices, however, phonon-like modes have been reported in amorphous solids,<sup>[11]</sup> DNA,<sup>[12]</sup> and liquid helium,<sup>[11]</sup> among others. The simplest way of visualising phonons is to look at a one-dimensional chain of particles. If all particles are indistinguishable, they then can move to make two different types of waves, longitudinal and transverse ones, as seen in Fig. 1.10. In a longitudinal phonon, the particles move on the line of their starting positions while in a transverse phonon they move perpendicularly to that line. Therefore, as there are two vectors both perpendicular to the line and to each other, two transverse phonons exist. However, if the two transverse directions are identical, the phonons degenerate into one mode. This is called the acoustic phonon branch, as it is similar to an acoustic wave travelling through a solid because neighbouring particles tend to move in the same direction. The longitudinal and transverse modes are commonly referred to as the longitudinal acoustical phonon (LA) and transverse acoustical phonon (TA) phonon modes.



**Figure 1.10.:** Illustrations of the TA and LA phonon in a one-dimensional chain of particles.

If the chain is made up of at least two alternating, distinguishable types of particles, an additional phonon branch emerges. It is called the optical phonon branch and, unlike in the acoustic branch, the neighbouring particles move in opposite directions, as illustrated in Fig. 1.11. The longitudinal and transverse modes are then called the longitudinal optical phonon (LO) and transverse optical phonon (TO) phonon modes. Given the distinguishable particles are the anions and cations of an ionic crystal, the oscillating charges of the phonon can be excited by electromagnetic waves, such as light, hence the term “optical phonon”. In general, the number of phonons is defined by the number of atoms found in the primitive unit cell, which is the smallest repeatable unit in the crystal lattice.<sup>[13]</sup> For a three-dimensional crystal with  $p$  atoms in the primitive unit

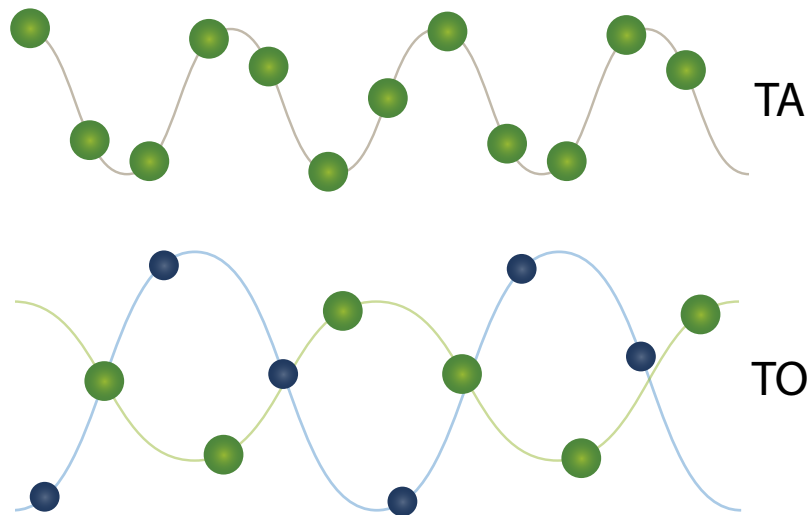


**Figure 1.11.:** Illustrations of the TA and TO phonon in a one-dimensional chain of particles.

cell, the possible number of phonon modes is  $3p$ . Out of these, 3 are acoustic phonons and  $3p - 3$  are optical phonons.

The periodic order of the crystal lattice lends itself to a Fourier transformation, which yields the reciprocal lattice. The reciprocal lattice, and reciprocal space in general, are useful concepts, particularly for the understanding of scattering processes. Instead of distances, like in real space, the underlying quantity in reciprocal space is the wavevector  $k$ . Alternatively,  $k$  can be understood as the momentum of quasiparticles, here phonons, which are the quasiparticles of the lattice vibrations. The positions of the reciprocal lattice points is related to the distances between planes of atoms in the crystal lattice and therefore can be directly measured in X-ray diffraction patterns (compare Section 1.2.3). The primitive unit cell in the reciprocal lattice is called the “Brillouin zone”, which is the smallest repeatable unit in reciprocal space. The Brillouin zone is an important concept, as it contains all scattering wavevectors  $q$  (see X-ray scattering in Section 1.2.3) as well as all wavevectors necessary to describe lattice motions. Because of the wave-particle duality, the wavevector of the phonon can be related to its frequency, which is expressed in the dispersion relation  $\omega(k)$ . The dispersion relation of a linear diatomic chain can be seen in Fig. 1.12 and two extreme cases can be observed. One is the behaviour at the Brillouin zone centre with  $k = 0$  and the other is the behaviour at the Brillouin zone edge, which is located at  $k = \pi/a$  where  $a$  is the size of the unit cell in real space. At the zone edge, the phonon has a wavelength equivalent to the size of the unit cell in real space. This can be interpreted as an oscillation of the two atoms located in the unit cell. Meanwhile, the low  $k$  value near the zone centre is associated with long wavelengths. As the wavelength becomes much longer than the crystal

lattice spacing, the lattice is effectively seen as a continuum. At wave vectors very close to  $k = 0$ , the wavelength approaches the size of the crystal and the phonon can be interpreted as delocalised.

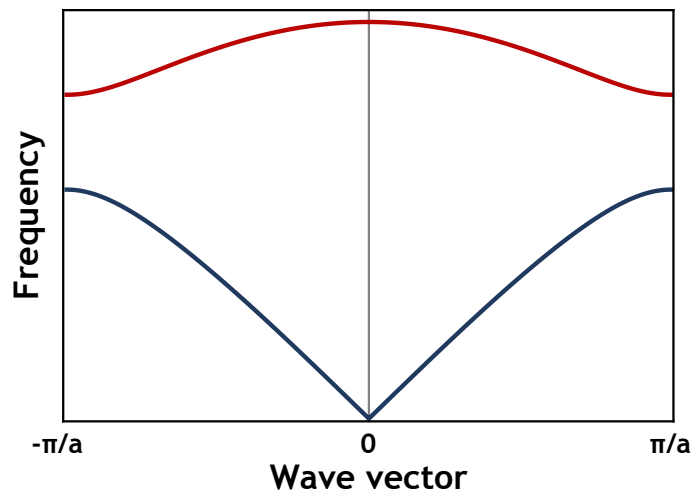


**Figure 1.12.:** Phonon dispersion relation for a diatomic one-dimensional chain. Shown are the optical phonon branch (red) at high frequencies and the acoustic phonon branch (blue) at low frequencies.

In ionic crystals, differently charged ions oscillate in different directions for the optical phonon modes. This produces an electric field, which interacts differently with the TO modes than with the LO mode. The frequency difference is described by the Lyddane-Sachs-Teller relation, <sup>[11]</sup>

$$\omega_{LO}^2 = \frac{\epsilon_0}{\epsilon_\infty} \omega_{TO}^2, \quad (1.6)$$

where  $\epsilon_0$  and  $\epsilon_\infty$  are the dielectric constant at low and high frequencies, respectively. Therefore, the TO modes are generally expected to be at lower frequencies than the LO mode in ionic crystals.

Usually, the technique of choice to measure phonons is neutron diffraction, which was not employed in the presented studies. However, in an ionic crystal, optical phonons are equivalent to oscillating charges and therefore can interact with light, making them accessible through spectroscopic techniques. Because momentum conservation is observed in the measurements, phonons can only be observed at wavevectors equal to the momentum imparted on the lattice during the measurement. Neutrons are particles with a mass and therefore can impart a momentum onto the lattice, making them able to probe the  $k$ -dependence of the phonon dispersion. Photons, on the other hand, are quasiparticles with an infinitesimally small momentum. Therefore, they cannot impart an appreciable momentum on the lattice and only phonon frequencies at  $k \approx 0$  are accessible.

In short, this means that spectroscopic techniques typically can only measure phonons at the zone centre. So far, the treatments of phonons has been done for the case of crystal lattices. However, in liquids, thermally induced disorder will disturb long-range order, leaving the concept of phonons ill-defined. On the other hand, as mentioned earlier, phonon-like modes have been found for amorphous substances.<sup>[11]</sup> Generally, a large unit cell is necessary to account for the variations in the structure. Therefore, liquids with a defined enough long-range order should be able to support phonons. This makes phonons an important concept to keep in mind for the study of ILs, where charge ordering is expected to result in a quasi-lattice.

### 1.1.2. Ionic liquids

Ionic liquids (ILs), as the name implies, are liquids made up (almost) exclusively of ions, differentiating them from (aqueous) salt solutions. This definition, of course, includes high-temperature molten salts, but colloquially “ionic liquids” is used for salts with melting points around or below 100 °C. For the liquid state to be preferred at such low temperatures, large and non-symmetric ions with inefficient packing tend to be necessary. Therefore, most ionic liquids are organic salts or mixtures of organic with inorganic salts. This is especially true for the cation, which generally includes alkyl groups and a nitrogen or phosphorus atom, while the anion can range from halide ions to nitrate and alkyl sulfonates. It follows that the potential number of simple ionic liquids is large, around  $10^6$ , with about 1500 reported so far. The possible number of binary and tertiary mixtures is exponentially larger.<sup>[14,15]</sup>

For a class of substances this large, it can be hard to generalise properties. Some, such as the refractive index, the solubility, and the miscibility, depend on the specific anion and cation combination.<sup>[14]</sup> Furthermore, it has been found that impurities, often evidenced by discolouration of the salt, have a profound impact on the physical, spectroscopic and chemical characteristics of ionic liquids<sup>[14,16]</sup>, for example leading to a different melting point.<sup>[17-22]</sup> The melting point, as mentioned earlier, is lowered by large ions with little symmetry due to their inefficient packing.<sup>[14,15]</sup> The ion size also increases the viscosity, which is usually between 10 and 500 cP<sup>[23]</sup> and as such one to two orders of magnitude higher than those of conventional molecular solvents.<sup>[14]</sup> Other commonly shown properties are electrical conductivity, as expected of a substance made of ions, and a wide electrochemical window of 2 - 6 V.<sup>[14]</sup> However, one of the most important features of ionic liquids is their low vapour pressure caused by the strong

Coulomb interactions between the ions, due to which they have been promoted as alternative solvents with less pollution or health concerns.<sup>[14,15]</sup> While distillation of selected ionic liquids at high temperatures and reduced pressure has been reported,<sup>[24]</sup> they are generally still less volatile than molecular solvents.<sup>[14,15]</sup>

The birth of ILs as a field is generally dated back to the synthesis of the first room-temperature ionic liquid, ethylammonium nitrate (EAN), by Walden in 1914,<sup>[25]</sup> due to Walden's recognition of its properties. Interest in ionic liquids as a research field peaked around 1998 due to their possible use in clean technology.<sup>[15,26,27]</sup> Industrially, ionic liquids have been used by several companies, for example BASF and Linde, in applications ranging from the removal of byproducts from a reaction,<sup>[28]</sup> over aluminium plating,<sup>[29]</sup> and gas capture,<sup>[30,31]</sup> to use as a piston<sup>[32]</sup> in a compressor.<sup>[15]</sup> Furthermore, they are studied for a variety of applications. Their low vapour pressure and dependence of some physical properties on the constituting ions, for example, makes them attractive as solvents for synthesis<sup>[33,34]</sup> and catalysis.<sup>[34,35]</sup> The combination of conductivity and a wide electrochemical window coupled with low vapour pressure and low flammability, on the other hand, makes them interesting candidates as electrolytes<sup>[33,36-39]</sup> in batteries and fuel cells, or as a medium for electrodeposition.<sup>[37]</sup> They can also serve as functional materials<sup>[40,41]</sup> by incorporating functional groups into the cation or anion, leading to photoresponsive materials, among others.

For furthering all this research, and especially for designing task-specific ionic liquids, it is of paramount importance to understand how the structure of ionic liquids impacts their properties. While classically, liquids are seen simply as diffusion disordered solids, this picture has recently been called into question.<sup>[40]</sup> Instead of an irregular but homogeneous medium, understandable through simple packing considerations,<sup>[42]</sup> evidence of defined structure has been found in different molecular liquids<sup>[43-45]</sup> which can be induced by hydrogen bonding or  $\pi$ - $\pi$  interactions, among others. This opens up several important questions regarding the structure of liquids, namely what the responsible interactions are and the length and time scales for which they apply. For ionic liquids, major interactions to take into account are VdW forces, Coulomb interactions, polar-apolar ordering as well as hydrogen bonding. The exact local arrangements can vary depending on the dominant interactions as well as their relative strength. Coulomb-induced charge ordering, for example, is a major structure factor in ionic liquids. On supramolecular length scales, ion pairs or ion clusters have to be taken into account, while on mesoscopic length scales hydrogen bond networks and polar-apolar ordering need to be considered. Illustrations of these types of ordering can be found in Figs. 1.13, 1.14 and 1.16, respectively, and an overview will be given below.

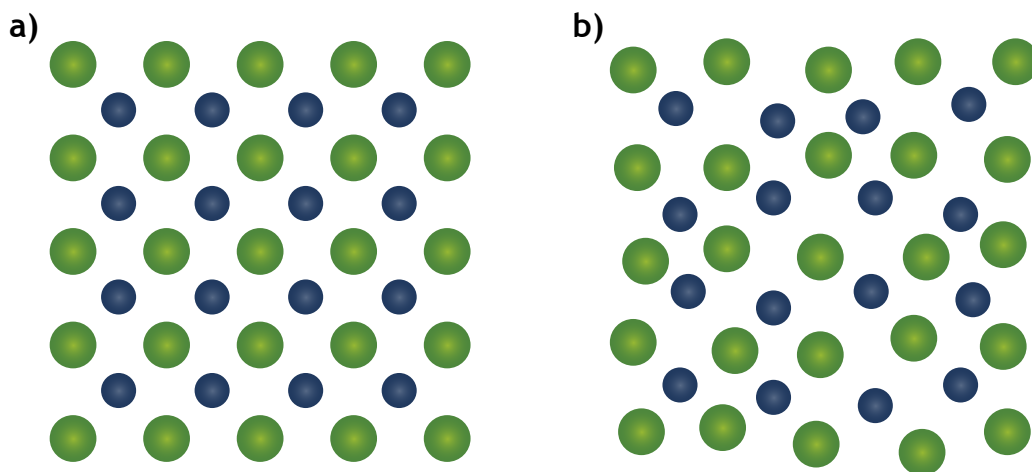


**Figure 1.13.:** Charge ordering in ionic solids and liquids. The illustrations show a) a simple charge-ordered lattice in a crystal and b) a diffusion-disordered quasilattice in the corresponding liquid.

Charge ordering, as illustrated in Fig. 1.13, is one of the most prominent structural influences in ionic liquids. Here, ions are surrounded by shells of oppositely charged ions due to the coulombic forces between them. The range of the coulombic interactions depends on how well the ion charge is screened, but generally decays with the square of the distance. The structure in liquids with charge ordering is often approximated from the crystal structure. Here, the ideally infinite lattice found in crystals is disturbed by diffusion. This shortens the length over which the lattice describes the liquids, so the term “quasi-lattice” or “pseudo-lattice” is often used. Further considerations on disturbed lattices can be found in Section 1.1.1.

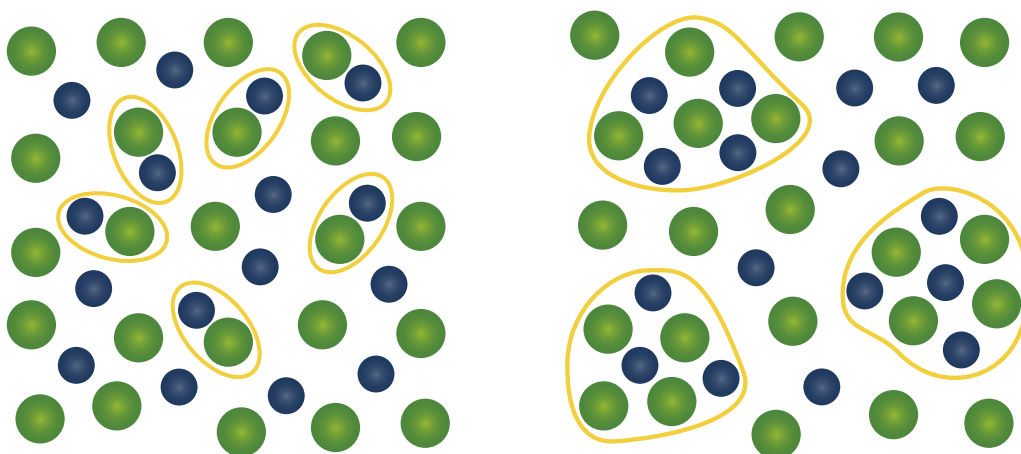


**Figure 1.14.:** A schematic of ion pairs and clusters in an ionic liquid.

The association of one cation and one anion to form a neutral, “quasimolecular” unit, as illustrated in Fig. 1.14a, is generally described as ion pair formation. The bulk ionic liquid is then described as a mixture of ion pairs and “free” ions.<sup>[40]</sup> Ion pairs as a concept originated in aqueous electrolyte solutions, where ions are separated by solvent molecules. As ionic liquids are solely made of ions, the

short distances between anions and cations lead to the expectation that close contact ion pairs will be formed.<sup>[40]</sup> However, this picture is inconsistent with much of the data collected on ionic liquids.<sup>[40]</sup> Unless the lifetime of ion pairs is very short, below several picoseconds,<sup>[46,47]</sup> a signal from their rotational diffusion should be picked up in dielectric,<sup>[48-52]</sup> OKE,<sup>[50-52]</sup> or nuclear magnetic resonance (NMR)<sup>[47]</sup> spectroscopy. Molecular dynamics (MD) simulations<sup>[53,54]</sup> offer an explanation for this, with calculations indicating that the short ion-ion distances support the association of one ion with multiple counterions, instead of just one, as illustrated in Fig. 1.15. Due to the surrounding shell of counterions, the potential towards any specific one would be shallow and any association forming an ion pair would be transient. Most importantly, ion pairs are known to be the gas phase species of evaporated ILs.<sup>[55]</sup> Therefore, if tightly bound ion pairs were a major species in the ionic liquid bulk, it would be hard to explain how ionic liquids retain their generally low vapour pressure.

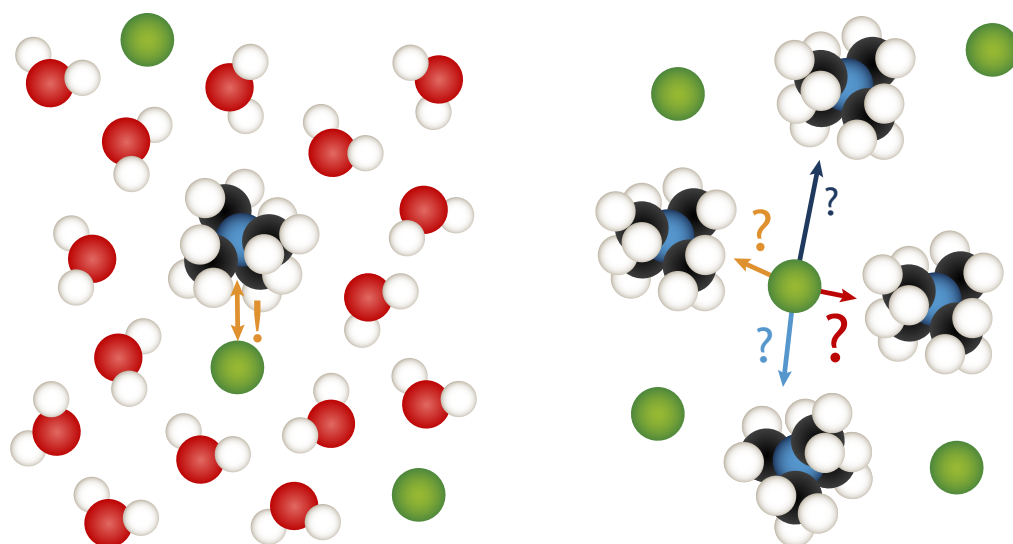


**Figure 1.15.:** Schematic comparison between ion pairs in a solvent and an ionic liquid.

In a similar fashion, ion clusters are used to explain ionic liquids as a sea of poly-disperse aggregates, which is illustrated in Fig. 1.14b. Much of the evidence concerning ion clusters is based on electrospray ionisation mass spectrometry (ESI-MS) results.<sup>[40,56-58]</sup> However, mass spectrometry (MS) does not measure the bulk liquid, meaning that results are vulnerable to artefacts introduced by cluster formation at the gas-liquid interface or through the ionisation method.<sup>[40]</sup> Theoretical calculations have been used to underpin MS,<sup>[59]</sup> far-IR,<sup>[60-64]</sup> and Raman spectroscopic results<sup>[65]</sup> on the basis of clusters. The preferred cluster size, will vary depending on the calculation.<sup>[40,59,65]</sup> NMR results which pointed to clusters existing in the liquid bulk<sup>[66,67]</sup> could not be reproduced in later studies with more precise instruments.<sup>[68,69]</sup> In summary, while ion clusters are used to describe the behaviour of ionic liquids, the evidence is ambiguous and many of the counterpoints raised against ion pairs also apply against ion clusters.

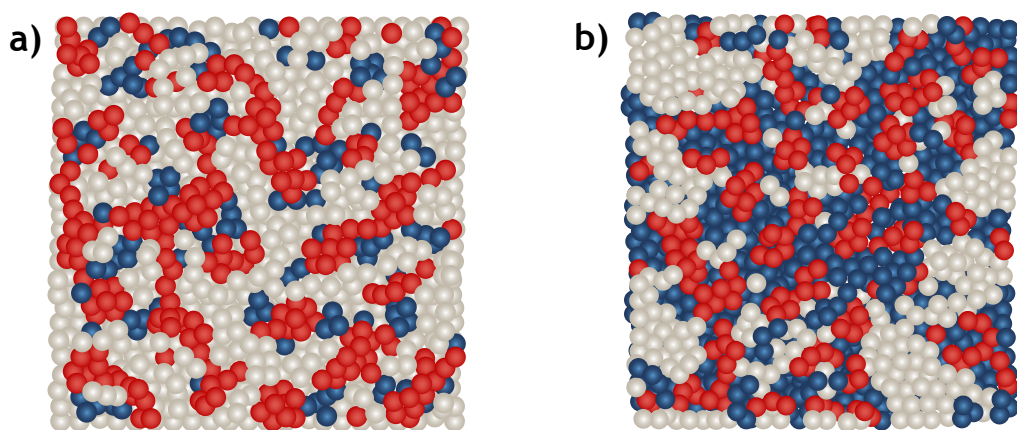


**Figure 1.16.: Mesoscopic polar-apolar networks in ionic liquids.** a) A filament network illustration based on alkylammonium ionic liquids. b) An illustration of a globular network with stronger ion correlation, as found in imidazolium ionic liquids. Apolar regions are coloured grey and polar regions are coloured blue and red for cations and anions, respectively. The illustrations were based on simulations of tributylmethylammonium bis(trifluoromethanesulfonyl)amid<sup>[70]</sup> and 1-butyl-3-methylimidazolium hexafluorophosphate<sup>[71]</sup> by Shimizu *et al.*

Moving on to the longer scale mesoscopic ordering, hydrogen bonds have been proven to exist in ionic liquids<sup>[60]</sup> and the existence of hydrogen-bonded networks themselves is generally accepted.<sup>[40]</sup> However, the strength and importance of hydrogen bonds compared to other factors depend on the ionic liquid in question. On the other hand, nanostructures can arise due to polar-apolar ordering, which is illustrated in Fig. 1.16. Domains of polar and apolar groups are formed because electrostatic interactions are experienced between the polar groups, while the apolar groups mainly have VdW attraction between themselves. This effect is well known in molecular liquids, for example in the micelle formation of amphiphiles. In ILs, many studies<sup>[40]</sup> have investigated polar-apolar ordering using techniques such as neutron diffraction,<sup>[72-75]</sup> X-ray scattering,<sup>[76-79]</sup> and MD simulations.<sup>[70,71,79-83]</sup> They found polar-apolar ordering to be a major structural influence on the nanoscale in addition to charge ordering. The resulting structures range from well-defined globular networks in imidazolium ionic liquids (Fig. 1.16b) to poorly defined filament networks in alkylammonium ionic liquids (Fig. 1.16a).<sup>[71]</sup> In the former, strong correlation between different ions lead to concentrated, globular domains in the network<sup>[71]</sup> while in the latter charge ordering tends to be the dominant factor,<sup>[40,83]</sup> leading to the weakly defined filament network. Generally, long alkyl chains and asymmetry in their distribution strengthens polar-apolar ordering, while short chains and a sterically hindered or very delocalised charge on the ion weakens it.<sup>[40]</sup>

As the literature on ionic liquids is vast, this introduction could only briefly touch on many points. While some will be elaborated on in latter chapters, the inter-

ested reader is referred to the excellent introductory book by Freemantle,<sup>[14]</sup> as well as some of the many review articles on topics of interest regarding ionic liquids.<sup>[15,33,34,38-41,84]</sup>

## 1.2. Measuring techniques

Intermolecular dynamics, as well as the structures which govern them, were reviewed in Section 1.1.1. Since these tend to occur on timescales above 100 fs, the corresponding frequency domain bands can be found in the gigahertz to terahertz region. This region can be probed through both Raman and IR spectroscopic techniques. In the studies presented in this work, the low-frequency Raman spectra were measured by OKE spectroscopy and the far-IR spectra through Fourier transform infrared (FTIR) spectroscopy. A general background of these techniques will be given below in Sections 1.2.1 and 1.2.2, respectively. A treatment of the origin of the spectral intensities and their relation to each other can be found in Section 3.1. It is furthermore possible to directly measure the interatomic and intermolecular distances, most commonly through the scattering of neutrons or X-rays. Here, X-ray scattering was measured to corroborate spectroscopic results indicating the formation of nanoscale structures in salt solutions. Therefore, this section finishes with a short introduction to X-ray scattering in Section 1.2.3.

### 1.2.1. Optical Kerr effect spectroscopy

In 1875, John Kerr<sup>[85,86]</sup> discovered that applying an electric field to a material induced a change in the refractive index proportional to the square of the electric field. This differentiates the Kerr effect from the similar Pockels effect,<sup>[87]</sup> which has a linear dependency. The Kerr effect can also be induced by the electric field of light, which is referred to as the optical Kerr effect (OKE).<sup>[88,89]</sup> However, the effect is not observable unless intense light sources, such as lasers,<sup>[90]</sup> are used, which delayed the discovery of OKE for roughly 90 years. The refractive index of light passing through a material depends on the molecules making up the material, as well as their orientation. The latter is modified in the Kerr effect, as illustrated in Fig. 1.17. For isotropic molecules, a dipole moment ( $\mu$ ) in the direction of the electric field ( $E$ ) is induced for the duration of the electric field. However, no change remains after the field is switched off. In anisotropic molecules, the induced dipole moment ( $\mu_{\text{ind}}$ ) points

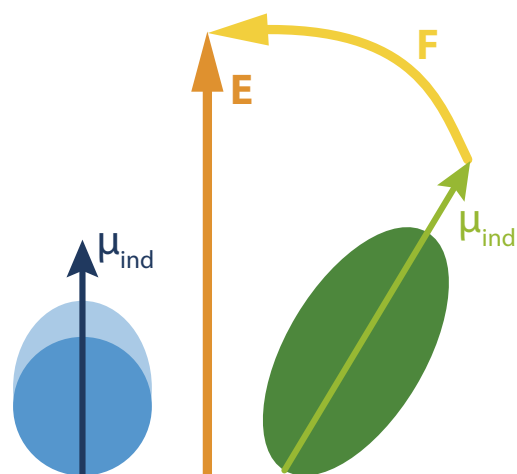


**Figure 1.17.: Kerr effect diagram.** Shown is the effect of an electric field  $E$  on isotropic (left) and anisotropic (right) molecules. The electric field  $E$  induces a dipole moment  $\mu_{\text{ind}}$  in the molecules. This leads to the anisotropic molecule experiencing a torque (rotational force)  $F$ , which pushes it towards alignment with the direction of the electric field.

along the axis of anisotropy. Through the interaction between the induced dipole moment and the electric field, a rotational force ( $F$ ), or torque, is applied to the molecule which nudges it into alignment with the electric field. Therefore, an orientational order along the electric field direction is induced. This order leads to different refractive indices along different axes of a material called birefringence. In practice this means that one polarisation component of light will be slowed down more than the one perpendicular to it, leading to a shift in phase between them. In materials made of anisotropic molecules, this birefringence decays with time once the electric field is switched off. On the other hand, however, anisotropic molecules need to be able to move for the birefringence to occur in the first place. As a consequence, the Kerr effect is preferentially observed in liquids, as molecules have more freedom of movement.

The decay of the induced birefringence can be measured in a spectroscopic pump-probe experiment, which is referred to as OKE spectroscopy.<sup>[90,91]</sup> Using linearly polarised femtosecond laser pulses, birefringence is first induced by a laser pulse and then measured by a second pulse with the polarisation rotated  $45^\circ$  with respect to the first pulse. The relative delay of the two linear polarisation components will then lead to an elliptical polarisation in the second pulse, where the degree of elliptical polarisation is related to the strength of the birefringence.<sup>[90,91]</sup> Depending on the spectroscopic set-up used, the method of detecting the elliptical component varies. The detection will be explained in more detail in Sections 2.1.2 and 2.1.3 for the set-up used in this study. The resulting time-dependent decay of the birefringence is Fourier transformed to obtain the low-frequency Raman spectrum.

Given a long observation time of the system, the resulting spectrum lies in the gigahertz to terahertz frequency range. This is where the intermolecular dynamics described in Section 1.1.1 can be found, allowing the *in-situ* observation of these processes. For all studies presented in this work, OKE spectroscopy was the main investigation tool.

### 1.2.2. Infrared spectroscopy

The interaction of light in the IR frequency range with matter is measured in IR spectroscopy. Most commonly, the absorption of IR light is measured to gain information on the vibrations, rotations and, in the far-IR, intermolecular interactions characterising the molecules of the sample. Often, the IR frequency range is partitioned into three parts characterised by the information which can be gained from them. Although the exact values differ between different publications,<sup>[92,93]</sup> the near-IR typically covers a frequency range of  $14000\text{ cm}^{-1}$  to  $4000\text{ cm}^{-1}$  (420-120 THz), which contains mostly overtone and combination bands of vibrational modes. The mid-IR, between  $4000\text{ cm}^{-1}$  and  $400\text{ cm}^{-1}$  (120-12 THz), contains rotations and the fundamental modes of vibrations. Because many functional groups of organic molecules have characteristic frequencies in this range, mid-IR spectroscopy is a widely used analytical technique for detecting and characterising organic components. The far-IR, meanwhile, ranges from  $400\text{ cm}^{-1}$  to  $10\text{ cm}^{-1}$  (12-0.3 THz) and covers vibrations, rotations as well as intermolecular dynamics in condensed phases. To appear in the IR spectrum, the motion needs to exhibit a change in the dipole moment.<sup>[92-94]</sup> Then, light of the corresponding frequency will resonate with the motion, resulting in excitation of the mode and therefore absorption at this specific frequency.

IR absorption spectroscopy can be done using two main methods, dispersive IR spectroscopy or FTIR spectroscopy. Modern instruments are nearly all FTIR spectrometers,<sup>[92]</sup> as they offer a higher signal-to-noise ratio (SNR) with shorter measurements times. In dispersive methods, the absorption is measured separately for each frequency, while in FTIR spectroscopy a broadband spectrum is measured in one shot as an interferogram. Briefly, two main advantages of the FTIR technique are considered.<sup>[92]</sup> For one, when selecting a monochromatic wavelength from the spectrum, intensity is lost as the light passes through the narrow monochromator slit. Secondly, the whole measurement time is devoted to each frequency in FTIR spectroscopy, instead of only a fraction as in dispersive IR spectroscopy. The SNR, which is proportional to the square root of the scans taken, therefore can be higher even at shorter measurement times.

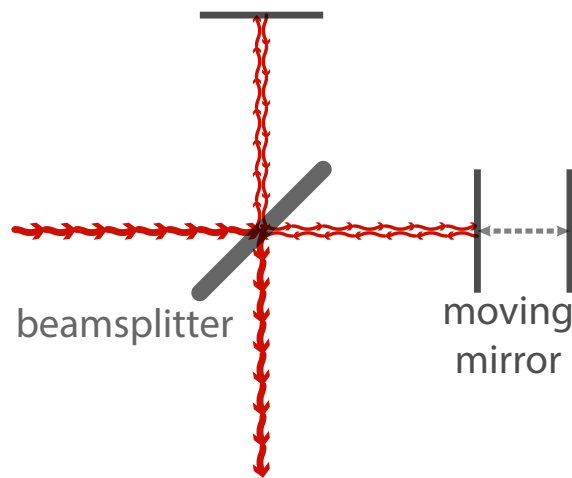


**Figure 1.18.:** Schematic of a Michelson interferometer. A beamsplitter splits the incoming collimated beam in two, of which one is delayed in time relative to the other using a moving mirror. The two beams are then recombined and passed through the sample.

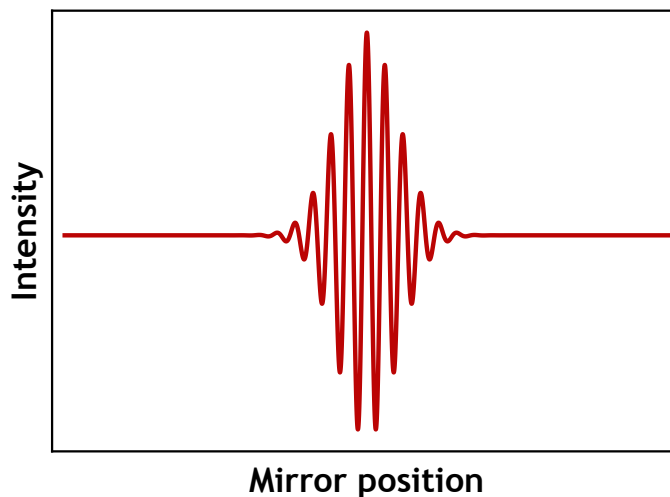


**Figure 1.19.:** Example of an interferogram. An interferogram records the light intensity with regards to the optical path between the two split parts of a recombined light beam.

The defining component in FTIR spectrometers is the Michelson interferometer, shown in Fig. 1.18.<sup>[92,95]</sup> A collimated beam from a polychromatic light source passes through a beamsplitter and is split into two components, ideally with equal intensities. One component encounters a moveable mirror, which modifies the path length, and therefore delays this component in time relative to the other component. The recombined intensity of the light as a function of the difference in the path lengths is recorded, resulting in an interferogram (Fig. 1.19). When the path lengths are equal, the two recombined beams interfere constructively with each other, resulting in a maximum of the recorded intensity. At differing path lengths, the interference tends to be destructive and the intensity is attenuated. The Fourier transform of the interferogram yields a frequency domain spectrum.<sup>[95]</sup>

Depending on the selected frequency region, information on vibrations, rotations, and intermolecular interactions can be gained from FTIR spectra. Here, the focus was on the intermolecular dynamics (see Section 1.1.1) measured in the far-IR. As most of the motions in the far-IR tend to not have as strict a symmetry as simple intramolecular modes, the exclusion usually found between Raman and IR spectra is weakened, and complementary information to the OKE spectra can be gained from the far-IR measurements.

### 1.2.3. X-ray scattering

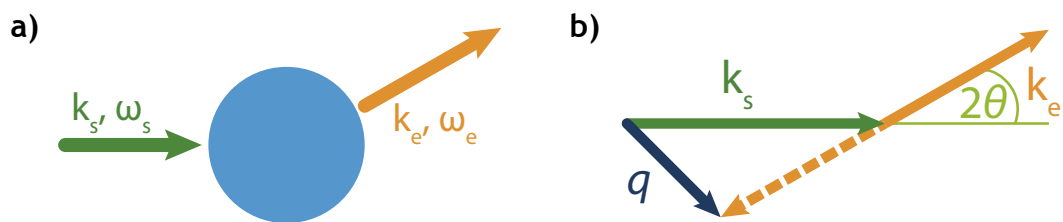


**Figure 1.20.: Scattering diagrams.** a) General diagram of a scattering process from a particle. b) Definition of the scattering vector  $q$  related to an angle  $2\theta$  for elastic scattering.

X-rays are electromagnetic waves with wavelengths between 0.01 and 10 nm. Since their discovery in 1895 by Wilhelm Conrad Röntgen<sup>[96]</sup> they have been used for medical imaging and structure determination. Classically, X-ray diffraction has been used to investigate crystal structures, but with the advent of stronger X-ray sources, less structured materials such as liquids and glasses were studied by X-ray scattering.<sup>[97]</sup> The reason they are used is because their short wavelengths allow the resolution of structure on an atomic level. As electromagnetic waves, X-rays probe structure by interacting with the electrons in a material, giving a picture of the electron density distribution.<sup>[97,98]</sup> Furthermore,

the scattering strength of an atom is proportional to the number of electrons it has.<sup>[98]</sup> X-ray scattering or diffraction traces are usually plotted as a scattering intensity versus either the scattering angle  $2\theta$  or the scattering vector  $q$  (see Fig. 1.20), which are related by<sup>[97,98]</sup>

$$q = \frac{4\pi}{\lambda} \sin(\theta) \quad (1.7)$$

for the X-ray wavelength  $\lambda$ . The scattering vector expresses a separation in reciprocal space and is related<sup>[97]</sup> to a distance  $L$  in real space by

$$q = \frac{2\pi}{L}. \quad (1.8)$$

Therefore, structures with large spacing, for example in the nanometer range, are revealed at small  $q$  (or small angles) and structures with spacing at the atomic level are revealed at larger  $q$  (or at large angles). Two dimensional scat-

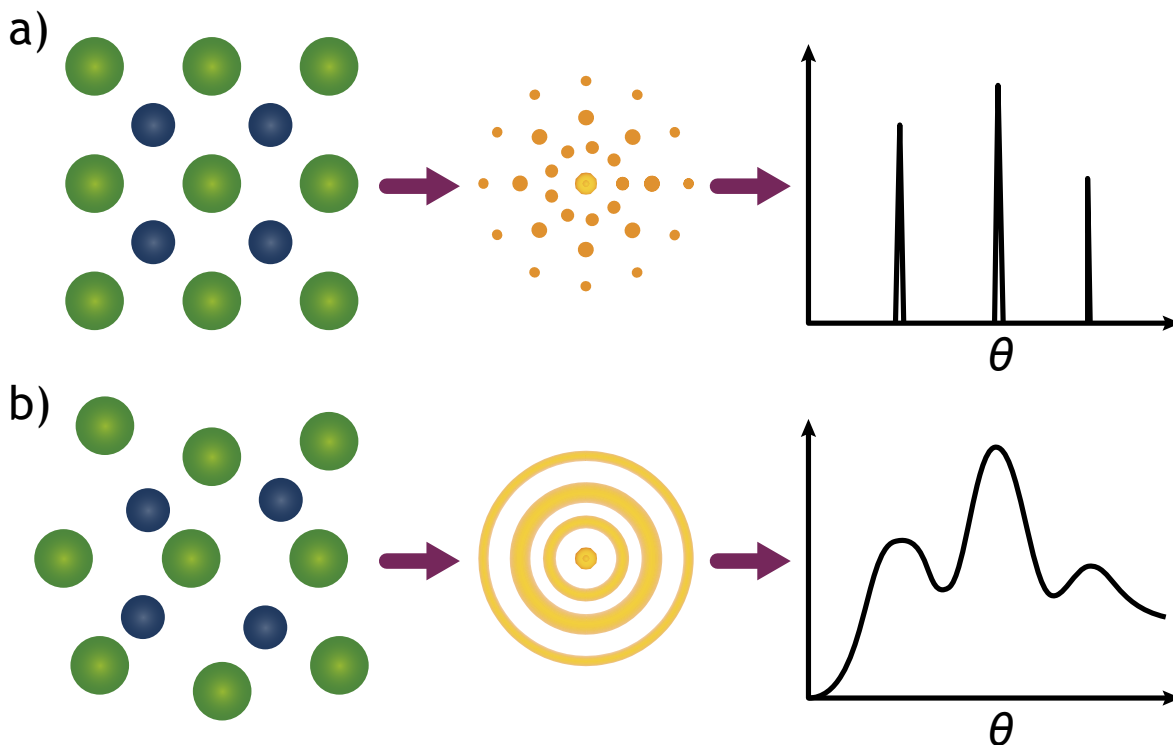


**Figure 1.21.: Dependence of scattering patterns on ordering.** Illustrations of the relation between (from left to right) structure, scattering pattern and scattering trace for a) a crystalline and b) an amorphous substance.

tering patterns (middle part of Fig. 1.21), instead of scattering traces (right side of Fig. 1.21) which are only dependent on  $2\theta$  or  $q$ , reveal even more information, as scattering traces can be extracted from a scattering pattern by azimuthal integration. In a single crystal, such as the one shown on the left in Fig. 1.21a, the interference of the scattered X-rays will lead to point maxima of the scattering intensity in reciprocal space. Polycrystalline materials or powders, which consist of many single crystals with different orientations to the incoming

X-rays, lead to an orientational distribution of these point maxima, which result in rings of maximum intensity in the scattering pattern. The case is similar for liquids or amorphous solids, where the material shows a distribution of lengths in addition to the orientational distribution. This leads to broadened rings in the scattering pattern as seen in the middle part of Fig. 1.21b. As a result, crystalline materials show sharp peaks in their scattering traces while those of amorphous materials are broadened.<sup>[97]</sup>

These scattering traces can be converted from reciprocal to real space, giving information about interatomic distances. Because repetition of a distance is needed to get a significant scattering intensity, structural motives can be deduced from the scattering traces. This structural information can then be related to the intermolecular dynamics found in other measurements.

### 1.3. Summary

In Section 1.1, the different states of matter were introduced. In general, relatively simple models exist which can explain the behaviour in the crystalline and gaseous phase. The liquid phase, however, can be seen as an intermediary state between those two, resulting in more complicated structures and dynamics. The aim of the presented work is to learn more about the different factors contributing to the observed structures and dynamics in liquids. This was mostly done through OKE spectroscopy (see Section 1.2.1), which exploits the anisotropic polarisability of particles to induce birefringence and observe its decay. This information can then be related to the dynamics of liquids and solutions occurring from tens of femtoseconds to several nanoseconds. Complementary information in the related frequency region can be gained from FTIR spectroscopy (see Section 1.2.2), as the complex nature of the observed motions tends to weaken the exclusion usually found between IR and Raman spectra. Meanwhile, X-ray scattering allows direct confirmation of structure at the interatomic scale and above. This can be necessary for the interpretation of complex samples, such as ILs (Section 1.1.2), in which the structure is determined by competing factors such as charge and polar-apolar ordering.



## 2. Experimental

### 2.1. OKE set-up

#### 2.1.1. Laser

The word laser is an acronym of “light amplification by stimulated emission of radiation” and the light source it describes emits an intense, collimated light beam. Often, this light is comprised of waves with a very narrow distribution around one wavelength, making it monochromatic. While lasers have a futuristic ring to them, they are used in many everyday applications. This ranges from using their well-defined light to read, write, and send information to using their high energy for the cutting, drilling, and welding of very hard or easily deformed materials.<sup>[99]</sup> In research, lasers are often used to measure things, from distances to spectra. Again, this is because laser light makes for reliable measurements, as lasers stay collimated over long distances, have coherent light of defined wavelengths and usually a high intensity. All of these properties derive from the way lasers work, of which an overview is covered below.

First and foremost, lasers rely on stimulated emission to produce their light. Given two electronic levels separated by energy  $E$ , a molecule can transition to an excited state by absorbing light at a wavelength  $\lambda$  according to  $E = hc/\lambda$ , where  $h$  is the Planck constant and  $c$  is the speed of light. An excited molecule can spontaneously emit light to transition to a lower energy state, with the wavelength  $\lambda$  corresponding to the energy between the levels. However, there is another pathway for emission called “stimulated emission”. Here, an incident photon at the transition wavelength  $\lambda$  stimulates the transition from an excited state to a lower energy state through the emission of a second photon of the same wavelength and in phase with the original photon. The population distribution between energy states, for example  $n$  and  $m$  with  $E_n < E_m$ , is determ-

ined by a thermal equilibrium given through the Boltzmann distribution,

$$\frac{N_m}{N_n} = e^{-\frac{E_m - E_n}{k_B T}}, \quad (2.1)$$

where  $E_i$  is the energy of state  $i$ ,  $N_i$  the population of state  $i$ ,  $k_B$  is the Boltzmann constant, and  $T$  the temperature. Therefore, under regular conditions, the population of the lower state is larger than that of the higher state. In this case, absorption will initially be stronger than stimulated emission, as the chance of encountering populated lower state is higher. Over time, the system will reach equilibrium again according to Eq. 2.1.

The probabilities of absorption and of emission, both stimulated and spontaneous, are given with the help of their respective Einstein coefficients.<sup>[94]</sup> These are  $B_{n \rightarrow m}$ ,  $B_{m \rightarrow n}$ , and  $A_{m \rightarrow n}$ , respectively, for transition between energy levels  $n$  and  $m$ , with  $E_n < E_m$ . Briefly,  $B_{n \rightarrow m} = B_{m \rightarrow n}$  and the transition probability for both absorption and stimulated emission is otherwise proportional to the product of the population number of the state as well as the number of photons at the frequency difference between the energy levels. Spontaneous emission, however, is independent of incoming photons and the transition probability is otherwise proportional to the lifetime of the higher energy state. This highlights an intrinsic problem of a two level laser. For stimulated emission to dominate, as is needed in lasers, the population of the higher energy state needs to be larger than that of the lower energy state, a situation which is called a “population inversion”. This is impossible to achieve for interactions with light in a two level system, because when absorption and stimulated emission are in an equilibrium with each level having half the total population, spontaneous emission will depopulate the higher energy level. Therefore, lasers need at least three energy levels, though typically lasers have four or more energy levels involved in the lasing process. Generally, as systems tend to strive towards the lowest energy state, population inversions are rare and need to be manufactured. Yet they are the defining aspect of lasers, since without stimulated emission lasing cannot occur.

In practice, this is achieved by selecting laser materials with a suitable energy structure. The energy levels will need to adhere to certain criteria, and at least three or four energy levels are involved, as seen in Fig. 2.1. First, molecules are excited from the ground state (G) to an excited state (G\*) with pump energy, which can be given in different forms such as light of a different wavelength or electricity, among others. From the excited state G\* the molecule decays into the upper laser level (L\*). For the system to work well, two factors are of importance here. For one, the upper laser level L\* should have a long lifetime on

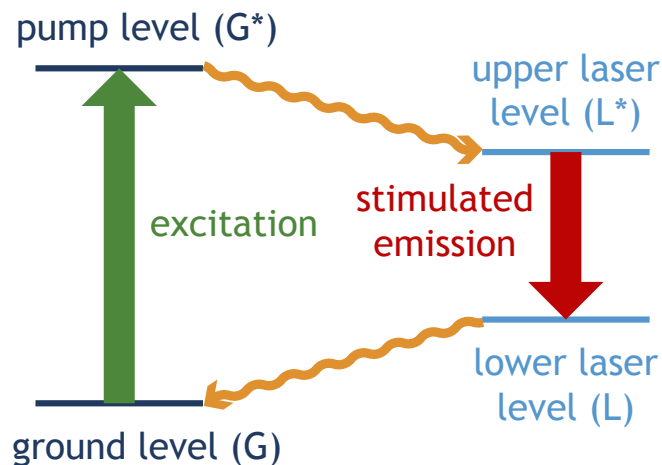


**Figure 2.1.:** Diagram of the energy levels involved in a four level laser. Shown are the ground level (G) and the excited pump level ( $G^*$ ), whose energy difference determines the excitation energy needed, as well as the two laser levels (L and  $L^*$ ), whose energy difference defines the wavelength of the emitted laser light (and the stimulated emission). It is desirable for the upper laser level  $L^*$  to have a long lifetime, as it helps with sustaining the population inversion. Similarly, fast depopulation of the lower laser level L improves the population inversion.

the order of nanoseconds to milliseconds, which allows the build up of the population inversion. Additionally, it is desirable that the transition from the pump level  $G^*$  to the upper laser level  $L^*$  has a high probability, so that populating the pump level actually leads to a population inversion. From the upper laser level  $L^*$ , the molecules decay into the lower laser level L. Given a long enough lifetime of the upper laser level  $L^*$ , this occurs via stimulated emission and contributes to lasing, with the wavelength of the emitted light given by the energy difference between the levels  $L^*$  and L. The lower laser level L can be the ground level G, as is the case in three level lasers, or a separate level, as in four level lasers. The advantage of a separate lower laser level lies in its depopulation through decay to the ground state. Not only does decreasing the population of the lower laser level L make it easier to build up a population inversion, but it also helps with sustaining it, especially if the decay to the ground level G is fast. In practice, having several closely spaced pump levels means a range of excitation energies can be used, making it easier to give the laser the energy needed for the population inversion. The same is true for a range of ground levels, which also help with depopulating the lower laser level if a separate one exists. Multiple laser levels result in several wavelengths being accessible for laser light, meaning the laser is tunable.

The laser material itself, however, does not automatically lead to the highly collimated, intense beam which is associated with laser light. The second crucial part in a laser is the cavity, the schematic for which is shown in Fig. 2.2 for a solid-state laser. The cavity is defined by two mirrors, which are placed at

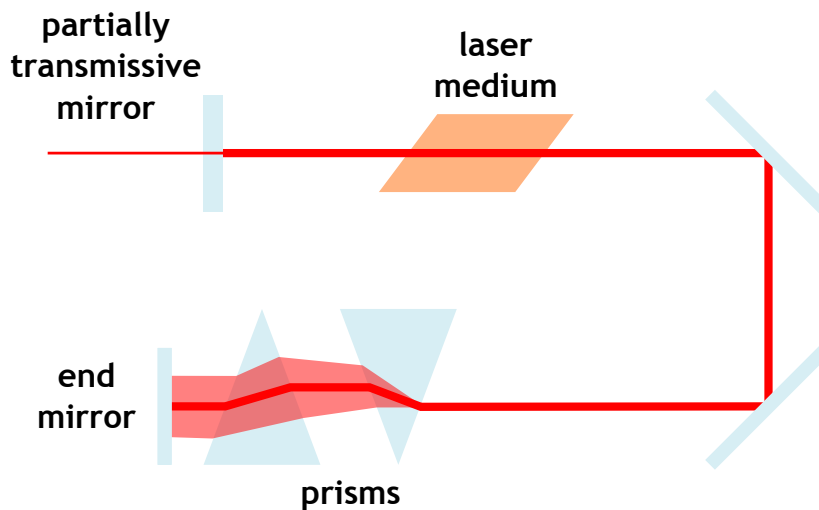


**Figure 2.2.:** Schematic laser cavity for a solid-state laser. Two mirrors, one of which transmits a few percent of the incidental light, define the ends of the cavity. The exact transmitted percentage depends on the gain (and loss) within the cavity. The reflected light extracts more radiation from the laser material and the preferred wavelength - or bandwidth - can be stabilised by attuning the prisms.

either end of the laser medium. Out of these mirrors, the output mirror is partially transmissive and allows a fraction of the incident light to escape, the exact amount of which depends on the loss in the cavity and the gain by stimulated emission in the laser medium. The reflected light in the cavity constructively interferes to form longitudinal standing waves between the mirrors, amplifying themselves through stimulated emission in the laser medium. The distance between the mirrors, or the cavity length  $L$ , is related to the wavelength of the stable standing waves through  $\lambda = \frac{2Ln_{LM}}{m}$ , where  $n_{LM}$  is the refractive index of the laser medium and  $m$  is the mode number. The probability of the stimulated emission at a certain wavelength determines whether this wavelength dominates in the laser output, unless measures are taken to make its standing wave unstable in the cavity. Additional prisms, or gratings, can be used to tune the cavity, extracting laser light at wavelengths for which the stimulated emission probability is not dominant. Depending on the cavity configuration and on how well the population inversion can be sustained, lasers can emit either a continuous laser beam (continuous wave (cw) operation) or short laser pulses (pulsed operation). For pulsed operation, it is beneficial to have laser light over a broad range of frequencies, yielding short laser pulses. Here, gratings or prisms can be used to tune the bandwidth of the emitted radiation.

A staple laser for the generation of ultrafast pulses is the Ti:sapphire laser. Here, titanium ions are substituted for a fraction of aluminium ions in the sapphire ( $\text{Al}_2\text{O}_3$ ) lattice. This results in an energy structure with a wide range of wavelengths available for lasing around 800 nm, from 660 nm in the red part of the light spectrum to 1180 nm in the infrared.<sup>[99]</sup> Furthermore, Ti:sapphire

lasers can sustain both pulsed as well as cw operation. This, in addition to good thermal conductivity, makes it a great candidate for solid state lasers.

## Laser pulses

Normally, the different longitudinal modes, or the standing waves that are valid in a given cavity, do not have a fixed phase relationship. Therefore, light is continually emitted, with possible temporary fluctuations due to interference effects between the modes. All this changes if the laser becomes mode-locked, which means that a fixed phase-relationship is introduced between the longitudinal modes. As a result, interference effects will be more defined, leading to the formation of laser pulses by superposition of the longitudinal modes. The temporal pulse-length  $\Delta t$  is then related to the range of frequencies of the involved modes, or the bandwidth  $\Delta\nu$ , by  $\Delta t \propto 1/\Delta\nu$ , in which the proportionality is related to the shape of the pulse.<sup>[99]</sup> These ideal pulses are also called “transform-limited”, as the length of the pulse is only limited by the spectral bandwidth. Other methods for pulse generation exist, such as Q switching or cavity dumping. However, they generally produce pulses of longer duration than mode-locking and will be ignored in the following. Mode-locking can occur through either an external signal (active mode-locking) or the amplification of noise spikes in the cavity (passive mode-locking). Most passive mode-locking depends upon preferential transmission of high-intensity light, such as noise spikes. One passive mode-locking scheme, called self mode-locking, relies on inducing a Kerr lens in the laser medium. The Kerr lens focuses light according to its intensity because the change in refractive index scales quadratically with intensity (see Section 1.2.1). Thus noise spikes, such as those introduced by tapping a mirror mount, will be selectively amplified, locking the longitudinal modes together in a pulse.

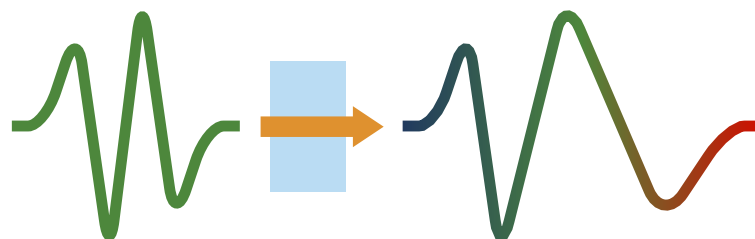


**Figure 2.3.:** Illustration of laser pulse dispersion. As an effect of the differing refractive index at different frequencies, some frequency components are delayed with respect to others. The right side pulse illustrates the temporal separation due to passing through a material with a frequency-dependent refractive index.

However, just because a pulse starts out transform-limited does not mean it will

stay that way while traversing optical elements. Because the refractive index of a material can be frequency dependent, passing through such an element will delay certain frequencies with respect to others as shown in Fig. 2.3. This causes a temporal separation of the pulse by frequency, also known as “chirp” or group velocity dispersion. Chirp can be corrected for by using prism pairs, grating pairs or specially coated mirrors, which all modify the distance specific frequencies in the pulse have to travel. For further discussion on higher order dispersion and their correction through optics, the interested reader should consult the relevant literature.<sup>[100]</sup>

The pulse length, defined as the full width at half-maximum (FWHM), obviously depends on the pulse shape. The shape of a pulse is measured through its cross- or auto-correlation. A cross-correlation is the measurement of two signals with one delayed relative to the other. The auto-correlation is a special case of cross-correlation, in which both signals are from the same source. As in all the following ultrafast set-ups the initial laser beam is separated into two parts by a beam-splitter, only the auto-correlation will be discussed in the following. After the beam is split into two, one goes through an optical delay line while the other has a fixed path. Therefore, one beam will be delayed with respect to the other and their intensity can be measured as a function of this delay. For this, a measurement of either the second-harmonic frequency generated in a nonlinear crystal or the two-photon absorption of a photodiode can be used, the latter of which was done in our set-ups. The averaged auto-correlation signal then corresponds to

$$I_{AC}(\tau) \propto \int I_1(t)I_2(t - \tau)dt, \quad (2.2)$$

with  $\tau$  denoting the relative delay between the two pulses. While conversion factors of the pulse-length to the bandwidth have been published for different pulse shapes, nonlinear curve fitting determining the pulse shape and conversion factor can be better in practice.<sup>[100]</sup> However, since these methods only measure the *average* autocorrelation signal, information on chirp and asymmetric pulse shapes will be lost. To measure this information, different techniques have to be used, such as interferometric autocorrelation or frequency-resolved optical gating (FROG). This concludes the brief overview of laser and laser pulse related topics provided for the explanation of the ultrafast laser set-ups.

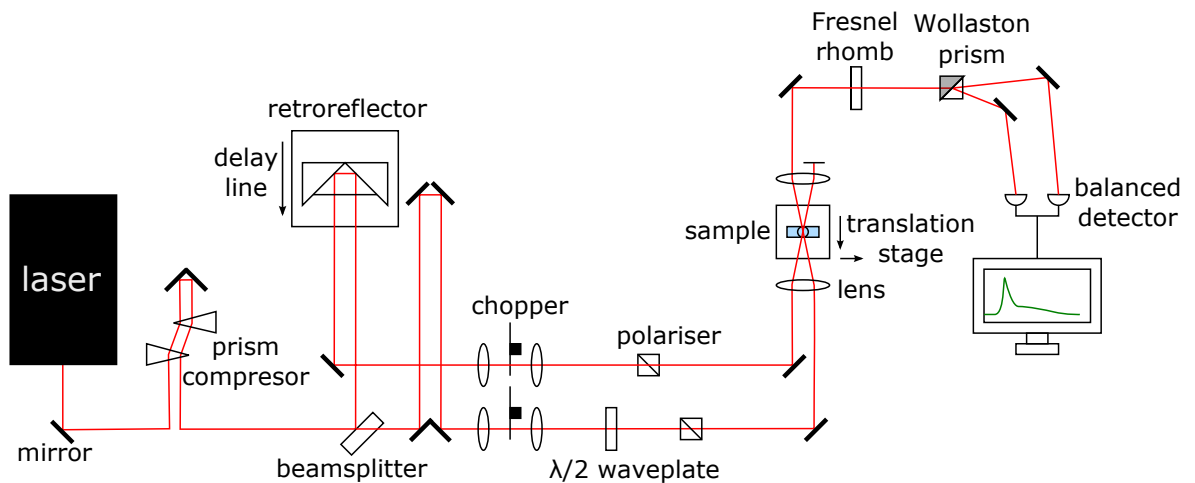


**Figure 2.4.:** Schematic of the high time-resolution OKE set-up using a Coherent Micra-10 Ti:sapphire laser.

### 2.1.2. High time-resolution OKE set-up

The high time-resolution pump-probe set-up used for OKE studies has been described previously<sup>[12,101]</sup> and its layout is shown in Fig. 2.4. It measures time-dependent changes of the induced birefringence in a sample through changes in the polarisation of laser pulses produced with a Micra-10 laser (Coherent). For this, the probe beam is split into its two orthogonal linearly polarised components after exiting the sample and the difference in their intensity is recorded using balanced photodiodes. If the sample is not birefringent, for example when the delay between the pump and the probe beam is negative, the two intensities will be equal and the signal is taken as zero. This is accomplished through the combination of a Fresnel rhomb, a Wollaston prism, and the aforementioned balanced photodiodes. First, the Fresnel rhomb delays one polarisation component by a quarter wavelength relative to its counterpart, leading to circular polarisation if the incident light was linearly polarised. This could also be achieved through a simple waveplate, however, the achromaticity of a Fresnel rhomb reduces noise caused by small wavelengths fluctuations in the laser. The Wollaston prism then splits the circularly or elliptically (if the sample was birefringent) polarised light into its two orthogonal linearly polarised components, which emerge at slightly different angles. Therefore, they can each be reflected onto one of the two balanced photodiodes. These are wired so the signals will be subtracted from each other, before passing the difference to a lock-in amplifier. By passing the difference of the two intensities, the risk of saturating the dynamic range of the lock-in amplifier is reduced, allowing for a bigger dynamic range in the measurement. The lock-in amplifier itself increases the SNR of the measurement by removing contributions from scattered pump light and ambient light. This is accomplished by demodulating the signal with the difference frequency of choppers placed in the path of the pump beam and the probe beam, which run at a

ratio of 5:7 with rates around 3 kHz. Because the frequency of both the pump as well as the probe chopper is taken into account, the measurement signal will be modulated by both of these frequencies, meaning that any signal which does not fit this description can be safely discarded. The SNR is further increased by placing both choppers into the focus of 16 cm telescopes. This reduces the beam diameter at the chopper, minimising effects caused by partially chopped beams.

Both the pump as well as the probe beam originate from the Micra-10, which is a Ti:sapphire laser with a repetition rate of 82 MHz, meaning one pulse is emitted about every ten nanoseconds. The produced laser light has a broad spectral range centred at 800 nm with width of usually 160 nm. This broad spectral range allows for pulses with pulse-lengths of 20 fs to 25 fs to be achieved, each of which has about 10 nJ of energy, giving an average power of 0.8 W. As mentioned in Section 2.1.1, the pulse-length does not only depend on the bandwidth of the laser spectrum but also on the frequency-dependent refractive indices of encountered materials. Therefore, it is necessary to compensate for the accumulated chirp in order to deliver short pulses to the sample. In our case, this is done using a compressor made of a homosil prism pair which is calibrated with the help of the autocorrelation measured in a two-photon diode.

After this, the beam is split into a pump and a probe beam by passing through a 9:1 beamsplitter. The probe then continues on a fixed path through the set-up, while the pump path contains an optical delay line (Newport IMS600LM). While it would be more intuitive to use a delay line in the probe path, using it in the pump path avoids walking the beam on the detector since the pump beam is blocked beforehand. The delay line, which has a length of 600 mm and an average accuracy of 3  $\mu\text{m}$ , allows for a maximum pump-probe delay of 4 ns. After the delay line, the pump beam passes through the aforementioned chopper as well as a polariser, before being focused into the sample. The probe beam, meanwhile, is delayed for a half wavelength by a waveplate positioned between its chopper and polariser. Afterwards, the probe is also focused into the sample, where it crosses the pump. Therefore, only the birefringence created in the overlap of the pump with the probe beam is measured, meaning the thickness of the sample is not critical for the signal strength. While the probe beam travels on towards the balanced detection, the pump beam is discarded after encountering the sample. To capture the refractive index of both orthogonal linear polarisations, the probe beam is polarised at  $45^\circ$  relative to the pump. Here, heterodyne detection is used, which extracts information from the combination of two different light waves by looking at the modulation of the phase or frequency. In OKE spectroscopy, the birefringence leads to a small electric field which is phase-shifted with regard to the probe field. Usually, heterodyne detection is

achieved by phase-matching both electric fields with a quarter-waveplate and using cross-polarisers which only let a small part of the probe field pass.<sup>[9,91]</sup> In this set-up, however, heterodyne detection is achieved by means of balanced detection. Again, the electric fields are matched using a quarter-waveplate, or more accurately a Fresnel rhomb which serves the same purpose. Balanced detection of the linearly polarised components results in a direct measurement of the term describing the interaction between the electric field resulting from the birefringence and that of the probe pulse. Unlike in the usual method for heterodyne detection, the electric field of the probe is not mostly blocked by a polariser, resulting in the measurement of a stronger signal and therefore giving a better SNR.

To sum it up, the high time-resolution OKE set-up measures the time-dependence of an induced birefringence in a sample using 20 fs to 25 fs laser pulses. The measurement of the heterodyne contribution to the OKE signal is achieved in one experiment through the use of balanced detection. An optical delay line allows measurements up to 4 ns, accessing frequencies down to 250 MHz.

### 2.1.3. Long delay OKE set-up

The long delay OKE set-up using a Legend Elite USX (Coherent) has been described previously<sup>[51,52]</sup> and its layout is shown in Fig. 2.5. It is in principle very similar to the set-up described above, as balanced detection is used to measure the time-dependent decay of birefringence. Here, SNR is sacrificed in favour of a higher dynamic range, allowing the use of more intense laser pulses to accurately measure the relaxational tail in the time domain. The major changes are a doubled maximum delay time of 8 ns, achieved by traversing the delay stage twice, and a higher dynamic range of the measurement, realised through the combination of a boxcar integrator and amplified laser pulses. The probe pulse, after passing the sample, is analysed by the combination of a quarter waveplate and a Wollaston prism, first elliptically polarising the light and then splitting it into its two orthogonal linearly polarised components. These are then directed onto balanced photodiodes, where their intensities are subtracted from each other. This difference is passed to a boxcar integrator, which processes two values for each datapoint. One value is taken with the pump beam blocked by a mechanical chopper while the other value is taken with the sample exposed to the pump beam. By taking the difference of these values, variable background contributions are eliminated. This also means only one chopper, instead

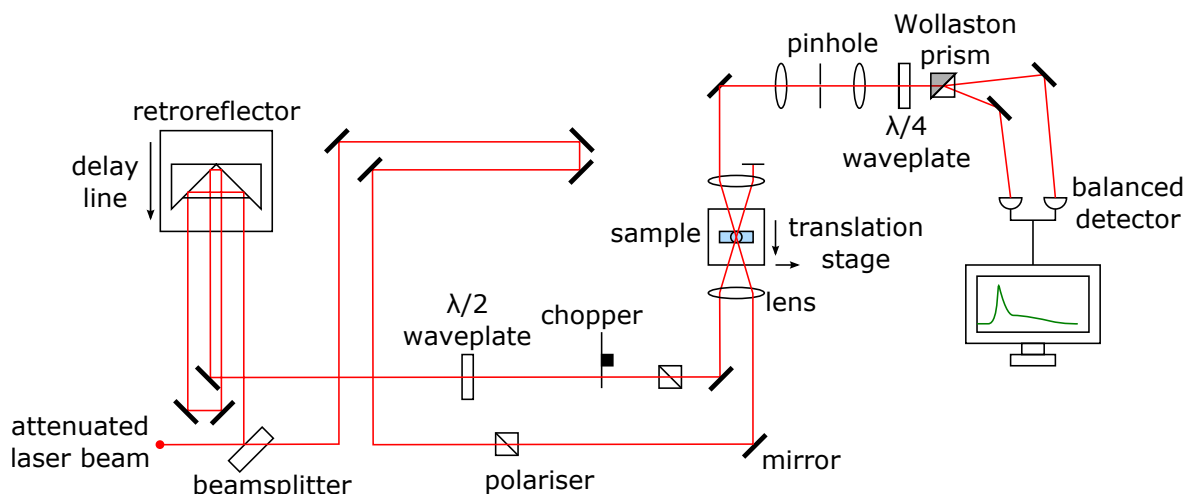


**Figure 2.5.:** Schematic of the long delay OKE set-up using the attenuated beam of a Coherent Legend Elite USX Ti:sapphire regenerative amplifier. The schematics of the beam attenuation are shown in Fig. 2.6.

of two as in the high time-resolution set-up, is needed for the measurement. The baseline of the measurement is established at negative delay times by rotating the waveplate until the signal is adjusted to zero, maximising the dynamic range available in the boxcar integrator. Furthermore, scattered light can, if necessary, be eliminated from the probe beam by adjusting the pinhole placed before the waveplate.

Laser pulses originate from a Mantis DS (Coherent) Ti:sapphire laser and are amplified in the Legend Elite USX, a pulsed regenerative Ti:sapphire amplifier generating pulses centred around 800 nm at a repetition rate of 1 kHz. Due to the high pulse energy, steps have to be taken in order to avoid nonlinear effects as well as damage to the sample and the set-up components. Therefore, the pulse is stretched from 23 fs to 1 ns before it is amplified, reducing the peak intensity. After amplification, the pulse is recompressed to 1 ps, resulting in an energy of up to 2.5 mJ per pulse. Focusing pulses like this with a focusing lens could lead to white light generation in the focus. As the sample is positioned in the focus of the lens, this could also damage any measured samples. As a consequence, the beam is attenuated before being fed into the OKE set-up, which is shown in Fig. 2.6. First, 80% of the beam intensity is discarded using a beamsplitter, before the beam passes through a waveplate and polariser, allowing fine tuning of the beam intensity. Through this, the pulse energy was reduced from 2.5 mJ to 2.5  $\mu$ J. During the course of the presented studies, the attenuation had been modified to allow easier alignment. As can be seen in Fig. 2.6a, the apertures used for alignment are placed partially within a telescope used to reduce the beam diameter. This was done due to space restraints on the table and makes aligning the beam difficult, with small misalignments being carried forward into the set-up. The later version seen in Fig. 2.6b, on the other

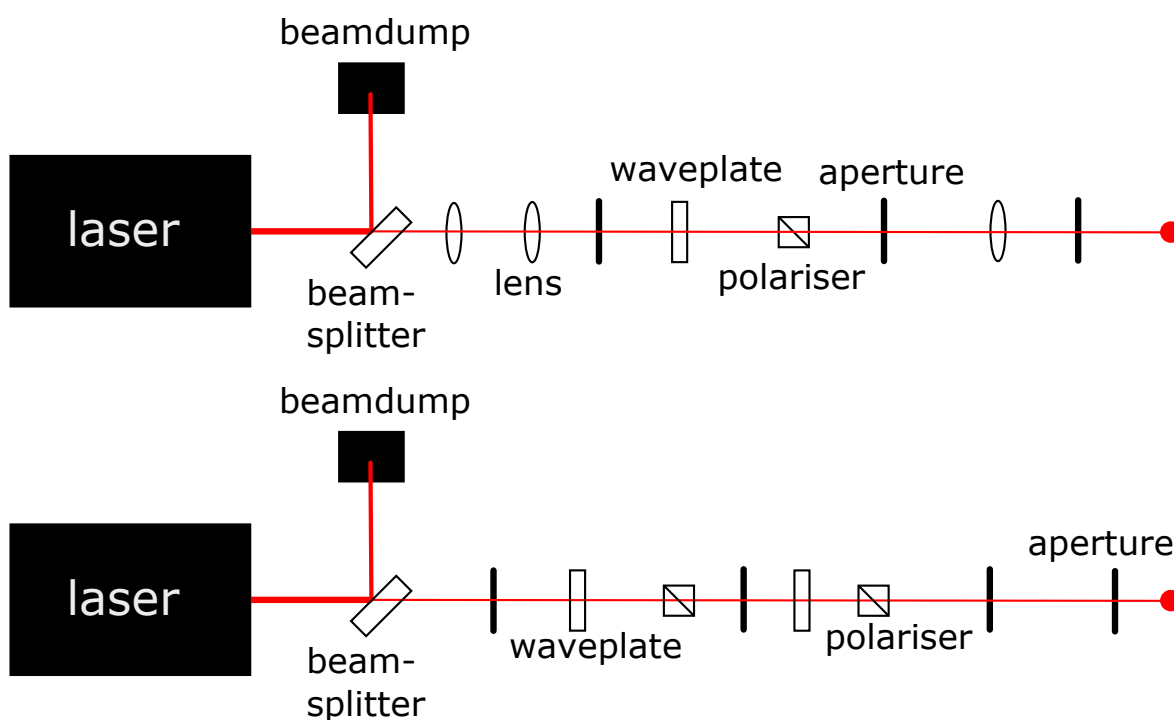


**Figure 2.6.:** Attenuation of the amplified Legend Elite USX pulses. Shown are the schematics of the attenuation method used for measuring (a) sodium thiosulfate solutions (see Chapter 6) and (b) lithium thiocyanate solutions (see Chapter 5). The major difference between the attenuation methods lies in the ease of alignment, since the apertures used for alignment in (a) lie in the middle of a telescope.

hand, avoids this. Additionally, two waveplate-polariser combinations are used to allow for fine-tuning of the pulse energy. In the earlier studies presented in Chapter 6 version (a) was used, while in the studies shown in Chapter 5 it had been changed to version (b). Alignment at this stage is important, as the OKE set-up shown in Fig. 2.5 is very intricate due to space restraints on the table caused by the use of the Legend Elite USX for more than one set-up.

The attenuated beam then passes through a 9:1 beamsplitter and is separated into a pump as well as a probe beam. The probe only passes a polariser before encountering the sample and going on towards detection. The pump, meanwhile, passes through the optical delay line twice, doubling the maximum delay time to 8 ns. Then, it encounters a half waveplate, a chopper, and a polariser, before being focused into the sample and then being discarded. The half waveplate rotates the polarisation of the pump pulses, resulting in a  $45^\circ$  difference between the polarisation of the pump and the probe. Due to spacial restraints, the waveplate was placed in the pump instead of the probe path, unlike in the high time-resolution set-up. However, just like in the high time-resolution set-up the induced birefringence is only measured in the small overlap of pump and probe beam in the sample.

In conclusion, the long delay set-up is optimised to allow the measurement of

the low-intensity birefringence relaxation tail up to 8 ns. To reach higher intensities, amplified laser pulses from a Legend Elite USX are attenuated to safe pulse energies for OKE samples. As a consequence, a higher dynamic range is necessary and SNR was sacrificed to achieve this by using a boxcar integrator. Due to the long pulse-lengths, however, it is advisable to use this set-up in conjunction with the high time-resolution set-up, concatenating the datasets to achieve a good measurement of the relaxation together with a good resolution at short times.

## 3. Data analysis of terahertz spectra

Spectra in the gigahertz to terahertz frequency range contain information on the dynamics, intermolecular interactions and structure of liquids and solutions. Due to this, however, they also include many contributions, for example, slow diffusional modes, librations, and intramolecular vibrational modes. Additionally, coulombic and hydrogen-bonded interactions can be seen, depending on the liquid or solution studied. The dissection of these contributions tends to be non-trivial and over the years a number of functions were shown to work well as empirical models for describing these motions. These functions are described in Section 3.2. Furthermore, many of these motions show a collective character, resulting in a low symmetry. This weakens the exclusion between IR and Raman spectra, which then show complementary information in both types of spectra. Expressions for the far-IR and OKE spectra will be derived in Section 3.1 and will be expanded upon to show the relationship between OKE and far-IR. Section 3.3 will cover the implementation of this into fit programs written in *Mathematica*.<sup>[102]</sup>

### 3.1. Correlation between OKE and IR terahertz spectra

OKE spectroscopy, as introduced in Section 1.2.1, measures the time-dependent decay of induced birefringence in a sample. Expressions for both the signal and spectrum have been derived previously<sup>[91,103-105]</sup> for the case of optically heterodyne detection. The signal intensity in the time domain can be described as<sup>[106]</sup>

$$S(\tau) \propto \int_0^{\infty} dt' G(\tau - t') \chi_{\alpha\alpha}(t'), \quad (3.1)$$

in which  $G(t)$  is the pump and probe auto-correlation function, with  $\tau$  the delay time between pump and probe, and  $\chi_{\alpha\alpha}(t)$  is the response function describing

how the material responds in the time domain. Defining the Fourier transform as

$$\begin{aligned}\mathcal{F}[x(t)] &= \frac{1}{2\pi} \int_{-\infty}^{\infty} x(t)e^{i\omega t} dt, \\ \mathcal{F}[\hat{x}(\omega)] &= \int_{-\infty}^{\infty} \hat{x}(\omega)e^{-i\omega t} d\omega,\end{aligned}\tag{3.2}$$

the frequency spectrum for an OKE measurement is obtained by the Fourier transform of the time domain data after the deconvolution from the auto-correlation function. Given  $\tilde{S}(\omega) = \mathcal{F}[S(\tau)]$  and  $\tilde{G}(\omega) = \mathcal{F}[G(\tau)]$ , the auto-correlation can be deconvoluted from the frequency domain intensity by<sup>[106]</sup>

$$\tilde{S}_{OKE}(\omega) = \frac{\tilde{S}(\omega)}{\tilde{G}(\omega)} \propto \int_0^{\infty} dt \chi_{\alpha\alpha}(t)e^{i\omega t}.\tag{3.3}$$

The sample response in the time domain has both an electronic and nuclear contribution, which is easy to picture when recalling description of the optical Kerr effect, as presented in Section 1.2.1. The electronic contribution is governed by electrons following the electric field of the pump pulse. The nuclear contribution, meanwhile, arises mainly from the rearrangement of molecules. This rearrangement is due to the alignment of the induced dipole moment in the molecules with the electric field of the pump pulse, which decays over time. These two contributions can be separated by invoking the Born-Oppenheimer approximation, which is generally valid as electrons move faster than nuclei. McMorow<sup>[107]</sup> has shown that the electronic response only contributes to the real part of the OKE signal, allowing the extraction of the nuclear contribution according to

$$S_{OKE}(\omega) = \text{Im}[\tilde{S}_{OKE}(\omega)].\tag{3.4}$$

$S_{OKE}$  can be understood as the OKE spectral intensity, containing the information of low-frequency nuclear motions sought after in the study of dynamics. It is equivalent to the low-frequency depolarized Raman spectrum<sup>[91,105]</sup> and all presented OKE spectra will be plotted in this form.

The far-IR spectra, meanwhile, were measured in units of absorbance. As this is a relative unit, the absorbance ( $A(\omega)$ ) values were transformed into the absorption coefficient ( $\alpha(\omega)$ ) using Lambert's law

$$10^{A(\omega)} = e^{\alpha(\omega)d}\tag{3.5}$$

in which  $d$  is the sample thickness. All IR spectra presented in Chapter 4 were plotted in this form. To further understand the absorption coefficient, the relation between the absorption coefficient and the complex refractive index  $\tilde{n}(\omega)$

can be looked at, which is

$$\tilde{n}(\omega) = \sqrt{\tilde{\epsilon}(\omega)} = n(\omega) + i \frac{c\alpha(\omega)}{2\omega}, \quad (3.6)$$

with the refractive index ( $n(\omega)$ ) and the speed of light ( $c$ ). From Eq. 3.6, it can also be seen that the complex refractive index is related to the complex dielectric function  $\tilde{\epsilon}(\omega)$ . This is expected, as the complex dielectric function describes the interaction between matter and an applied electric field. Further transformation of Eq. 3.6 then shows how the absorption coefficient depends on the complex dielectric function, following

$$\alpha(\omega) = \frac{2\omega}{c} \text{Im}[\sqrt{\tilde{\epsilon}(\omega)}]. \quad (3.7)$$

The dielectric function itself can be described using the Fourier transform of a time domain response function, <sup>[106,108-110]</sup>

$$\tilde{\epsilon}(\omega) = - \int_0^{\infty} dt \chi_{\mu\mu}(t) e^{i\omega t}, \quad (3.8)$$

meaning that the absorption coefficient also depends on a time domain response function.

Comparing Eqs. 3.3 and 3.8 it can be seen that both the OKE as well as the IR spectrum depend on the Fourier transform of time domain response functions. Recalling Sections 1.2.1 and 1.2.2, the OKE spectrum depends on the (anisotropic) polarisability, while the IR spectrum depends on changes in the dipole moment. Both these quantities are related to the positions (and motions) of the nuclei, the nuclear coordinates. Following Giraud and Wynne, <sup>[106]</sup> the time domain response function for OKE depending on the polarisability operator  $\hat{\alpha}(t)$  can be defined as

$$\chi_{\alpha\alpha}(t) = \frac{N}{i\hbar} \langle [\hat{\alpha}(t), \hat{\alpha}(0)] \rangle_{eq} \quad (3.9)$$

and the IR time domain response function depending on the dipole moment operator  $\hat{\mu}(t)$  as

$$\chi_{\mu\mu}(t) = \frac{N}{i\hbar} \langle [\hat{\mu}(t), \hat{\mu}(0)] \rangle_{eq}. \quad (3.10)$$

Here,  $[a, b]$  is the commutator of  $a$  and  $b$ , while  $\langle x \rangle_{eq}$  denotes the expectation value for  $x$  in the equilibrium state of the system. Both the polarisability operator as well as the dipole moment operator, assuming the Born-Oppenheimer approximation holds, can be expanded around the equilibrium configuration  $q_0$  following

$$\hat{x}(q) = \hat{x}_0 + \sum_i \left( \frac{\partial x}{\partial q_i} \right)_{q=q_0} \hat{q}_i + \dots, \quad (3.11)$$

giving a dependence on the nuclear coordinates  $q$ . Then, the time domain response functions can be expressed as

$$\chi_{xx}(t) = \frac{N}{i\hbar} \sum_i \left\langle \left( x'_i \right)^2 [\hat{q}_i(t), \hat{q}_i(0)] \right\rangle_{eq}, \quad (3.12)$$

where  $x$  stands for the polarisability or dipole moment, respectively. It is therefore clear that the time domain response functions only vary in the prefactor  $(\alpha'_i)^2$  and  $(\mu'_i)^2$ . Since  $\hat{q}_i$  describes the nuclear coordinates, this means that the OKE and IR modes are in principle caused by the same motions and only show different amplitudes. While it is expected that molecules with a centre of inversion will be found either IR or Raman (OKE) active, which is called the “exclusion principle”, two factors need to be taken into account. Unlike molecules in a crystal or gas, molecules in liquids are both disordered yet strongly interacting. Therefore, the influence of a molecule’s surroundings can lead to the loosening of symmetry restraints. Furthermore, low-frequency motions tend to be delocalised over many atoms, or even molecules, possibly leading to a reduction in the symmetry for the motion. Therefore, low-frequency modes could be both Raman and IR active, which Giraud and Wynne<sup>[106]</sup> showed in their study. However, they also found that there is no simple relationship for the amplitude between OKE and IR spectra.

In conclusion, both OKE and far-IR spectra can be described by a common set of motions with differing amplitudes, meaning that they in principle be described by the same fit functions. These fit functions, however, would need to be transformed according to Eqs. 3.4 and 3.7 to emulate the quantity used for the amplitude of the spectra.

## 3.2. Fit functions

The measured terahertz spectra were fitted with a set of empirical functions often used to describe dynamics in the terahertz range.<sup>[111]</sup> These are the Havriliak-Negami, the Brownian oscillator, and the anti-symmetrised Gaussian functions, which are described in further detail below. In order to fit the far-IR absorption data, the complex dielectric function is needed (Eq. 3.7) in contrast to the OKE data (Eq. 3.4), which only uses the imaginary part. Therefore, complex fit models are required that represent the real and imaginary part of the dielectric function.

### 3.2.1. Anti-symmetrised Gaussian

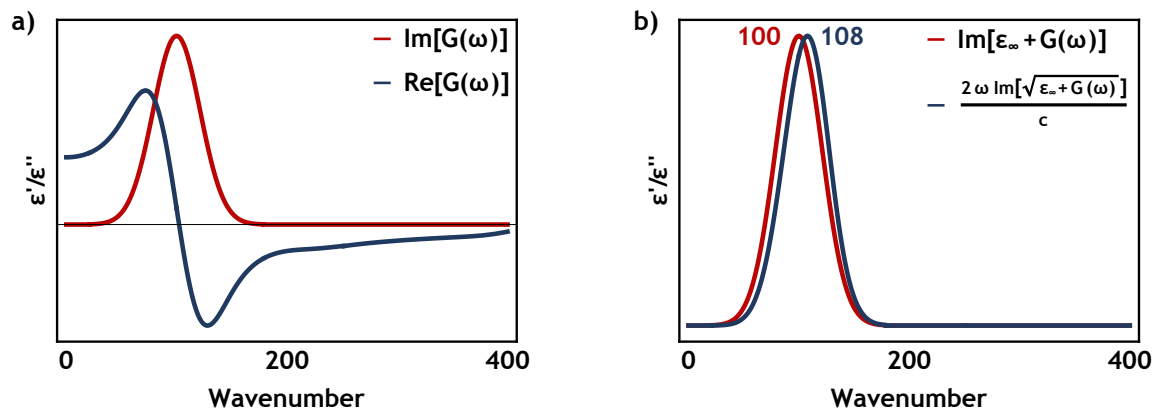


**Figure 3.1.:** Graphs showing the anti-symmetrised Gaussian function. a) Shown are the real (blue) and imaginary (red) part of an anti-symmetrised Gaussian function with an undamped oscillator frequency of  $100 \text{ cm}^{-1}$ . b) Scaled comparison between the shape of the anti-symmetrised Gaussian shown in a) after being transformed for fitting to OKE (red) and far-IR (blue) data.

In OKE spectra, anti-symmetrised Gaussian functions<sup>[111]</sup> are often used to fit intermolecular modes that are inhomogeneously broadened due to a distribution of environments, such as librations. The complex anti-symmetrised Gaussian can be found using the Kramers-Kronig relations and is given by

$$ASG(\omega) = A_{ASG} e^{-\frac{(\omega - \omega_0)^2}{\gamma^2}} \left( i - \operatorname{erfi} \left[ \frac{\omega - \omega_0}{\gamma} \right] \right) - A_{ASG} e^{-\frac{(\omega + \omega_0)^2}{\gamma^2}} \left( i - \operatorname{erfi} \left[ \frac{\omega + \omega_0}{\gamma} \right] \right), \quad (3.13)$$

where  $\omega$  is the angular frequency,  $A_{ASG}$  is the amplitude,  $\omega_0$  is the undamped oscillator angular frequency,  $\gamma$  is a damping parameter, and  $\operatorname{erfi}(z)$  is the imaginary error function defined by

$$\operatorname{erfi}(z) \equiv \frac{\operatorname{erf}(iz)}{i} \quad (3.14)$$

using the error function  $\operatorname{erf}(x)$ .

### 3.2.2. Brownian Oscillator

The Brownian oscillator function<sup>[111]</sup> is often used to model homogeneously-broadened intramolecular modes. In the frequency domain, the Brownian oscil-

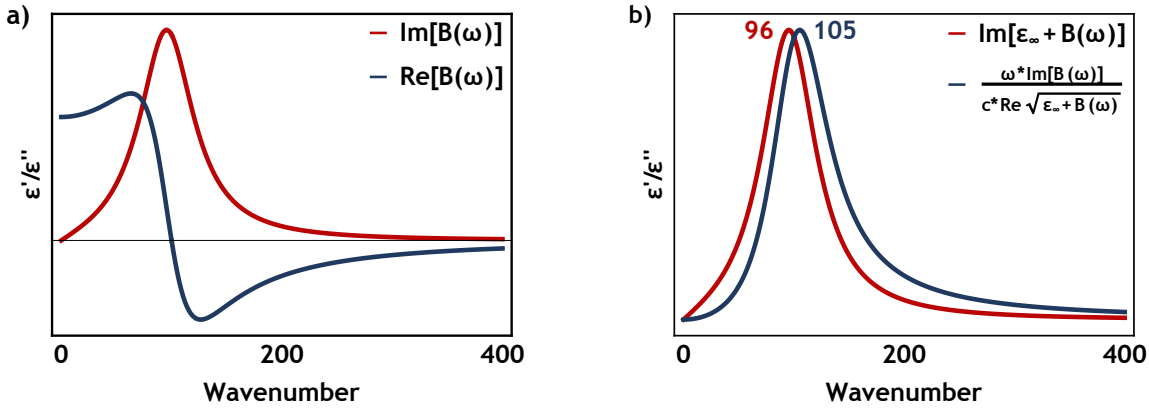


**Figure 3.2.:** Graphs showing the Brownian Oscillator function. a) Shown are the real (blue) and imaginary (red) part of a Brownian oscillator with an undamped oscillator frequency of  $100 \text{ cm}^{-1}$ . b) Scaled comparison between the shape of the Brownian oscillator shown in a) after being transformed for fitting to OKE (red) and far-IR (blue) data.

lator is defined by

$$B(\omega) = \frac{A_B \omega_0^2}{\omega_0^2 - \omega(\omega + 2i\gamma)}, \quad (3.15)$$

with  $A_B$  denoting the amplitude.

### 3.2.3. Havriliak-Negami function

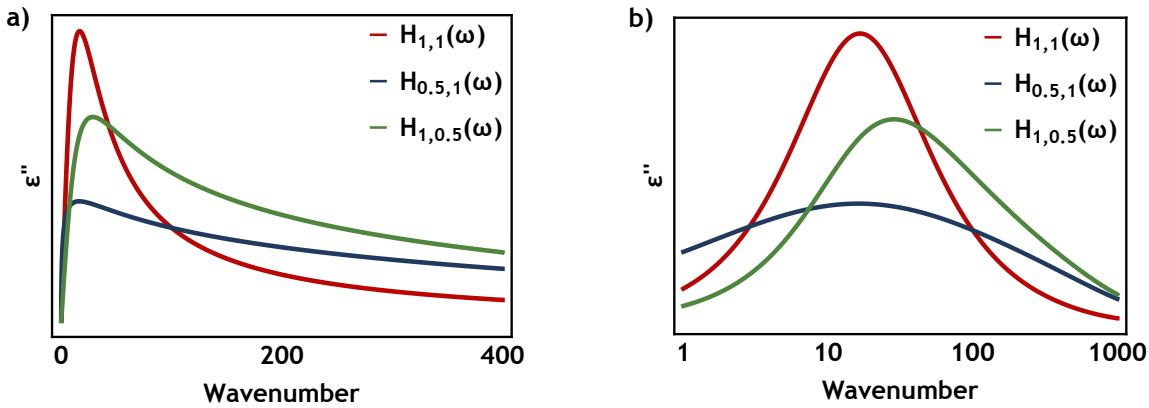


**Figure 3.3.:** Graphs showing the Havriliak-Negami function. a) Linear and b) logarithmic plots of rise-modified Havriliak-Negami functions with different  $\alpha$  and  $\beta$  parameters. The differences between a Debye function ( $H_{1,1}$ ), a Cole-Cole function ( $H_{0.5,1}$ ) and a Cole-Davidson function ( $H_{1,0.5}$ ) are most obvious in the logarithmic plot.

The Havriliak-Negami function is commonly used to model diffusive relaxation<sup>[111]</sup> and can be written in the frequency domain as

$$H_{\alpha,\beta}(\omega) = \frac{A_{HN}}{(1 + (-i\omega\tau)^\alpha)^\beta}, \quad (3.16)$$

where  $A_{HN}$  is the amplitude and  $\tau$  is the relaxation time. Here,  $\alpha$  and  $\beta$  are

broadening and asymmetry parameters taking on values between zero and one. Restraints on  $\alpha$  and  $\beta$  denote special cases of the Havriliak-Negami function. The **Debye function** corresponds to an exponential decay in the time domain and is mostly used to model the slowest diffusive orientational relaxation band. It is equivalent to a Havriliak-Negami function with both  $\alpha$  and  $\beta$  held at 1. Furthermore, all Havriliak-Negami functions with values of  $\alpha$  and  $\beta$  that are not both 1 can be interpreted as superpositions of Debye functions with a distribution of relaxation times  $\tau$ . In the case of  $\alpha = 1$  the Havriliak-Negami function is reduced to a **Cole-Davidson function**. Compared to the Debye function, the Cole-Davidson function is asymmetrically broadened, having a less steep slope on the high-frequency side which is best seen on a  $\log(\omega)$  scale as in Fig. 3.3b. When  $\beta = 1$ , the Havriliak-Negami function reduces to a **Cole-Cole function**, which is symmetrically broadened with respect to the Debye function and as such shows less steep slopes on both sides (see Fig. 3.3b). Cole-Cole functions with a small value in  $\alpha$  have been used previously<sup>[111]</sup> to model translational diffusive relaxations that resemble white noise in the time domain.

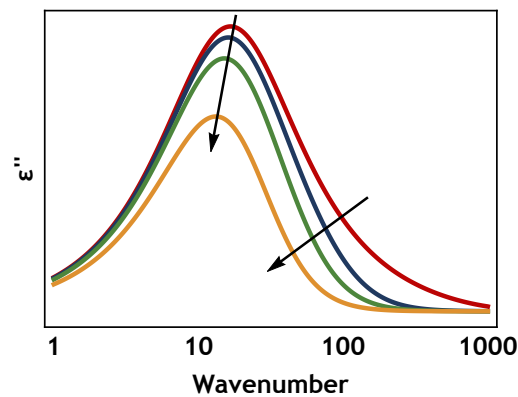


**Figure 3.4.:** The influence of the rise modification on the shape of a Debye function. The value of the rise parameter  $\Gamma_{Rise}$  decreases in the direction of the arrows (red, blue, green, orange) and a stronger suppression effect can be seen.

The Havriliak-Negami function falls off too slowly at high frequencies, which is unphysical and affects the overall fit.<sup>[111,112]</sup> This can be understood by looking at the corresponding time domain functions and is easiest to see for the Debye function, which is an exponential decay in the time domain. Because high frequencies correspond to short times, it is necessary to examine the exponential decay near zero on the time scale. There, the amplitude of an exponential decay is at its maximum when the time is exactly zero and afterwards decreases. Therefore, the described system starts at its maximum value, which is illogical when talking about induced effects such as birefringence. Here, the molecules would be exposed to the electric field of the pump pulse at time zero, and then move into alignment with the field. This movement is not instantaneous but rather carries a small delay, which means that describing it using an exponential decay is unphysical. However, this can be corrected by multiplying the Havriliak-

Negami function with a rise function in the time domain to change from a discontinuous to a continuous rise,

$$F'(t) = F(t)(1 - e^{-\Gamma_{Rise}t}), \quad (3.17)$$

where  $F(t)$  stands for the function that will be modified,  $t$  is time, and  $\Gamma_{Rise}$  is a rise parameter. An exponential form is chosen for the rise function because its Fourier transform does not need to take into account the convolution with the Havriliak-Negami function. The Fourier transform into the frequency domain yields

$$F'(\omega) = F(\omega) - F(\omega + i\Gamma_{Rise}), \quad (3.18)$$

which can be used on functions without an analytical Fourier transform in the time domain. Fig. 3.4 shows the influence of the decreasing rise parameter on a Debye function. The effect of the rise parameter depends on how much larger it is than the centre frequency of the Havriliak-Negami function, with the effect increasing the smaller the difference gets. Experimentally, the rise parameter cannot be measured. However, it is insensitive to small changes and can be estimated from values such as the free rotation time or the librational frequency.<sup>[112]</sup>

### 3.3. Curve fitting

The data presented in this thesis consist of terahertz spectra where either both the OKE and far-IR spectrum (see Chapter 4) or only the OKE spectrum (see Chapters 5 and 6) was measured. The weighted nonlinear least-squares curve fits for these were carried out with programs written in *Mathematica*.<sup>[102]</sup> These programs will be described in further detail below.

#### 3.3.1. OKE and far-IR spectra

For each sample, both the OKE and far-IR spectra were loaded into the program. A combination of fit functions was then fitted to both spectra simultaneously using the in-built `NonlinearModelFit`. The weights depended on the frequency  $f$  as

well as the maximum intensity. They were given by

$$w_s(f) = \frac{1}{I_{s,max}^2} \begin{cases} f & , f \leq 1\text{THz} \\ 1 & , 1\text{THz} < f < 10\text{THz} \\ \frac{10^3}{f^3} & , f \geq 10\text{THz} \end{cases} \quad (3.19)$$

with  $I_{s,max}$  denoting the maximum intensity of either the OKE or far-IR spectrum and  $f$  being given in THz. Note that far-IR data are only measured at frequencies  $>1$  THz. The weighting takes into account that the far-IR data become increasingly noisy due absorption by the window material poly(4-methyl-1-pentene) (TPX) at high frequencies. The origin of the high- and low-frequency weights in the OKE spectrum is less straightforward and is due to errors caused by the Fourier transform of the measured time domain data. At low frequencies, random errors occur if the measured time was not long enough to fully capture the slowest relaxation. The high-frequency limit, on the other hand, is given by the pulse width and errors usually manifest themselves as changes in the slope of the spectrum.

While it can be seen from Eq. 3.4 that the real part of the fit functions has no influence on the OKE spectra, Eq. 3.7 shows that it cannot be neglected in the far-IR spectra. For the IR measurements, the sum of the fit functions can be seen as the dielectric function and the real part of the dielectric function is connected to the refractive index through Eq. 3.6. Due to the limited frequency range of the far-IR measurement it is not possible to fully fit the real part of the dielectric function. As such a constant,  $\epsilon_\infty = n_\infty^2$ , has to be added to the superposition of fit functions,  $\tilde{\epsilon}(\omega) = \epsilon_\infty + \sum_i \tilde{f}(\omega)$ , to take into account the influence of the refractive index at higher frequencies. This was estimated as  $n_\infty = 1.5$  since the refractive index at 589 nm of alkylammonium ILs varies between 1.4 and 1.5.<sup>[113-115]</sup> For the reflection corrections in the far-IR it was also necessary to use the refractive index of TPX,  $n_{\text{TPX}} = 1.457$ , which is approximately frequency independent in the far-IR, varying between 1.4555 and 1.4570.<sup>[116]</sup>

Some of the ionic liquids studied with both OKE and far-IR spectroscopy (see Chapter 4) have very strong absorption bands in the far-IR. These give rise to large refractive index changes well above the high-frequency refractive indices of ionic liquids ( $n_D \approx 1.4-1.5$ )<sup>[113-115]</sup> and the window material, TPX ( $n_{\text{FIR}} = 1.457$ ),<sup>[116]</sup> resulting in significant interfacial reflections as illustrated in Fig. 3.5. By incorporating Fresnel reflections using transmission coefficients defined by

$$T_{ij} = \frac{2n_i}{n_i + n_j} \quad (3.20)$$

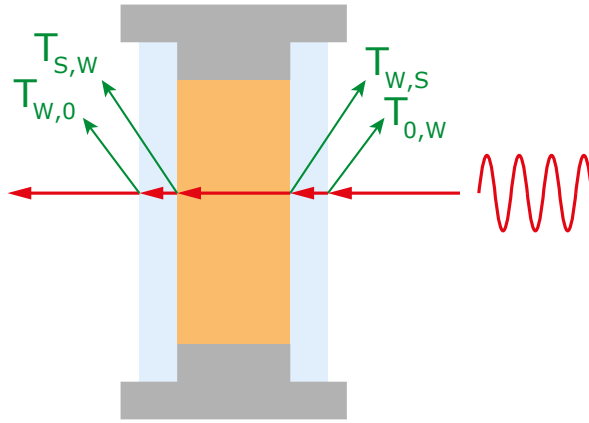


**Figure 3.5.:** Illustration of possible reflections in an IR cell. These arise from differing refractive indices between the air (0), the windows (W) and the sample (S).

where  $i$  and  $j$  are equal to window (w) or sample (s), one can relate the experimentally measured absorption coefficient  $\alpha_{exp}$  with the actual absorption coefficient ( $\alpha(\omega)$ ) by

$$\frac{I}{I_0} = e^{-\alpha_{exp}(\omega)d} = e^{-\alpha(\omega)d} T_{ws}^2 T_{sw}^2 \quad (3.21)$$

where  $d$  is the sample thickness and multiple reflections have been ignored.

Further approximations were made to the imaginary error function,  $\text{erfi}(z)$ , used in the anti-symmetrised Gaussian. This was done to increase the speed of the calculations compared to the imaginary error function built into *Mathematica*.<sup>[102]</sup> For this, the error function with complex arguments,  $\text{erf}(z) = \text{erf}(x + iy)$ , was defined using the method outlined by Salzer<sup>[117]</sup> in the case of  $\text{Re}[z] = 0$ , leading to

$$\text{erf}(0 + iy) = \frac{iy}{\pi} + \frac{2}{\pi} \sum_n n \frac{\sinh[ny]}{n} e^{-\frac{n^2}{4}}. \quad (3.22)$$

In the present case, it can be seen from the definition of the anti-symmetrised Gaussian, Eq. 3.13, that the argument given to the imaginary error function will always be purely real. Thus, we can use Eq. 3.22 in Eq. 3.14 to get

$$\text{erfi}(x + 0i) = \frac{x}{\pi} + \frac{2}{\pi} \sum_n n \frac{\sinh[nx]}{n} e^{-\frac{n^2}{4}}. \quad (3.23)$$

for the imaginary error function. In this,  $n$  ran from 1 to 20 to strike a balance between speed and precision.

Additional approximations were made in the anti-symmetrised Gaussian to avoid errors due to very small or large numbers and to speed up computations. The definition of the anti-symmetrised Gaussian, Eq. 3.13, can be split up into four terms in which the dominant factor is either an exponential or the product of an

exponential and the imaginary error function. These terms can be written as

$$iAe^{\Omega_{\pm}^2} \quad (3.24)$$

$$Ae^{\Omega_{\pm}^2} \operatorname{erfi}(\Omega_{\pm}) \quad (3.25)$$

with  $\Omega_{\pm} = (\omega \pm \omega_0)/\gamma$ . Each term was set to zero once the value of the exponential, for Eq. 3.24, or the product of the exponential and the imaginary error function, for Eq. 3.25, was less than  $10^{-3}$ . For the terms following Eq. 3.24, this was the case for  $|\Omega| \geq 2.63$  and for the terms following Eq. 3.25 this was reached when  $|\Omega| \geq 11.71$ .

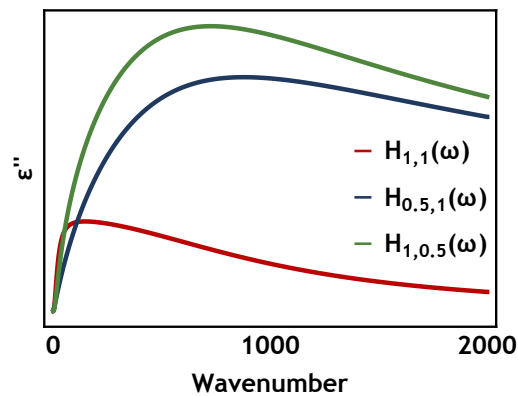


**Figure 3.6.:** Influence of the IR transformation (Eq. 3.7) on the Havriliak-Negami function depending on the  $\alpha$  and  $\beta$  parameters

In the definition of all functions, separate far-IR and OKE amplitudes,  $A_{IR}$  and  $A_{OKE}$ , were used instead of one amplitude. This allowed the use of the exact same functions (apart from amplitude) in both the OKE and far-IR fit simultaneously. If a band was clearly symmetry excluded in one spectrum, the corresponding amplitude was simply set to zero. Furthermore, the Havriliak-Negami function was only used in the form of Debye functions. The cause of this lies in the transformation to the absorption coefficient for the IR spectra fit, which is given by Eq. 3.7. To be precise, the multiplication with frequency leads to a faster rise than the rise function can suppress for all versions of the Havriliak-Negami function besides the Debye function. The results are long, slowly decaying high-frequency tails, as shown in Fig. 3.6, which are not supported by the spectra.

In the end, it is often useful to show the individual components of a fit to OKE or far-IR data in a figure. This presents no problem in the case of OKE but is more involved in the case of far-IR. The visualisation of the individual components in the OKE spectrum is trivial because the fit is a simple superposition. In the far-IR spectrum, on the other hand, the influence of the real part of the dielectric function on each mode needs to be taken into account. Thus, Eq. 3.7 cannot be

used to plot individual fit functions in the far-IR. However, Eq. 3.7 can be written as

$$\alpha(\omega) \cong \frac{\omega \text{Im}[\tilde{\epsilon}(\omega)]}{c \text{Re}[\sqrt{\tilde{\epsilon}(\omega)}]} \quad (3.26)$$

in the limit  $\text{Im}[\tilde{\epsilon}(\omega) \rightarrow 0]$ ,<sup>[106]</sup> which allows us to plot the absorption of an individual component using

$$\alpha_i(\omega) \cong \frac{\omega \text{Im}[\tilde{f}_i(\omega)]}{c \text{Re}[\sqrt{\sum k \tilde{f}_k(\omega)}]}. \quad (3.27)$$

### 3.3.2. OKE spectra

The program used in fitting only the OKE spectra was a modified version of the program described in Section 3.3.1. Here, only the OKE spectrum was loaded into the program. The spectrum was then fitted with a combination of fit functions with the in-built NonlinearModelFit algorithm. For the data shown in Chapter 5 the weights described in Section 3.3.1 were used. Due to the high-frequency vibrations and the long delays measured for the data shown in Chapter 6, uniform weights were used for fitting.

It can be seen from Eq. 3.4 that the OKE spectrum depends only on the imaginary part of the complex dielectric function. This does not lead to any changes in the fit functions save for the anti-symmetrised Gaussian. Considering Eqs. 3.13 and 3.23, it can not only be seen that the imaginary error function will only ever be supplied with real arguments, but also that its output will always be real. As such, the anti-symmetrised Gaussian function simplifies from Eq. 3.13 to

$$G(\omega) = iA_G e^{-\frac{(\omega-\omega_0)^2}{\gamma^2}} - iA_G e^{-\frac{(\omega+\omega_0)^2}{\gamma^2}}, \quad (3.28)$$

where  $\omega$  is the angular frequency,  $A_G$  is the amplitude,  $\omega_0$  is the undamped oscillator angular frequency and  $\gamma$  is a damping parameter.

Furthermore, in Chapter 6 the shape of the rotational relaxation was of priority and therefore sequential relaxation (see Section 1.1.1) had to be taken into account in the fit. The idea behind sequential relaxation is that the dynamics in liquids depend on structures, which are sequentially destroyed as different relaxation mechanisms set in. As described in Section 1.2.1, the first structure dependent motions, expected at short times, are librations, which are hindered rotations in a cage. Then the  $\beta$ -relaxation sets in, which consists of “cage-rattling” or “cage-diffusion” motions. These would destroy the “static” cages needed for

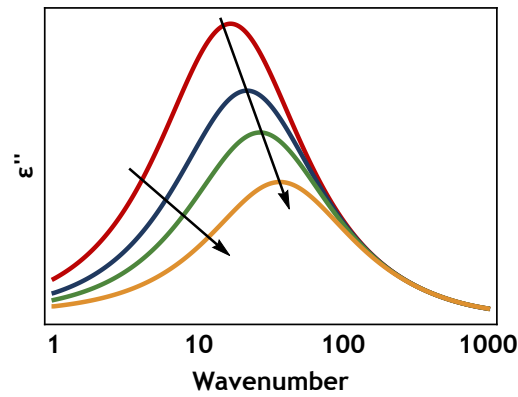


**Figure 3.7.:** The influence of the decay modification on the shape of a Debye function. An unmodified Debye function (red) is compared to Debye functions with an increasingly larger value for the decay parameter (blue, green, orange) in the direction of the arrows.

the librations and therefore should signal the end of the librational spectral components. After the  $\beta$ -relaxation, the  $\alpha$ -relaxation can be seen, which is the rotational relaxation of the particles. Since this indicates the total randomisation of the liquid, the  $\beta$ -relaxation components should cease to influence the spectrum at these frequencies. Sequential relaxation can be incorporated into the fit by introducing a rise and decay modification into the Havriliak-Negami function used to model the  $\alpha$ -relaxation and  $\beta$ -relaxation components. The rise modification,  $F'(t) = F(t)(1 - e^{-\Gamma t})$  (Eq. 3.17), has already been shown in Eq. 3.18 and Fig. 3.4 (Section 3.2.3), where it addresses the unphysical fall off at high frequencies. For the decay the form

$$F'(t) = F(t)e^{-\Gamma_{Decay}t} \quad (3.29)$$

is used where  $\Gamma_{Decay}$  is a decay parameter. The Fourier Transform of this is

$$F'(\omega) = F(\omega + i\Gamma_{Decay}) \quad (3.30)$$

and the effect on a Debye function can be seen in Fig. 3.7. Inserting Eq. 3.30 into Eq. 3.18 yields

$$F'(\omega) = F(\omega + i\Gamma_{Decay}) - F(\omega + i(\Gamma_{Decay} + \Gamma_{Rise})). \quad (3.31)$$

The thus modified Havriliak-Negami function can then be used to model sequential relaxation by setting the  $\Gamma$  parameters to the appropriate frequencies for the preceding and following function. A value of 0 in  $\Gamma_{Decay}$  returns the fully modified Havriliak-Negami function to a rise-modified Havriliak-Negami function.



## 4. Low frequency spectra of ionic liquids

### 4.1. Introduction

Ionic liquids (ILs), which have been introduced in more detail in Section 1.1.2, are salts with low melting points. In fact, their melting points tend to be closer to those of traditional solvents than to those of classical inorganic salts. Their ionic nature, however, shines through in their low vapour pressures and wide electrochemical windows. Due to this, they are under investigation for use in synthesis,<sup>[35,118]</sup> catalysis,<sup>[35]</sup> electrochemistry,<sup>[37,38,118]</sup> and battery development,<sup>[37,38,118]</sup> among others. This interest is heightened by a dependence of the physical properties of ILs on the constituting ions, which opens the door to tailoring ILs to specific applications. While this prospect is tempting, the number of possible ion combinations is in the order of millions, meaning that the synthesis and measurement of their properties is a humongous task. Therefore, it is vital to understand how the physical properties depend on the choice of ions. One way to do this is to study how interionic interactions influence the structure of the IL.

Below, a short summary of structural motifs in ILs will be given with a focus on the alkylammonium ILs used during this study. A broader and more detailed explanation of the structural motifs can be found in Section 1.1.2, including the different techniques used to gain evidence for or against their existence. Arguably the strongest structural influence on alkylammonium ILs is charge ordering, which is driven by Coulombic interactions between the ions. The attraction and repulsion between ions of the opposite and same charge, respectively, imposes a thermally disturbed but relatively ordered distribution similar to the lattice found in crystals or in short a “quasi-lattice”. Therefore, behaviour reflecting that of classical, high-temperature molten salts is expected from this influence. Another possibility is a behaviour more consistent with that of traditional molecular solvents. This is connected with the concept of ion pairs

or clusters, which result in the formation of charge-neutral, quasi-molecular particles through association of cations and anions. Ion pairs were found to be the dominant structure for the gaseous phase of ILs.<sup>[55]</sup> Therefore, their existence as a major species in the liquid phase is in direct contrast with the low vapour pressure reported for most ILs. Instead, polar-apolar ordering has been found to be the second major structural influence besides charge ordering.<sup>[40]</sup> Here, the unfavourable entropic contribution of having a strongly ordered polar cage around each apolar chain is reduced by aggregation of the apolar chains, resulting in the formation of polar and apolar domains on a mesoscopic scale. The importance of polar-apolar ordering strongly depends on the structure of the ions. Asymmetric distributions of alkyl chain lengths and long alkyl chains lead to stronger polar-apolar ordering, while short chains and a delocalised or sterically hindered charge on the ions leads to weak polar-apolar ordering. Generally, charge ordering is strong compared to polar-apolar ordering in alkylammonium ILs, leading to weakly defined filament networks (see Fig. 1.16a). Last but not least, hydrogen bonds can be formed in protic ILs. The existence of hydrogen-bonded networks is generally accepted for ILs, however, their importance in comparison with other factors is a contested topic. In short, there are several competing structural influences possible in ILs, with the relative strength dependent on the ions making up the IL in question.

The structure of ILs has been experimentally probed by techniques ranging from MS,<sup>[56-58]</sup> neutron diffraction,<sup>[72-75]</sup> X-ray scattering,<sup>[76-79]</sup> NMR spectroscopy,<sup>[47]</sup> far-IR or terahertz time-domain (THz-TDS) spectroscopy,<sup>[62-64,119-122]</sup> and dielectric relaxation spectroscopy (DRS)<sup>[48-52]</sup> to OKE and Raman spectroscopy.<sup>[50-52,77,120,123-126]</sup> Furthermore, theoretical methods including MD simulations<sup>[53,54,70,71,79-83]</sup> and density functional theory (DFT) calculations<sup>[59-64,120,125]</sup> have been used to model ILs. Specifically, the gigahertz to terahertz frequency range can be investigated to yield information on relaxational, librational or vibrational modes connected to the dynamics in the liquid. Techniques used to conduct these studies on ILs include far-IR and THz-TDS spectroscopy<sup>[62-64,122]</sup> as well as Raman and OKE spectroscopy.<sup>[50,123,124,126,127]</sup>

The group of Ludwig<sup>[128]</sup> has done much work on ILs in the terahertz frequency range including the observation of a double band structure in the far-IR for protic alkylammonium ILs with three alkyl groups.<sup>[63,64]</sup> Out of these two bands, they assigned the high-frequency one to the hydrogen bond-enhanced anion-cation interaction and the low-frequency one to a mixture of librations and the hydrogen bond bend mode, respectively, on the basis of DFT calculations of clusters. However, no further effort was made to isolate and characterise the contributions in the lower frequency band. Interestingly, for alkylammonium ILs with

only one alkyl chain on the cation, such as ethylammonium nitrate (EAN), no distinct two band structure was observed in the spectra.<sup>[60]</sup> While a correlation between protic and aprotic ILs was made,<sup>[64]</sup> it failed to use an aprotic alkylammonium IL, using instead an imidazolium IL. Generally, the work of Ludwig *et al.* is strongly rooted in the assumption of hydrogen-bonded ion clusters and pairs. For imidazolium ILs, their interpretation of the major spectral feature having contributions from C—H···X hydrogen bonds has been challenged on the basis that it can be explained by librational and cage-rattling modes<sup>[120]</sup> as well as lattice vibrations<sup>[119]</sup> similar to those in the crystalline state. Buffeteau *et al.*<sup>[119]</sup> argued that more detailed systematic studies were needed for a proper assignment. The oversight of not discussing lattice vibrations is particularly surprising, as most of the spectra used to argue for the hydrogen-bonded cluster model of alkylammonium ILs in their original study<sup>[63]</sup> were taken in the solid state, rather than the liquid one. Furthermore, the DFT calculations, on which the assignment was based, were of clusters in the gas phase, with the total system size equal to the number of ions in the cluster. Therefore, the agreement of the calculated spectra for larger clusters could also be due to the better simulation of cooperative effects. In fact, cooperative effects seem to have been observed in their calculations<sup>[128]</sup> but were only looked at for sizes above their usual cluster size of up to ten ion pairs. On this basis, they concluded that the low-frequency modes originate from local and directional interactions and cooperative effects can be neglected. Whether cooperative effects might show for system sizes ranging between one and ten ion pairs is unknown. Therefore, a systematic study is needed to clarify the assignment of the terahertz bands in alkylammonium ILs and determine the relative influences of hydrogen bonding, ion clusters, and charge ordering.

To achieve this, far-IR and OKE spectroscopy was employed in combination with selected alkylammonium ILs. However, spectra in the terahertz range tend to be complicated due to an overlap of contributions from vibrations, librations, and rotational as well as translational relaxation, making assignments difficult. In order to simplify the spectra and unravel the different contributions, the symmetry of the chosen ions in the ILs was exploited. Previous work on (non-ionic) liquids and solutions done in the group showed that highly symmetric molecules or even atoms can be used to “switch off” single-molecule related dynamics in order to isolate intermolecular dynamics.<sup>[129,130]</sup> For this, it is necessary to look at the origin of the IR and OKE signal detailed in Section 3.1. In short, the OKE spectrum depends on the anisotropic part of the polarisability operator (compare Eqs. 3.3 and 3.4 and Fig. 1.17) while the IR spectrum depends on the dipole moment (see Eqs. 3.7 and 3.8), or more accurately changes in the dipole moment with the motions corresponding to the measured mode. Here, vibrations

tend to be visible because they are connected to changes in the structure. Rotations, however, are dependent on the initial symmetry of the ion, as they do not change the structure with the motion. Therefore, the symmetry of ions can be exploited to suppress the intensity of librations and rotational relaxations, leaving only intermolecular contributions and vibrations. As a result, we choose halide anions,  $\text{Cl}^-$  and  $\text{Br}^-$ , for our ILs. Halide ions have a spherical symmetry, which means they have neither a permanent dipole moment nor an anisotropic polarisability, rendering them basically invisible in our techniques. This only leaves symmetry considerations for the cations. Here, the tetrabutylammonium

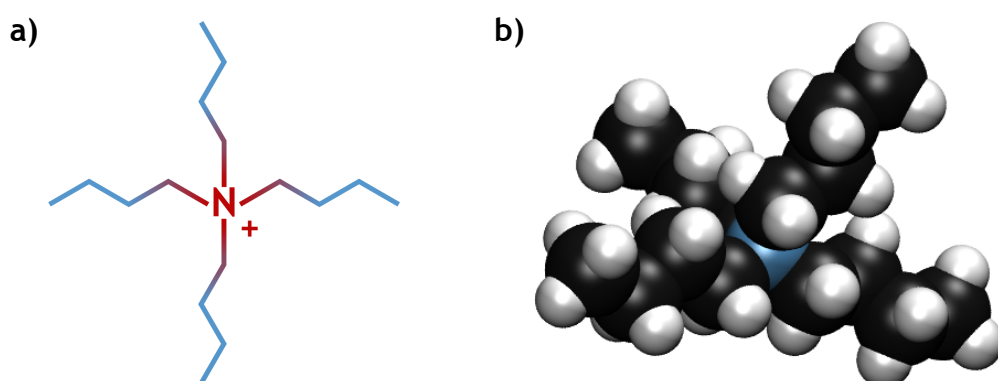


**Figure 4.1.:** Structure of the tetrabutylammonium cation. a) 2D formula with the polar region coloured in red and the apolar region coloured in blue. b) 3D structure with nitrogen coloured in blue, carbon in black and hydrogen in white.

cation (Fig. 4.1) was chosen because it is expected to have a (nearly) tetrahedral symmetry. As all four alkyl chains are butyl groups, the tetrabutylammonium cation should have a vanishing permanent dipole moment as well as a nearly isotropic polarisability, making it again practically invisible in the chosen techniques. In summary, the tetrabutylammonium halides are expected to show only intermolecular contributions as well as vibrations. Furthermore, no hydrogen bonds are expected in the tetrabutylammonium halides. This allows us to test whether the assignment of the low-frequency alkylammonium IL band to a libration made by the Ludwig group<sup>[63,64]</sup> is correct. To further determine which contributions are made by the  $\text{N}-\text{H}\cdots\text{X}$  hydrogen bond and which are due to the asymmetry inherent in the cation due to the hydrogen group, two more cations were chosen. The first of these is the tributylmethylammonium cation shown in Fig. 4.2. Here, one of the four butyl groups is substituted by a methyl group, leading to an aprotic IL with an asymmetric cation. Therefore, contributions from the rotational motions of the cation are expected and the influence of librations as well as the rotational relaxation can be judged by comparing the tributylmethylammonium halide spectra with those of the tetrabutylammonium halides. Finally, the influence of hydrogen bonding can be observed by comparing the tributylmethylammonium halide spectra with those of a protic alkylammonium IL. For this, tributylammonium halides were chosen, which have a hydro-

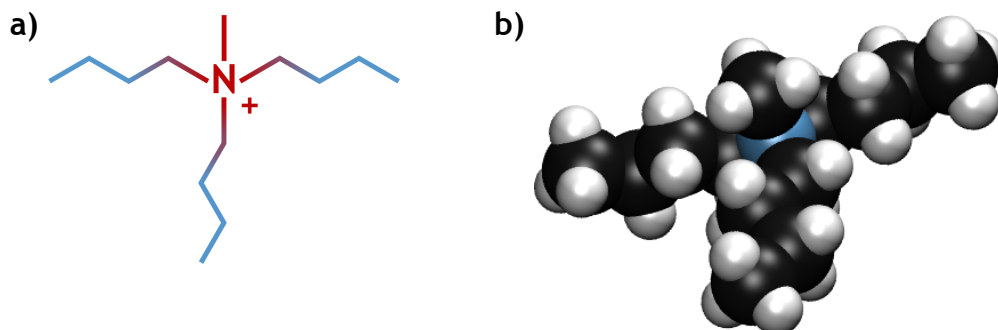


**Figure 4.2.:** Structure of the tributylmethylammonium cation. a) 2D formula with the polar region coloured in red and the apolar region coloured in blue. b) 3D structure with nitrogen coloured in blue, carbon in black and hydrogen in white.

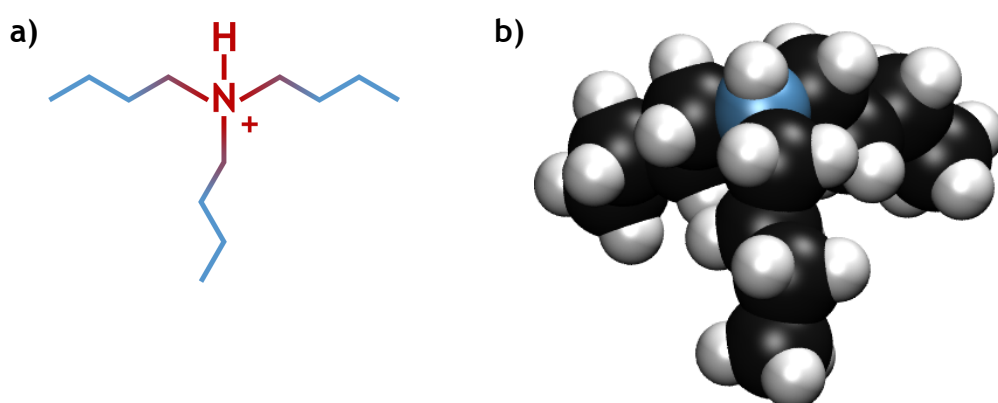


**Figure 4.3.:** Structure of the tributylammonium cation. a) 2D formula with the polar region coloured in red and the apolar region coloured in blue. b) 3D structure with nitrogen coloured in blue, carbon in black and hydrogen in white.

gen atom instead of a methyl group. As the quasi-lattice contributions were of interest, far-IR spectra of the solids were taken in addition to the far-IR and OKE spectra of the liquids. Comparison of the chlorides and bromides then allowed to judge the dependence on the anion mass. While the cation mass-dependence was taken into account by measuring the ethylammonium chloride analogues, their high melting points only allowed for measurements of the solid far-IR spectra. Alkylammonium halides have the further advantage of having little polar-apolar ordering, as less than 5% of the interaction energy<sup>[83]</sup> is expected to come from polar-apolar ordering.

In general, IR and Raman (or OKE) spectra are not expected to show the same modes due to symmetry exclusion. However, symmetry tends to be distorted by the changing environments in liquids, leading to a weakening of the exclusion. Furthermore, intermolecular modes are by nature collective and a low symmetry is expected. Because the dynamics should be measured in both spectra, complementary information is then obtainable from the far-IR and OKE spectra, as previously found for molecular liquids<sup>[106]</sup> (see Section 3.1). As there is no simple relation between the IR and OKE intensity, however, the measured modes are expected to have different relative amplitudes. Additional contributions from alkyl torsions may arise at low frequencies, though their intensity was found to be very weak in IR spectroscopy.<sup>[7]</sup> While it is difficult to predict intensities, they are also expected to be weak in the OKE spectrum because of the low polarisability of alkyl groups. This, however, is based on the assumption that twists of the alkyl chains will not lead to major changes in the structure of the ions and therefore their anisotropic polarisability.

In summary, this study was built to use a selection of alkylammonium halides to dissect the different contributions in the terahertz spectra of ILs. Careful choice of symmetry allows to suppress the intensity of rotational motions, separating them from the intermolecular and vibrational contributions. On this basis we hope to clarify which terahertz bands arise from librations, hydrogen bonds and perhaps even the quasi-lattice.

## 4.2. Experimental details

### 4.2.1. Samples

Tetrabutylammonium chloride ( $\geq 99.0\%$ , Sigma-Aldrich), tetrabutylammonium bromide ( $\geq 98.0\%$ , Sigma-Aldrich), tributylmethylammonium chloride ( $\geq 98.0\%$ , Sigma-Aldrich) and tributylmethylammonium bromide ( $\geq 98.0\%$ , Sigma-Aldrich) were used without further purification. Tributylammonium chloride ( $\geq 95\%$ ) and tributylammonium bromide ( $\geq 95\%$ ) were synthesised (see Section A.1) by David J. France and Stuart A. Ruddell (University of Glasgow) and their purity confirmed by  $^1\text{H-NMR}$ , mass spectrometry and CHN microanalysis.<sup>[131]</sup> Melting points for these ILs can be found in Table 4.1. Tetraethylammonium chloride ( $\geq 98.0\%$ ), triethylmethylammonium chloride ( $\geq 98.0\%$ ) and triethylammonium chloride ( $\geq 98.0\%$ ) were synthesised (see Section A.1) by Natalia V. Plechkova (Queen's University of Belfast) and their melting points can be found in Table 4.2. For these, purities and melting points were measured at Queen's University using  $^1\text{H-NMR}$  and a melting point apparatus equipped with capillaries, respectively. All ILs were dried as powders for at least 16 hours at approximately  $70\text{ }^\circ\text{C}$  under vacuum before use. Any further handling was done in a glove box under dry nitrogen ( $\geq 99.998\%$ , BOC).

**Table 4.1.: Relevant temperatures for the butylammonium halides measurements.** This includes the melting point  $T_m$  as reported in the literature (lit.) and as observed when melting the ILs during the OKE experiment (exp.), as well as the temperatures at which OKE ( $T_{\text{OKE}}$ ) and IR ( $T_{\text{IR}}$ ) measurements of the liquids were taken. Lower melting points have been reported<sup>[17,19,20]</sup> but seem to be caused by the dryness, preparation or purity of the sample.<sup>[22]</sup>

	$T_m$ (exp.) / $^\circ\text{C}$	$T_m$ (lit.) / $^\circ\text{C}$	$T_{\text{OKE}}$ / $^\circ\text{C}$	$T_{\text{IR}}$ / $^\circ\text{C}$
<b>Bu<sub>4</sub>NCl</b>	$80 \pm 5$	90-92 <sup>[21,22]</sup>	90	90
<b>Bu<sub>4</sub>NBr</b>	$120 \pm 5$	121.4-122.4 <sup>[17,18]</sup>	125	125
<b>Bu<sub>3</sub>NMeCl</b>	$110 \pm 5$	108-110 <sup>[132]</sup>	120	120
<b>Bu<sub>3</sub>NMeBr</b>	$130 \pm 5$	120.5-121.5 <sup>[133]</sup>	135	145
<b>Bu<sub>3</sub>NHCl</b>	< 80	-	80	80
<b>Bu<sub>3</sub>NHBr</b>	$80 \pm 5$	-	85	100

Table 4.2.: Melting points for the ethylammonium halides.

	$T_m / ^\circ\text{C}$
$\text{Et}_4\text{NCl}$	249
$\text{Et}_3\text{NMeCl}$	284 <sup>[133]</sup> ; 310 <sup>[132]</sup> (decomposition)
$\text{Et}_3\text{NHCl}$	261 (decomposition)

#### 4.2.2. Measurements

The far-IR data were taken using a dry-air purged Bruker Vertex 70 spectrometer equipped with a mercury arc lamp, a DLaTGS detector, and a silicon solid-state beamsplitter. For the liquid spectra, a drop of the respective liquid was sandwiched between two 2 mm thick TPX windows in a preheated temperature-controlled liquid cell (Harrick Scientific, precision  $\pm 1.5^\circ\text{C}$ ) using a 10  $\mu\text{m}$  or 56  $\mu\text{m}$  PTFE ring spacer. 128 scans were taken between 30 and 600  $\text{cm}^{-1}$  with 5  $\text{cm}^{-1}$  resolution. For the pellet spectra, 1 volume equivalent of IL powder was mixed with polyethylene (PE) powder (40-48  $\mu\text{m}$  diameter, Sigma-Aldrich) in an agate mortar and pressed into 7 mm pellets under a dry nitrogen atmosphere using a hand press (Pike Technologies). 64 scans were taken at room temperature between 30 and 400  $\text{cm}^{-1}$  with 2  $\text{cm}^{-1}$  resolution. The pellet thickness was ill defined, preventing a conversion of the measured absorbance into an absorption coefficient. This was due to the high absorbance of both the ILs themselves and the PE powder used to dilute the ILs. Therefore, only roughly 20  $\mu\text{m}^3$  of the powder mixture were used in making a pellet that was as thin as experimentally possible. The variability in the volume and pressure used for making each pellet made it virtually impossible to define a thickness.

The OKE data were taken in a purpose-built time domain pump-probe setup<sup>[12,101]</sup> described in Section 2.1.2. Measurements were taken with delay times of up to 1 ns, resulting in spectral coverage down to 1 GHz ( $< 0.033\text{ cm}^{-1}$ ) in the frequency domain. Samples were held in quartz cuvettes inside a temperature-controlled aluminium block with a precision of  $\pm 0.1^\circ\text{C}$ . Prior to the measurement, the powdered ILs were transferred into modified rectangular quartz cuvettes (Starna, thickness 1 or 2 mm), which were equipped with a valve and a connector for tubing. The solid was melted inside the cuvette. During the melting process, reduced pressure and dry nitrogen were applied as necessary to avoid gas bubbles becoming trapped in the liquid.

Calculations of dipole moments and molecular polarisability tensors were made using the *Gaussian 09* software package<sup>[134]</sup> with a B3LYP/6-311++G(2df,p) Polar

SCRF=(PCM,Solvent=Ethanol) level of theory.

X-ray powder diffraction patterns were measured using an X'Pert PRO MPD diffractometer (Panalytical) utilizing a Cu sealed tube X-ray source. Measurements were taken for  $\theta$  between 5 and 60° with a resolution of 0.034° for tetrabutylammonium chloride and 0.017° for tetrabutylammonium bromide. The powders were compressed into a hole on a flat plate and the surface was kept as even as possible. The plate itself was contained in a closed off sample holder with Mylar windows under a dry nitrogen atmosphere during transport and measurement.

DSC data of tetraethylammonium chloride were measured in a DSC Q100 (TA Instruments, V9.9 Build 303) in the temperature range 25 °C to 300 °C at a rate of 5 °C min<sup>-1</sup>. The sample was measured in hermetically sealed DSC pans, which were filled and pressed shut under normal atmospheric conditions. This introduced some water to the sample, as evidenced by a water peak at 100 °C visible in the data shown in Fig. A.1.

### 4.2.3. Fitting procedure

For the raw IR data the averaging and Fourier transform were automatically done in the *OPUS* software package<sup>[135]</sup> supplied with the spectrometer. The liquid IR spectra were extracted by subtracting a spectrum of the TPX windows, shown in Fig. 4.4a, at the appropriate temperature. The TPX spectrum was scaled to the intensity between 386 and 392 cm<sup>-1</sup> of the liquid IL spectrum, where the TPX spectrum shows a shoulder with very small temperature variations (see Fig. 4.4a) and which is not close to any sample modes (see Fig. 4.4c). The background corrected liquid spectrum was then used for further analysis, as detailed below. In the pellet spectra, a background caused by the PE used for sample dilution had to be subtracted from the spectra. For this, the spectrum of a pure PE pellet at room temperature, Fig. 4.4b, was scaled to the intensity between 300 and 400 cm<sup>-1</sup> and then subtracted. The pellet spectra were not processed any further afterwards.

The raw OKE data were processed in a *LabVIEW*<sup>[136]</sup> program. The time domain traces were checked manually for the influence of scattering. Scattering changes the time domain trace due to stray light from the pump reaching the detector. The average was then taken over all traces in which the shape had not been influenced by scattering, which were at least 45 (compare Table A.1). This av-

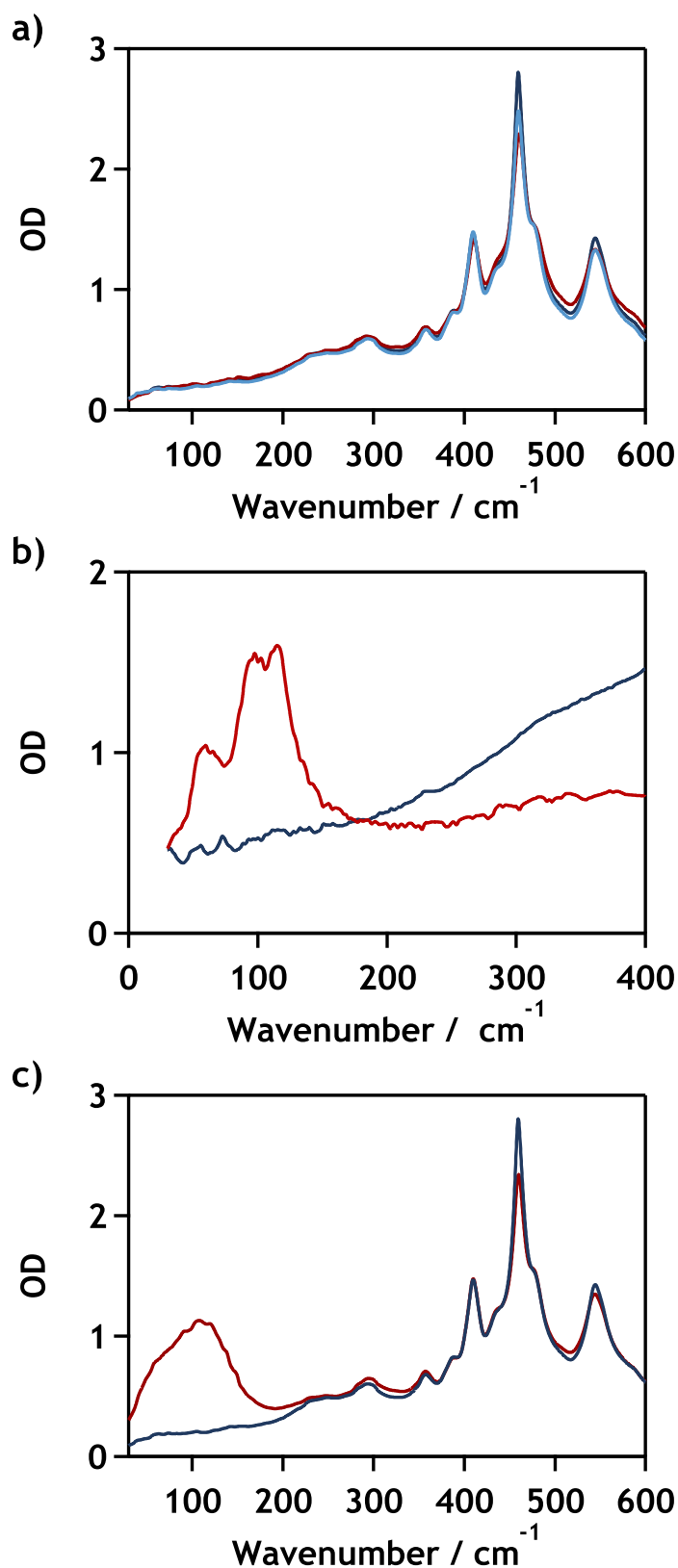


**Figure 4.4.:** Background spectra of the IL far-IR measurements. a) Spectrum of the TPX windows used in the liquid cell at 80 °C, 90 °C and 120 °C (blue to red). A very slight temperature dependence can be seen below 400  $\text{cm}^{-1}$ . b) Spectrum of a pure PE pellet (blue) compared with the raw pellet spectrum taken for tetrabutylammonium chloride (red). c) Comparison of the raw liquid tetrabutylammonium chloride (red) and TPX (blue) spectra, taken at the same temperature.

erage was deconvoluted from a  $\text{sech}^2$  autocorrelation function fitted to the instantaneous response at negative times, and then Fourier transformed. The resulting spectrum was used for further analysis as described below.

A detailed description of the fitting algorithms and functions used can be found in Sections 3.2 and 3.3.1, respectively. It was assumed that high-frequency vibrational modes, fitted to Brownian oscillator functions, were affected by the mutual IR and Raman exclusion and as such different for both the IR and OKE spectrum of a given sample. Therefore, they only had a non-zero amplitude for the spectrum of one of the methods. The lower frequency bands, however, were not assumed to be symmetry excluded. As such they had both an IR and OKE amplitude, which could be varied independently. Otherwise they had a damping and frequency parameter which were the same for both the OKE and IR spectrum.

Due to the general scarceness of features in the alkylammonium IL spectra, a good starting estimate of the fit parameters was essential. To determine these, a number of steps were used. Firstly, two anti-symmetrised Gaussians were placed in the far-IR spectrum (see Fig. 4.5a). In the protic ILs, these were placed on the two distinctive bands. In the aprotic ILs one anti-symmetrised Gaussian was each placed at the low and high-frequency end of the main band, respectively, and the damping was initially based on the damping of the corresponding band in the protic IL spectrum. The oscillator frequencies were also compared to those found in the solid spectra and adjusted if necessary. Another anti-symmetrised Gaussian was then added to correct for the slope on the high-frequency side of the main band as shown in Fig. 4.5a. In the second step a Debye function was placed at the low frequency end of the OKE spectrum and all OKE amplitudes were varied to fit the main band (see Fig. 4.5b). In the last step Brownian oscillators were added to model the vibrational bands at the high frequency end of the spectrum.

After this parameters were varied in small batches by the fitting algorithm and additional functions were added to improve the fit if necessary. The final fit parameters can be found in Table 4.3 for the anti-symmetrised Gaussian functions and in Table 4.4 for the Brownian oscillator and Debye functions.

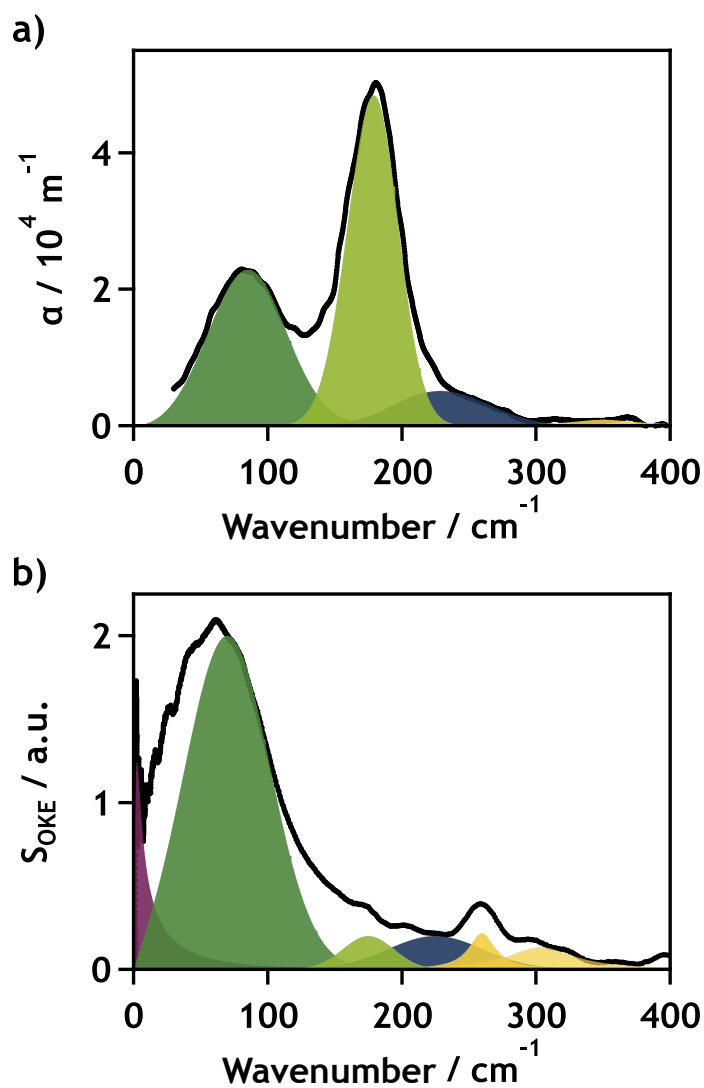


**Figure 4.5.:** Fitting process for the alkylammonium ILs. Shown are the a) IR and b) OKE spectrum for tributylammonium chloride. The green area fills denote the two anti-symmetrised Gaussian functions placed at each end of the main band in the IR spectrum. The high-frequency anti-symmetrised Gaussian added afterwards to correct for the slope is shown in blue. The Debye function is coloured purple and the Brownian oscillators are yellow.

**Table 4.3.:** IL fit parameters. Shown are the parameters for the anti-symmetrised Gaussian functions.

	Bu <sub>4</sub> NCl	Bu <sub>4</sub> NBr	Bu <sub>3</sub> NMeCl	Bu <sub>3</sub> NMeBr	Bu <sub>3</sub> NHCl	Bu <sub>3</sub> NHBr
<b>A</b>						
$A_{OKE}$	0.17	0.21	0.16	0.14	0.21	0.21
$A_{IR}$	7.26	17.52	0.66	0.73	0.77	0.97
$\omega_0 / \text{cm}^{-1}$	47.13	32.53	45.14	25.49	61.21	38.46
$\gamma / \text{cm}^{-1}$	40.81	25.70	44.82	33.15	51.00	40.12
<b>B</b>						
$A_{OKE}$	0.017	0.17	0.026	0.054	0.030	0.14
$A_{IR}$	$2.44 \times 10^{-9}$	$2.15 \times 10^{-9}$	$7.45 \times 10^{-9}$	0.026	0.077	0.081
$\omega_0 / \text{cm}^{-1}$	121.82	61.64	77.72	57.00	131.50	72.22
$\gamma / \text{cm}^{-1}$	20.81	18.44	20.41	19.15	29.79	34.42
<b>C</b>						
$A_{OKE}$	0.10	0.11	0.064	0.097	0.025	0.037
$A_{IR}$	2.87	0.46	0.53	0.33	0.62	0.56
$\omega_0 / \text{cm}^{-1}$	88.99	84.47	105.78	77.62	174.78	121.18
$\gamma / \text{cm}^{-1}$	32.85	21.13	36.71	28.52	27.04	21.60
<b>D</b>						
$A_{OKE}$	0.034	0.082	0.014	0.027	0.015	0.032
$A_{IR}$	0.45	0.45	0.052	0.068	0.055	0.14
$\omega_0 / \text{cm}^{-1}$	141.61	104.50	153.50	116.78	221.16	151.41
$\gamma / \text{cm}^{-1}$	54.10	42.93	47.81	33.00	49.06	46.55

**Table 4.4.: IL fit parameters.** Shown are the parameters the Brownian Oscillator (BO) and Debye functions. For the Debye functions the parameters  $\alpha$  and  $\beta$  were held at 1.

	Bu <sub>4</sub> NCl	Bu <sub>4</sub> NBr	Bu <sub>3</sub> NMeCl	Bu <sub>3</sub> NMeBr	Bu <sub>3</sub> NHCl	Bu <sub>3</sub> NHBr
<b>BO1</b>						
$A_{OKE}$	0	0	0	0	0	0
$A_{IR}$	0.019	0.014	0.0027	0.0022	0.0010	0
$\omega_0 / \text{cm}^{-1}$	313.00	318.59	313.00	318.62	349.93	0
$\gamma / \text{cm}^{-1}$	30.00	17.04	30.00	33.13	29.95	0
<b>BO2</b>						
$A_{OKE}$	0.0020	0.0031	0.0037	0.0021	0.0027	0.0049
$A_{IR}$	0	0	0	0	0	0
$\omega_0 / \text{cm}^{-1}$	251.00	250.52	260.39	258.84	260.00	258.18
$\gamma / \text{cm}^{-1}$	8.00	14.99	25.79	20.03	12.00	19.11
<b>BO3</b>						
$A_{OKE}$	0.0082	0.0077	0.0042	0.0039	0.0026	0.0019
$A_{IR}$	0	0	0	0	0	0
$\omega_0 / \text{cm}^{-1}$	292.00	295.00	315.52	314.42	305.00	300.88
$\gamma / \text{cm}^{-1}$	35.00	30.02	18.91	21.92	30.00	32.03
<b>BO4</b>						
$A_{OKE}$	0.00014	0.0067	0	0.0066	0.00044	0.00084
$A_{IR}$	0	0	0	0	0	0
$\omega_0 / \text{cm}^{-1}$	395.00	186.57	0	167.73	395.00	399.00
$\gamma / \text{cm}^{-1}$	5.00	30.07	0	47.31	10.00	10.00
<b>Debye</b>						
$A_{OKE}$	0.11	0.21	0.13	0.12	0.19	0.20
$A_{IR}$	$1.23 \times 10^{-8}$	0.10	$6.28 \times 10^{-8}$	2.29	$6.05 \times 10^{-7}$	$3.64 \times 10^{-9}$
$\tau / \text{ps}$	8.99	10.52	7.96	13.14	7.85	13.13
$\Gamma / \text{cm}^{-1}$	55.00	30.00	50.00	25.00	65.00	40.00

## 4.3. Results and discussion

### 4.3.1. Tetrabutylammonium halides

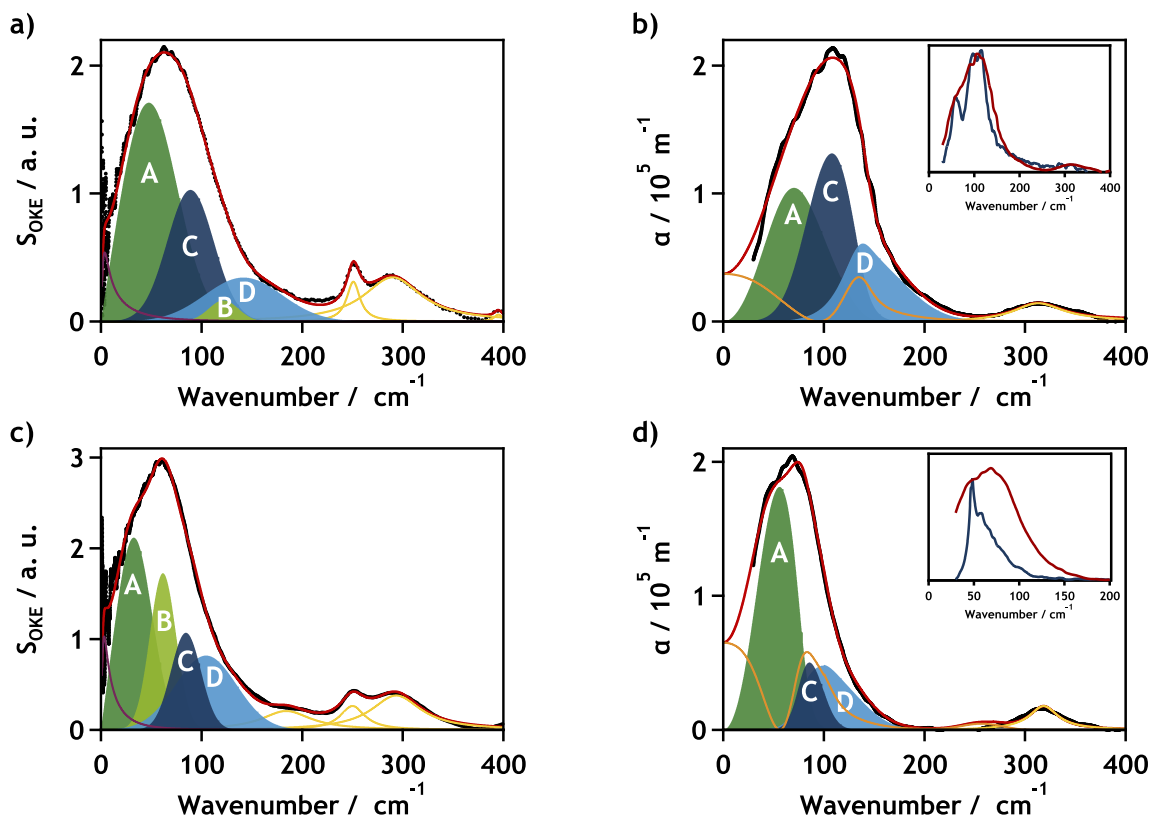


**Figure 4.6.:** Terahertz spectra and fits of the liquid and crystalline tetrabutylammonium halides. a) Shown is the experimental OKE spectrum of liquid tetrabutylammonium chloride at 90 °C (black), the overall fit (red), and component functions of the fit (blue, green and yellow). b) The experimental far-IR spectrum of of liquid tetrabutylammonium chloride at 90 °C (black), the overall fit (red), the contribution to the absorption due to reflectivity (orange), and component functions of the fit (blue, green and yellow). (inset) A comparison of the far-IR spectra of liquid tetrabutylammonium chloride (red) and the crystal (dark blue, 2:1 by volume mixture of polyethylene with tetrabutylammonium chloride) at room temperature. c) Shown is the experimental OKE spectrum of liquid tetrabutylammonium bromide at 125 °C. d) The experimental far-IR spectrum of of liquid tetrabutylammonium bromide at 125 °C. (inset) A comparison of the far-IR spectra of liquid tetrabutylammonium bromide and the crystal (3:1 by volume mixture of polyethylene with tetrabutylammonium bromide) at room temperature.

The tetrabutylammonium cation had been chosen because the four identical side chains should give it a high symmetry while still having an experimentally accessible melting point (compare Tables 4.1 and 4.2). As explained in Section 4.1, it is expected that only the interaction-induced spectral contributions will be shown. Since these contributions rely on an induced dipole moment or anisotropic polarisability, respectively, for the IR and OKE spectrum, their intensities tend to be weak. However, it can be clearly seen from Fig. 4.6 that the recorded spectra are not weak. The far-IR absorption coefficient of  $\sim 10^5 \text{ m}^{-1}$  is very high, compar-

able to that of water in this frequency region.<sup>[137]</sup> The OKE intensity itself is only a factor of 2-3 smaller than those observed for pyridinium ILs in which librations are observed.

Both tetrabutylammonium chloride and bromide show one main band below  $150\text{ cm}^{-1}$  in their IR and OKE spectra. At higher frequencies, less intense vibrational bands can be found which were fitted with Brownian oscillator functions (see Section 3.2.2). The number of vibrational bands and their centre frequency varies between the IR and OKE spectrum for the same IL, indicating they are symmetry excluded. For tetrabutylammonium chloride, two vibrational bands were found in the OKE spectrum and one in the IR spectrum. In tetrabutylammonium bromide, the numbers of vibrational bands were three and two, respectively, for IR and OKE. While the bands which are common to both OKE and IR spectra appear to be frequency shifted (for example A in Fig. 4.6), this is a result of the different frequency dependences of the techniques used. A more in-depth discussion of this can be found in Section 3.1.

As described in Section 4.2.3, the vibrational bands were fitted with distinct Brownian oscillator functions for each type of spectrum. The main band was fitted with anti-symmetrised Gaussian functions in which the frequency and damping were the same for both spectra while the amplitude was allowed to differ. Additionally a Debye function was fitted below  $10\text{ cm}^{-1}$  to cover diffusive bands visible in the OKE spectrum. The measured far-IR spectrum, on the other hand, did not go to low enough wavenumbers to determine the presence of diffusive modes. To access lower wavenumbers in the far-IR spectrum, THz-TDS or DRS measurements would need to be made as the absorption coefficient measured in FTIR spectroscopy scales with frequency (see Eq. 3.7). Fitting the tetrabutylammonium halide spectra was more complicated than fitting the other IL spectra in the experimental series. Their high absorption coefficient led to strong variations in the parts of the fit function associated with the refractive index (compare Eq. 3.27). This can be most easily seen when comparing the reflectivity contributions in the IR spectra of the different ionic liquids, e.g. Fig. 4.6b and d versus Fig. 4.10b and d. In the former, the reflectivity correction makes a visible contribution to the fit while in the latter, the reflectivity contribution is negligible on the scale of the spectrum.

More interesting than the vibrations is the region below  $150\text{ cm}^{-1}$ . Looking at the tetrabutylammonium chloride OKE spectrum (Fig. 4.6a), the band found here appears to be symmetric. In the corresponding IR spectrum (Fig. 4.6b), however, a shoulder is visible at lower frequencies. As such this band was mainly described by two Gaussians, A at  $47\text{ cm}^{-1}$  and C at  $89\text{ cm}^{-1}$ . A further Gaussian

D was needed to fit the high frequency tail in both spectra as well as a low intensity Gaussian B, which was only visible in the OKE spectrum. The fitting of the main band with two high-intensity Gaussians was further validated when looking at the IR spectrum of a tetrabutylammonium chloride pellet at room temperature, shown in the inset of Fig. 4.6b. This pellet spectrum covers the same IR frequency range as the liquid spectrum, however the band with a shoulder is resolved into two peaks. No quantitative comparison with the pellet spectrum was made because the intensity is not given in absolute units. A conversion in absolute units, as done for the liquid spectrum, was impossible due to experimental difficulties in defining the thickness of the pellet, as described in Section 4.2.

In tetrabutylammonium bromide, the main peak in the OKE spectrum (Fig. 4.6c) does not look as symmetric as it does in tetrabutylammonium chloride, possibly indicating a low frequency shoulder. However, between the increased noise at low frequencies in the OKE spectrum and the proximity to the diffusional band it is hard to assign a shoulder in the OKE spectrum. A comparison with the IR spectrum (Fig. 4.6d) is not helpful in this case either, since the measurement did not go to sufficiently low frequency. A comparison between the chloride and bromide spectra of the less symmetric ILs covered in Sections 4.3.2 and 4.3.3 below showed systematic similarities between the spectra. As such tetrabutylammonium bromide was fitted in a manner similar to tetrabutylammonium chloride. The combination of insufficient low frequency data and the high far-IR absorption coefficient, however, made this challenging. As in tetrabutylammonium chloride, one Gaussian D was needed to fit the high frequency tail of the spectra (see Fig. 4.6d). Furthermore, two other Gaussians showed a sufficient intensity to be visible in the IR fit, A at  $33\text{ cm}^{-1}$  and C at  $84\text{ cm}^{-1}$ . Unlike in tetrabutylammonium chloride, C was less intense, comparable to D in intensity (see Table 4.3). A further Gaussian B was needed to fit the OKE spectrum and showed a higher relative intensity towards A compared with the tetrabutylammonium chloride OKE spectrum. Comparing the pellet and liquid IR spectrum of tetrabutylammonium bromide (inset Fig. 4.6d) shows a further difference to tetrabutylammonium chloride. While the tetrabutylammonium bromide pellet spectrum is in the same frequency range as the liquid spectrum it has less high-frequency components and they are also less intense. Additionally, there is no clear two peak structure as found in the tetrabutylammonium chloride pellet spectrum. To further investigate this difference, the X-ray powder diffraction patterns of tetrabutylammonium chloride and bromide are compared in Fig. 4.7. While the powder diffraction patterns can not be easily converted into a crystal structure, the spacing and intensity differences clearly show that tetrabutylammonium chloride and bromide have different crystal structures at room temperature. This indicates different structures in the liquids as well, since charge or-

dering is a major structural influence in butylammonium ionic liquids<sup>[83]</sup> (as discussed in Sections 1.1.2 and 4.1). The implications of this for the spectra will be further discussed in Section 4.3.6.

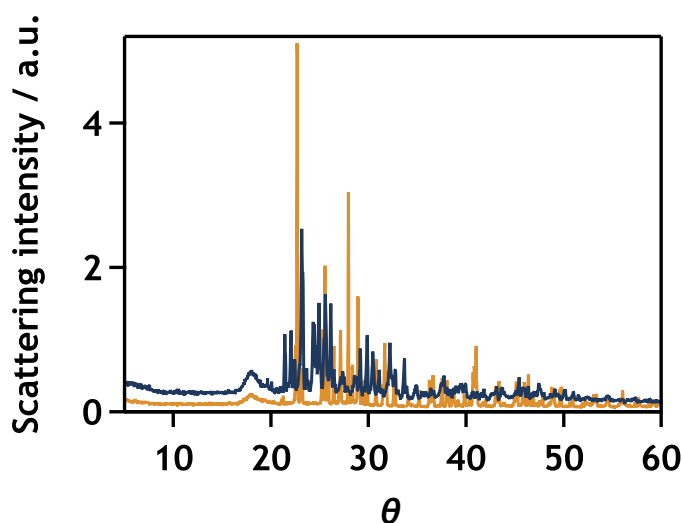


**Figure 4.7.:** Comparison of the X-ray powder scattering of the tetrabutylammonium halides. Shown are the X-ray powder scattering patterns for tetrabutylammonium chloride (blue) and tetrabutylammonium bromide (orange). It can be seen that the scattering patterns are systematically different, indicating fundamentally different crystal structures. The broad peak at  $\theta = 18^\circ$  is caused by the Mylar used for the windows of the sample holder.

To quantify the change in the spectrum caused by changing the anion from chloride to bromide an average frequency ratio  $\frac{\omega_{Br}}{\omega_{Cl}}$  was calculated. For this the centre frequencies of the anti-symmetrised Gaussian fit functions were ordered by frequency and then the bromide frequency was divided by the chloride frequency was averaged over all four Gaussians. This gave an average frequency ratio of  $\frac{\omega_{Br}}{\omega_{Cl}} = 0.70$ . For the tetrabutylammonium halides no frequency ratios were specifically calculated for the A and C band. This was due to the difficulties in fitting explained earlier, specifically because in tetrabutylammonium chloride the C band is found at a lower frequency than the B band.

### 4.3.2. Tributylammonium halides

Compared to the tetrabutylammonium cation, the tributylammonium cation is less symmetric and has the additional capacity to develop hydrogen bonds. Therefore, a difference in their spectra was expected. Looking at the OKE spectra (compare Fig. 4.8a and c with Fig. 4.6a and c), however, there hardly seems to any difference between the ILs. The OKE intensities are basically the same for the chlorides and bromides. The main band of the chloride again looks symmetric, while that of the bromide has a slight hint of a low frequency shoulder.

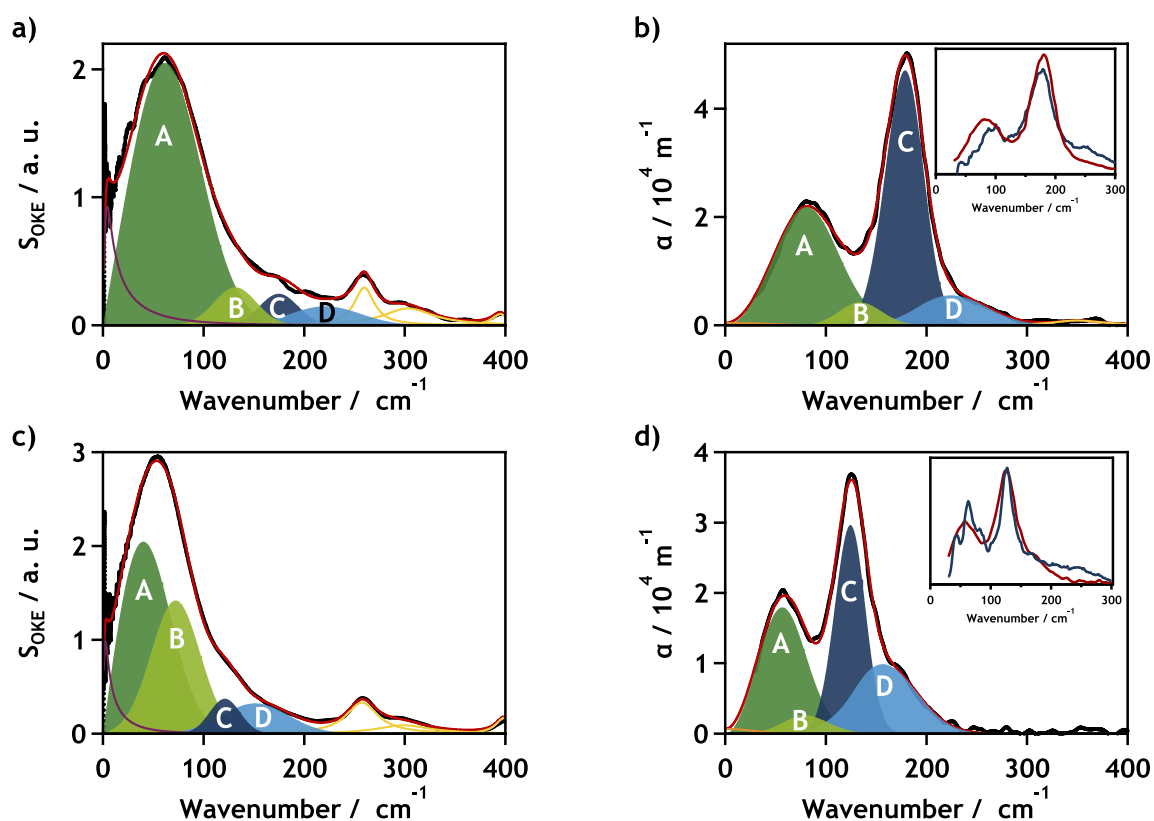


**Figure 4.8.:** Terahertz spectra and fits of the liquid and crystalline tributylammonium halides. a) Shown is the experimental OKE spectrum of liquid tributylammonium chloride at 80 °C. b) The experimental far-IR spectrum of of liquid tributylammonium chloride at 80 °C. (inset) A comparison of the far-IR spectra of liquid tributylammonium chloride and the crystal (1:1 by volume mixture of polyethylene with tributylammonium chloride) at room temperature. c) Shown is the experimental OKE spectrum of liquid tributylammonium bromide at 85 °C. d) The experimental far-IR spectrum of of liquid tributylammonium bromide at 100 °C . (inset) A comparison of the far-IR spectra of liquid tributylammonium bromide and the crystal (5:1 by volume mixture of polyethylene with tributylammonium bromide) at room temperature. Colour coding as in Fig. 4.6.

Two vibrational bands can be found as well at higher frequencies. The IR spectra (compare Fig. 4.8b and d with Fig. 4.6b and d) in contrast are vastly different. For one, the absorption coefficient here is weaker by a factor of 9 for the chloride and 18 for the bromide. Additionally, instead of a main band with a shoulder two clearly separated bands can be seen. This structure is very closely mirrored in the respective pellet spectra as well (insets Fig. 4.8b and d), if a bit noisily. Furthermore, no vibrational bands can be seen in the IR spectra at higher frequencies and the reflectivity component is negligible. All spectra were described by a set of four Gaussians. Two main Gaussians, A and C, one for each band visible in the IR spectrum. While A was intense in both types of spectra the relative intensity of C compared to A dropped significantly when going from IR to OKE. One Gaussian D to fit the high frequency tail and another Gaussian, B, at a frequency between A and C. Due to the defined structure in the IR spectrum the tributylammonium halide spectra were easy to fit. As described in Section 4.3.1, the apparent frequency shift between the OKE and IR spectra is caused by the frequency dependence of the techniques used (see Section 3.1 for more detail).

For tributylammonium chloride the A band could be found at  $61\text{ cm}^{-1}$  and the C band at  $175\text{ cm}^{-1}$ , giving a split between the bands of  $114\text{ cm}^{-1}$ . Compared to  $42\text{ cm}^{-1}$  for tetrabutylammonium chloride and  $61\text{ cm}^{-1}$  for tributylmethylammonium chloride, this is a factor of at least 1.8 difference. In tributylammonium bromide A was at  $38\text{ cm}^{-1}$  and C at  $121\text{ cm}^{-1}$  which is a difference of  $83\text{ cm}^{-1}$ . This differs from both tetrabutylammonium bromide and tributylmethylammonium bromide, which showed differences of  $52\text{ cm}^{-1}$ , by a factor of 1.6. As in tetrabutylammonium bromide, the B band showed a higher relative intensity in the OKE spectrum in the bromide than in the chloride. Comparing the Gaussian centre frequencies in the chlorides and bromides leads to an average frequency ratio  $\frac{\omega_{Br}}{\omega_{Cl}} = 0.64$ , which is lower than in the tetrabutylammonium halides. For the A and C band the ratios are 0.62 and 0.69, respectively.

Tributylammonium chloride is very hygroscopic and therefore draws water from the air if not handled under a dry atmosphere. Fig. 4.9 shows a comparison between an OKE spectrum taken completely under dry conditions with one taken when the sample had been exposed to air. It can be seen that the spectrum suffers a loss of defining features as well as an intensity reduction of roughly an order of magnitude. These are drastic changes for a simple contamination and indicate that the salt shows a different behaviour in solution than in the melt. The importance of this will be further discussed below in Section 4.3.6.

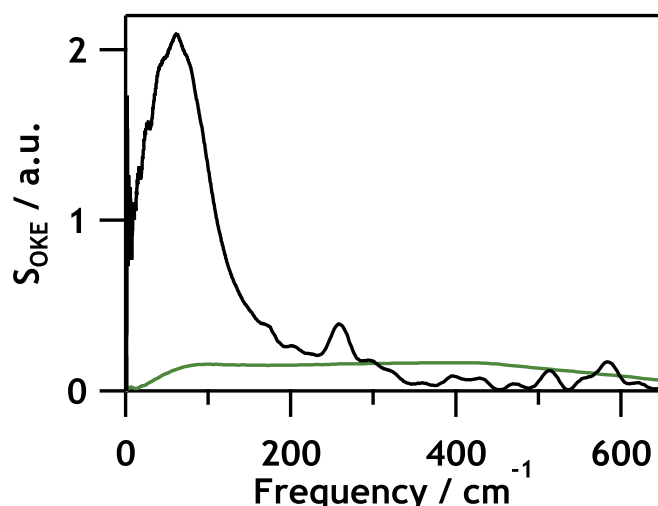


**Figure 4.9.:** Comparison of the OKE spectra for dry and wet tributylammonium chloride. Shown are the liquid spectra for tributylammonium chloride when handled under a dry nitrogen atmosphere (black) and when exposed to air during the preparation process (green). The wet tributylammonium chloride shows a loss in intensity of roughly an order of magnitude as well as a loss of defining features.

### 4.3.3. Tributylmethylammonium halides

The tributylmethylammonium cation is less symmetric than the tetrabutylammonium cation, however, it does not have the capacity to form hydrogen bonds, as the tributylammonium cation does. Therefore, the tributylmethylammonium halide spectra will help to differentiate which effects seen in the tetrabutylammonium halides (see Section 4.3.1) and tributylmethylammonium halides (see Section 4.3.2) are caused by reduced symmetry and which ones are caused by hydrogen bonding. Comparing Figs. 4.6, 4.8 and 4.10 it is clear that the tributylmethylammonium halides closely resemble the tetrabutylammonium halide spectra. As described in Section 4.3.1, the apparent frequency shift between the OKE and IR spectra is caused by the frequency dependence of the techniques used (see Section 3.1 for more detail).

In the OKE spectra, this is not as obvious. Similar to the other measured butylammonium halides, we see some vibrational modes and then a main band below  $150\text{ cm}^{-1}$ . For the chloride this main band appears to be symmetric while for the bromide a slight low frequency shoulder can be seen. The intensity of the OKE spectra is lower than that observed in the other spectra. It is, however, comparable once corrections are made for instrumental influences.

The IR spectra, in comparison, do not show the distinct two band structure seen in the tributylmethylammonium halides but rather the band with a shoulder structure seen in the tetrabutylammonium halides. The absorption coefficient of

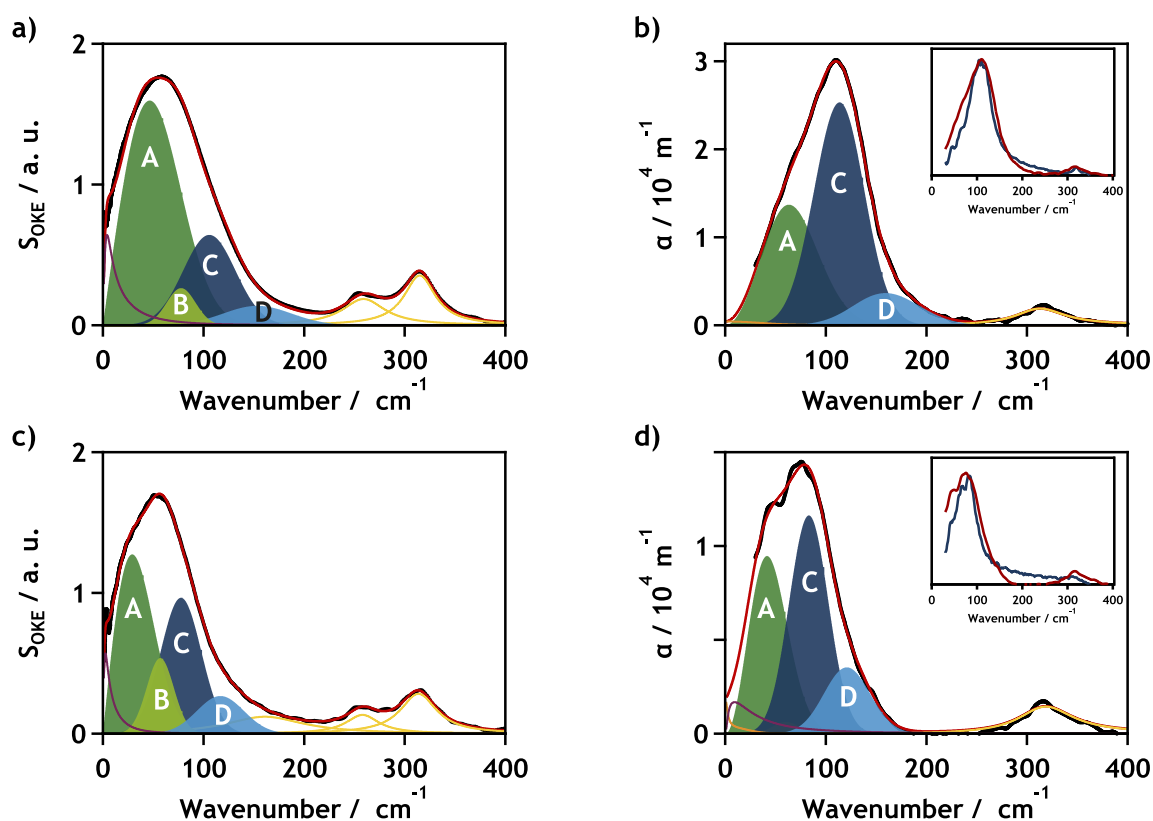


**Figure 4.10.:** Terahertz spectra and fits of the liquid and crystalline tributylmethylammonium halides. a) Shown is the experimental OKE spectrum of liquid tributylmethylammonium chloride at 120 °C. b) The experimental far-IR spectrum of liquid tributylmethylammonium chloride at 120 °C. (inset) A comparison of the far-IR spectra of liquid tributylmethylammonium chloride and the crystal (2:1 by volume mixture of polyethylene with tributylmethylammonium chloride) at room temperature. c) Shown is the experimental OKE spectrum of liquid tributylmethylammonium bromide at 135 °C. d) The experimental far-IR spectrum of liquid tributylmethylammonium bromide at 145 °C. (inset) A comparison of the far-IR spectra of liquid tributylmethylammonium bromide and the crystal (1:1 by volume mixture of polyethylene with tributylmethylammonium bromide) at room temperature. Colour coding as in Fig. 4.6.

the tributylmethylammonium halides, in contrast, is comparable to those found in the tributylmethylammonium halides and a factor of 11 and 24 lower than those found in the tetrabutylammonium chlorides and bromides, respectively.

For tributylmethylammonium chloride, the shoulder in the IR spectrum is not as clearly visible as it is in the tetrabutylammonium chloride, neither for the liquid nor pellet. Two major Gaussians were clearly needed to fit both the IR and OKE spectrum at the same time, though. These were A at  $45\text{ cm}^{-1}$  and C at  $106\text{ cm}^{-1}$  with a separation of  $61\text{ cm}^{-1}$ . This is a larger separation than in tetrabutylammonium chloride but a significantly lower one than in tributylammonium chloride. Again, additional Gaussians were needed to fully replicate the main band. One, D, was needed to fit the high frequency tail and another one, B, was positioned in between A and C, with a negligible IR and a small OKE intensity. Furthermore the relative intensity of C compared with A decreased when going from the IR to the OKE spectrum.

The tributylmethylammonium bromide may show a more developed shoulder than the tetrabutylammonium bromide. Due to the low frequencies, however, this is hard to make out. Unlike in tetrabutylammonium bromide the pellet spectrum of tributylmethylammonium bromide (inset Fig. 4.10d) shows good qualitative agreement with the liquid spectrum. Again there are two main Gaussians in the fit, A at  $25\text{ cm}^{-1}$  and C at  $78\text{ cm}^{-1}$ , with a separation of  $52\text{ cm}^{-1}$ . This separation is the same for tetrabutylammonium and tributylmethylammonium bromide, unlike for their respective chloride counterparts. Further Gaussians were needed to fit the high frequency tail (D) and the area between A and C (B). As in the other bromides, B showed a higher relative intensity in tributylmethylammonium bromide than in the corresponding chloride. Unlike tetrabutylammonium bromide, however, the pellet spectrum of tributylmethylammonium bromide (inset Fig. 4.10d) is in good qualitative agreement with the liquid spectrum.

Calculating the change in centre frequency due to the change in anion leads to an average frequency ratio  $\frac{\omega_{Br}}{\omega_{Cl}}$  of 0.70, the same as in the tetrabutylammonium halides. The ratios for the A and C band are 0.56 and 0.73, respectively. However, assigning any meaning to this is difficult because the separation of the A and C band in the spectra is not as well defined in the aprotic IL spectra as it is in the protic ones.

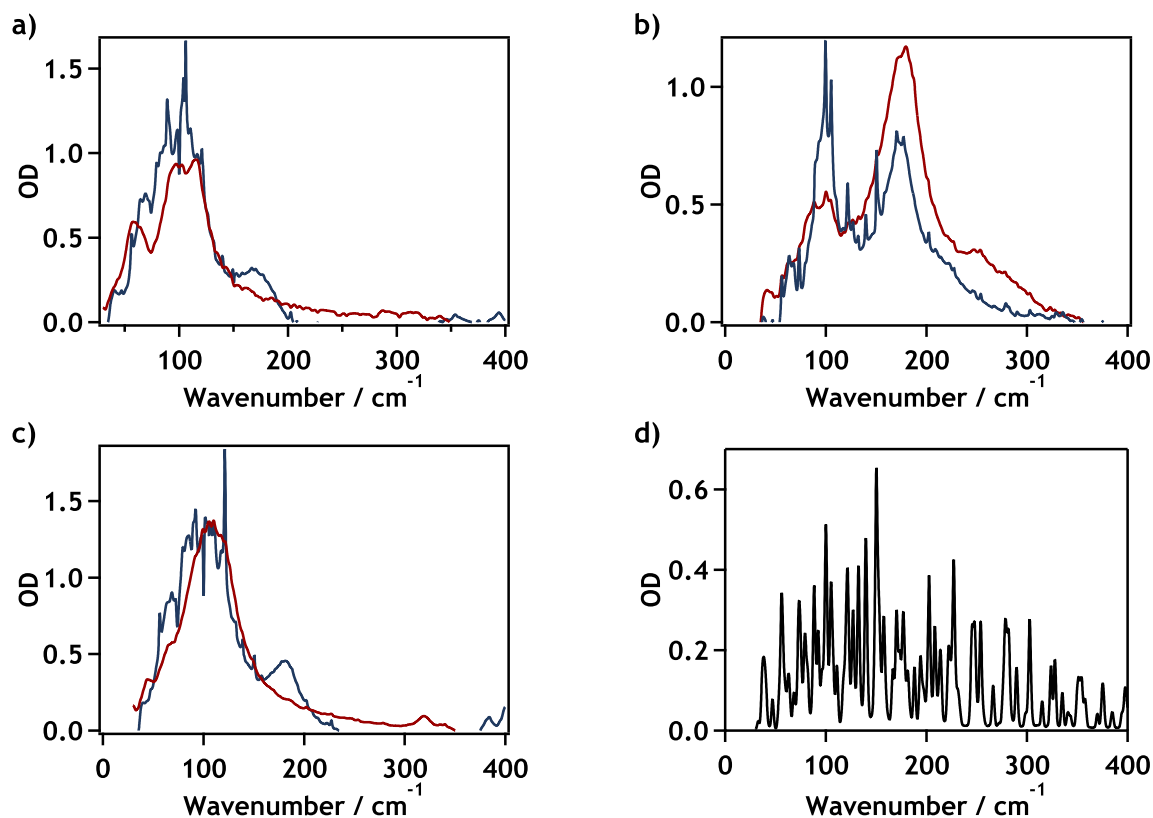


**Figure 4.11.:** Terahertz spectra of the crystalline ethylammonium chlorides compared to their butylammonium chloride counterparts. a) A comparison of the far-IR spectra of crystalline tetraethylammonium chloride (blue) and tetrabutylammonium chloride (red) (5:1 and 2:1 by volume mixture of polyethylene with the tetraalkylammonium chloride, respectively) at room temperature. b) A comparison of the far-IR spectra of crystalline triethylammonium chloride and tributylammonium chloride (8:1 and 1:1 by volume mixture of polyethylene with the trialkylammonium chloride, respectively) at room temperature. c) A comparison of the far-IR spectra of crystalline triethylmethylammonium chloride and tributylmethylammonium chloride (4:1 and 2:1 by volume mixture of polyethylene with the trialkylmethylammonium chloride, respectively) at room temperature. Coloring for b) and c) as for a). d) Atmospheric far-IR spectrum, mainly showing water vapour. Spectrum courtesy of Andrew J. Farrell (University of Glasgow).

#### 4.3.4. Ethylammonium chlorides

Due to their high melting points, only far-IR pellet spectra were taken of the ethylammonium chlorides. These spectra were unusually noisy because of problems with the dryness of the air used for purging, as can be seen by comparing Fig. 4.11d, which is a spectrum of the atmospheric absorbance, with Fig. 4.11a-c, the pellet spectra. Additionally, increasing the purging time did not lead to a decrease in the spikes. By qualitatively comparing the pellet spectra of the ethylammonium chlorides with those of the butylammonium chlorides, as seen in Fig. 4.11a-c, it can be seen that a very similar frequency range is covered. Any difference due to the weight in the cation is therefore small and likely undetectable within the noise inherent in the pellet spectra. Because of this, the spectra were not retaken in better quality. A new low intensity band can be seen in the spectra of the aprotic ILs, tetraethylammonium and triethylmethylammonium chloride. Whether this band also appears in the spectrum of triethylammonium chloride, however, could not be determined due to overlap with the second main band.

The expected shift due to cation mass in acoustic phonons can be approximated as  $\frac{\omega_A}{\omega_B} = \sqrt{\frac{M_{cat,B}}{M_{cat,A}}}$  if the force constants are assumed to be similar. This gives values of 0.74 for  $\frac{\omega_{Et_3NHCl}}{\omega_{Bu_3NHCl}}$ , 0.76 for  $\frac{\omega_{Et_3NMeCl}}{\omega_{Bu_3NMeCl}}$  and 0.84 for  $\frac{\omega_{Et_4NCl}}{\omega_{Bu_4NCl}}$ . Assuming either a harmonic oscillator or an optical phonon in the zone middle the corresponding ratios would be 1.05 for the aprotic ILs and 1.06 for the protic IL. For an optical phonon at the zone boundary no shift is expected.

#### 4.3.5. Cation calculations

To further supplement the spectral assignment, permanent dipole vectors and molecular polarisability tensors were calculated for equivalents of the cations used in this study. Due to restrictions in computational resources, and to speed up calculation times, the butyl groups in the original cations were replaced with ethyl groups for the calculations. As such, the tetraethylammonium ( $Et_4N^+$ ), triethylmethylammonium ( $Et_3NMe^+$ ) and triethylammonium ( $Et_3NH^+$ ) cation were calculated in *Gaussian 09*.<sup>[134]</sup> For the calculation of the permanent dipole moments, the centre of nuclear charge was taken as the origin of coordinates and the dipole moment vector was expressed relative to it.

The isotropic polarisability,

$$\alpha_{iso} = \frac{1}{9} (\alpha_X + \alpha_Y + \alpha_Z)^2, \quad (4.1)$$

and anisotropic polarisability,

$$\alpha_{aniso} = \frac{1}{2} \left( (\alpha_X - \alpha_Y)^2 + (\alpha_X - \alpha_Z)^2 + (\alpha_Y - \alpha_Z)^2 \right), \quad (4.2)$$

were calculated from the eigenvalues  $\alpha_X$ ,  $\alpha_Y$ , and  $\alpha_Z$  of the diagonalised polarisability matrix<sup>[138]</sup> and can be found in Table 4.5. Several isomers were calculated for the cations to judge the influence of the starting structure on the calculation results and mimic the different configurations the cations are likely to take in the liquid phase. Furthermore, the anisotropic and isotropic polarisability were compared using  $\frac{\alpha_{aniso}}{\alpha_{iso}}$  to judge the magnitude of the anisotropic polarisability, since the isotropic polarisability is a good approximation for the volume of a molecule if no double bonds are present.

**Table 4.5.: Polarisability values calculated for the ethylammonium cations.** Given are the eigenvalues as well as the derived isotropic and anisotropic polarisabilities. For comparison, the relative value of the anisotropic to the isotropic polarisability is given as well as additional calculations on water.

	$\alpha_X / \text{\AA}^3$	$\alpha_Y / \text{\AA}^3$	$\alpha_Z / \text{\AA}^3$	$\alpha_{iso} / \text{\AA}^3$	$\alpha_{aniso} / \text{\AA}^3$	$\frac{\alpha_{aniso}}{\alpha_{iso}} / \%$
Et <sub>4</sub> N <sup>+</sup>	19.5	19.1	18.2	357.1	1.3	0.36
EtNMe <sup>+</sup>	17.4	16.6	15.7	275.2	2.1	0.76
Et <sub>3</sub> NH <sup>+</sup>	15.2	14.4	13.5	206.2	2.1	1.01
	14.6	14.6	13.9	205.2	0.5	0.24
water	1.4	1.2	1.2	1.6	0.03	2.06

The tetraethylammonium cation had a small number of conformations which all had a small dipole moment of approximately 0.7 D, which is less than the 1.9 D<sup>[139]</sup> of water. Interestingly enough, however, the far-IR intensities of water and liquid tetrabutylammonium halides are nonetheless comparable (see Section 4.3.1). The calculation on the tetraethylammonium cation furthermore yielded a small anisotropic polarisability of 1.3 Å<sup>3</sup>, about 0.4% of its isotropic polarisability of 357.1 Å<sup>3</sup> (Table 4.5). For comparison, benzene has an isotropic polarisability of 10.4 Å<sup>3</sup> and an anisotropic polarisability of 5.6 Å<sup>3</sup> - about half the value of its isotropic polarisability.<sup>[140]</sup> Water, meanwhile, was calculated to have an anisotropic polarisability of 0.03 Å<sup>3</sup>, about 2% of its isotropic polarisability. Therefore, the assumption that the tetraethylammonium cation has a dominantly isotropic polarisability is justified.

For the triethylmethylammonium cation, the calculated dipole moment is again

relatively small at approximately 1.0 D. The anisotropic polarisability of only 2.1 Å<sup>3</sup>, or 0.8% of the isotropic polarisability, is again small as in the case of the tetraethylammonium cation. The dipole moment of the triethylammonium cation strongly depended on the conformation and ranged 2.4 to 3.4 D, which is significantly larger than for the other two cations. Depending on the conformation, small anisotropic polarisabilities of only 0.5 to 2.1 Å<sup>3</sup> were found as before, which are between 0.25 and 1% of the isotropic polarisability. It is worth to note that the tetraethylammonium cation has the smallest calculated dipole moment out of the three cations, yet has a far-IR absorption which is an order of magnitude larger.

#### 4.3.6. Discussion

The far-IR and OKE spectra of the studied ILs could consistently be fitted with several inhomogeneously broadened modes 30 and 150 cm<sup>-1</sup> (0.9 to 4.5 THz), a range and shape which usually corresponds to librational modes. However, as explained in Section 4.1, the halide anions and the tetrabutylammonium cation were specifically chosen to switch off the librational contributions to the spectra. This can be done by choosing ions with no (or negligible) permanent dipole moment and anisotropic polarisability. As the anions in question, chloride and bromide, are spherical, this is a given. For the tetrabutylammonium cation, the tetrahedral symmetry should lead to negligible values in either quantity, even if distortions due to changing environments in the liquid state are taken into account. This was further supported by DFT calculations (see Section 4.3.5), which showed a small dipole moment and anisotropic polarisability compared to the volume of the ion. In contrast to the expectations, the measured spectra of the tetrabutylammonium halides showed strong intensities in both the far-IR and OKE measurements. In fact, the far-IR intensity is comparable to that of water<sup>[137]</sup> in the terahertz region, which is known to be strong to the point that far-IR spectrometers have to be purged to remove the spectral contributions of water vapour in air. Water is also a useful comparison for a weak OKE spectrum, as its nearly spherical polarisability means the spectrum is mainly interaction-induced.<sup>[111,141,142]</sup> The OKE intensity of the tetrabutylammonium halide spectra, however, is roughly five times that of water and only a factor of two smaller than those observed for pyridinium ILs in which librations are visible. In summary, the tetrabutylammonium halide spectra show a surprisingly strong intensity in both the far-IR and OKE spectra.

Comparison with the other butylammonium ILs shows similar OKE intensities,

while the far-IR intensity of the less symmetric tributylmethylammonium and tributylammonium ILs is roughly an order of magnitude smaller. Given that the calculations of the ethyl analogues (see Section 4.3.5) gave similar anisotropic polarisabilities, this is no more surprising than the strength of the tetrabutylammonium halide spectrum. The far-IR intensity, on the other hand, behaves oppositely to what would be expected from the calculations. There, the tetraethylammonium cation had the smallest dipole moment, especially when compared to the triethylammonium cation. Yet its far-IR intensity is an order of magnitude larger than that found in the ILs of the less symmetric cations. All together, this indicates that the far-IR and OKE intensity is determined less by the molecular properties of the cations than by other factors.

From the beginning, this study was meant to probe the influence of structure on the IL spectra and therefore the different structure factors laid out in Sections 1.1.2 and 4.1 will be considered in the following to explain the intensities of the OKE and far-IR spectra. First off, the intensities can clearly not be explained by hydrogen bonding. The overall intensity of the protic ILs is in good agreement with that of the aprotic and asymmetric ILs. Furthermore, polar-apolar ordering has been studied in alkylammonium ILs with the help of MD simulations and was found to be only a weak influence.<sup>[83]</sup> Therefore, the discussion will focus on the influences of ion pairs (or clusters) and charge ordering. Here, the formation of ion pairs would lead to quasi-molecular aggregates with likely a larger anisotropy and dipole moment than the isolated ions. Charge ordering, on the other hand, imposes a quasi-lattice structure which could support delocalised vibrations of the whole lattice, or in short phonons (see Section 1.1.1).

As both phonon modes and ion pair librations could be responsible for the observed terahertz modes, the question of how they can be differentiated poses itself. The most obvious difference lies in the presence or absence of rotational relaxation modes, as they would be expected for ion pairs but would not be found for phonons. However, whether the rotational relaxation of ion pairs are observed depends on their lifetime. Rotational relaxations usually have timescales between a few picoseconds and several nanoseconds (or even longer). Librations, meanwhile, have typical timescales from hundreds of femtoseconds to picoseconds. Therefore, an ion pair may live long enough that librations can be observed, but not long enough for the observation of its rotational relaxation. A different approach is the measurement of the solid state spectra. The studied ILs are expected to be crystalline in the solid and for the tetrabutylammonium halides this was confirmed through X-ray diffraction (Fig. 4.7). Therefore, if the liquid spectrum is caused by phonons in a quasi-lattice, a similar, if better defined, spectrum is expected in the crystalline state. It was found that

the far-IR spectra of the liquid ILs showed good agreement save for those of tetrabutylammonium bromide. In tetrabutylammonium bromide (inset Fig. 4.6d), the profile of the crystalline IR spectrum in tetrabutylammonium bromide deviates from that found in the liquid. The bands appear sharper and higher frequency components, which are intense in the liquid, are missing in the crystalline spectrum. Assuming a similar spectrum in the crystal and liquid, however, hinges on the liquid retaining a disturbed version of the crystal structure. The X-ray powder scattering, Fig. 4.7, shows that both tetrabutylammonium chloride and bromide are crystalline, but with clearly distinct crystal structures. Heat capacity studies on tetraalkylammonium bromides have furthermore found that only tetrabutylammonium bromide shows anomalous thermal transitions consistent with the existence of several mesophases.<sup>[17,18]</sup> No anomalous thermal transitions have, to the best of the author's knowledge, been reported for the tetrabutylammonium chloride. A study of several ethylammonium-based ILs<sup>[143]</sup> has shown that the appearance of anomalous thermal transitions depends on both the anion and the cation, even if the anions have similar structures. Therefore, the discrepancy between the crystalline and liquid IR spectrum of tetrabutylammonium bromide can be explained by different structures in the crystal and liquid causing changes in the phonon mode frequencies. In summary, it can be concluded that the experimental evidence favours phonon modes over ion pairs as the explanation for the measured spectra.

Further evidence can be found in the OKE spectrum of tributylammonium chloride. Comparing the spectrum of a sample prepared under a dry atmosphere with that of one exposed to air during the preparation, as shown in Fig. 4.9, exposes a drastic change. The spectrum of the air-exposed sample is roughly an order of magnitude less intense and devoid of its defining features. It is important to note that tributylammonium chloride is very hygroscopic and exposure to air will therefore result in the contamination of the sample with water. This is enlightening because ion pairs as a concept originate from aqueous solutions. In fact, the shielding provided by water molecules should stabilise ion pairs. Therefore, their librational modes are, at most, expected to show a slight frequency shift due to a differing environment, which is not in line with the observed change. Phonon modes, on the other hand, are dependent on an extended lattice which can be disturbed by the water contamination. Considering the extreme intensity and feature loss, the observed spectral change with water contamination strongly supports phonon modes over ion pairs.

Two different branches of phonon modes can be found in ionic lattices, acoustic and optical phonons, which are described in more detail in Section 1.1.1. In short, the oppositely charged ions in acoustic phonons move in the same dir-

action, while they move in opposite direction in optical phonons. Here, it is more likely that optical phonons are observed because of two reasons. First, we use light to measure the spectra, and optical phonons are named as such because they can be excited by light. Secondly, light imparts approximately no momentum on the ions and momentum conservation therefore dictates that we are looking at phonons at the zone centre ( $k = 0$ ) of the Brillouin zone. A look at the phonon dispersion curve (see Fig. 1.12 for a diatomic chain) shows that the acoustic phonon branch is at zero frequency for the zone centre, leaving only the optical phonon branch for observation. Optical phonons can be simplified as the lighter ion oscillating in an approximately static lattice of the heavier ions, given a large enough mass difference. Here, the lighter ion is the anion and therefore the dependence of the spectra on the anion mass was studied. For this, the assumption was made that the interaction strength is similar for both chloride and bromide, meaning that all frequency changes are due to the change in the anion mass. For the zone centre, this frequency change can be calculated according to<sup>[144]</sup>

$$\frac{\omega_1}{\omega_2} = \sqrt{\frac{M_{anion,1}^{-1} + M_{cation,1}^{-1}}{M_{anion,2}^{-1} + M_{cation,2}^{-1}}}, \quad (4.3)$$

with  $M$  denoting the ion mass and 1 and 2 indicating the two different ILs. If the zone centre is seen as one limiting case in the phonon dispersion, the opposite limit would be given by the zone edge ( $k = \pi/a$ ). There, the dependence on the mass of the heavier ion disappears and the change only depends on the mass of the lighter ion, which here is the anion. The associated frequency change can then be calculated using<sup>[144]</sup>

$$\frac{\omega_1}{\omega_2} = \sqrt{\frac{M_{anion,2}}{M_{anion,1}}}. \quad (4.4)$$

The average ratio calculated from our fits is 0.64 for the PILs (tributylammonium chloride and bromide, 0.62 for the A and 0.69 for the C band) and 0.70 for the non-protic ILs (tetrabutylammonium chloride/bromide and tributylmethylammonium chloride/bromide). The expected shift is 0.67 at the zone edge and 0.72 to 0.73 at the zone centre. Thus, the experimental values are closer to those predicted for the zone edge. Recalling the discussion on the zone edge and centre given in Section 1.1.1, a phonon at the zone edge can be understood as being localised in real space, while one at the zone centre is completely delocalised over the whole real space lattice. However, this does not mean the observed phonons are at the zone edge in reciprocal space. Rather, the experimental values reflect the disorder of the liquid quasi-lattice, which limits the length over which the lattice is correlated. This loss of correlation restricts the possible wavelengths and makes the phonons appear to have a behaviour similar

to that at the zone edge. Therefore, the physical limit on the delocalisation of the phonon due to disorder in the lattice is reflected in frequency values which are shifted towards their zone edge values.

In optical phonons a change in the mass of the heavier ion, in this case the cation, only leads to negligible changes in the phonon frequency. This is different for the acoustic phonon branch, where the mass of the heavier ion is the deciding factor. Since the frequency of an acoustic phonon at the zone centre is zero, only the frequencies in the limit of the zone edge can be compared. There, a change of 0.74 to 0.84 according to<sup>[144]</sup>

$$\frac{\omega_1}{\omega_2} = \sqrt{\frac{M_{cation,2}}{M_{cation,1}}}. \quad (4.5)$$

is expected if the butyl groups in the cation are substituted for ethyl groups. Comparing the crystalline IR spectra of the respective alkylammonium chlorides, however, shows no change of the frequency within the noise. Again, this indicates that optical phonons are observed in the spectra.

Compared to the less symmetric alkylammonium halides, tributylmethylammonium and tributylammonium halides, the tetrabutylammonium halides show an absorption coefficient which is roughly an order of magnitude larger (compare Figs. 4.6, 4.8 and 4.10). The absorption coefficient, however, is frequency dependent and therefore does not lend itself very well to direct comparison. Due to this the amplitudes of the fitted modes (as found in Table 4.3) were compared. These are not frequency dependent, and scale with the square of the transition dipole moment. Out of all modes, A shows the highest amplitude in the spectra of all measured ILs. Comparing the tetrabutylammonium halides to the tributylammonium halides it is found that the amplitude is reduced by a factor of more than 9 in the chloride and by a factor of 18 in the bromide. For the tributylmethylammonium halides the corresponding factors are 11 for the chlorides and 24 for the bromides, respectively. Relating the transition dipole moment of these modes to the translation of the anion relative to the cation, this finding can be interpreted as the anion in the tetrabutylammonium halides being more mobile than in its counterparts with less symmetric cations. Since the tributylmethylammonium halides are not capable of forming hydrogen bonds connecting the cation and anion, the greater anion mobility in the tetrabutylammonium halides implies weaker coulomb interactions than in the other measured ILs. The simplest explanation for this is that the positive charge in the tributylmethylammonium and tributylammonium cations is more accessible. Looking at the cation, the positive charge is expected to be distributed over its surface. Because nitrogen is more electronegative than carbon, it will draw electron

density from the alkyl groups as described by the inductive effect. The partial charge such imparted on the carbon and hydrogen atoms should be larger the closer they are to the nitrogen atom. Therefore, it is expected that the tributylmethylammonium and tributylammonium cations have a site of higher net positive charge at the methyl and hydrogen group, respectively.

In the IR spectra of the protic ionic liquids, tributylammonium chloride and bromide, a larger separation of the A and C modes can be seen compared to the aprotic ionic liquids. For tributylammonium chloride the separation is  $114\text{ cm}^{-1}$ , compared with  $42\text{ cm}^{-1}$  and  $61\text{ cm}^{-1}$  for tetrabutylammonium and tributylmethylammonium chloride, respectively. Tributylammonium bromide shows an A-C separation of  $83\text{ cm}^{-1}$ , in contrast to  $52\text{ cm}^{-1}$  in both its aprotic counterparts. This clearly shows that the larger frequency separation between the A and C mode is due to the additional hydrogen bonding and not the asymmetry. In an ionic substance, as explained in Section 1.1.1, it is expected that the optical phonon is split into the TO and LO branch. Furthermore the TO mode is generally expected at a lower frequency than the LO mode (compare Eq. 1.6).<sup>[11,144]</sup> As such we assign A to the TO mode and C to the LO mode. This is similar to the behaviour of water, which shows  $\sim 2\text{ THz}$  TA and  $\sim 5\text{ THz}$  LA phonon modes at the zone edge. In water, these are also associated with the hydrogen bond bend and stretch modes, respectively. Furthermore, the assignment of the lower frequency mode to the hydrogen bond bend and the higher frequency mode to the hydrogen bond stretch is consistent with other assignments in the IL literature.<sup>[60,64,145]</sup> Due to this we assign the TO mode to the hydrogen bond bend and the LO mode to the hydrogen bond stretch. The increase in the A-C separation seen in the protic ILs is likely connected to the change in the force constants due to the hydrogen bond modes.

At  $42\text{ cm}^{-1}$ , the A-C separation in tetrabutylammonium chloride is surprisingly small. First off, the separation in the chlorides tends to be larger than that in the bromides, as seen for tributylmethylammonium and tributylammonium chloride. Additionally the A-C separation in tributylmethylammonium and tetrabutylammonium bromide is identical. This in itself is not evidence of a general trend. However, the fit in tetrabutylammonium chloride had the B mode at a higher frequency than the C mode, with both assigned according to their amplitudes and not frequencies. As such it is highly likely that the A-C separation in tetrabutylammonium chloride is underestimated. The discrepancy is likely caused by the difficulty of fitting the tetrabutylammonium halide far-IR data. As mentioned previously, the high absorption coefficient causes strong changes in the refractive index which strongly modifies the anti-symmetrised Gaussians. While flawed, the fit was sufficient for the analysis presented here. Improve-

ments to the fit could be made by using experimental instead of fitted refractive index data in the studied frequency region. Such data, however, were not available for this study. Lower frequency data in the far-IR might also yield useful information, however it is unlikely this will improve the fit significantly. Furthermore, it would be experimentally difficult to access lower frequency regions in the far-IR due to the high temperature needed for the measurement.

While the A and C band have been assigned to the TO and LO phonon mode, respectively, no specific assignment of B and D were made. Their main purpose was to be fudge functions, catching shape effects like broadening, which the anti-symmetrised Gaussians did not account for, as well as small, collision-induced effects. Of interest is that the B band consistently shows a larger OKE intensity in the bromides than in the chlorides. Currently, however, no viable explanation exists for this behaviour.

Far-IR spectra of similar ILs have been reported previously by Ludwig *et al.* [60,63,64,128,146] In their work, A was attributed mainly to librations of the ions overlapping with H-bond bending modes. Librational modes are expected around  $30 - 100 \text{ cm}^{-1}$  ( $1 - 3 \text{ THz}$ ) for particles with a dipole moment (in the IR) or an anisotropic polarisability (in OKE). While dipole moments are not properly defined in ions, charge distributions in the ions should lead to them showing librations in the IR spectra unless the symmetry in the ion is high. As such the assignment in the studies of Ludwig *et al.* is not surprising, considering the symmetry of the ions used. In this study, however, anion librations were ruled out by choosing chloride and bromide, as discussed above and in Section 4.1. Furthermore, the tetrabutylammonium cation is expected to be of high enough symmetry to not show librations. This is supported by dipole moment calculations on the ethyl equivalents of the studied cations (see Section 4.3.5). Here, dipole moments were defined relative to the centre of charge and it was found that the cations studied had small dipole moments relative to their volume. Nonetheless they show a strong absolute far-IR absorption, which is strongest in the cation with the smallest calculated dipole moment and surpasses the cations with stronger dipole moments by an order of magnitude. This clearly rules out librations as the cause of the A band in the far-IR. For comparison with the OKE spectra the molecular polarisability tensor for the ethyl equivalents of the cations was calculated as well and found to be nearly isotropic for all of them (see Section 4.3.5). This is at odds with the strong OKE spectrum observed. The IL intensity was found to be an order of magnitude larger than that of water, which also has a molecular polarisability tensor which is close to being isotropic. On the other hand, the intensity is only a factor of roughly 3 smaller than that of *N*-methylacetamide (NMA), which is strongly anisotropic.<sup>[111]</sup> Again this shows

that librations cannot be responsible for the majority of the low frequency signal. Therefore, it is reasonable to conclude that the major contribution to our spectra comes from translational motions of the anion, which can be described as optical phonons.

Furthermore, this interpretation of A is in agreement with DFT calculations presented by Ludwig *et al.* [63] In their work, far-IR spectra were calculated for an increasing number of trimethylammonium nitrate ions. The calculations shows an increasing relative intensity of both the A and C band equivalents with increasing ion number. Additionally, a small shift to lower frequencies was reported in the C band equivalent on increasing the number of trimethylammonium nitrate ions from two to four. For the A band equivalent, the number of low frequency components seemed to increase with increasing ion number. This was interpreted as evidence that the spectra were caused by clusters of ion pairs. In light of the interpretation presented in this study, however, it can also be seen as evidence of localised phonon modes, which only show in the calculations if a sufficient number of ions is considered. MD simulations by Mondal and Balasubramanian [145] reproduced the two band structure of protic ILs in the terahertz spectrum. They assigned the lower frequency mode to cage-rattling motions of the anion and the higher frequency mode to the intermolecular hydrogen bond stretch. However, no mention was made whether the rattling the anions showed any spatial correlation. If so, this would be theoretical evidence of optical phonons. In any case, the experimental evidence shows that the OKE intensity of the lower frequency mode A is too strong for simple cage rattling.

## 4.4. Conclusions

The aim of this study was to simplify the terahertz spectra of ILs and the studied ILs were selected for the structure of their ions. Specifically, high symmetry ions, such as the halide anions and the tetrabutylammonium cation, were used to suppress contributions from rotational motions. Surprisingly, it was found that the OKE spectra of the tetrabutylammonium halides showed a strong intensity and, in fact, were as intense as those of their less symmetric counterparts. In the far-IR spectra, the tetrabutylammonium halides were even an order of magnitude more intense than the less symmetric ILs, with an absorption coefficient comparable to that of water in the terahertz region. Furthermore, the combined analysis of both types of spectra resulted in a fit featuring two major modes for each IL, though the separation of these modes was significantly larger in the protic ILs. Other groups had assigned similar modes to librations or cage-rattling.

The cage-rattling explanation, quite simply, does not agree with the measured OKE intensity, as translational motions tend to be weak in the OKE spectrum. Furthermore, a combination of symmetry considerations and DFT calculations excluded the possibility of the modes originating from librations of the pure ions. Therefore, it was concluded that the structure of the ILs was responsible for the appearance of these two modes.

The good agreement between the solid and liquid spectra, as well as calculations of the frequency shift upon anion substitution, favoured an origin of the intensity from optical phonons rather than a reorientation of ion pairs. This was further supported by the loss of intensity and spectral features encountered in the OKE spectrum of tributylammonium chloride when water contaminations were introduced. Therefore, optical phonons were found in all measured ILs and the modes were assigned to the TO and LO phonon, respectively. Furthermore, it was concluded that the hydrogen bond of the protic ILs interacts with the phonon modes, resulting in a widening of the split between them.

A comparison with other types of ILs showed a similar absorption coefficients for alkylammonium<sup>[50,52]</sup> and imidazolium<sup>[124]</sup> ILs. The OKE spectra of alkylammonium ILs, on the other hand, were only a factor of 2 to 3 weaker than those of typical pyridinium and imidazolium ILs, which also feature contributions from librations of the ions. This then implies that TO and LO bands are likely to be significant in the terahertz far-IR and OKE spectra of all ILs, irrespective of whether they have significant hydrogen-bonding between ions or not. The masses of typical anions used in ILs (e.g.,  $\text{BF}_4^-$ , dicyanamide, methylsulfonate) are all rather similar to chloride and bromide and, therefore, one expects TO and LO bands at terahertz frequencies in the spectra of all ILs. While it will be more difficult to observe the TO and LO bands in ILs with less symmetric and strongly anisotropically polarizable cations such as pyridinium and imidazolium, the TO and LO contributions are still expected to be significant. This will require a reinterpretation of ILs spectra and will provide new insights into the structure and interactions of these liquids.

Further information could be gleaned by measuring a wider range of anions and cations to better quantify the observed effects. However, the biggest restriction here arises from experimental considerations, as more symmetric and smaller ions lead to higher melting points. Not only does this complicate the handling of the ILs, but also restricts measurements to high-temperature resistant devices only. Therefore, the measurement of similarly symmetric ILs with lighter ions would be very difficult. A different approach would be to improve the quality of the measurements on the current set of ILs. Most notably, this could be

achieved by measuring the far-IR spectrum to lower frequencies. This, however, would need to be done via THz-TDS or DRS measurements to avoid the frequency dependence of the absorption coefficient measured in FTIR (see Eq. 3.7). THz-TDS and DRS, on the other hand, measure changes in the refractive index, therefore avoiding the scaling with frequency. Additionally, the interpretation of the presented data could be greatly improved by measuring the refractive indices of the studied ILs in the frequency range of 0 - 400  $\text{cm}^{-1}$  (0 - 12 THz). A THz-TDS spectrometer currently in possession of the group would have allowed a measurement of up to 2.5 THz (83  $\text{cm}^{-1}$ ) only and currently has no capacities for heating the sample to the required temperature. For the refractive index to be useful in fitting, it would need to be measured between at least 40 and 160  $\text{cm}^{-1}$ . Therefore, an instrument with a higher maximum frequency and temperature-dependent measurement capacity would be needed.

Theoretical calculations are an important tool to support and enhance the assignment of terahertz modes. Due to the (partially) delocalised nature of phonons, however, calculations would need to be done for sufficiently large system sizes. Furthermore, hydrogen bonding would need to be explicitly taken into account for the calculation of the protic ILs, as the directionality of the hydrogen bond is very likely behind the observed increase in the split between the TO and LO phonon modes. As pointed out by Fumino *et al.*, it is not clear whether DFT methods or the force fields used in MD simulations can reproduce this sort of intermolecular behaviour accurately.<sup>[64]</sup> However, using quantum mechanical methods in the MD simulation to account for this, as done in *ab initio* molecular dynamics (AIMD) simulations, strongly increases the computational cost of the calculation. Therefore, they are restricted to small system sizes and short simulation runs. In viscous liquids, such as most ILs, this means the system may not reach equilibrium, making the results questionable. Reported AIMD simulation spectra<sup>[147]</sup> below 200  $\text{cm}^{-1}$ , for example, were broad and featureless. However, advances in computer capacities may soon make AIMD simulations an efficient tool.

# 5. Structure and supercooled behaviour of eutectic salt solutions

## 5.1. Introduction

Water is the most ubiquitous liquid on earth and plays an important role in so many chemical, geological and biological processes that it is practically regarded as the epitome of a solvent. However, it is also a highly unusual liquid. For starters, judging by the molecular structure and weight, water should be a gas between 0 °C and 100 °C, not the liquid it is. The deciding factor here lies in the intermolecular structure of water, which is stabilised by hydrogen bonds. Another example is the density maximum at 4 °C, which is caused by changes in the hydrogen bonds of the liquid. When liquid water crystallises into ice, the hydrogen bond structure becomes more ordered and tetrahedral, leading to bigger distances between water molecules. Therefore, the crystalline phase of water, ice, becomes lighter than the liquid phase and floats on top. It is this property which allowed life to evolve in bodies of water, as they do not freeze over at cold temperatures. However, not all anomalous properties of water can be explained solely using its hydrogen-bonded structure. Several thermodynamical properties, such as the heat capacity, thermal expansion coefficient, and the isothermal compressibility, are extrapolated to diverge<sup>[148-150]</sup> around 228 K. This is unusual, as these properties are expected to monotonously decrease. The direct experimental observation of this divergence, however, is difficult, as it lies in the “no man’s land” below 232 K, the onset of homogeneous ice crystallisation.<sup>[151]</sup> Therefore, even though water has been known for a long time, its study is still important today, which is highlighted by *Chemical Reviews* devoting an entire issue in 2016 for a state-of-the-art review on current water research.<sup>[152]</sup>

Different theories have been proposed to explain these anomalies of which the

four most prominent<sup>[153]</sup> are the “Speedy stability limit conjecture”,<sup>[154]</sup> the “second critical-point hypothesis”,<sup>[155]</sup> the “critical point free scenario”,<sup>[156]</sup> and the “singularity free scenario”.<sup>[157]</sup> A brief description<sup>[153]</sup> of these scenarios will be given in the following. The “stability limit conjecture” postulates that the liquid-vapour spinodal reverses its temperature dependence at negative pressures, specifically at the point at which it intersects with the line of maximum density. The reversed liquid-vapour spinodal then gives the instability limit for supercooling water. Meanwhile, the “second critical-point hypothesis” assumes two different liquid states for water in the supercooled temperature range. The transition line separating them ends in a liquid-liquid critical point (LLCP), a second critical point in water which causes the observed anomalies. While the transition line follows the first-order transition with its associated discontinuous change (see Section 1.1), a Widom line is also expected to emerge from the LLCP. The Widom line, in contrast to the transition line, follows maxima in the thermodynamic response functions (such as the heat capacity) caused by a continuous change in the thermodynamic state.<sup>[158]</sup> The “critical point free scenario” is closely related to the “second critical-point hypothesis” and also features a liquid-liquid transition. The main difference lies in the position of the LLCP, which in the “critical point free scenario” is far enough in the negative pressure range that it crosses the liquid-vapour spinodal and cannot be separated from it anymore. The liquid-liquid transition and second critical point are not present in the “singularity free scenario”, in which the response functions show sharp maxima but do not diverge. Out of these, the “second critical-point hypothesis” has had the biggest impact on water research and is widely supported by different experimental studies<sup>[159-167]</sup> and theoretical calculations,<sup>[155,168-170]</sup> though it is not fully proven. A brief overview of some experimental studies supporting the existence of a LLCP will be given below and more details can be found in recent reviews.<sup>[153,171,172]</sup>

Of particular importance is the extensive work of Mishima *et al.*, who discovered what appears to be a first-order transition between low-density amorphous ice (LDA) and high-density amorphous ice (HDA).<sup>[160,161]</sup> Examples of their further work are on high-pressure ices and the temperature changes connected with their melting behaviour when compressing or decompressing the ices.<sup>[164,173]</sup> Based on this work, they located the LLCP between 223 K and 230 K at high pressures of 0.02 - 0.07 GPa (roughly 200 - 700 bar). Neutron diffraction<sup>[174]</sup> has shown both HDA and LDA to have tetrahedral, fully hydrogen-bonded networks, though in HDA a fifth first neighbour molecule sits onto an interstitial position. Further neutron and X-ray scattering studies have shown HDA is formed from liquid water at high pressures, while LDA is formed at low pressures.<sup>[162,163]</sup> Additionally, high-density liquid water (HDL) and low-density liquid water (LDL)

have been observed with neutron diffraction and were found to show an LDL to HDL transition at increased pressure.<sup>[165,166]</sup> A recent X-ray scattering study on micrometer-sized liquid water droplets<sup>[175]</sup> at temperatures down to 227 K shows increased tetrahedral ordering of water in the no man's land, which is a potential factor for the fast homogeneous nucleation observed there. Small-angle X-ray scattering (SAXS) studies found nm-sized density inhomogeneities, attributable to HDL and LDL structures, at ambient temperatures, which increased in length on cooling both for pure water and dilute sodium chloride solutions.<sup>[150,176]</sup> This is supported by OKE data,<sup>[177]</sup> which shows evidence of HDL and LDL configurations at ambient temperatures and an increased dominance of LDL at supercooled temperatures.

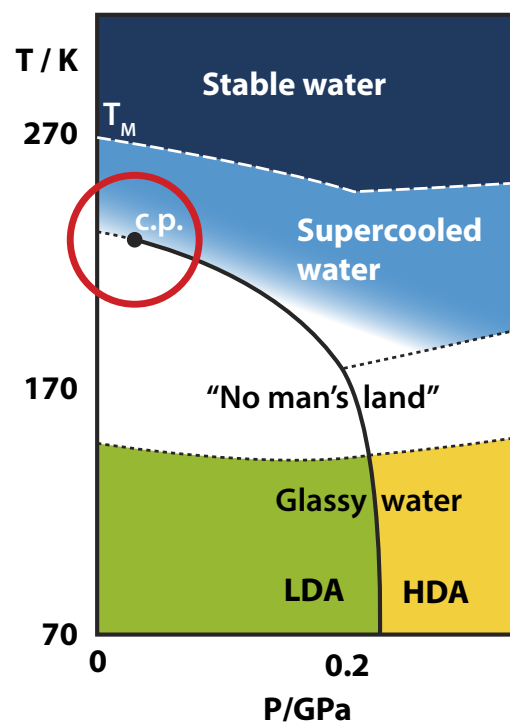


**Figure 5.1.:** Proposed phase diagram for non-crystalline water including the LLCP. The existence of the LLCP and its location have not yet been proven beyond doubt. Rapid crystallisation of ice  $I_h$  is expected in the white no man's land region, complicating experimental efforts to find the LLCP. Designed by Klaas Wynne (University of Glasgow) based on a phase diagram proposed by Mishima.<sup>[169,178-180]</sup>

Fig. 5.1 shows the postulated phase diagram for non-crystalline water in the case that an LLCP exists. In the white no man's land region, rapid homogeneous nucleation of ice  $I_h$  is expected, thwarting experimental efforts to prove the existence of the LLCP. The first-order transition between LDA and HDA has been proven experimentally<sup>[160,161]</sup> and the transition line was extrapolated towards the proposed LLCP. As detailed previously, evidence for two distinct water structures corresponding to the two amorphous ice forms, LDL and HDL, has been found experimentally.<sup>[150,162,163,165,166,176,177]</sup> Not shown in this diagram are the

third known amorphous ice form, very-high-density amorphous ice (VHDA), as well as the different crystalline ice forms, ice  $I_h$ , ice  $I_c$ , and ice 0.

As ice crystallisation makes measurements of pure water below the homogeneous nucleation temperature extremely difficult, many studies resort to using negative pressures (stretched water), confined water, or salt solutions instead.<sup>[153]</sup> Of course, each of these approaches brings its own difficulties. The experimental preparation of stretched water, for one, is difficult and the sample is sensitive to small perturbations. Meanwhile, not many probes are able to extract bulk information from confined water, as a considerable fraction of water molecules is bound to surfaces. Similar concerns can be applied to concentrated salt solutions and it is known that the addition of many common solutes destroys the response function anomalies at higher concentrations. However, this does not automatically prevent observation of a liquid-liquid separation and concentrated salt solutions allow measurement far into the no man's land, as the added solute simulates the effect of increased pressure and lowers the liquidus temperature.

Lithium chloride (LiCl) aqueous solutions, among others, have been used as model systems to investigate the no man's land. Suzuki and Mishima<sup>[181]</sup> found two distinct glassy states in dilute LiCl aqueous solutions, which they linked to the HDA and LDA states of water. Further investigation showed the transition between the two glasses to be of first-order, with the high-density glass rich in solute and the low-density glass rich in water.<sup>[179,182]</sup> This was reproduced theoretically in MD simulations,<sup>[183]</sup> which found nanosegregated glasses with predicted domain sizes of 4 to 5 nm. Indications of this can also be found in temperature-dependent X-ray scattering studies<sup>[184,185]</sup> of concentrated lithium halide solutions, which developed low-temperature peaks indicative of long-range correlations with a length of 1 nm on the low- $q$  end of the measurement. Specifically for lithium chloride, it was found that the chloride hydration shell became more ordered at low temperatures, while that of the lithium cation became more disordered. While the structure of the aqueous lithium chloride solution at different temperatures was resolved, the study was limited by measuring only three temperatures below room temperature. Therefore, further X-ray scattering measurements with a better temperature resolution were taken in the present study to investigate the behaviour of the temperature change. OKE studies<sup>[186]</sup> have previously established that the TA and LA modes remain intact in eutectic aqueous lithium chloride solutions. This indicates the hydrogen-bond network to be largely undisturbed by the solute ions, even though the number of water molecules per solute ion is quite low. This notion receives further support by Omta *et al.*,<sup>[187]</sup> who used IR pump-probe spectroscopy to measure the orientational correlation time of water in aqueous solutions of  $Mg(ClO_4)_2$ ,  $NaClO_4$ ,

and  $\text{Na}_2\text{S}_2\text{O}_4$ , finding the hydrogen-bond structure largely undisturbed.

Work on aqueous solutions is, however, not restricted to LiCl. Recently, Murata and Tanaka<sup>[188]</sup> observed a liquid-liquid transition for mixtures of water and glycerol with phase-contrast microscopy, differential scanning calorimetry (DSC), Raman spectroscopy, dielectric spectroscopy and X-ray scattering. This was questioned by Suzuki and Mishima,<sup>[189]</sup> who located the LLCP in aqueous glycerol solutions towards lower temperatures by using isothermal volume measurements and Raman spectroscopy. On the other hand, Popov *et al.*<sup>[190]</sup> contested that the observed transition was a liquid-liquid transition and attributed it to ice crystallisation. They backed their assertion with DSC and dielectric spectroscopy measurements. Finally, Bruijn *et al.*<sup>[191]</sup> studied the water-glycerol system with conventional and two-dimensional IR spectroscopy, finding that the liquid-liquid transition proposed by Murata and Tanaka is immediately followed by rapid ice crystallisation. In summary, compelling evidence exists that a liquid-liquid transition exists in aqueous glycerol solutions. For aqueous salt solutions, even more compelling evidence has been reported by Zhao and Angell,<sup>[192]</sup> who used DSC to investigate mixtures of the ILs ethylammonium nitrate and triethylammonium methanesulfonate in water. They found a first-order liquid-liquid transition and at the right composition, these aqueous solutions were found to not suppress the response function anomalies even at high concentrations, unlike many other solutes. Zhao and Angell's interpretation was supported with further FTIR measurements,<sup>[193]</sup> in which the  $\nu_{OH}$  stretch mode developed a broad, low-frequency peak on cooling, which was not consistent with ice crystallisation. On reheating, the low-frequency peak disappeared again and ice crystallisation was observed at the expected temperature. This, however, was only observed at the right solute to solvent fraction, while the anomaly was suppressed again in a more concentrated solution.

On this basis, we set out to investigate the temperature-dependent behaviour of aqueous salt solutions using the  $\text{SCN}^-$  ion as a probe of the environment. Its  $\nu_{CN}$  stretch is sensitive to electrostatic interaction<sup>[194]</sup> with surrounding molecules, making it environmentally sensitive, and it is known to have a strong intensity in IR measurements, making it easy to detect. Additionally, the anisotropy inherent in the rod-like structure of  $\text{SCN}^-$  gives it a large anisotropic polarisability, which leads to high intensities in OKE measurements. In aqueous lithium thiocyanate (LiSCN) solutions, its higher than average number of electrons will furthermore make it a good X-ray scatterer. For the lithium cation, on the other hand, the situation is basically reversed. Its spherical symmetry is expected to make it practically invisible in both the IR as well as OKE measurements (see the considerations presented in Section 4.1), while its low number of

electrons scatter X-rays only weakly. Eutectic concentrations of salt were chosen for the solutions as they have the lowest liquidus temperatures, which are 181 K and 193 K for LiSCN<sup>[195]</sup> and LiCl,<sup>[196]</sup> respectively. These are very similar, as well as a lot lower than the 232 K of pure water, and therefore similar behaviour was expected. In the IR measurements, a eutectic LiCl solution was doped with both LiSCN and D<sub>2</sub>O to allow for measurement of the  $\nu_{CN}$  and  $\nu_{OD}$  stretch modes without saturation. This was not a concern in the OKE and X-ray scattering measurements, which used eutectic LiSCN solutions. Further X-ray scattering measurements were taken for eutectic LiCl solutions, both to compare with the previously published data<sup>[184,185]</sup> and the IR measurements.

An unexpected strength of all measurement techniques lies in their ability to address the controversy around ice crystallisation seen for previous studies. Especially the  $\nu_{OD}$  stretch, measured in the FTIR spectra, is sensitive to the hydrogen-bonded structure and shows a clearly different shape and position if ice is present. X-ray scattering detects intermolecular distances and the structured environment in crystalline materials leads to intense diffraction peaks (or thin rings for polycrystalline samples) in the scattering images, which translate into sharp peaks in the scattering traces. For OKE, the situation is not as clear cut, but crystals are expected to increase scattering from the sample, which can be easily seen in the time domain traces. Therefore, all techniques are expected to give insight into the changes of environment (and associated dynamics) in salt solutions on cooling, including on whether ice crystallisation takes place.

## 5.2. Experimental details

### 5.2.1. Samples

Aqueous stock solutions of LiSCN and LiCl were prepared by dissolving lithium thiocyanate hydrate ( $\geq 98.0\%$ , Sigma-Aldrich) and LiCl ( $\geq 99.0\%$ , Sigma-Aldrich), respectively, in HPLC gradient grade water (Fisher). Their concentrations were determined by flame photometry. Aqueous eutectic LiSCN ( $38.3 \pm 0.7$  wt-%, **LiSCN:5.8H<sub>2</sub>O**) and LiCl ( $25.2 \pm 0.4$  wt-%, **LiCl:7H<sub>2</sub>O**) solutions as well as a less concentrated aqueous LiSCN ( $23.2$  wt-%, **LiSCN:12H<sub>2</sub>O**) solution were made by diluting the respective stock solutions further.

Additional samples were made for IR measurements in the Hunt group (University of Strathclyde). A stock solution of LiCl at the eutectic concentration ( $6.76$  M,

25.2 wt-%) was prepared by dissolving anhydrous LiCl ( $\geq 99.9\%$ , Sigma-Aldrich) in distilled water. This solution was then diluted to a 6.36 M LiCl solution (24.1 wt-%) and, to maintain an eutectic concentration, LiSCN was added until a LiSCN concentration of 0.4 M (2.3 wt-%) was reached (**LiCl-SCN:7H<sub>2</sub>O**). 9% D<sub>2</sub>O was included in the water used as a solvent. A non-eutectic 5.4 M solution (**LiCl-SCN:9H<sub>2</sub>O**, equivalent to 20.4 wt-% aqueous LiCl) was prepared by keeping the SCN concentration constant at 0.4 M (2.3 wt-%) and changing the LiCl concentration to 5 M (18.9 wt-%). To minimize water absorption of the LiCl and LiSCN salts, weighing and dissolution was done under a dry nitrogen atmosphere. The water content of the salts was determined by a Volhard titration and taken into account when calculating concentrations.

### 5.2.2. Measurements

For OKE measurements, the solutions were filtered with a 20  $\mu\text{m}$  hydrophilic poly(1,1,2,2-tetrafluoroethylene) (PTFE) filter (Millex), transferred to a 2 mm quartz cuvette (Starna) and degassed for at least 1 min in an ultrasound bath. 128 traces of **LiSCN:12H<sub>2</sub>O** were measured at 298 K in the high time resolution set-up (see Section 2.1.2) up to 1 ns delay time. The temperature was controlled using an aluminum sample holder with a precision of  $\pm 0.1$  K. **LiSCN:5.8H<sub>2</sub>O** was measured in a liquid nitrogen-cooled cryostat (Oxford Instruments) with a temperature precision of  $\pm 0.1$  K under a dry nitrogen atmosphere to avoid water condensation. Measurements were taken at 300 K, 275 K, 250 K, 220 K, 200 K, 180 K, 150 K and 90 K using the high time resolution set-up (see Section 2.1.2). Each measurement lasted between 0.5 to 1 hour and consisted of at least 33 traces with a maximum time delay of 1 ns. Since all were taken during the same day, their intensities are comparable. Further measurements were taken at 90 K, 150 K, 180 K, 200 K, 220 K, 250 K, 275 K and 300 K utilizing the long delay set-up (see Section 2.1.3) with a maximum time delay of 7 ns. For each measurement, the sample was held at the set temperature for 20 minutes before measuring at least 46 traces, which took between 1.5 and 2 hours.

WAXS measurements of **LiSCN:5.8H<sub>2</sub>O** and **LiCl:7H<sub>2</sub>O** were taken with the microfocus set-up at the Diamond Light source I22 beamline in a temperature controlled stage (Linkam THMS600). Samples were held between 25  $\mu\text{m}$  Mica windows separated by a 1 mm spacer. The diffuse scattering background of the Mica windows was measured at 294 K as well as at 200 K using an empty sample container and found to be nearly temperature independent. Sample measurements were scripted to be temperature-dependent runs with an acquisition time of 5 s

and a wait time of 0.1 s for each scan. Over long periods of exposure, the high intensity of the X-ray beam caused burns on the Mica windows, which lead to intense reflections. To avoid damaging the detector, the sample was moved regularly to expose different spots within the measurable space. However, some scans in the runs were unusable due to automatic detector shut-down. For our measurements, a 14 ( $\pm 0.0016$ ) keV X-ray beam ( $\lambda = 0.89 \text{ \AA}$ ) was used and the Pilatus 2M detector (Dectris) was calibrated with a silver behenate standard. The sample detector distance of 0.37 m resulted in a scattering vector ( $q$ ) range of 0.1 to 4  $\text{\AA}^{-1}$  with an estimated resolution of 0.003  $\text{\AA}^{-1}$ .

FTIR absorption measurements were made and analysed by Andrew J. Farrell (then University of Strathclyde, now University of Glasgow) using a Bruker Vertex 70 FTIR spectrometer operating in the range of 800-4000  $\text{cm}^{-1}$  with a resolution of 1.0  $\text{cm}^{-1}$ . Three measurements of 20 scans each were averaged to produce the final spectra. The samples were loaded between two  $\text{CaF}_2$  windows separated by a PTFE spacer of 25  $\mu\text{m}$  thickness. For the room temperature measurements, this was housed in a standard transmission cell. For low-temperature measurements, the samples were kept in a cryostat (Oxford Instruments). Before inserting the sample, the cryostat sample space was evacuated to less than  $10^{-6}$  mbar and purged for 15 min with a 0.2 bar overpressure of dry nitrogen, with the purge being maintained throughout the experiment. Then the sample was set to the required temperature and, after stabilising, held at this temperature for 10 min before measurements were taken. The results of the eutectic solution were consistent regardless of whether the sample was cooled to a given temperature, or cooled to 90 K and then heated to a given temperature.

Furthermore, IR pump-probe spectra were taken and analysed by Paul D. Lane (then University of Strathclyde) using the spectrometer<sup>[197]</sup> of the Hunt group. There, mid-IR pulses of roughly 100 fs duration with a centre frequency of 2083  $\text{cm}^{-1}$  and a bandwidth of approximately 250  $\text{cm}^{-1}$  were produced at a repetition rate of 1 kHz by an optical parametric amplifier (OPA) pumped with a regeneratively-amplified Ti:sapphire laser system. The pump-probe measurements were performed by splitting the output of the OPA into pump (95% intensity) and probe beams. The pump beam was routed through an optical delay stage in order to control the pump-probe time delay before being overlapped with the probe in the sample. Pump-probe measurements were recorded with parallel and perpendicular polarization of the pump beam with respect to the probe beam. These results were used to calculate the magic angle response, which serves to suppress the effects of molecular rotation in the recovered data.

### 5.2.3. Fitting procedure

The raw WAXS data was processed in *DAWN*<sup>[198]</sup> using the recommended data processing pipeline for I22. In this, the data is transformed from pixels into  $q$ -values using the detector calibration and then azimuthally integrated to obtain a 1D scattering trace from the recorded 2D pattern. For this, masking was applied to areas of no intensity, such as the beamblock and the space between detector panels, as well as to high intensity reflections caused by degradation in the sample cell windows. Before the integration, the Poisson error was automatically determined by the program. Afterwards the data were normalised using the sample thickness and the beam intensity. The polarisation of the beam was assumed to be horizontal for this. Due to the nature of the set-up, corrections besides those for the background are minor and can be ignored. The scattering intensity is comparable between measurements, but is not given in absolute units due to lacking the necessary calibration data. The diffuse scattering background at 200 K was processed in the same way as the sample data and then subtracted. For the subtraction, the scaling between  $0.1 \text{ \AA}^{-1}$  and  $0.6 \text{ \AA}^{-1}$  of the background trace to the sample data was calculated until a region was found in which the subtraction after the scaling did not lead to a negative trace (compare Fig. 5.2). The scaling and subtraction were handled by an algorithm written in *Mathematica*.<sup>[102]</sup>

The background corrected data were further processed in *Igor Pro*.<sup>[199]</sup> A sum of two Gaussian lineshape functions and one Lorentzian lineshape function (compare Fig. 5.7) were fitted from  $0.5$  to  $3 \text{ \AA}^{-1}$  using the integrated Batch fitting algorithm, which consecutively fitted the data sets to the same function with the same starting parameters. The Gaussian lineshape function was defined as

$$G(q) = A_G e^{-\frac{(q-q_0)^2}{w_G^2}}, \quad (5.1)$$

in which  $A_G$  is the amplitude,  $q_0$  is the peak position and the width  $w_G$  is  $\sqrt{2}$  times the standard deviation of the peak. The formula for the Lorentzian lineshape function was

$$L(q) = \frac{A_L}{(q - q_0)^2 + B_L} \quad (5.2)$$

with  $A_L$  and  $q_0$  denoting the amplitude and the peak position, respectively, and  $B_L$  being a width parameter. For the fit, the position and width of the Lorentzian lineshape function were held constant at  $1.7707$  and  $0.2$ , respectively, to avoid complications caused by too many variables. The values of the constants and the starting parameters were obtained from a manual fit. An additional

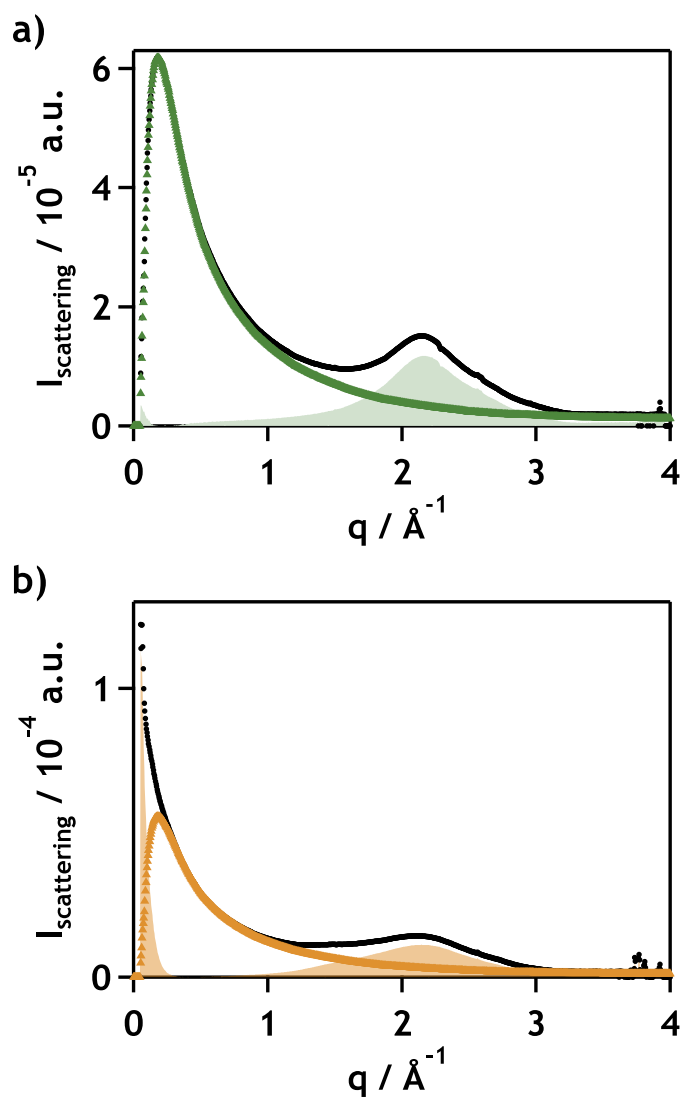


Figure 5.2.: X-ray background subtraction for aqueous eutectic LiSCN solutions at a) 119 K and b) 213 K. Shown are the raw data (black circles), the scaled background spectrum (green/magenta triangles) and the resulting background-subtracted spectrum (green/magenta transparent area fill). Compared to a), b) shows the effect of the iterative background scaling described below and illustrates the difficulties in background scaling encountered due to the low-frequency peak.

Gaussian lineshape function was added in the **LiSCN:5.8H<sub>2</sub>O** fit at  $0.068 \text{ \AA}^{-1}$  (see Fig. 5.14) to model a low-q peak developing during the run. Due to insufficient low-q data it was held at the fixed position of  $0.068 \text{ \AA}^{-1}$  and at a width of 0.02, with only the amplitude allowed to vary. Furthermore, the fit was made between 0 and  $3 \text{ \AA}^{-1}$  to allow for inclusion of the low-q peak.

Gaussian lineshape functions as defined in Eq. 5.1 were also used to fit the IR absorption and pump-probe spectra. The extracted amplitudes and centre frequencies were then used to further investigate the temperature dependence of the spectra.

The raw OKE data were processed in a *LabVIEW*<sup>[136]</sup> program and averaged over all traces. This average was deconvoluted from an  $\text{sech}^2$  autocorrelation function fitted to the instantaneous response at negative times, and then Fourier transformed. The resulting spectrum was used for further analysis as described below. Contributions of water to the OKE spectra were judged as negligible after comparing the recorded spectra to calculated water spectra (see Chapter D) scaled with the water fraction, as seen in Fig. 5.3 for the **LiSCN:12H<sub>2</sub>O** sample.

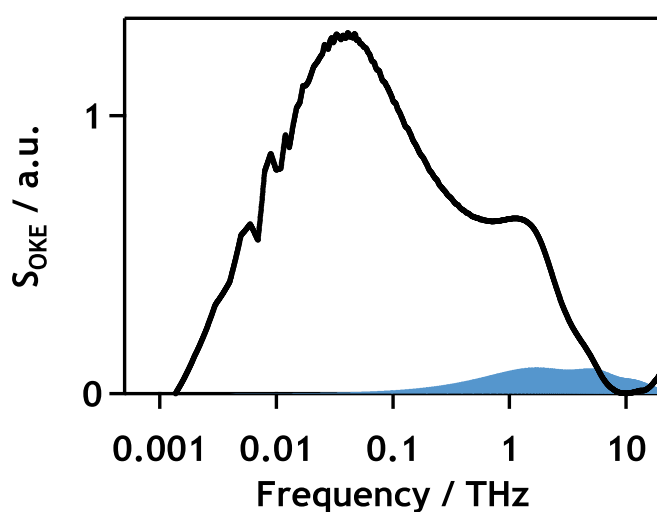


Figure 5.3.: Comparison of the OKE spectrum of **LiSCN:12H<sub>2</sub>O** (black dots) with the calculated spectrum of the water fraction (blue area fill).

A detailed description of the fitting algorithms and functions used can be found in Sections 3.2 and 3.3.2, respectively. The  $\alpha$ -relaxation was modelled with a Cole-Davidson function while anti-symmetrised Gaussian functions were used for the librational bands. In between these, contributions from cage rattling and cage diffusion modes can be found, which were collectively described by a Debye function. While usually a strongly stretched Cole-Cole function (which has a low  $\alpha$  value) is preferred for the  $\beta$ -relaxation, this led to unwanted higher and lower frequency components in the fit and therefore a Debye function was used.

For an illustration of a fit see Fig. 5.6. Due to the broad nature of the spectra, a good starting guess is paramount. Therefore, parameters were first varied in small batches to avoid codependence. Furthermore, the extreme ends of the temperature dependence were fitted first and used as a basis for the following spectra. For the final step, all parameters, as far as possible, were allowed to vary to achieve convergence. In the low temperature measurements, this was not always possible for the relaxational components due to insufficient data at low frequencies. In that case, parameters were held at sensible guesses. Similarly, the high-frequency end at 12 THz sometimes showed a band which was modelled with an anti-symmetrised Gaussian with the parameters held at the initial guesses. Parameters which were held constant at certain temperatures were not included in determining the temperature dependence.

Temperature-dependent fits of parameters for the OKE and X-ray data sets were done in *Igor Pro*.<sup>[199]</sup> For this, linear and sigmoidal functions were used. The linear dependence was defined by

$$y = y_0 + b_{lin} * x, \quad (5.3)$$

where  $y_0$  is the y-axis intercept and  $b_{lin}$  is the slope. For the sigmoidal fit the formula

$$y = y_{Base} + \frac{y_{Max}}{1 + \exp\left[\frac{x_{1/2}-x}{b_{sig}}\right]} \quad (5.4)$$

was used. Here  $y_{Base}$  is the y-value at small  $x$ ,  $y_{Base} + y_{Max}$  the y value at large  $x$ ,  $b_{sig}$  is the rise rate and  $x_{1/2}$  the halfway point, defined as the  $x$  value at  $(y_{Base} + y_{Max})/2$ .

## 5.3. Results and discussion

### 5.3.1. OKE spectra of aqueous LiSCN solutions

OKE spectra of aqueous LiSCN solutions were taken to probe for temperature-dependent changes. The proposed liquid-liquid critical point in water is expected around 228 K<sup>[148-150]</sup> and as such the investigation was geared towards this temperature. However, because solutes mirror the effect of pressure on water, lower temperatures were in the focus as well. As the rotational relaxation is expected to slow down significantly with lower temperatures, it was expected that not much information could be gained from it at the temperature of interest,

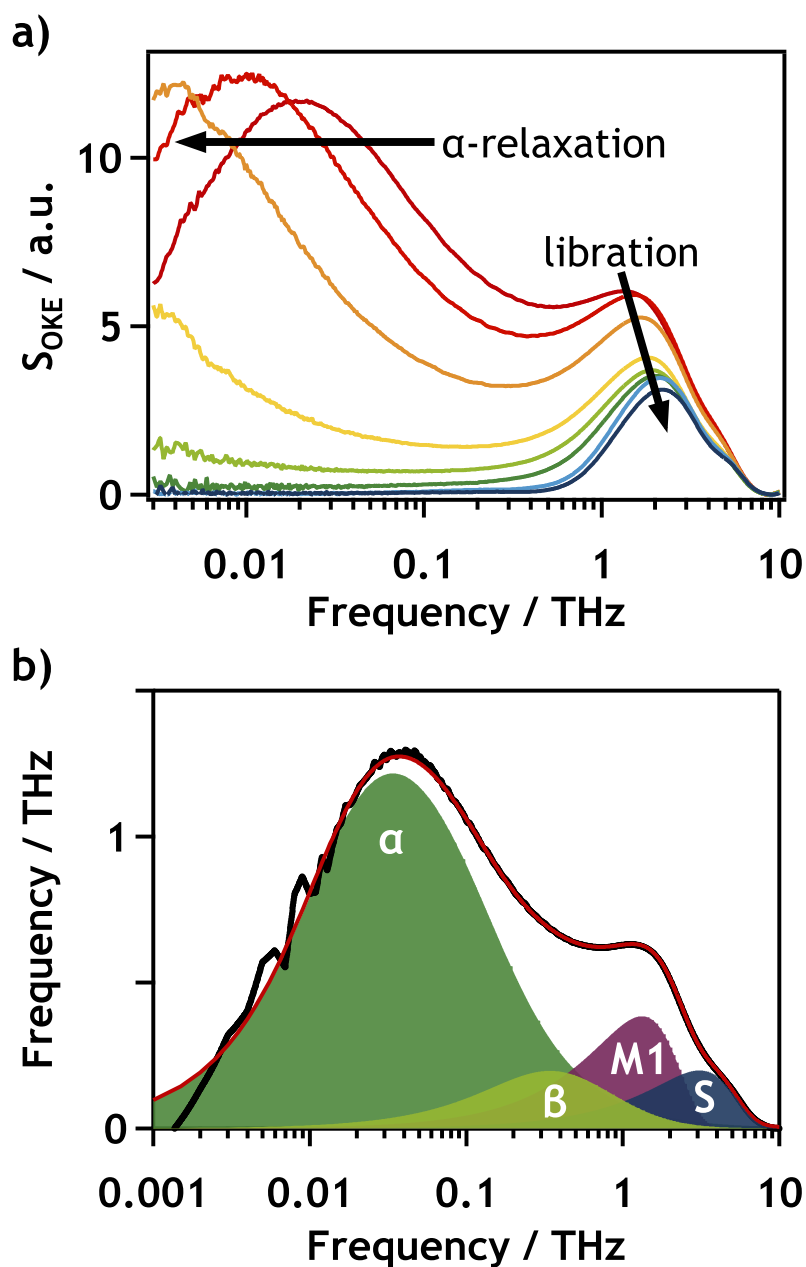


**Figure 5.4.:** OKE spectra of aqueous LiSCN solutions. a) Temperature-dependent OKE spectra for an aqueous eutectic LiSCN solution (LiSCN:5.8H<sub>2</sub>O). The temperatures, in the direction of the arrow, were 300, 275, 250, 220, 200, 180, 150, and 90 K (red to blue). It can be clearly seen that the rotational relaxation ( $\alpha$ -relaxation) moves to lower frequencies with decreasing temperatures, in line with longer relaxation times, indicating slower movements. The intensity of the librational bands decreases with the temperature and shifts to higher frequencies. b) OKE spectrum at 298 K for LiSCN:12H<sub>2</sub>O.

228 K, or below. Therefore, the changes in the librational modes were of greater interest for this study. From the measured temperature dependence of the eutectic  $\text{LiSCN:5.8H}_2\text{O}$  solution (Fig. 5.4a), well-defined changes with temperature can be seen. The rotational relaxation, labelled  $\alpha$ -relaxation, moves from 30 GHz at room temperature to lower frequencies when the sample is cooled. The librational modes around 2 THz, on the other hand, move to slightly higher frequencies. At first glance this might seem as if it is only caused by the retreat of the  $\alpha$ -relaxation, as well as the intermediate  $\beta$ -relaxation, to lower frequencies. Further analysis shown in Fig. 5.5a, however, reveals this shift persists even after the movement of the relaxational components is taken into account.

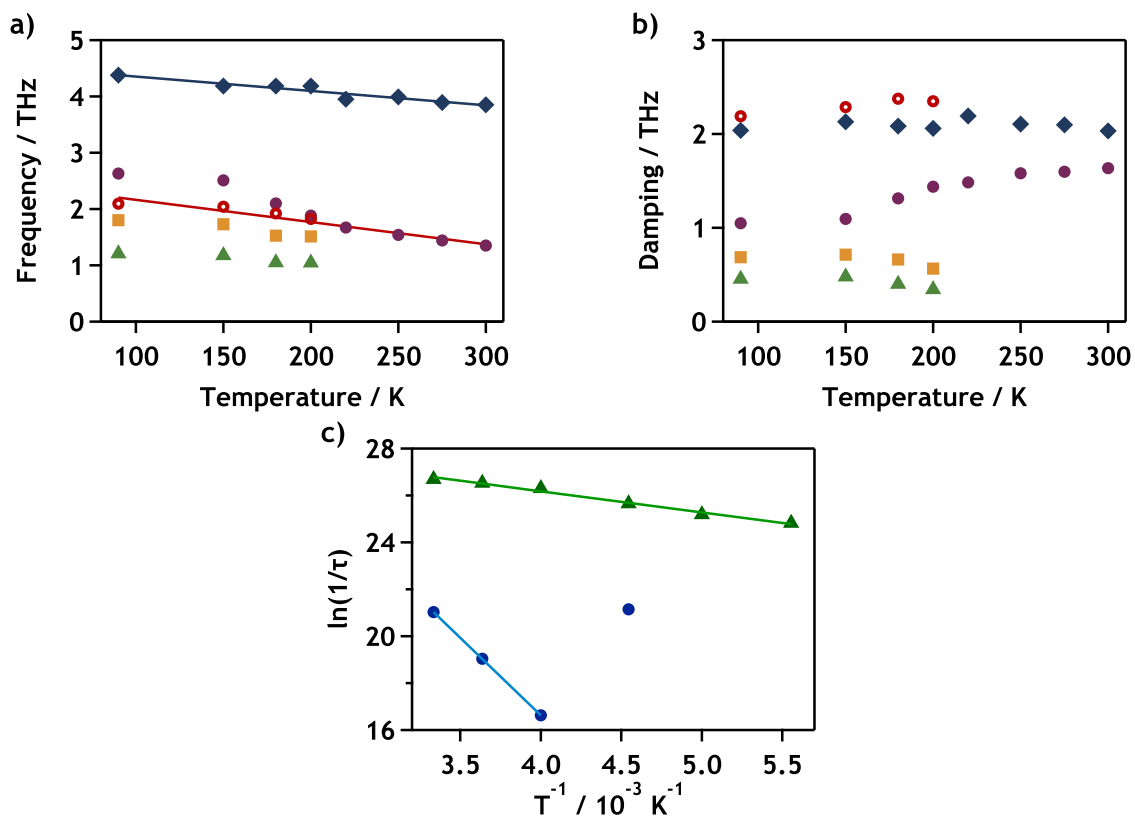


**Figure 5.5.: Temperature-dependence of the fit parameters for an aqueous eutectic  $\text{LiSCN}$  solution.** a) Plot of the centre frequencies for the librational modes (colouring as in Fig. 5.6). The solid lines give linear fits for S (dark blue) and the amplitude-weighted average of M1, M2 and M3 (red). The empty red symbols mark the position of said averages. b) Plot of the damping parameter for the librational modes. It can be seen that the damping of S does not show an appreciable temperature dependence. The damping of M1, M2 and M3 is similarly nearly temperature-independent for the summed values (empty, red circles). c) Arrhenius plot and fits of the temperature dependence for the relaxation times of the  $\alpha$ -relaxation (blue) and  $\beta$ -relaxation (green). It can be seen that the lowest  $\alpha$ -relaxation time at 220 K was underestimated in the fit due to the low-frequency cut-off of the data.

To help with analysing the contributions to the  $\text{LiSCN}$  OKE spectrum, measurements at room temperature were also taken for a more diluted solution,  $\text{LiSCN:12H}_2\text{O}$ , for which the spectrum is shown in Fig. 5.4b. The relaxational components of the spectra could easily be extracted by fitting them to a Cole-

Davidson function and Debye function for the  $\alpha$ -relaxation and  $\beta$ -relaxation, respectively. In the spectra of both concentrations, furthermore, the librational band could be modelled with two anti-symmetrised Gaussian functions, one for the main band (**M1**) and one for the high-frequency shoulder (**S**). Population fractions were extracted for the librational modes by assuming the population in a librational mode was equal to its amplitude and that the sum of the amplitudes of all librations was equal to the total population. Using this, it can be seen in Fig. 5.6b that the population fraction for the main band **M1** is reduced at lower concentrations, while that of the shoulder **S** is increased by a similar amount. The concentration dependence of the relative population indicates that the librational modes are associated with different solvation environments, and the implications of this are further discussed in Section 5.3.5.

In the temperature dependences found for the eutectic **LiSCN:5.8H<sub>2</sub>O** solution (Fig. 5.4a), the slow down of the relaxations shows Arrhenius behaviour (see Fig. 5.5c and d), save for the  $\alpha$ -relaxation time at 220 K which was underestimated. A linear fit results in activation energies of 54.9 kJ mol<sup>-1</sup> and 7.5 kJ mol<sup>-1</sup> for the  $\alpha$ -relaxation and  $\beta$ -relaxation, respectively. If the SED relation is assumed to be valid, and ion aggregation neglected, increased relaxation times indicate higher viscosities, as expected on cooling a liquid. However, the data used for fitting the relaxations are limited on the low-frequency side, resulting in a cut-off  $\alpha$ -relaxation peak at only 250 K. As the  $\alpha$ - and  $\beta$ -relaxation fits tend to be dependent on each other, errors in the relaxation times are hard to estimate. The librational modes, on the other hand, show interesting behaviour at lower temperatures. Above 200 K, they can be described with two anti-symmetrised Gaussian functions, **M1** and **S**, just like at lower concentrations in **LiSCN:12H<sub>2</sub>O**. Below 200 K, however, two additional anti-symmetrised Gaussian functions, **M2** and **M3**, are necessary to fit the librational band. The case of 200 K itself is curious. At first glance, its librational band can be fitted like the higher temperature spectra with only two anti-symmetrised Gaussian functions, which are shifted appropriately. The temperature dependence of the fit parameters, however, then revealed a strong shift in parameters contrary to the generally observed temperature dependence. Introducing the additional functions used in the lower temperature spectra, **M2** and **M3**, with small amplitudes (compare Fig. 5.6b) rectified this and led to the consistent temperature dependence shown in Fig. 5.5a and b. While **M1**, **M2**, and **M3** appear to show sigmoidal behaviour in their peak position, this can be traced back to the sigmoidal temperature dependence of their population fractions shown in Fig. 5.6b. Plotting an amplitude-weighted average of the peak position, as done in Fig. 5.5a, shows a linear temperature dependence as that seen for the shoulder **S**. The damping shown in Fig. 5.5b is approximately temperature-independent, even for the summed-up values of **M1**,

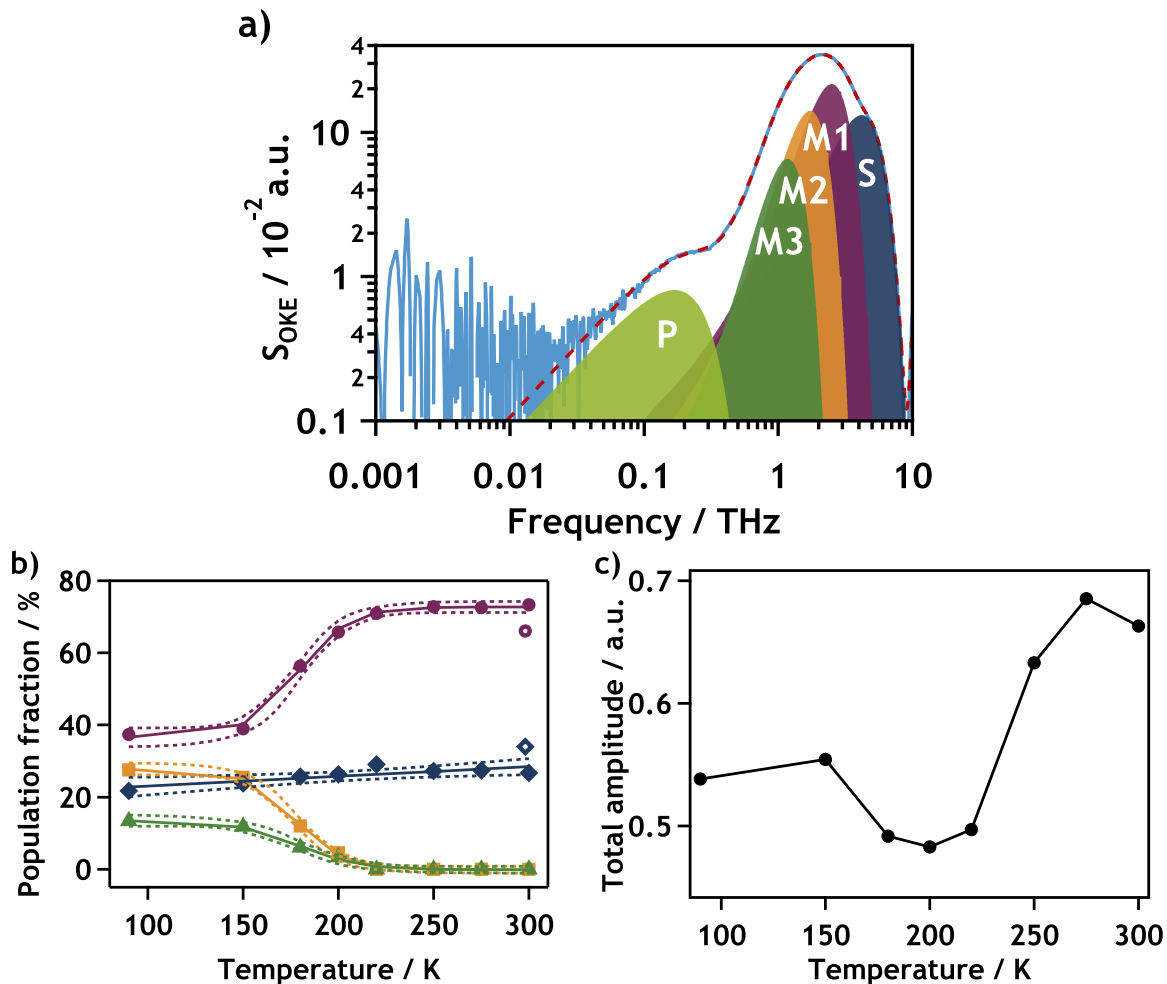


**Figure 5.6.:** OKE spectrum analysis for an aqueous eutectic LiSCN solution. a) Shown is the OKE spectrum of an aqueous eutectic LiSCN (LiSCN:5.8H<sub>2</sub>O) solution at 150 K with both axes on a logarithmic scale. The raw data is shown as a solid blue line while the fit is shown as a dashed red line. It can be seen that the noise increases with decreasing frequency. The four librational modes are given as area fills in dark blue (S), purple (M1), orange (M2) and dark green (M3). An additional low-temperature mode P is shown as a light green area fill. b) Temperature-dependent changes in the population fraction associated with each librational mode (coloured, filled symbols, assignment as in a)). Fits and 95% confidence intervals are shown as solid and dashed lines, respectively. For comparison, the population fractions of a less concentrated solution (LiSCN:12H<sub>2</sub>O) at 298 K are shown as empty symbols. c) Sum of the amplitude of the libration modes depending on temperature for the LiSCN:5.8H<sub>2</sub>O sample.

**M2**, and **M3**. While a jump is seen in the latter value, this can be explained by the overlap of the area occupied by the fit functions (Fig. 5.6a). It is notable that **S** consistently shows a linear temperature dependence, from the shift to higher frequency to the decrease in population fraction on cooling, while **M1**, **M2**, and **M3** show a sigmoidal temperature dependence in their population fractions, with a halfway point around 178 K (Table 5.1). The OKE data alone would make assignments speculative, and a discussion of the librational modes in light of the complementary information gained from IR measurements can be found in Section 5.3.5.

**Table 5.1.:** Sigmoidal fit parameters for the temperature dependence of the LiSCN:5.8H<sub>2</sub>O OKE population fractions.

Mode	$T_{1/2}$ / K	Population <sub>Base</sub> / %	Population <sub>Max</sub> / %	Rise rate
<b>M1</b>	179.0 ± 5	0.37 ± 0.03	0.36 ± 0.04	13.1 ± 5
<b>M2</b>	177.4 ± 4	0.28 ± 0.02	-0.28 ± 0.02	12.4 ± 4
<b>M3</b>	178.8 ± 8	0.14 ± 0.02	-0.14 ± 0.02	15.6 ± 7

At 150 K, an additional low-frequency mode **P** can be seen in the OKE spectrum at 144 GHz (Fig. 5.6a), which has a low intensity and is slightly overdamped (see Table B.4). It, however, remains in this position even at 90 K, indicating a non-diffusive mode. On the other hand, it can't be seen in the 180 K spectrum and, unlike with **M2** and **M3** at 200 K, no shift in the parameters points towards its existence. While a weak amplitude and overlap with the  $\beta$ -relaxation, which already starts at 180 K, complicates figuring out at which temperature **P** starts to appear in the spectrum, it is likely below 180 K. Typically, modes in the hundred gigahertz range are relaxational processes, which would show diffusive behaviour. Furthermore, the progression of temperature-dependent spectra indicates that at 150 K, the  $\beta$ -relaxation modes have frozen out together with the  $\alpha$ -relaxation. Librational modes, on the other hand, tend to lie at higher frequencies and usually are not overdamped. Another possibility in this frequency region are phonon modes, such as those seen in Chapter 4, which do, however, require a structured environment (see Section 1.1.1). This can be probed for by using X-ray scattering and measurements taken with synchrotron radiation are described below.

### 5.3.2. X-ray scattering of aqueous LiCl solutions

Scattering traces for the eutectic LiCl:7H<sub>2</sub>O solution between 0.1 and 4 Å<sup>-1</sup> contain information about structure ranging from 0.15 nm to 6.3 nm. While the-

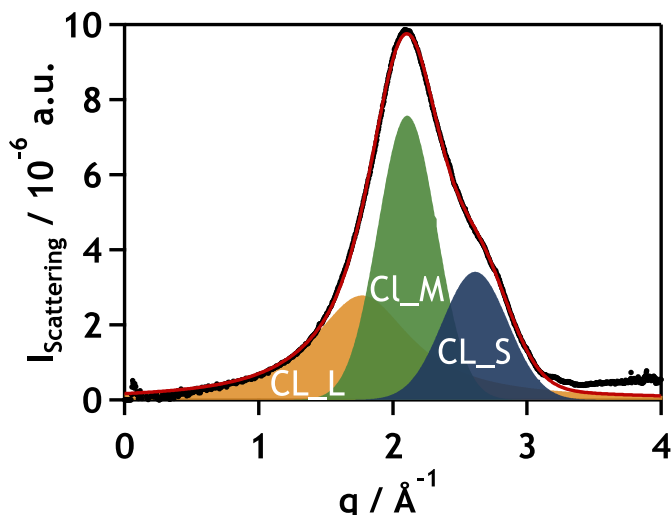


**Figure 5.7.:** Fit for the X-ray scattering of the eutectic  $\text{LiCl:7H}_2\text{O}$  solution at 124 K. Shown are the low- $q$  Lorentzian tail ( $\text{CL}_L$ , orange), the main peak ( $\text{CL}_M$ , green), and the shoulder ( $\text{CL}_S$ , blue). Data points are given as black dots while the red line shows the fit.

oretically the 5 nm domains expected from MD simulations<sup>[183]</sup> should be resolved, increased noise below  $0.5 \text{ \AA}^{-1}$  (above 1.3 nm) and the proximity to both the beamblock and the unscattered beam at the given resolution leads to uncertainty. The major scattering features, as seen in the fit at 124 K in Fig. 5.7, are found between 1 and  $3 \text{ \AA}^{-1}$ , consisting of a main peak ( $\text{CL}_M$ ) at 2.0 to  $2.2 \text{ \AA}^{-1}$  (0.29 - 0.31 nm) and a shoulder ( $\text{CL}_S$ ) at roughly  $2.6 \text{ \AA}^{-1}$  (0.24 nm). A clear temperature dependence of the shape is visible, as seen in Fig. 5.8a and b. At lower temperatures,  $\text{CL}_M$  sharpens and is located towards lower  $q$  values while  $\text{CL}_S$  is broader. In Fig. 5.8a, the scattering intensity also seems lower at higher temperatures. This, however, is not reproduced in Fig. 5.8b where the intensity shows jumps, which is possibly related to the difficulties encountered during recording of the data as described in Section 5.2.2.

The scattering traces at all temperatures could be fitted using two Gaussian lineshape functions for  $\text{CL}_M$  and  $\text{CL}_S$ , with an additional Lorentzian lineshape function ( $\text{CL}_L$ ) centred at  $1.8 \text{ \AA}^{-1}$  (0.35 nm) to compensate for the tail (see Fig. 5.7). A very weak peak at around  $0.1 \text{ \AA}^{-1}$  was not accounted for in the fit. The resulting temperature-dependent parameters are shown in Figs. 5.10 and 5.11. Comparing the amplitudes in Fig. 5.10 it can be seen that the amplitude of  $\text{CL}_S$  increases at lower temperatures, while the amplitude of  $\text{CL}_L$  decreases. The amplitude of  $\text{CL}_M$  is noisier than the amplitude of the other functions. While there seems to be a trend towards higher amplitudes at lower temperatures, this change is within the noise. During heating, all amplitudes show a dip around 200 K not seen in the data when the sample was cooled down. Comparing Fig. 5.10 with Fig. 5.9, this coincides with a large chunk of missing tem-

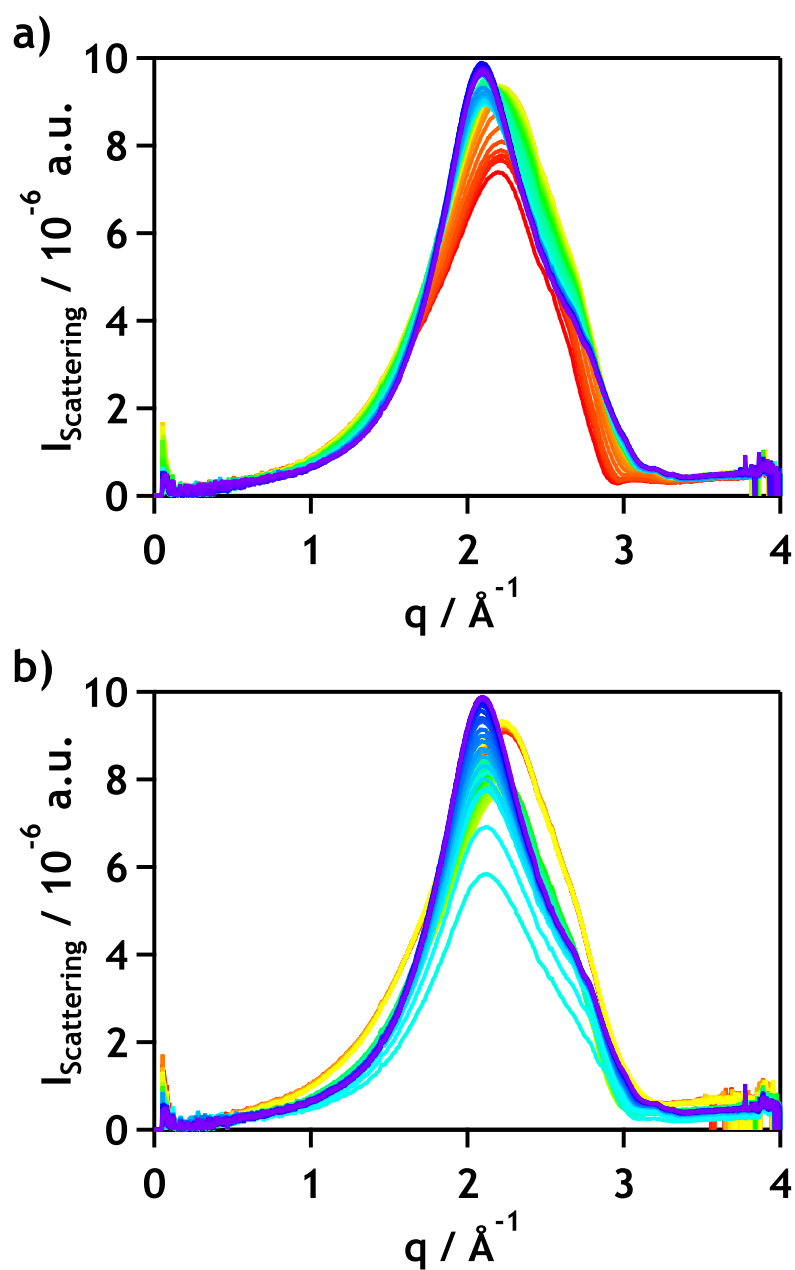
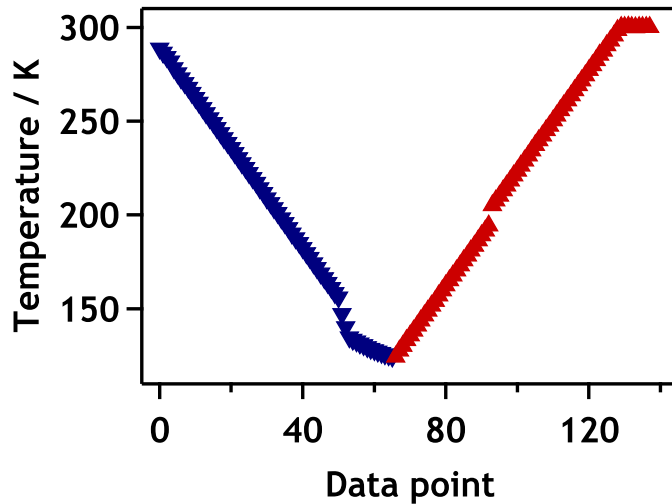
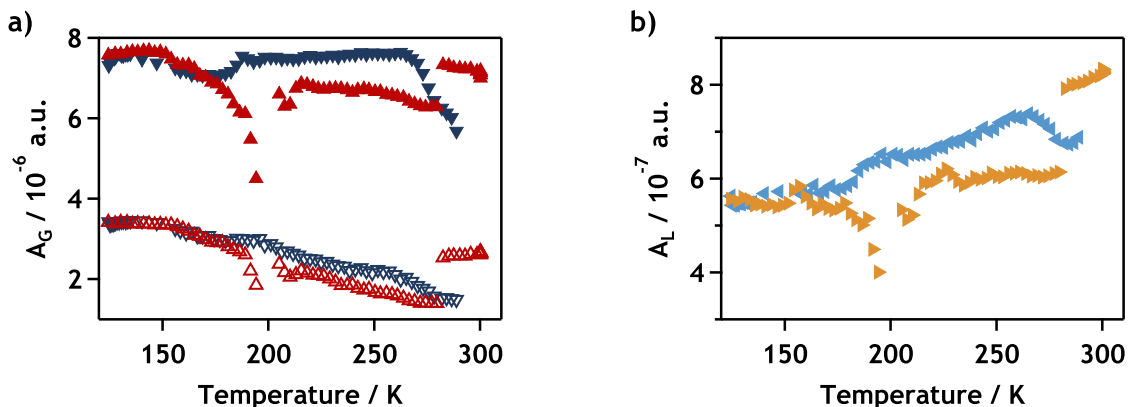


Figure 5.8.: Temperature-dependent X-ray scattering of the eutectic LiCl:7H<sub>2</sub>O solution. a) Shows the scattering traces when cooling from 289 K to 125 K (red to blue) at 20 K min<sup>-1</sup>. b) Shows the scattering traces when heating from 124 K to 300 K (blue to red) at 20 K min<sup>-1</sup>.



**Figure 5.9.:** Temperature of the scans taken for the eutectic  $\text{LiCl:7H}_2\text{O}$  solution. Depicts the analysed scattering traces versus the temperature they were taken at. Breaks from a linear dependence show temperatures at which no scattering traces of sufficient quality could be taken (see Section 5.2.2). Blue symbols denote cooling of the sample, while red ones denote heating.

peratures in the data. Therefore, this is likely an artefact caused by the experimental difficulties described in Section 5.2.2.



**Figure 5.10.:** Temperature dependence of the X-ray scattering amplitudes for  $\text{LiCl:7H}_2\text{O}$ . a) Temperature dependence of  $\text{CI}_M$  and  $\text{CI}_S$ . Blue, downward-facing triangles denote the sample being cooled down, while upwards-facing red triangles indicate the sample being heated up. Filled symbols belong to  $\text{CI}_M$ , while empty symbols belong to  $\text{CI}_S$ . Both amplitudes show a slight increase at lower temperatures, however, the one seen in  $\text{CI}_M$  is within the noise. b) Temperature dependence of  $\text{CI}_L$ . The amplitude shows a decrease towards lower temperatures. Light blue symbols denote cooling of the sample, while orange symbols denote heating.

This artefact can also be found in the temperature dependence of the width, and centre position of the two Gaussian lineshape functions,  $\text{CI}_M$  and  $\text{CI}_S$ , plotted in Fig. 5.11. Additionally, some divergent behaviour can be seen between 280 and 300 K. In the cooling run this manifests as a decrease in the parameter value from 280 K to 300 K for the amplitude, width and centre position of all functions. In the heating run, it is seen as a sudden jump in parameter values, breaking the

otherwise observed trend. It manifests as a decrease in the width and position of  $Cl_M$  and as an increase in all other parameters. This divergence cannot be explained by the quality or lack of data. However, as it starts near the density maximum of water, it possibly is related to the density anomaly.

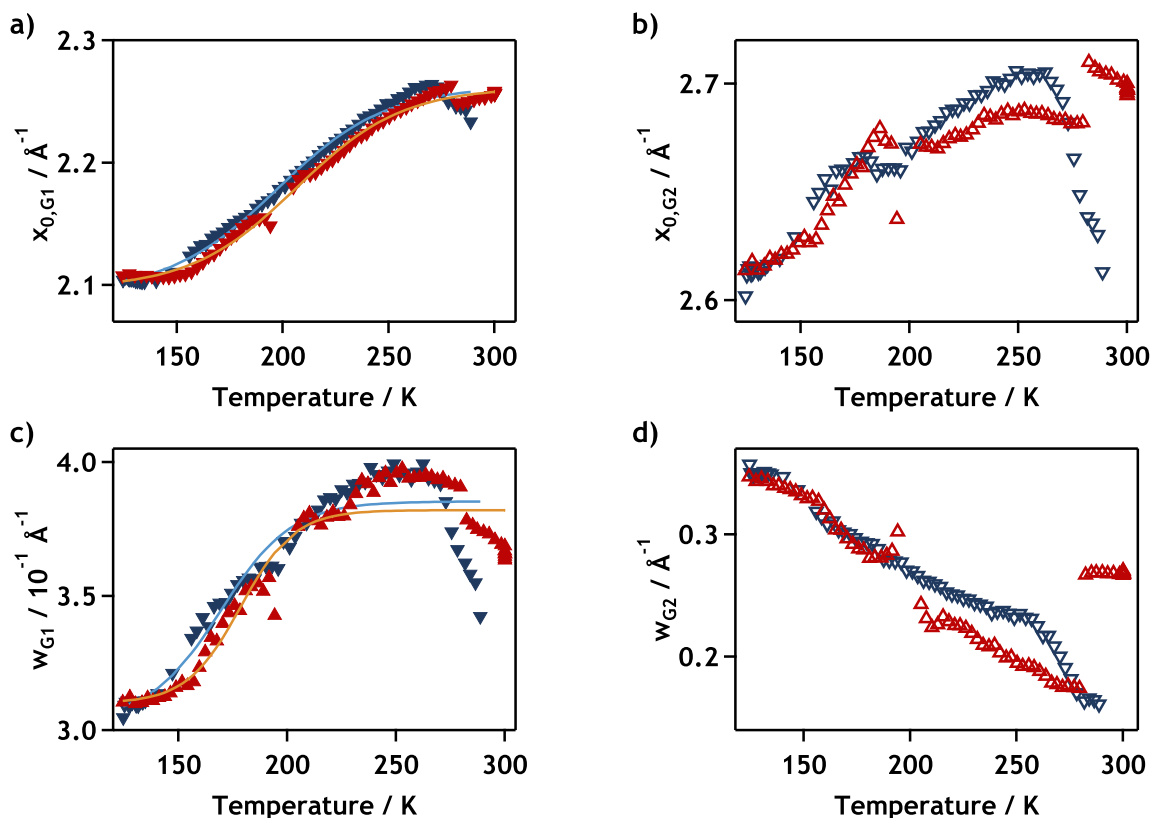


**Figure 5.11.:** Temperature dependence of the X-ray scattering Gaussian lineshape function positions and widths for an aqueous eutectic LiCl solution. Blue and red symbols denote the sample being cooled down and heated up, respectively. a) Temperature dependence of the centre position for the main Gaussian lineshape function (symbols). It shows a quite clear sigmoidal temperature dependence, for which the fit is shown as a line for both the cooling (light blue) and heating (orange). The fits appear to show a hysteresis curve. b) Temperature dependence of the centre position for the high- $q$  shoulder. It appears to show a qualitatively similar behaviour as the main Gaussian lineshape function shown in a), however the uncertainty is too large for further analysis. c) Temperature dependence of the width for the main Gaussian lineshape function (symbols). It seems to show a sigmoidal temperature dependence as seen in the position in a). d) Temperature dependence of the width for the high- $q$  shoulder.

From Fig. 5.11a and b it can be seen that both  $Cl_M$  and  $Cl_S$  shift to lower  $q$  upon cooling. During this,  $Cl_M$  sharpens while  $Cl_S$  broadens, as seen in Fig. 5.11c and d. In  $Cl_M$  this change appears sigmoidal below 280 K. The position of  $Cl_M$  shows a halfway point between 195 and 210 K, as well as parallel heating and cooling lines reminiscent of a hysteresis curve. This is reproduced in the width, even though it is noisier and the divergence above 280 K is larger. For  $Cl_S$ , the effect of noise is too great to fit any further relationships. A comparison of the features in the 1 to 3  $\text{\AA}^{-1}$  with correlation lengths known from literature will be made in Section 5.3.5. Furthermore, the extracted temperature

dependences and the possible peak around  $0.1 \text{ \AA}^{-1}$  will be discussed in more detail in light of data found in this study and the literature.

### 5.3.3. X-ray scattering of aqueous LiSCN solutions

Fig. 5.12 shows the temperature-dependent X-ray scattering traces for **LiSCN:5.8H<sub>2</sub>O** between  $0.1$  and  $4 \text{ \AA}^{-1}$ . While many scattering images in the run had not been usable due to reflections, the only large gap is between  $140$  and  $120 \text{ K}$  (Fig. 5.13). As in **LiCl:7H<sub>2</sub>O**, information about structures between  $0.15 \text{ nm}$  and  $6.3 \text{ nm}$  is contained in the scattering traces, with the larger end of the scale limited by the low- $q$  resolution. In contrast to **LiCl:7H<sub>2</sub>O**, the most striking feature is a large, strongly temperature-dependent peak (**SCN\_LQ**) below  $0.3 \text{ \AA}^{-1}$ . The major features found in **LiCl:7H<sub>2</sub>O** between  $1$  and  $3 \text{ \AA}^{-1}$  are still present, however, **SCN\_LQ** at its maximum is an order of magnitude more intense. Besides **SCN\_LQ**, the scattering traces show a peak between  $2.1$  and  $2.3 \text{ \AA}^{-1}$  (**SCN\_M**) and a shoulder to **SCN\_M** between  $2.4$  and  $2.8 \text{ \AA}^{-1}$  (**SCN\_S**), as seen in the fit presented in Fig. 5.14. Again a sharpening of **SCN\_M** as in **LiCl:7H<sub>2</sub>O** can be seen at low temperatures. **SCN\_LQ**, **SCN\_M** and **SCN\_S** were fitted using three Gaussian lineshape functions in total and an additional Lorentzian lineshape function (**SCN\_L**) was used to model the low- $q$  tail (see Section 5.2.3 and Fig. 5.14).

The temperature-dependent amplitudes of all four functions can be found in Fig. 5.15. **SCN\_M** and the Lorentzian tail **SCN\_L** do not show a clear temperature dependence within the noise, while **SCN\_S** shows a sigmoidal temperature dependence with a halfway point of  $230 \text{ K}$ . **SCN\_LQ**, on the other hand, seems to follow a Gaussian distribution centred at  $208 \text{ K}$ . However, due to the lack of low- $q$  data it cannot be determined whether the amplitude truly shows a maximum or if it appears this way because the peak is moving to lower  $q$  values upon cooling.

The temperature dependence of the width and centre position, on the other hand, clearly follow the trends already found in **LiCl:7H<sub>2</sub>O**. The width of **SCN\_S** increases with decreasing temperature, while all others decrease. The same divergence above  $280 \text{ K}$  can be found as well. Within the noise the parameters showed a sigmoidal temperature dependence, which gave halfway points around  $230 \text{ K}$  (Table 5.2). The discrepancy of the halfway point temperatures found in the X-ray scattering of the eutectic **LiSCN:5.8H<sub>2</sub>O** solution compared to the corresponding OKE data, as well as the X-ray scattering of **LiCl:7H<sub>2</sub>O**, is puzzling.

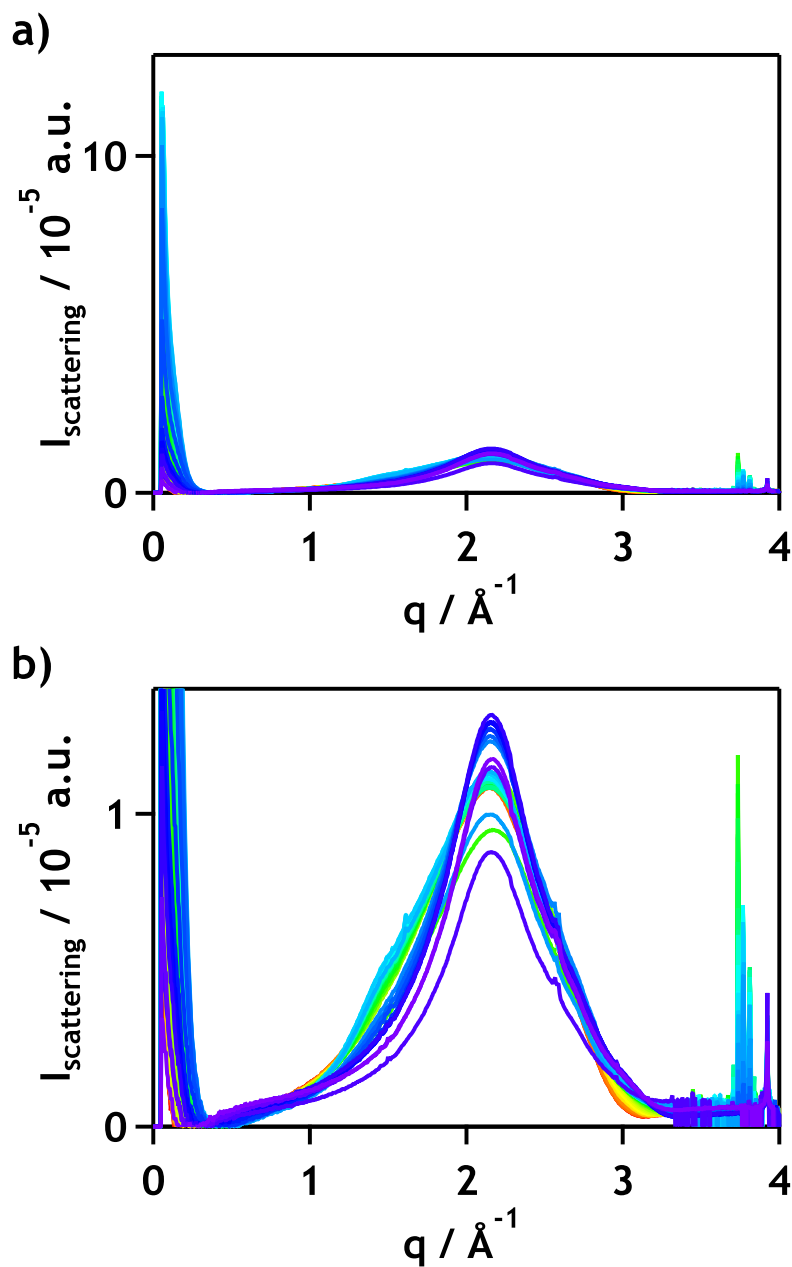


Figure 5.12.: Temperature-dependent X-ray scattering of the eutectic  $\text{LiSCN:5.8H}_2\text{O}$  solution. a) Shows the scattering traces when cooling from 294 K to 119 K (red to blue) at  $20 \text{ K min}^{-1}$ . A very strong peak develops at low- $q$  when decreasing the temperature. b) Same as a), but with the intensity axis scaled to the peak intensity in the  $1$  to  $3 \text{ \AA}^{-1}$  region.

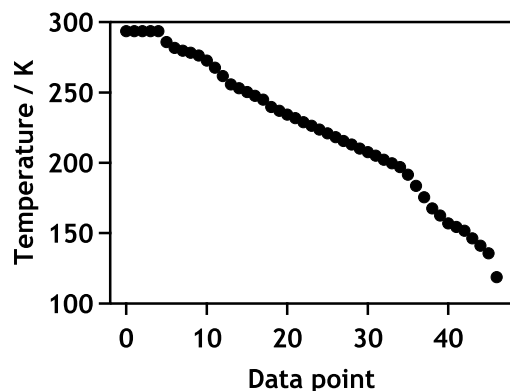


Figure 5.13.: Temperature of the scans taken for the eutectic LiSCN:5.8H<sub>2</sub>O solution. Depicts the analysed scattering traces versus the temperature they were taken at. Breaks from a linear dependence show temperatures at which no scattering traces of sufficient quality could be taken (see Section 5.2.2).

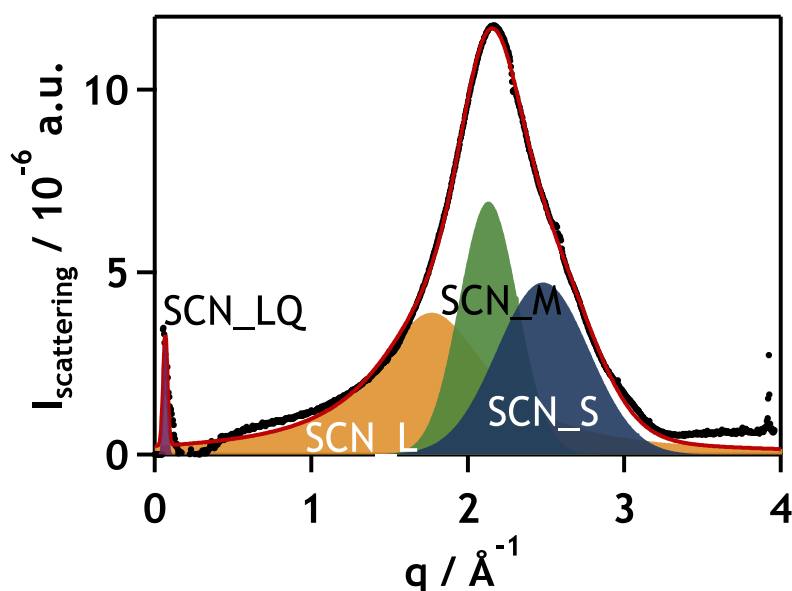
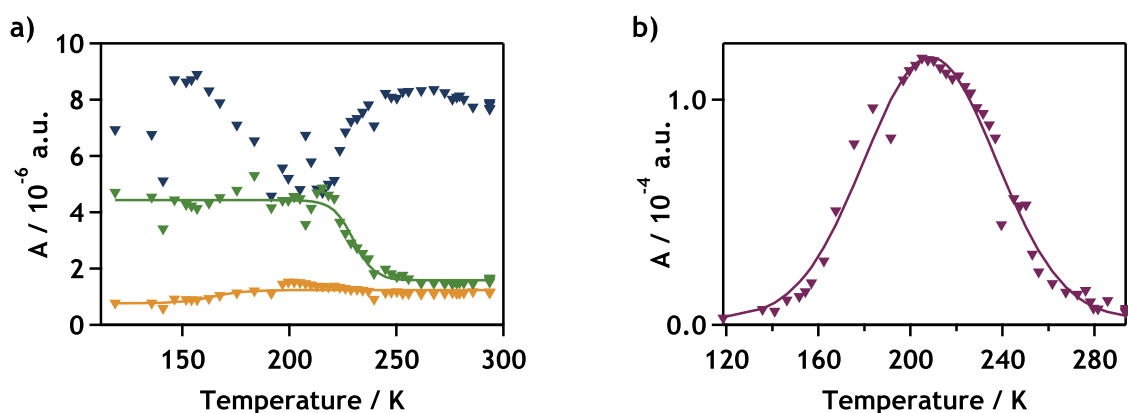
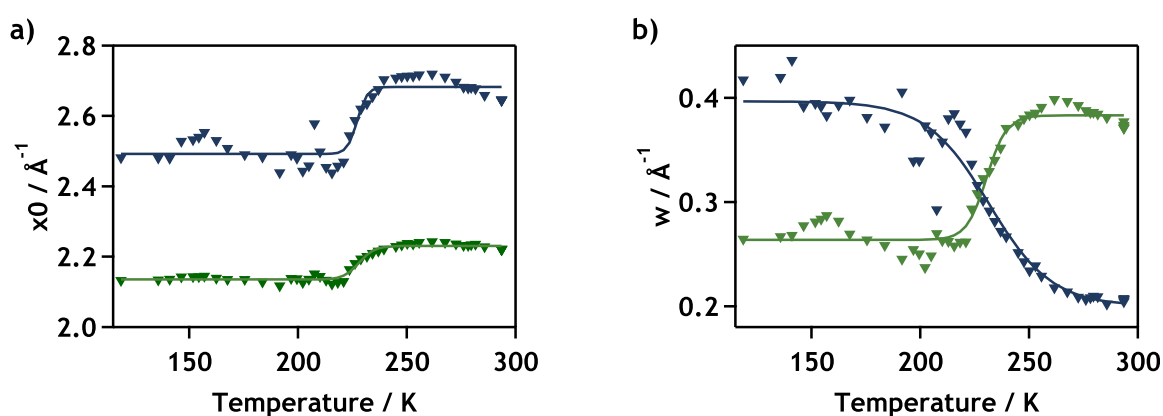


Figure 5.14.: Fit for the X-ray scattering of the eutectic LiSCN:5.8H<sub>2</sub>O solution at 119 K. Shown are the low- $q$  peak (SCN\_LQ, purple), the Lorentzian tail (SCN\_L, orange), the main peak (SCN\_M, green), and the shoulder (SCN\_S, blue). Data points are given as black dots while the red line shows the fit.



**Figure 5.15.:** Temperature-dependent X-ray scattering amplitudes of the eutectic LiSCN:5.8H<sub>2</sub>O solution. Depicted are the amplitudes for a) SCN\_M, SCN\_S, and SCN\_L as well as for b) SCN\_LQ. It cannot be determined whether the amplitude shown in b) truly has a peak at 208 K or if this is due to the peak shifting to lower  $q$  values. Colouring as in Fig. 5.14.



**Figure 5.16.:** Temperature-dependent X-ray scattering fit parameters of the eutectic LiSCN:5.8H<sub>2</sub>O solution. The temperature dependence of SCN\_M and SCN\_S is shown for a) the centre position and b) the width. Both follow a sigmoidal curve with halfway points around 230 K (see Table 5.2). Colouring as in Fig. 5.14.

However, errors may have been introduced during data analysis, as the background subtraction was made difficult by `SCN_LQ`. Most importantly though, evidence for temperature-dependent nm-scale structures was found in the scattering traces, which will be further discussed in Section 5.3.5.

Table 5.2.: Halfway points for the sigmoidal temperature dependences of the centre position and width in `SCN_M` and `SCN_S`.

	position <code>SCN_M</code>	position <code>SCN_S</code>	width <code>SCN_M</code>	width <code>SCN_S</code>
$T_{1/2} / \text{K}$	228	227	230	231
$\Delta / \text{K}$	2	3	2	5

### 5.3.4. IR spectroscopy of aqueous SCN-doped LiCl solutions

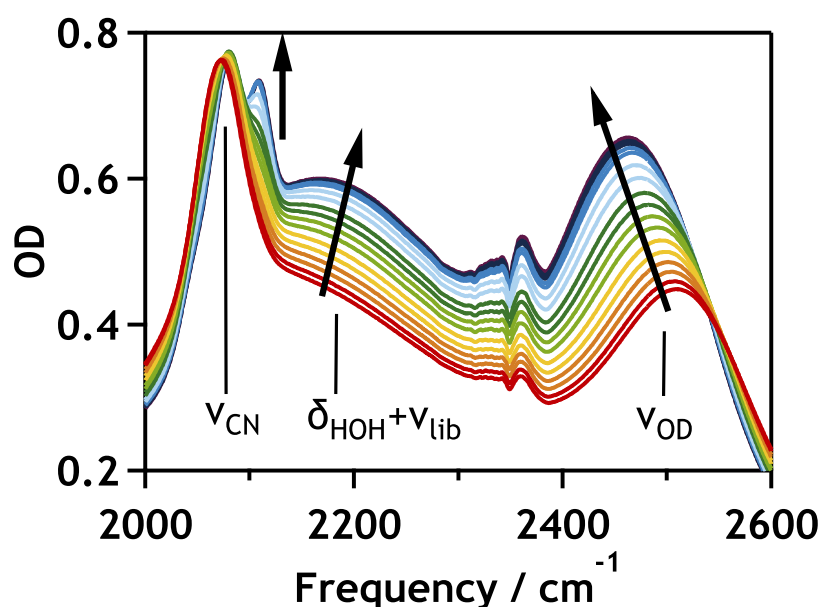
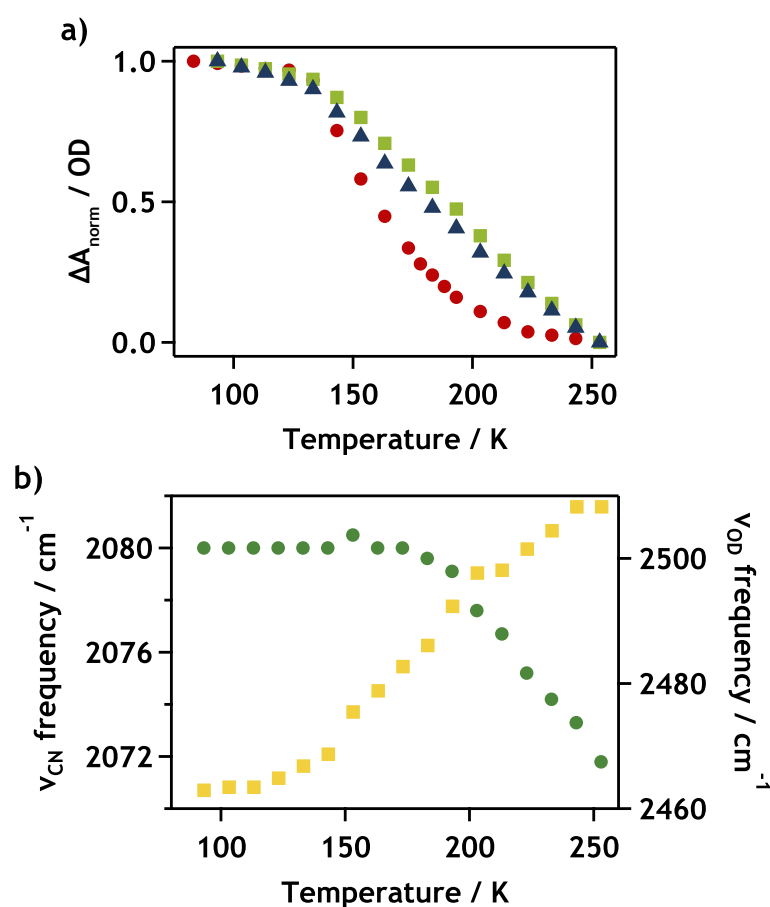


Figure 5.17.: The temperature-dependent IR spectrum of an aqueous eutectic SCN and  $\text{D}_2\text{O}$ -doped LiCl solution ( $\text{LiCl}:\text{SCN}:7\text{H}_2\text{O}$ ) between 253 and 93 K (red to blue, in direction of arrows). Shown is the raw absorbance spectrum between 2000 and 2600  $\text{cm}^{-1}$  covering the  $\nu_{\text{CN}}$  asymmetric stretch at  $\sim 2080 \text{ cm}^{-1}$ , the  $\text{H}_2\text{O}$  combination band of the H-O-H bend and librational modes ( $\delta_{\text{HOH}}+\nu_{\text{lib}}$ ) at  $\sim 2200 \text{ cm}^{-1}$  as well as the  $\nu_{\text{OD}}$  stretching mode at  $\sim 2500 \text{ cm}^{-1}$ . An additional feature visible near  $2350 \text{ cm}^{-1}$  is due to a vibrational mode of atmospheric  $\text{CO}_2$ .

Monitoring the  $\nu_{\text{CN}}$  asymmetric stretch of an aqueous thiocyanate solution reveals information about the environment the  $\text{SCN}^-$  ion finds itself in, while the  $\nu_{\text{OD}}$  stretch contains information on the H-bond network. Most importantly, the  $\nu_{\text{OD}}$  stretch shape and frequency can be used to determine whether crystalline ice is present in the sample or not. The FTIR absorption measurements were performed by Andrew J. Farrell (then University of Strathclyde, now University of Glasgow) and his results will be summarised in the following. Fig. 5.17 shows the

absorption spectra between 2000 and 2600  $\text{cm}^{-1}$  for temperatures between 253 K and 93 K. The most pronounced features are two bands, centred around 2500  $\text{cm}^{-1}$  and 2200  $\text{cm}^{-1}$ , as well as a peak at 2080  $\text{cm}^{-1}$ . An additional small feature at 2350  $\text{cm}^{-1}$  is caused by a vibrational mode of atmospheric  $\text{CO}_2$  and could not be fully removed experimentally. The other features can be divided into the water bands, consisting of the  $\nu_{OD}$  stretching mode at 2500  $\text{cm}^{-1}$  as well as the  $\text{H}_2\text{O}$  combination band ( $\delta_{HOH+\nu_{lib}}$ ) at  $\sim 2200 \text{ cm}^{-1}$ , and the peak caused by the  $\nu_{CN}$  asymmetric stretch mode of  $\text{SCN}^-$ . The  $\nu_{OH}$  stretching mode can theoretically be seen around 3600  $\text{cm}^{-1}$ , however it was not investigated because it would be saturated due to the large amount of  $\text{H}_2\text{O}$  molecules in the solution. This is also the cause behind the sample composition, a  $\text{SCN}^-$  doped  $\text{LiCl}$  solution, as otherwise the  $\nu_{CN}$  stretch would be saturated as well.



**Figure 5.18.:** Temperature-dependence of fit parameters for the absorbance spectrum of  $\text{LiCl-SCN:7H}_2\text{O}$ . a) Shows the normalised change in absorbance  $\Delta A_{norm}$  for the  $\nu_{OD}$  stretch band (blue triangles), the  $\delta_{HOH+\nu_{lib}}$  combination band (light green squares) as well as for the 2105  $\text{cm}^{-1}$  shoulder of the  $\nu_{CN}$  stretch band (red circles). The  $\nu_{CN}$  stretch band itself does not show a temperature-dependent change in absorbance (compare Fig. 5.17b). b) Frequency of the  $\nu_{OD}$  stretch (yellow squares) and the  $\nu_{CN}$  stretch (dark green circles) depending on temperature. On cooling the  $\nu_{CN}$  frequency shifts to higher values until  $\sim 180 \text{ K}$  is reached, at which point it stays approximately constant.

Focusing on the water modes, it can be seen that both water bands increase in amplitude with decreasing temperature (Fig. 5.18a). Their frequencies, however, shift in opposite directions, with the  $\nu_{OD}$  band shifting to lower and the

$\delta_{HOH+\nu_{lib}}$  band to higher frequencies. These changes are linear down to the glass transition temperature at 140 K, where they slowly stop (Fig. 5.18b for the  $\nu_{OD}$  stretch). Both shifts in the water band frequencies are consistent with stronger H-bonding at lower temperatures, though this influence is only obvious for the shift to lower frequencies in the  $\nu_{OD}$  band. The  $\delta_{HOH+\nu_{lib}}$  combination band is rooted in the simultaneous excitation of both the H-O-H bend and low-frequency librations of water and the shift to higher frequencies on cooling is caused by a shift in the librational frequencies.<sup>[200]</sup> Specifically, stronger H-bonds lead to a steeper intermolecular potential which increases the frequency of librations.<sup>[201]</sup> Furthermore, ice formation is excluded experimentally as the sharp ice  $\nu_{OD}$  stretch peak at  $2430\text{ cm}^{-1}$  is not present at any temperature.

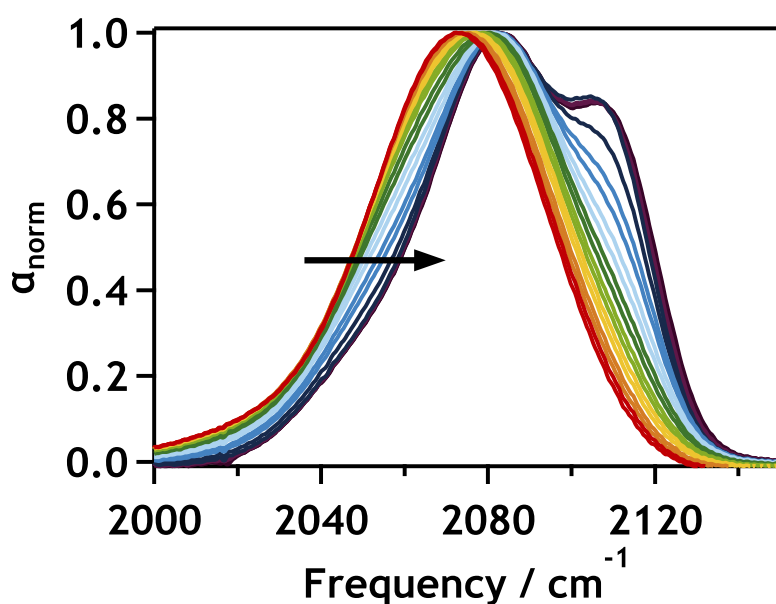


**Figure 5.19.:** The temperature-dependence of the  $\nu_{CN}$  asymmetric stretch in an aqueous eutectic SCN and  $D_2O$ -doped LiCl solution (LiCl-SCN:7H<sub>2</sub>O) between 253 and 93 K (red to blue, in direction of arrows). Shown is the  $\nu_{CN}$  asymmetric stretch peak extracted from Fig. 5.17 by baseline fitting, which shifts to higher frequencies with decreasing temperature. It can be seen that an additional peak at  $2105\text{ cm}^{-1}$  grows visible below 190 K.

The temperature-dependent changes observed in both the amplitude and frequency of the  $\delta_{HOH+\nu_{lib}}$  combination band make it difficult to see the changes in the  $\nu_{CN}$  stretch peak, which sits on top of it. Therefore, the  $\delta_{HOH+\nu_{lib}}$  band was fitted with Gaussian lineshape functions and subtracted to isolate the  $\nu_{CN}$  stretch peak shown in Fig. 5.19. With this, it can be seen that the amplitude of the  $\nu_{CN}$  stretch peak does not change with temperature, while the frequency shifts linearly to higher values on cooling until 183 K is reached (Fig. 5.18b). Below 173 K, the frequency appears to stay approximately constant. Furthermore, on reaching 193 K a shoulder at  $2105\text{ cm}^{-1}$  starts to visibly appear on the  $\nu_{CN}$  stretch peak and does not shift in frequency with temperature. The growth in amplitude of the shoulder was extracted and plotted in Fig. 5.18a, where

it shows an exponential growth down to 133 K, from which point on it shows a slight linear increase.

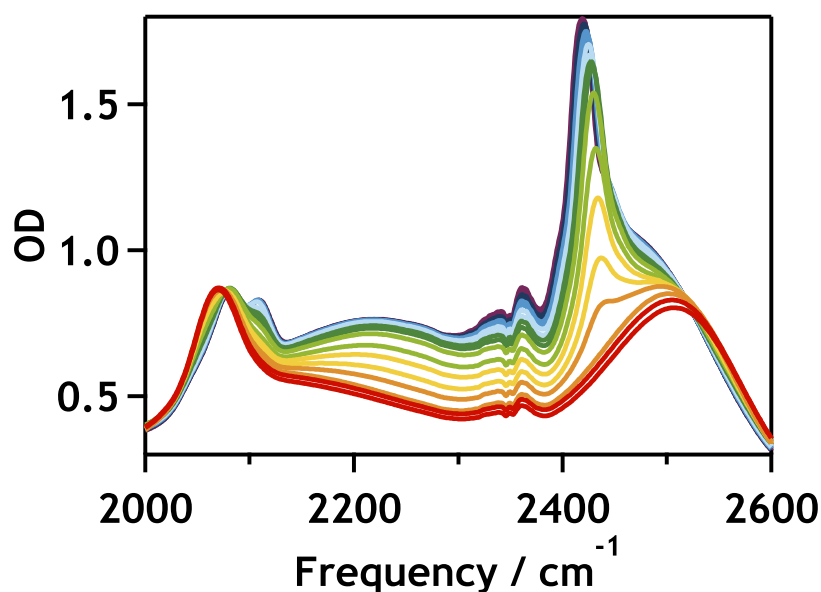


**Figure 5.20.:** The temperature-dependent IR spectrum of an aqueous SCN and D<sub>2</sub>O-doped LiCl solution (LiCl-SCN:9H<sub>2</sub>O) between 253 and 83 K (red to blue, in direction of arrows). Shown is the raw absorbance spectrum between 2000 and 2600 cm<sup>-1</sup> covering the  $\nu_{CN}$  asymmetric stretch at  $\sim 2080$  cm<sup>-1</sup>, the H<sub>2</sub>O combination band of the H-O-H bend and librational modes ( $\delta_{HOH} + \nu_{lib}$ ) at  $\sim 2200$  cm<sup>-1</sup> as well as the  $\nu_{OD}$  stretching modes of liquid water at  $\sim 2500$  cm<sup>-1</sup> and of ice at 2430 cm<sup>-1</sup>. An additional feature visible near 2350 cm<sup>-1</sup> is due to a vibrational mode of atmospheric CO<sub>2</sub>.

Of importance in the absorbance spectrum of the eutectic LiCl-SCN:7H<sub>2</sub>O solution (Fig. 5.17) is the absence of the  $\nu_{OD}$  stretch of ice. This can be clearly seen by comparing the spectrum of the eutectic LiCl-SCN:7H<sub>2</sub>O solution (Fig. 5.17) with the spectrum of the non-eutectic LiCl-SCN:9H<sub>2</sub>O solution (Fig. 5.20), where the ice  $\nu_{OD}$  stretch is visible at 2430 cm<sup>-1</sup> and disappears again upon heating above 233 K. Otherwise, the spectrum of the non-eutectic LiCl-SCN:9H<sub>2</sub>O solution behaves like that of the eutectic solution, showing the same spectral features. The ice  $\nu_{OD}$  amplitude in LiCl-SCN:9H<sub>2</sub>O shows rapid growth with decreasing temperature until 173 K, from which point the increase in amplitude mirrors that of the underlying water  $\nu_{OD}$  band.

Further information on the  $\nu_{CN}$  stretch and its temperature-dependent changes were collected through pump-probe IR spectroscopy measurements conducted by Paul D. Lane (then University of Strathclyde). Fig. 5.21 pictures two such spectra, taken at 289 K and 93 K, respectively. Near room temperature, as in Fig. 5.21a, the lineshape is straightforward and consists of one negative and one positive feature, with the latter located at lower frequencies. The negative peak is attributable to bleaching/stimulated emission associated with the  $0 \rightarrow 1$  transition of the  $\nu_{CN}$  stretch mode, while the positive feature is assigned to the

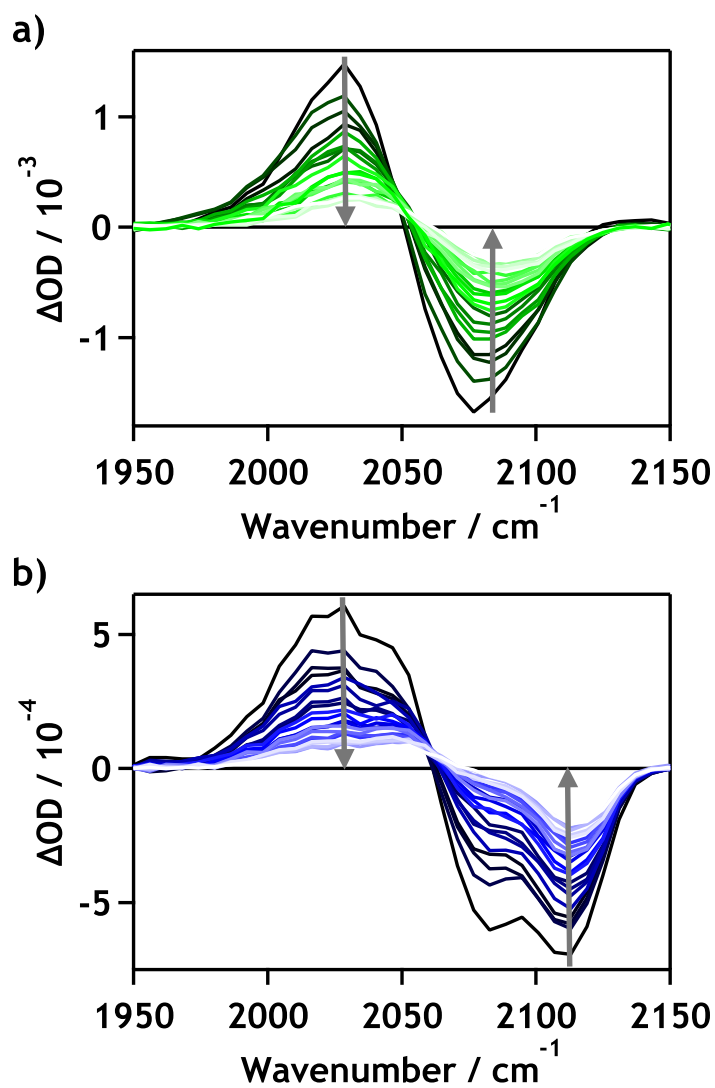


Figure 5.21.: Pump-probe IR spectra for LiCl-SCN:7H<sub>2</sub>O at a) 289 K and b) 93 K. The different traces correspond to different pump-probe delay times between 0 and 5 ps (from dark to light in direction of the arrows).

accompanying  $1 \rightarrow 2$  transition. Below 200 K, a second set of features appears in the spectra, as seen in Fig. 5.21b. The temperature dependence of this appearance is consistent with the appearance of a shoulder in the  $\nu_{CN}$  stretch peak observed in the IR absorption spectra (Fig. 5.19). The pump-probe features were fitted with Gaussian lineshape functions, which showed a decrease in their amplitude with increasing pump-probe delay time. This decrease followed a single exponential decay, giving a vibrational relaxation time  $T_1$  for which the temperature dependence is shown in Fig. 5.22. It can be seen that the vibrational relaxation time of the main peak and shoulder show opposite behaviour, with the vibrational relaxation time of the main peak decreasing linearly on cooling while the vibrational relaxation time of the shoulder increases linearly. Both, however, stop changing appreciably at the glass transition temperature at 140 K. This decoupled behaviour indicates different relaxation mechanisms and will be further discussed in Section 5.3.5.

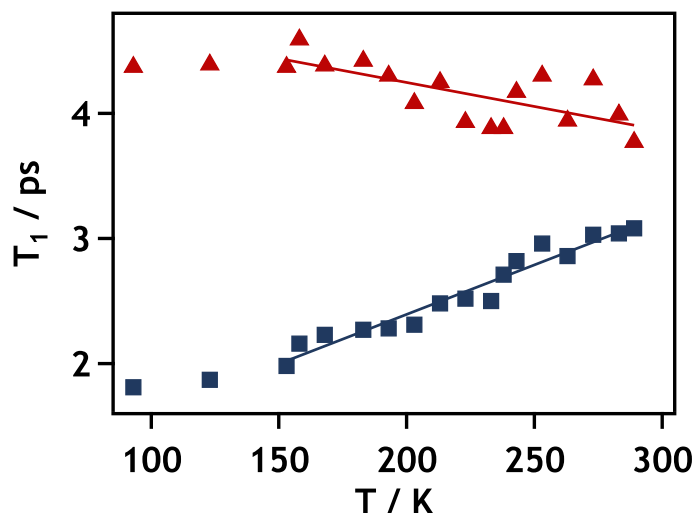


Figure 5.22.: Pump-probe vibrational lifetimes of the  $\nu_{CN}$  stretch mode for LiCl-SCN:7H<sub>2</sub>O. Shown are the vibrational lifetimes for the main band (blue squares) and shoulder (red triangles) of the  $\nu_{CN}$  stretch mode.

### 5.3.5. Discussion

In the preceding sections several notable temperature-dependent features could be seen. These are, in no particular order, the split of the main band in the OKE librations, the emergence of a low-frequency OKE mode, the low-q peak emerging in the X-ray scattering traces of the eutectic lithium thiocyanate solution and the shoulder which appears at low temperatures in the thiocyanate stretch peak. While the temperature dependences show some spread, the changes in the IR and OKE measurements become notable below 200 K. Additionally, the OKE libration populations exhibit halfway points around 180 K, the low frequency OKE

mode likely appears below 180 K, and the frequency shift of the  $\text{SCN}^-$  stretch changes between 173 K and 183 K. The temperature-dependence of the low- $q$  X-ray peak in the eutectic LiSCN solution with a maximum at 208 K is questionable, as the peak was only captured partially and could simply have shifted towards lower  $q$  values. Additionally, the question poses itself how the halfway points of the temperature dependence extracted from the X-ray scattering, 170 K to 207 K for LiCl and 227 K to 231 K for LiSCN, fit into this. For this purpose, a short evaluation of the presented datasets will be given below.

First off, ice or salt crystallisation could be experimentally excluded in all eutectic solutions. For the IR data, this is seen from the absence of the ice peak at  $2430\text{ cm}^{-1}$  seen in non-eutectic solutions and, for the salt, the disagreement of the measured  $\nu_{\text{CN}}$  stretch with the spectrum of crystalline LiSCN.<sup>[202]</sup> In the OKE data, no distinct scattering was observed in any time domain data besides that taken at 200 K. Even small crystals should lead to scattering in OKE measurements and therefore, as no persistent scattering is seen at several temperature, can be excluded. Furthermore, crystals would have been visible as sharp rings in the X-ray scattering images taken for the eutectic solutions, which would give rise to sharp peaks in the scattering traces shown. Again, no such thing was visible in the data, excluding crystal formation in the samples as a possibility. Instead, the solutions are seen to vitrify at the known glass transition temperature.<sup>[203]</sup> This is witnessed by the continuous change in the water features of the IR spectra, as well as the long relaxation times inferable in the OKE measurements.

Secondly, the temperature resolution is, especially in the spectroscopic measurements, limited. For the IR and OKE measurements it varies from 5 K at best to 10 K and more, with especially the OKE measurements having few temperatures below 180 K. While the X-ray measurements have a better theoretical temperature resolution of 2.5 K, they also had a variety of other issues. For one, several temperatures are missing or compromised because reflections from the damaged window material interfered with the acquisition. Additionally, the most interesting  $q$ -range is missing from the measurements because the detector position was limited when the measurements were taken. Furthermore, subtraction of the background for the eutectic thiocyanate solution was difficult, as the high-intensity peak at low- $q$  made it hard to fix the background intensity. Therefore, the X-ray scattering temperature dependences will be given less weight in the following.

The appearance of additional librational modes in the OKE spectrum as well as that of the  $\nu_{\text{CN}}$  stretch shoulder both become notable below 200 K. Librational

frequencies tend to depend on the intermolecular potential as well as the moment of inertia of the moving molecule or ion, while the  $\nu_{CN}$  stretch has previously<sup>[194,201,204-207]</sup> been shown to be a good probe of the thiocyanate environment. Looking at the  $\nu_{CN}$  stretch, the expected frequency for fully solvated thiocyanate ions is  $2055\text{ cm}^{-1}$ , not the observed value of  $2070\text{ cm}^{-1}$ . Previous studies<sup>[194,208]</sup> have identified the  $2070\text{ cm}^{-1}$  peak as belonging to  $\text{Li}^+\text{SCN}^-$  contact ion pairs (CIPs), which are expected in concentrated solutions, and the shift to higher frequencies on cooling is consistent with stronger hydrogen bonding in the surroundings.<sup>[194]</sup> The high-frequency shoulder therefore cannot come from fully solvated ions or CIPs. In the literature,<sup>[194,208]</sup> its frequency has been assigned to aggregates of ions. Furthermore, clustering behaviour has been predicted in MD simulations<sup>[209]</sup> for thiocyanate near its solubility limit. As fully solvated ions, CIPs, and aggregates exist in an equilibrium with each other, the growth in intensity of the aggregate shoulder implies a higher ion concentration. Since the concentration of the solution is not changed during the experiment, the growth of the aggregates indicates that a separation into salt-rich and water-rich domains has occurred at low temperatures. The librations seen in the OKE spectra of the eutectic LiSCN solution further solidify this interpretation. For a rod-like molecule, such as thiocyanate, only one libration is expected in the simplest approximation. This is because the rotation around the long axis is not expected to lead to any change, while the rotations around the two axes perpendicular to it are expected to be degenerate. Therefore, the two observed librational modes at room temperature, the main band and the shoulder, are likely due to two different solvation environments. This is supported by measurements of a less concentrated solution at room temperature, in which the population fraction of the shoulder increased while that of the main band decreased (see Fig. 5.6). As a result, the main band and shoulder are tentatively assigned to CIPs and fully solvated ions, respectively. The split of the main peak into three contributions can then be linked to the formation of salt-rich and water-rich domains seen in the IR spectra at lower frequencies, with the lower frequency librations belonging to aggregates. The different librational frequencies can be explained through different moments of inertia in fully solvated ions, CIPs, and aggregates, while the general red-shift of the librational frequencies can be traced back to the steeper intermolecular potential at lower temperatures due to changes in the hydrogen-bonds. Therefore, good agreement in the interpretations of IR and OKE results can be established.

IR pump-probe spectroscopy then allows to take a closer look at the changes in the thiocyanate stretch. Again, a change from a one peak structure to a two peak structure is seen below 200 K. Here, the stretch mode associated with CIPs shows a decreasing vibrational relaxation time on cooling. This is unexpected, as

generally speaking relaxation takes longer at lower temperatures. It is known, however, that the relaxation of the thiocyanate stretch mode proceeds via energy transfer to the water combination band<sup>[201,206]</sup> and from Fig. 5.17 it can be seen that these two bands overlap significantly. The (constant) transition rate from one energy eigenstate to another can be understood, in a simple model, via a Fermi's golden rule analysis. For the transition from the thiocyanate CIP stretch to the water combination band, this shows a faster relaxation because the temperature-induced shift of the combination band leads to increased spectral overlap between the modes.<sup>[201]</sup> Therefore, the CIPs must interact with water and can be considered hydrated. This contrasts with the weak increase in relaxation time for the thiocyanate aggregate stretch and suggests a different relaxation mechanism. The relaxation mechanism likely features a reduced interaction with water molecules, which is consistent with clusters of ions in which not all ions interact with water molecules. Again, these results strengthen the picture of a highly concentrated solution with CIPs at room temperature, which then morphs into a liquid consisting of salt-rich and water-rich domains at lower temperatures.

So how does the X-ray scattering data fit into this? The most obvious agreement, and support of the presented picture, can be found in the low- $q$  peak seen in the eutectic LiSCN solution. It shows the temperature-dependent growth of nanoscale structure, which is in agreement with the domain separation concluded from the IR and OKE data. While no similarly intense peak is observed in the eutectic LiCl solution, a weak peak can be observed at low  $q$ -values in the data presented here and in the literature.<sup>[184,185]</sup> Specifically, Yamanaka *et al.*<sup>[184]</sup> see peaks corresponding to lengths of 0.4 nm and 0.7 nm evolve with decreased temperature, which they assign to an increasingly ice-like water structure. A further feature at 0.9 nm length was also noted and used to indicate that structure in the supercooled and glassy solutions reaches up to at least one nanometre. Therefore, data going to lower  $q$ -values in the eutectic LiCl solution is sorely needed to clarify whether nanoscale structures exist or not. An indirect confirmation can be taken from the comparison of previously published OKE data on eutectic LiCl solutions<sup>[186]</sup> with the OKE data presented here for eutectic LiSCN solutions. While the temperature-dependent OKE spectra presented by Turton *et al.*<sup>[186]</sup> mainly show slow, gradual changes in the water structure, a low-frequency mode, similar to that seen here in the eutectic LiSCN solution, was reported. There, it was only observed at one temperature and associated with the anomalous diffusion of a percolating ion-water network.<sup>[210]</sup> However, the data presented here shows the position of the mode at 144 GHz to be independent of temperature, which is not in line with a diffusive process, and rather points towards a phonon-like motion. Here it is important to emphasize that

phonon modes have been found previously in amorphous materials.<sup>[11]</sup> Since the appearance of the low-frequency mode coincides with the formation of domains and the X-ray scattering data indicates nanoscale structures, it was assigned to an acoustic phonon mode in the salt-rich domain. Using an appropriate speed of sound for a concentrated salt solution<sup>[211]</sup> of  $1.9 \text{ km s}^{-1}$ , the diameter of a spherical domain,  $d = v/(\pi * f)$ , can be calculated from the frequency  $f$  of the standing wave. This results in a diameter of 4.2 nm, which is in surprisingly good agreement with the nanosegregated domain size predicted by MD simulations.<sup>[183]</sup> Additionally, this is still of the same order of magnitude as the roughly ten (or larger) nm structure indicated by the X-ray scattering measurements of LiSCN and again strengthens the picture of a nanosegregated liquid.

Comparison with the X-ray study presented by Yamanaka *et al.*<sup>[184]</sup> also helps to assign interactions to the scattering traces, though they used a more concentrated solution and presented fewer temperatures. The main peak at  $2 \text{ \AA}^{-1}$ , **Cl\_M**, can mainly be attributed to the Cl-H<sub>2</sub>O distance in the anion hydration shell, which is expected to be 310 pm and becomes more ordered at lower temperatures.<sup>[184,185,212]</sup> As chloride is a strong scatterer, the other two contributions in this range will likely be overshadowed. These are the hydrogen-bonded H<sub>2</sub>O-H<sub>2</sub>O distances of roughly 280 pm and the distances between water molecules in the first hydration shell of Li<sup>+</sup> between 280 pm and 360 pm. The Lorentzian tail below  $2 \text{ \AA}^{-1}$ , **Cl\_L**, is attributed to several longer-ranged interactions, such as those between water molecules in the first hydration shell of Cl<sup>-</sup>, those of a cation and anion bridged by a water molecule, and long-range interactions between water molecules. While Yamanaka *et al.* did not make any formal assignment corresponding to the  $2.6 \text{ \AA}^{-1}$  shoulder (**Cl\_S**) seen here, it is also present in their data. Specifically, a peak with below average scattering intensity can be seen around 240 pm and neutron diffraction data<sup>[185]</sup> shows distances from the lithium ions to the oxygen and hydrogen atoms in water molecules of 202 pm and 261 pm, respectively. Due to their low electron density, both lithium and hydrogen are expected to be weak scatterers when probed with X-rays. Therefore, the **Cl\_S** shoulder is assigned here to interactions between the lithium ions and the water molecules in its first hydration shell, which is expected to become less ordered at lower temperatures. The observed shifts of the centre positions to smaller q-values with lower temperatures can then be interpreted as an increase in the ion-water distance of the first solvation shell. Furthermore, the sharpening of the peak denoting the chloride solvation shell on cooling, and conversely the broadening for the lithium solvation shell, denote the increased order, or disorder, in the arrangement. The same trends can be seen for the eutectic LiSCN solution and interpreted accordingly. While the structure of a thiocyanate and a chloride solution can not *ab initio* be assumed to coincide,

Yamaguchi *et al.* [185] measured similar X-ray scattering traces for aqueous solutions of lithium chloride and bromide, the latter of which has a larger number of electrons than thiocyanate. Therefore, the agreement between lithium chloride and lithium thiocyanate solutions is not surprising. Why the transitions has half-way points around 230 K in the LiSCN solution, compared to below 210 K in the LiCl solution, is unclear at the moment. However, for the LiSCN solution, less data was available and the available data was arguably of inferior quality. Furthermore, influences from the background subtraction cannot be fully excluded, as the fit functions showed strong codependency in the fit. In light of all the presented data, with which those half-way temperatures do not agree, further clarifying measurements seem therefore necessary.

In summary, a change in the environment of the probe ions connected with a segregation into salt-rich and water-rich domains could be seen below 200 K. The sigmoidal temperature dependences which were collected point to a half-way temperature of 180 K. As all changes were smooth, and not sudden, this can be interpreted as a crossing of the Widom-line associated with the water liquid-liquid critical point, rather than a direct observation of a first-order liquid-liquid phase separation.

## 5.4. Conclusions

Here, a combination of X-ray scattering, OKE spectroscopy, and IR spectroscopy was used to investigate the low-temperature behaviour of aqueous lithium chloride and lithium thiocyanate solutions. The observed changes, such as the increase in the number of thiocyanate librational modes and the growth of a shoulder in the  $\nu_{CN}$  stretch mode below 200 K, are compatible with a segregation of the solution into salt-rich and water-rich domains at low temperatures. This is interpreted as evidence of two distinct low-temperature water structures, which have been observed in the literature. [150,165,166,176,177] The observed smooth progression of the changes can then be understood as the crossing of a Widom line connected to the LLCP of water, instead of a phase transition, and the inferred domain sizes are in line with theoretical predictions. [183] The temperature range of the changes in the salt solutions, which is between 180 and 200 K, is lower than the 228 K expected in pure water because the solutes added to decrease the liquidus temperature emulate the effect of pressure on water. Therefore, the presented experiments add to the growing pile of evidence for the existence of a LLCP in water and are in accordance with other experimental studies, such as the ones presented by Murata and Tanaka, [188] Suzuki

and Mishima,<sup>[179,181,182,189]</sup> as well as Zhao and Angell.<sup>[192]</sup>

The presented data could, of course, be made more conclusive with additional as well as more detailed measurements. First and foremost, a better temperature resolution in the spectroscopic data is desirable to better fix the temperature range of the changes. Additionally, cooling as well as heating curves from all experimental methods would clear up whether the changes are reversible or not. Specifically for the OKE measurements, improvements can be made in the data analysis. While the  $\alpha$ -relaxation is unlikely to be fully captured at lower temperatures, due to limitations in the pump-probe delay time, a low-frequency cut-off in the Havriliak-Negami fit function could possibly improve the fit of the  $\beta$ -relaxation. As the  $\beta$ -relaxation overlaps with the librational region at many temperatures, an improved fit would allow more certainty for the subtleties observed in the behaviour of the librational modes. The largest number of improvements can be made for the X-ray scattering measurements, which were rather preliminary. First off, measurements at lower  $q$  values are needed to solidify the interpretation of the scattering data and prove the domain size more directly. Secondly, calibration of the detector for absolute intensities should allow further data treatment, which would result in a more detailed analysis. Last but not least, reducing the influence of reflections would improve the data quality. Considerations here are the use of a different window material, which would ideally take less damage during prolonged exposure to X-rays, or the use of less energetic X-ray wavelengths. Furthermore, programming the sample holder to move in between scans would decrease the exposure time on a spot and therefore hopefully reduce the damage leading to reflections.

A completely different approach lies in changing the solutes used, which currently suppress the response function anomalies shown in pure water. Zhao and Angell<sup>[192]</sup> have shown that certain mixtures of ionic liquids do not suppress the anomalies in aqueous solutions, and the study of their systems with our methods, as well as the study of other ionic liquid combinations, is a possible way to increase the experimental evidence concerning a LLC in water.



## 6. Supersaturated sodium thiosulfate solutions and the hunt for pre-nucleation clusters

### 6.1. Introduction

During crystallisation, a structured solid phase is formed from a liquid or solution and understanding it is crucial to practical applications. For example, water pipes get blocked by the crystallisation of calcium containing compounds from the water. Furthermore, crystallisation is used as a purification method during synthesis of organic compounds, such as those used in drugs. These compounds can form different crystal structures with the same molecular composition, which are called “polymorphs”. The properties of the solid can vary between polymorphs, meaning that the effect of the active compound in a medicine, or the speed of its release, can depend on the crystal structure it took during crystallisation.<sup>[213]</sup> To understand the end product of a crystallisation process, however, one needs to understand how it starts. Classically, crystallisation has been understood in the framework of CNT, which has been reviewed in Section 1.1. The principal assumption behind CNT is that the formation of a nucleus, which can then grow into a crystal, is defined by a balance between the favourable bulk free energy and the energy cost of forming an interface to the liquid phase. Crucially, both the bulk free energy and the energy of the interface are calculated using macroscopic properties, even though the nucleus is a microscopic entity made up of tens to hundreds of particles. In the case of heterogeneous nucleation, the nucleus forms on the surface of an impurity or disturbance in the system, such as dust or a scratch in the container wall. Crystallisation then proceeds rapidly because the cost of forming an interface is reduced and heterogeneous nucleation is the dominant pathway whenever it is possible. All further discussion will therefore assume that heterogeneous nucleation can be experimentally excluded as a pathway. In the case of homogeneous nucleation, on the other hand, CNT dictates that the nucleus is the result of random, transient density

fluctuations and that any nucleus below the critical nucleus size is inherently unstable. This specific assumption has recently been challenged by studies<sup>[214-218]</sup> which found stable clusters, amorphous phases and other precursors when investigating crystallisation.

Gebauer *et al.*<sup>[217]</sup> used ion concentration measurements, constant pH titration and analytical ultracentrifugation (AUC) to investigate calcium carbonate solutions, finding thermodynamically stable pre-nucleation clusters of 2 to 4 nm in size. The same system, for the biogenic template-directed formation, was studied by Pouget *et al.*<sup>[215]</sup> using cryo-TEM. They found pre-nucleation clusters which formed amorphous nanoparticles and assembled at the template to transform into the crystalline phase. Van Driessche *et al.*<sup>[216]</sup> used sample quenching and TEM to look at calcium sulphate precipitation and observed a phase of stable nanocrystals at undersaturated conditions, which grew into nanorods before ripening into gypsum crystals. Magnetite formation was observed by Baumgartner *et al.*<sup>[214]</sup> using cryo-TEM, X-ray diffraction and electron microscopy. The crystalline phase was shown to be formed by aggregation of particles in the nm-range. Jawor-Baczynska *et al.*<sup>[218]</sup> used dynamic light scattering (DLS), Brownian microscopy/nanoparticles tracking analysis (NTA) and cryo-TEM to observe aqueous solutions of small amino acids and found colloidal scale mesospecies even at undersaturated conditions.

Therefore, the question was raised whether these observations can be reconciled with an extended CNT framework<sup>[214,219]</sup> or justify the formulation of a new nucleation pathway.<sup>[220,221]</sup> Baumgartner *et al.*<sup>[214]</sup> included stable clusters as well as monomers in the CNT homogeneous nucleation pathway by adding an empirical cluster term to the interfacial contributions. Gebauer *et al.*<sup>[221]</sup> questioned the validity of this approach, noting that strongly curved surfaces on small particles are ill defined. Furthermore, they raised that interfacial terms would become more complicated if the interface was on the scale of atomic lengths instead of infinitesimal. This is especially valid for crystallisation in aqueous solutions, where the solvation shell of the cluster can be taken as the cluster-liquid interface. The main concern raised in their review, however, was that entities such as complexes, ion pairs and polymers are well known in chemistry to be stable in solutions. Due to the interface term, however, only the monomer can be considered thermodynamically stable in the CNT description, unless empirical corrections are made. Therefore, the reality of the solution is not adequately captured. In addition, the thermodynamic stability of different polymorphs has been shown<sup>[222]</sup> to depend on the particle size, rendering it questionable to choose the bulk free energy of the final polymorph. Gebauer *et al.*<sup>[220,221]</sup> instead propose a “pre-nucleation cluster pathway”. While heterogeneous nucle-

ation is considered the dominant pathway if it is applicable, homogeneous nucleation by the CNT mechanism is considered an exception. Instead pre-nucleation clusters (PNCs) exist in solutions even at concentrations below supersaturation. They are defined as small, thermodynamically stable entities and, in contrast to the CNT formulation, do not possess an interface and therefore can be considered solutes instead of a separate phase. PNCs consist mostly, but not exclusively, of the atoms, ions or molecules which later form the crystal and tend to have structural motifs similar to the polymorph they first form. Most crucially, in PNCs there is no phase boundary to the solution, meaning that all ions in the PNC are in a dynamic equilibrium with their solvated monomer. As a consequence, their configuration varies on the time-scale of molecular reorientation (hundreds of picoseconds). Therefore, nucleation is considered to have already taken place if the dynamics become slower than this, for example in stable clusters, or the PNCs becomes large enough to develop an interface.

As a consequence of this definition, intermolecular interactions are defining for PNCs. Their existence depends on the balance between monomer solvation and monomer-monomer interactions, for example through hydrogen bonds, Coulomb interaction or the formation of covalent bonds. This, of course, raises questions as to the average lifetime and size distribution of these PNCs. Many observations of PNCs are based on microscopic techniques, such as cryo-TEM, which rely on quenching.<sup>[221]</sup> To avoid recording artefacts caused by the quenching process, *in-situ* observation of these species is mandatory. OKE has long been established as a technique allowing the investigation of intermolecular dynamics in solution and liquids.<sup>[9,91,101,223]</sup> Specifically the rotational relaxation time  $\tau$  has been used to relate the measured spectra to the size of the relaxing particle using the SED relation (see Section 1.1.1, Eq. 1.5).<sup>[9,224]</sup> A distribution of rotational relaxation times corresponding to the size distribution is therefore expected, given that the species are long-lived enough to observe their rotational relaxation. To study the OKE spectra of a supersaturated solution, sodium thiosulfate ( $\text{Na}_2\text{S}_2\text{O}_3$ ) was chosen as the pentahydrate crystals are known<sup>[225]</sup> to form a stable supersaturated solution when the melt is cooled below 49 °C. Furthermore, the  $\text{S}_2\text{O}_3^{2-}$  ion is anisotropically polarisable, while the  $\text{Na}^+$  ions are isotropically polarisable, allowing only the thiosulfate contributions to be seen in the spectrum.

## 6.2. Experimental details

A  $\text{Na}_2\text{S}_2\text{O}_3$  pentahydrate solution (63.7 w-%,  $\text{Na}_2\text{S}_2\text{O}_3 \cdot 5\text{H}_2\text{O}$ ) was made by melting  $\text{Na}_2\text{S}_2\text{O}_3$  pentahydrate ( $\geq 99.5\%$ , Sigma-Aldrich) in a heated ultrasound bath

(Fisherbrand FB11002) at 65 °C for 1 h. During this, ultrasound was used for 30 min to speed up the solvation process and mix the solution. The  $\text{Na}_2\text{S}_2\text{O}_3$  pentahydrate solution ( $\text{Na}_2\text{S}_2\text{O}_3 \cdot 5\text{H}_2\text{O}$ ) was filled into a 2 mm quartz cuvette (Starna) one week after preparation. No signs of crystallisation were noticeable in the stock solution or the cuvette. An aqueous  $\text{Na}_2\text{S}_2\text{O}_3$  solution (21.2 w-%,  $\text{Na}_2\text{S}_2\text{O}_3 \cdot 32.7\text{H}_2\text{O}$ ) was made by dissolving 0.9930 g  $\text{Na}_2\text{S}_2\text{O}_3$  pentahydrate in 2 ml of HPLC gradient grade water (Fisher) and directly filled into a 2 mm quartz cuvette (Starna). Measurements were done using the high time resolution set-up (see Section 2.1.2) with a maximum delay time of 20 ps and the long delay set-up (see Section 2.1.3) with a maximum delay time of 2 ns. The cuvette was held in a temperature controlled aluminium sample holder with a precision of  $\pm 0.1$  °C for measurements at 25 °C of  $\text{Na}_2\text{S}_2\text{O}_3 \cdot 32.7\text{H}_2\text{O}$  and at 25, 50 and 75 °C of  $\text{Na}_2\text{S}_2\text{O}_3 \cdot 5\text{H}_2\text{O}$ . For the measurements of  $\text{Na}_2\text{S}_2\text{O}_3 \cdot 5\text{H}_2\text{O}$  at 0 and -25 °C the cuvette was held in a liquid nitrogen-cooled cryostat (Oxford Instruments) with a temperature precision of  $\pm 0.1$  °C under a dry nitrogen atmosphere to avoid water condensation. At least 16 scans were taken and averaged for the high time resolution set-up and 128 for the long delay set-up. In the high time resolution data of  $\text{Na}_2\text{S}_2\text{O}_3 \cdot 5\text{H}_2\text{O}$  at 25 °C 16 scans were taken but only 9 could be averaged over as the laser had lost the correct lasing mode for a short time during the experiment.

The raw OKE data was averaged and converted into a spectrum in a *LabVIEW*<sup>[136]</sup> program. The two averaged datasets with different maximum delay times were concatenated in *Igor Pro*<sup>[199]</sup> for each temperature. The concatenated time domain data was Fourier transformed into a frequency domain spectrum from 500 MHz to 20 THz after deconvoluting the instantaneous response. To do this, a  $\text{sech}^2$  autocorrelation function was fitted to the instantaneous response of the time domain data at negative times. The frequency domain spectrum was then fitted using the program described in Section 3.3.2 and the resulting fit parameters can be found in Chapter C. Brownian oscillators (Section 3.2.2) were used to model high-frequency vibrations while anti-symmetrised Gaussians (Section 3.2.1) were used for the librational modes. The initial fit parameters of the librational modes were determined from the -25 °C spectrum, in which the rotational relaxation had been slowed down enough to practically not be visible. The relaxational modes themselves were fitted with Havriliak-Negami functions (Section 3.2.3). A Cole-Cole function was used for intermediate relaxations including cage-rattling and cage-diffusion motions. The rotational relaxation band of all measured samples was broadened and could not be described by a single Debye function. As one of the aims is to study clustering, using a distribution of Debye functions for the rotational relaxation allows to study a possible distribution of clusters. Therefore, the broadening was accounted for by using two to

three Debye functions in  $\text{Na}_2\text{S}_2\text{O}_3\cdot 5\text{H}_2\text{O}$  above  $0^\circ\text{C}$  and a Cole-Davidson function in  $\text{Na}_2\text{S}_2\text{O}_3\cdot 32.7\text{H}_2\text{O}$  as well as in  $\text{Na}_2\text{S}_2\text{O}_3\cdot 5\text{H}_2\text{O}$  at  $0^\circ\text{C}$ . The Cole-Davidson function was chosen because the low-frequency cut-off at  $0^\circ\text{C}$  in  $\text{Na}_2\text{S}_2\text{O}_3\cdot 5\text{H}_2\text{O}$  as well as the lack of separation in the spectrum of  $\text{Na}_2\text{S}_2\text{O}_3\cdot 32.7\text{H}_2\text{O}$  made it unreliable to fit the rotational relaxation with a distribution of Debye functions. In  $\text{Na}_2\text{S}_2\text{O}_3\cdot 5\text{H}_2\text{O}$  at  $0^\circ\text{C}$  this was because the rotational relaxation band was mostly cut off at the low-frequency limit. In  $\text{Na}_2\text{S}_2\text{O}_3\cdot 32.7\text{H}_2\text{O}$ , on the other hand, the rotational relaxation band could not be well separated from the higher frequency bands, such as librations and translational diffusion, due to its position and intensity. Furthermore, water modes had to be taken into account for  $\text{Na}_2\text{S}_2\text{O}_3\cdot 32.7\text{H}_2\text{O}$ . Their parameters were taken from a water model developed for OKE spectra<sup>[12]</sup> (Chapter D) and the amplitude was scaled linearly with respect to pure water by the water weight fraction.

Further measurements of  $\text{Na}_2\text{S}_2\text{O}_3$  pentahydrate solutions were performed with different preparation methods, which were filled into cuvettes directly after preparation and measured on the same day. However, the samples showed visible crystal formation on the same or the following day and the collected data was therefore dismissed. One preparation method used was melting the  $\text{Na}_2\text{S}_2\text{O}_3$  pentahydrate crystals using the heated ultrasound bath, either with or without using ultrasound during the melting. The resulting solution was filled in a cuvette, either with or without filtering using a  $0.20\ \mu\text{m}$  hydrophilic PTFE filter (Millex-LG), both while the solution was already cooled down or still hot. Another preparation method was to melt the  $\text{Na}_2\text{S}_2\text{O}_3$  pentahydrate crystals with a heat gun and filtering the resulting solution while it was still hot, either degassing the cuvette in the ultrasound bath afterwards or not. Crystal structures were determined by single crystal X-ray diffraction by Claire Wilson (University of Glasgow) using a CCD detector equipped diffractometer with a Mo sealed tube X-ray source and an Oxford Cryosystem low temperature device.

## 6.3. Results and discussion

### 6.3.1. Crystal formation

Several samples showed visible crystals after being measured in the OKE set-up. All  $\text{Na}_2\text{S}_2\text{O}_3$  pentahydrate solutions that formed crystals had been prepared on the same day as they were measured. The crystals formed were monoclinic prisms in a surrounding brine and grew to visible size either on the day the meas-

urement was done or the following day. If the surrounding brine was removed the crystals would reduce in size and droplets of brine would form around them, indicating the crystal and brine are in an equilibrium. The surrounding brine could be completely crystallised by introducing a  $\text{Na}_2\text{S}_2\text{O}_3$  pentahydrate crystal and formed monoclinic rods if disturbed. X-ray diffraction showed that both the prisms and the rods had less than five water molecules in their unit cell. The unit cell of the prisms (see Fig. C.1) was found to be defined by  $a = 11.401$ ,  $b = 11.259$ ,  $c = 17.300$  and  $\beta = 94.883^\circ$ , which matches the  $P21/c$  structure published by Chan *et. al.* [226] for  $4\text{Na}_2\text{S}_2\text{O}_3 \cdot 5\text{H}_2\text{O}$ . For the rods a unit cell (see Fig. C.2) defined by  $a = 5.7777$ ,  $b = 19.316$ ,  $c = 11.5177$ ,  $\beta = 102.372^\circ$  and  $V = 1255.6$  was found with a composition of  $\text{Na}_2\text{S}_2\text{O}_3 \cdot 2\text{H}_2\text{O}$ .

### 6.3.2. Water influence

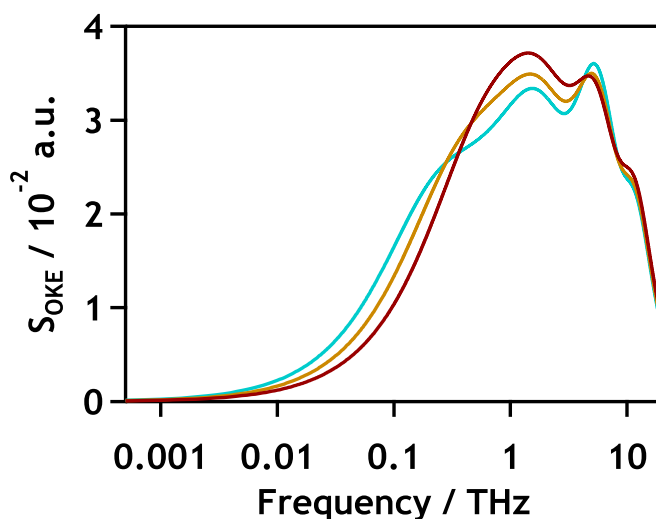


**Figure 6.1.:** Temperature-dependent water OKE spectra. Calculated spectra from 25 to 75 °C (cyan to red) for a 36.3 w-% water fraction. The intensity scales linearly with the weight fraction of water. Spectra for 0 and -25 °C are not shown, as the model was not made for supercooled temperatures.

The THz water spectrum (Fig. 6.1) in OKE spectroscopy features librational modes at and above 12 THz as well as acoustic phonon modes around 1.5 and 5.2 THz for the TA and LA phonon, respectively. However, the OKE spectrum of water tends to be very weak. Even though water has a flat and angular structure, its polarisability is nearly isotropic, leading to a weak OKE signal. This is because the electron density is mainly located at the oxygen atom. The thiosulfate anion, meanwhile, has a trigonal pyramidal structure (Fig. 6.2) and a more anisotropic polarisability, since the size difference between the oxygen and sulfur atoms renders it more rod-like. As such, the spectrum of a concentrated aqueous  $\text{Na}_2\text{S}_2\text{O}_3$  solution is expected to be dominated by the thiosulfate contributions.

Since the sodium cation is perfectly spherical, it is expected to not contribute to the OKE spectrum at all.

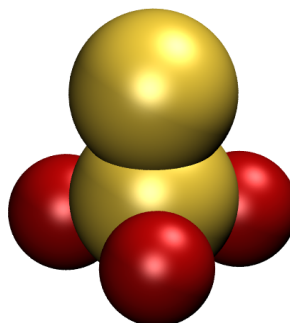


**Figure 6.2.:** Space-filling three-dimensional model of the thiosulfate anion. Sulfur is coloured yellow and oxygen is coloured red.

A model for OKE water spectra based on temperature-dependent water measurements had been developed in our group to extract the water contribution from DNA spectra<sup>[12]</sup> using a Cole-Cole function, a Brownian oscillator function, and two anti-symmetrised Gaussian functions (see Chapter D). Here, this model was used to judge the influence of the water spectrum at a given concentration and temperature. For this, the spectrum at the necessary temperature was calculated and then scaled by the weight fraction of water in the solution. From Fig. 6.3a it can be seen that the water spectrum is more than an order of magnitude weaker than the  $\text{Na}_2\text{S}_2\text{O}_3\cdot 5\text{H}_2\text{O}$  spectrum at 25 °C and therefore exerts a negligible influence. Comparing Fig. 6.1 and Fig. 6.3a furthermore shows that the change with temperature in the water spectrum is not significant on the scale of the  $\text{Na}_2\text{S}_2\text{O}_3\cdot 5\text{H}_2\text{O}$  spectrum. Due to this, the water spectrum was not taken into account in the analysis of the  $\text{Na}_2\text{S}_2\text{O}_3\cdot 5\text{H}_2\text{O}$  spectra. In contrast, the  $\text{Na}_2\text{S}_2\text{O}_3\cdot 32.7\text{H}_2\text{O}$  spectrum at 25 °C (see Fig. 6.3b) shows a significant water contribution, with roughly a third of the intensity at 1 THz being attributable to water. Because of this, the water functions were included in the  $\text{Na}_2\text{S}_2\text{O}_3\cdot 32.7\text{H}_2\text{O}$  fit with fixed parameters.

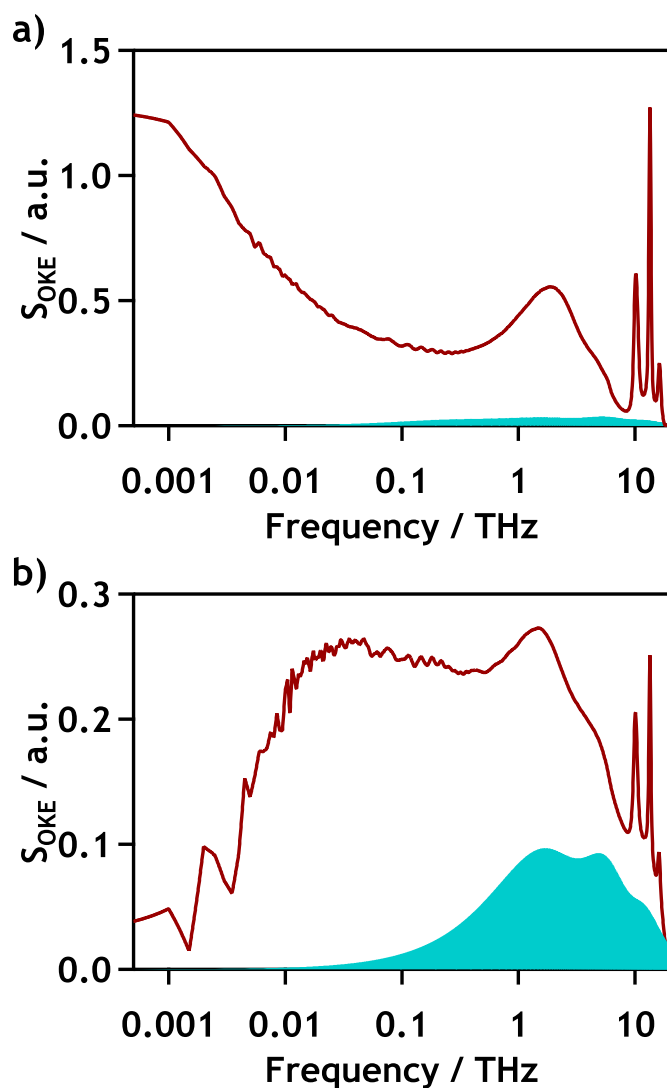


**Figure 6.3.:** Comparison of water and  $\text{Na}_2\text{S}_2\text{O}_3$  OKE spectra. a) Shows the OKE spectrum at 25 °C of  $\text{Na}_2\text{S}_2\text{O}_3:5\text{H}_2\text{O}$  (red) and the calculated spectrum of the corresponding water fraction (blue). It can be seen that the contribution of water to the solution spectrum is minimal. b) Comparison of the  $\text{Na}_2\text{S}_2\text{O}_3:32.7\text{H}_2\text{O}$  OKE spectrum (red) and the calculated spectrum of the corresponding water fraction (blue). Unlike in a), the water contribution is significant.

### 6.3.3. Sodium thiosulfate OKE spectrum

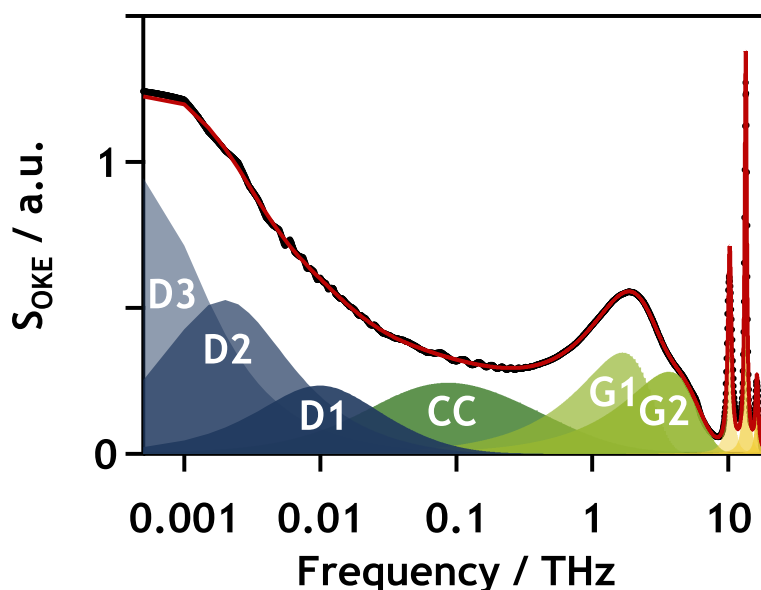


**Figure 6.4.:** OKE spectrum of  $\text{Na}_2\text{S}_2\text{O}_3 \cdot 5\text{H}_2\text{O}$  at 25 °C. Yellow area fills denote Brownian oscillator functions fitted to the vibrations and light green area fills denote anti-symmetrised Gaussian functions fitted to the librations. The dark green area fill denotes the Cole-Cole function fitted to the  $\beta$ -relaxation and the dark blue area fills denote the Debye functions used to fit the  $\alpha$ -relaxation.

The  $\text{Na}_2\text{S}_2\text{O}_3 \cdot 5\text{H}_2\text{O}$  OKE spectra contain negligible water contributions and no contributions from the sodium ion itself. Therefore, their features must be attributed to the thiosulfate ion. Fig. 6.4 shows the spectrum at 25 °C with a broad band below 20 GHz, a tail continuing up to 700 GHz, a moderately broad peak with a shoulder between 700 GHz and 8 THz as well as three sharp peaks above 8 THz. Sharp, high-frequency peaks like these originate from exciting vibrational modes of the molecule in question. The Raman spectrum of the thiosulfate ion is known<sup>[227,228]</sup> and the vibrations can be assigned to the S-O-S rock, S-S stretch, and the S-O asymmetric bend as shown in Table 6.1. The vibrational modes were found to be concentration independent both in this study and in the literature.<sup>[228]</sup> Further vibrational modes can be found above 20 THz, such as the S-O symmetric bend as well as the S-O symmetric and asymmetric stretch, but were not within the measurement range of this study.

**Table 6.1.:** Vibrational modes of the thiocyanate ion below 20 THz.

	OKE	Literature
S-O-S rock / THz	10.24	10.10 <sup>[228]</sup> , 10.04 <sup>[227]</sup>
S-S stretch / THz	13.43	13.43 <sup>[228]</sup> , 13.37 <sup>[227]</sup>
S-O asymmetric bend / THz	16.24	16.22 <sup>[227]</sup>

The peak with a shoulder around 2 THz is expected to arise from the librations

of the thiosulfate anion, with two distinct frequencies indicating two distinct types of motions or environments. For the thiosulfate ion, only one librational frequency is expected from symmetry considerations, as the rotation around the long axis does not lead to a change, while the rotations around the two shorter axes are degenerate. Therefore, it is likely that there are two distinct environments in the solution, which is a possible indicator for clusters. It was fitted using two anti-symmetrised Gaussian functions **G1** and **G2** for the peak at 2 THz and the shoulder at 4 THz, respectively. Below this, the  $\beta$ -relaxation, consisting of cage-rattling and cage diffusion motions, can be found and was fitted using a Cole-Cole function (**CC**). The lowest frequency contributions are expected to arise from the rotational relaxation of the thiosulfate ions, also called  $\alpha$ -relaxation, and were fitted with several Debye-functions (**D1**, **D2**, **D3**) where possible, otherwise they were fitted with a Cole-Davidson function. Since the  $\alpha$ -relaxation signifies the breakdown of structure in the sample it is expected to follow a Debye-function, indicative of an exponential decay in the time domain. A non-Debye shape, such as a Cole-Davidson function or one caused by a superposition of Debye functions, signifies the gradual decay of long-lived structures over time. A superposition of Debye functions, specifically, can be interpreted as a distribution of relaxation times. The OKE rotational relaxation time  $\tau_{rot} = \frac{1}{6D_{rot}}$  is often linked<sup>[9,224]</sup> to the particle volume through the SED relation (Section 1.1.1, Eq. 1.5). From Eq. 1.5 it can be seen that a distribution of relaxation times can be linked to a distribution of particle volumes and as such can be used to probe the size of clusters in solutions. Values for the temperature-dependent viscosity of  $\text{Na}_2\text{S}_2\text{O}_3$  solutions can be found in the literature.<sup>[229-231]</sup> The volume of the diffusing particle from OKE measurements can then be approximated<sup>[111,232]</sup> using

$$V = \frac{k_B T \tau_{rot}}{\eta}. \quad (6.1)$$

Fig. 6.5 shows temperature-dependent OKE spectra of a  $\text{Na}_2\text{S}_2\text{O}_3 \cdot 5\text{H}_2\text{O}$  solution, in which the spectra at -25 and 0 °C were scaled to the 16.2 THz bend mode. The cryostat used to measure these spectra introduces additional intensity losses into the set-up, leading to a lower overall intensity in the frequency spectrum. This was corrected by scaling to the bend mode, which showed a consistent intensity in the three spectra taken without the cryostat. In Fig. 6.5, it can be seen that the  $\text{Na}_2\text{S}_2\text{O}_3 \cdot 5\text{H}_2\text{O}$  solution exhibits a shift of the  $\alpha$  and  $\beta$ -relaxation to lower frequencies with lower temperatures. This is expected, since the viscosity increases with lower temperatures, making it harder for the particles to move. The librational and vibrational modes, on the other hand, do not show a pronounced shift with temperature. This can be seen more clearly when looking at the temperature dependence of the fit function parameters in Tables C.2

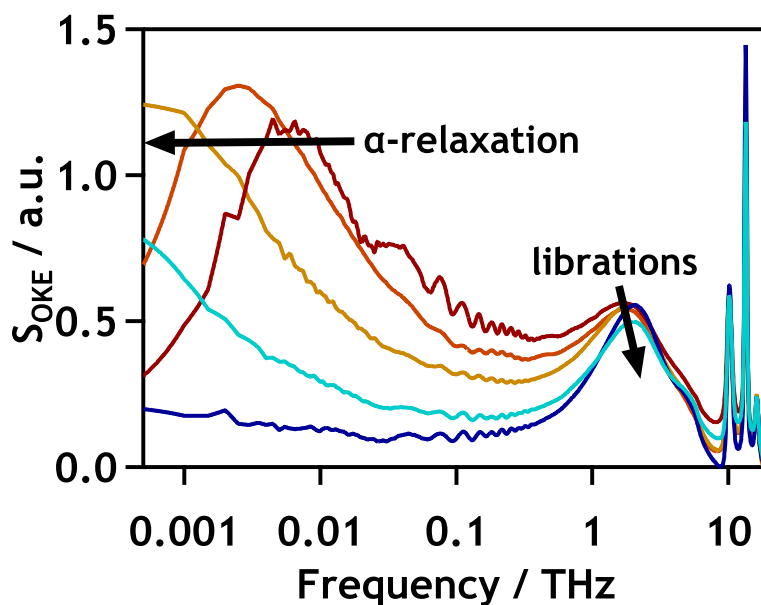
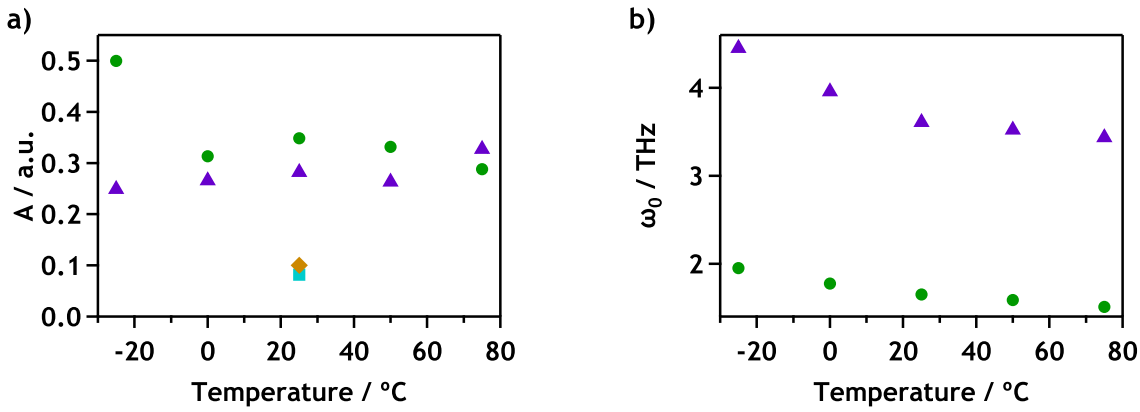


Figure 6.5.: Temperature-dependence of the  $\text{Na}_2\text{S}_2\text{O}_3:5\text{H}_2\text{O}$  OKE spectra from 75 to  $-25$  °C (red to blue in direction of the  $\alpha$ -relaxation arrow). The spectra at  $-25$  and  $0$  °C have been scaled at 16.2 THz because of their intensity loss in the cryostat compared to the other samples.

and C.3. There it can be seen that the vibrational frequencies are constant, with increased amplitudes at higher temperatures. While the librational peak seems to stay in place with temperature, a closer look at the frequencies of **G1** and **G2** (Fig. 6.6b) reveals a slight decrease in frequency with increasing temperature. This behaviour is expected of librations, since the general decrease in density with increasing temperature leads to a shallower intermolecular potential and as such to lower librational frequencies.<sup>[201]</sup> No general trend is seen in the damping parameters and amplitudes (Fig. 6.6a) of the librations, however, only at 75 °C is the amplitude of **G2** larger than that of **G1**. This is curious, as 75 °C is the only measured temperature at which the solution is not supersaturated, or at least very close to it in the case of 50 °C. In the study of eutectic salt solutions (Chapter 5), a similar change in relative amplitudes was found when looking at the concentration dependence of the librational modes belonging to free ions, CIPs, and clusters. This strengthens the hypothesis that one of the librational modes originates from clusters.

The relaxation times  $\tau$  of the  $\alpha$ - and  $\beta$ -relaxation (see Tables C.3 and 6.2) show a decrease in relaxation times with increasing temperature, as expected from the shift seen in Fig. 6.5. Table 6.2 shows the diffusing particle volumes calculated from the relaxation times of the Debye functions using Eq. 6.1 and the viscosity of the sodium thiosulfate solution,  $\eta_{sol}$ . Furthermore, a crude approximation of the expected volume of a  $\text{S}_2\text{O}_3^-$  ion can be made using the density ( $1.69 \text{ g cm}^{-3}$ ) and molar mass ( $158.108 \text{ g mol}^{-1}$ ) of the anhydrous crystal, which yields a



**Figure 6.6.:** Change in the Na<sub>2</sub>S<sub>2</sub>O<sub>3</sub>:5H<sub>2</sub>O librations with temperature. Shown are the a) amplitudes and b) centre frequencies of G1 and G2. Green circles denote the lower frequency libration G1 while purple triangles denote the higher frequency shoulder G2. For comparison, the amplitudes for G1 (cyan squares) and G2 (orange diamonds) of Na<sub>2</sub>S<sub>2</sub>O<sub>3</sub>:32.7H<sub>2</sub>O are included in a). It can be seen that, compared to the temperatures between -25 and 50 °C, the relative height of the amplitudes is switched for both for the dilute solution and 75 °C, which are not supersaturated.

volume of 147 Å<sup>3</sup>, assuming a volume of 8 Å<sup>3</sup> for the sodium cations. When comparing this approximation with the values found in Table 6.2, it becomes clear that the volumes calculated from the rotational diffusion are far too small. For the D3 relaxation times, only one value is above the approximated value, with the others in the same order of magnitude. Volumes calculated for D2 are smaller by a factor of 3 to 5 while those for D1 differ by at least an order of magnitude. Even using ion radii<sup>[139]</sup> of 1.21 Å for oxygen as well as 0.12 Å and 1.84 Å for sulfur and assuming a spherical ion with a tetrahedral conformation according to

$$V = \frac{4\pi}{3}(r_{S,1} + r_{S,2} + r_O * \sin(90^\circ - 54.75^\circ))^3 \quad (6.2)$$

gives an estimate of 79 Å<sup>3</sup>, which is only a factor of 2 smaller than the estimate from the density. This, again, is larger than the volumes calculated from the D1 and D2 relaxation times. Given that a water molecule itself has a volume of roughly 30 Å<sup>3</sup> this cannot be due to overestimating the thiosulfate volume. Therefore, it seems that either SED is not applicable here or the broadening in the rotational relaxation is caused by effects other than clustering. For SED to be applicable the rotational diffusion and the viscosity need to be linked.<sup>[10]</sup> This can be confirmed by comparing the slopes of the concentration or temperature-dependence of the viscosity and the rotational relaxation time. This, however, is not feasible here due to a lack of data. While the viscosity at a given temperature and concentration can be found in the literature<sup>[229-231]</sup>, the rotational relaxation of Na<sub>2</sub>S<sub>2</sub>O<sub>3</sub>:5H<sub>2</sub>O was only fully captured at two temperatures, at both of which the solution is not even supersaturated. Furthermore, only one other concentration, Na<sub>2</sub>S<sub>2</sub>O<sub>3</sub>:32.7H<sub>2</sub>O, was measured at 25 °C.

It is known that the viscosities of mixtures, such as mayonnaise, can be higher than expected from the components, which are mainly oil and water for mayonnaise. This is due to the influence of jamming. For the example of mayonnaise, small droplets oil in the water act similarly to colloidal particles and obstruct the flow of the mixture at a critical droplet concentration.<sup>[233]</sup> This results in the known slow flow of the sauce or, in other words, a high macroscopic viscosity. However, the viscosity on the microscopic level can be considered decoupled from the macroscopic viscosity, as one single oil droplet will still see itself surrounded by water.<sup>[130]</sup> Therefore, considering the possibility of large clusters in the solution, it is sensible to also investigate the rotational relaxation dependence assuming the correct viscosity is that of water,  $\eta_{H_2O}$ . For large clusters, there would also be less doubt about how valid it is to use the SED relation. The SED relation assumes a particle immersed in a homogeneous fluid, and the volume of the particle at which this assumption holds has been placed in the cubic nanometer range.<sup>[10,234]</sup>

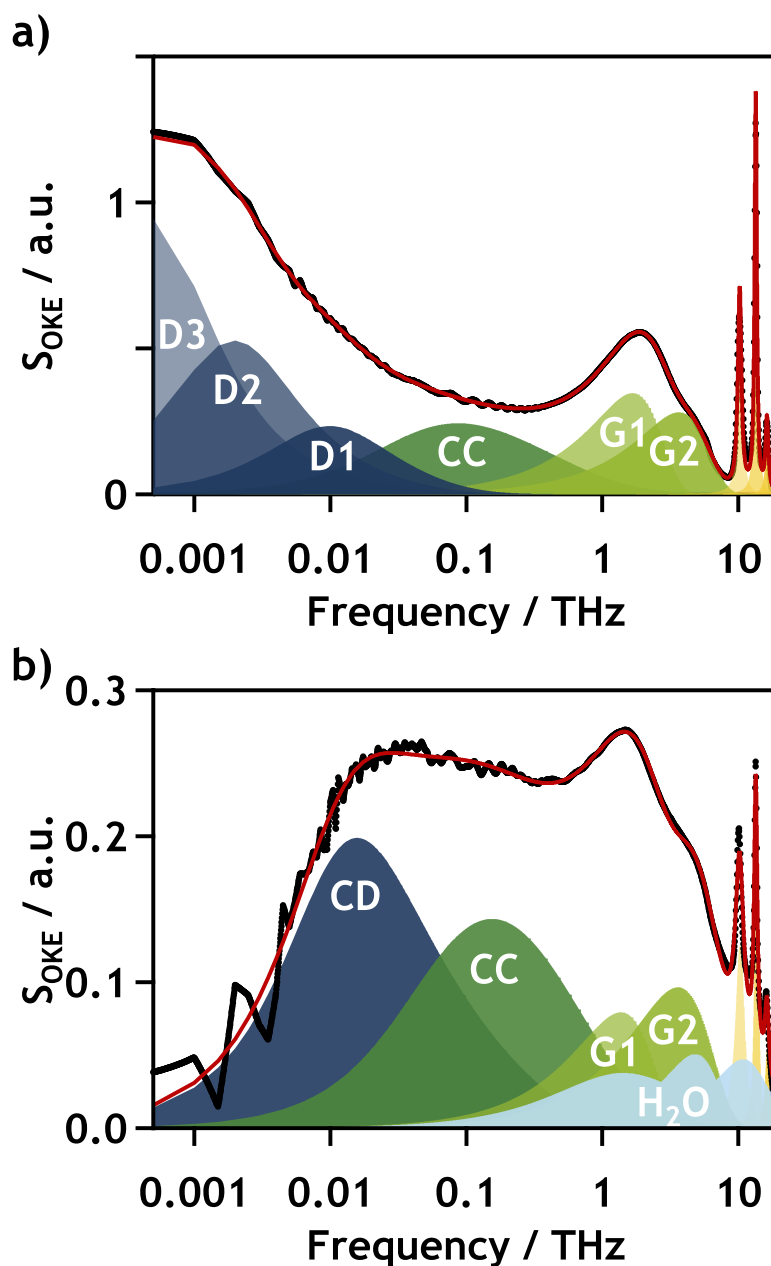
Table 6.2 contrasts the viscosities of water and the (macroscopic) solution at different temperatures, as well as the calculated volumes. First off, a large contrast of up to two orders of magnitude is found between the viscosity of water and the solution. Secondly, it can be seen that the volumes calculated using  $\eta_{H_2O}$  are considerably larger than those calculated with  $\eta_{sol}$ , easily accommodating dimers, trimers and clusters of up to 73 thiosulfate ions. Considering that only 7 thiosulfate ions are needed for a volume in the cubic nanometer range, using the SED relation seems justified. While no monomers were observed, it is feasible that the accompanying rotational relaxation is hidden between the first function of the  $\alpha$ -relaxation (**D1**) and the  $\beta$ -relaxation (**CC**), as only a minimal number of functions was used for the  $\alpha$ -relaxation. Furthermore, the calculated clusters are consistent with both the observation of two librational modes as well as the switch in relative amplitudes between them at 75 °C. At 75 °C, only two Debye functions were needed to fit the  $\alpha$ -relaxation, resulting in cluster sizes centred at dimers and clusters of eighteen ions. Consulting Table 6.2, this is lower than clusters of up to forty or seventy ions found in the supersaturated solutions at 50 °C and 25 °C, respectively. Therefore, it is in line with a highly concentrated, but not supersaturated solution. From the relative height of the librational modes, **G1** is tentatively assigned to clusters, while **G2** is assigned to fully solvated ions. This, again, resembles the results found in the study of eutectic salt solutions (Chapter 5).

Fig. 6.7 compares the spectra of  $\text{Na}_2\text{S}_2\text{O}_3 \cdot 5\text{H}_2\text{O}$  and  $\text{Na}_2\text{S}_2\text{O}_3 \cdot 32.7\text{H}_2\text{O}$  at 25 °C. The first and foremost difference in the spectra lies in the rotational relaxation, which is fully captured in  $\text{Na}_2\text{S}_2\text{O}_3 \cdot 32.7\text{H}_2\text{O}$ . Additionally, due to the reduced

**Table 6.2.: Relaxation times and calculated volumes for  $\text{Na}_2\text{S}_2\text{O}_3 \cdot 5\text{H}_2\text{O}$ .** Included are the viscosities used for the calculations ( $\eta_{\text{H}_2\text{O}}$  and  $\eta_{\text{sol}}$ ) as well as the average number of ions for the clusters based on the viscosity of water,  $n_{\text{H}_2\text{O}}$ .

	-25 °C	0 °C	25 °C	50 °C	75 °C
<b>Viscosities</b>					
$\eta_{\text{H}_2\text{O}}^{[139]} / \text{mPa s}$	-	1.79	0.89	0.55	0.38
$\eta_{\text{sol}}^{[231]} / \text{mPa s}$	36573.25	547.55	70.12	20.72	9.25
<b>CC</b>					
$\tau / \text{ps}$	$44.1 \cdot 10^3$	27.2	20.9	10.2	10.1
<b>D1</b>					
$\tau / \text{ps}$	-	-	99.6	45.4	25.4
$V_{\text{H}_2\text{O}} / \text{\AA}^3$	-	-	460.5	370.6	323.7
$n_{\text{H}_2\text{O}} / \text{\AA}^3$	-	-	3.1	2.5	2.2
$V_{\text{sol}} / \text{\AA}^3$	-	-	5.9	9.8	13.2
<b>D2</b>					
$\tau / \text{ps}$	-	5101.6	510.5	210.0	206.7
$V_{\text{H}_2\text{O}} / \text{\AA}^3$	-	-	2361.1	1714.1	2632.9
$n_{\text{H}_2\text{O}} / \text{\AA}^3$	-	-	16.1	11.7	17.9
$V_{\text{sol}} / \text{\AA}^3$	-	35.1	30.0	45.2	-
<b>D3</b>					
$\tau / \text{ps}$	-	5101.6	2201.9	704.7	206.7
$V_{\text{H}_2\text{O}} / \text{\AA}^3$	-	10741.6	10184.1	5752.9	-
$n_{\text{H}_2\text{O}} / \text{\AA}^3$	-	73.1	69.3	39.1	-
$V_{\text{sol}} / \text{\AA}^3$	-	-	129.3	151.7	107.5

amount of the probe molecule, the intensity of the  $\text{Na}_2\text{S}_2\text{O}_3\cdot 32.7\text{H}_2\text{O}$  spectrum is significantly lower than that of the  $\text{Na}_2\text{S}_2\text{O}_3\cdot 5\text{H}_2\text{O}$  spectrum, meaning that water contributions now cannot be neglected. As such, these were taken into account by scaling the calculated water spectrum at 25 °C with the fraction of water compared to pure water. From the fit parameters (compare Tables C.1 and C.2), it can be seen that the vibrational frequencies were not affected by the concentration change. The librational frequencies, meanwhile, shifted considerably to lower frequencies, more so than was observed in the temperature dependence of  $\text{Na}_2\text{S}_2\text{O}_3\cdot 5\text{H}_2\text{O}$  at higher temperatures.



**Figure 6.7.:** Comparison of the  $\text{Na}_2\text{S}_2\text{O}_3\cdot 5\text{H}_2\text{O}$  and  $\text{Na}_2\text{S}_2\text{O}_3\cdot 32.7\text{H}_2\text{O}$  OKE fits. a) Shown is the fit to the OKE spectrum at 25 °C of  $\text{Na}_2\text{S}_2\text{O}_3\cdot 5\text{H}_2\text{O}$  (red). The colouring is the same as in Fig. 6.4. b) Shown is the fit to the OKE spectrum at 25 °C of  $\text{Na}_2\text{S}_2\text{O}_3\cdot 32.7\text{H}_2\text{O}$  (red). Cyan area fills stand for the water model modes, otherwise the colouring is the same as in Fig. 6.4.

However, while the rotational relaxation band of  $\text{Na}_2\text{S}_2\text{O}_3:32.7\text{H}_2\text{O}$  was fully captured by the measurement, it was hard to separate from other contributions. In  $\text{Na}_2\text{S}_2\text{O}_3:5\text{H}_2\text{O}$ , the rotational relaxation band has about twice the intensity as the librational band and its peak frequency is roughly three orders of magnitude smaller, giving a clear separation between the two bands even on a logarithmic scale. In  $\text{Na}_2\text{S}_2\text{O}_3:32.7\text{H}_2\text{O}$ , meanwhile, the peak frequency is still about two orders of magnitude smaller, but the intensity of the rotational relaxation band is comparable to that of the librational band. Therefore, only the low-frequency slope could be used for fitting the rotational relaxation, making it hard to separate the rotational relaxation,  $\beta$ -relaxation and librations. Due to this uncertainty, it is difficult to draw conclusions about the nature of the broadening in the rotational relaxation. Using SED to calculate the particle volume according to the macroscopic solution viscosity  $\eta_{sol}$  (Table 6.3) gives  $193.5 \text{ \AA}^3$ , comparable to the volume expected for the thiosulfate ion. Using the viscosity of water,  $\eta_{\text{H}_2\text{O}}$ , results in a volume of  $402.4 \text{ \AA}^3$ , which is comparable to the expected volume of trimers. This is in line with the smallest volumes calculated for the supersaturated solution assuming the viscosity of water (compare Table 6.3).

While there is still no definite proof the SED relation is valid for the system, the overall agreement of the data with the calculated results when the viscosity of water is used justifies the assumption. Specifically for  $\text{Na}_2\text{S}_2\text{O}_3:32.7\text{H}_2\text{O}$ , a distribution of small aggregates centred around trimers and including monomers fits the extrapolation of the trend observed in  $\text{Na}_2\text{S}_2\text{O}_3:5\text{H}_2\text{O}$  at  $75 \text{ }^\circ\text{C}$ , which is highly concentrated but below supersaturation. Furthermore, the existence of two librational modes of the thiosulfate anion implies the existence of clusters, because symmetry considerations only yield one libration for the free ion, as discussed beforehand. The second librational mode must therefore be connected to the solution. Using the viscosity of the solution,  $\eta_{sol}$ , yield volumes below or corresponding to monomers, which does not explain the second librational mode nor the observed broadened rotational relaxation shape. On the other hand, calculations using the viscosity of water,  $\eta_{\text{H}_2\text{O}}$ , result in a distribution of volumes ranging from dimers to clusters of about seventy ions. The different rotational relaxation times of the clusters explain the broadening and the clusters also present a different environment, which explains the second librational mode. While it could be argued that the contribution of water to the  $\text{Na}_2\text{S}_2\text{O}_3:32.7\text{H}_2\text{O}$  spectrum was not properly calculated, it is not possible to fit the spectrum with only one thiocyanate librational mode without destroying the relation between the different water modes. Therefore, it is highly likely that the two distinct librations are observed even in dilute solutions. This is also in line with the consistent shape of the librations observed at different concentrations. Additionally, the relative height of the librational amplitude is the same

**Table 6.3.: Relaxation times and calculated volumes at 25 °C for Na<sub>2</sub>S<sub>2</sub>O<sub>3</sub>:5H<sub>2</sub>O and Na<sub>2</sub>S<sub>2</sub>O<sub>3</sub>:32.7H<sub>2</sub>O.** Included are the viscosities used for the calculations ( $\eta_{H_2O}$  and  $\eta_{sol}$ ) as well as the average number of ions for the clusters based on the viscosity of water,  $n_{H_2O}$ .

	Na <sub>2</sub> S <sub>2</sub> O <sub>3</sub> :5H <sub>2</sub> O	Na <sub>2</sub> S <sub>2</sub> O <sub>3</sub> :32.7H <sub>2</sub> O
<b>Viscosities</b>		
$\eta_{H_2O}$ <sup>[139]</sup> / mPa s	0.89	0.89
$\eta_{sol}$ / mPa s	70.12 <sup>[231]</sup>	1.85 <sup>[229]</sup>
<b>CC</b>		
$\tau$ / ps	20.9	9.3
<b>D1 and CD</b>		
$\tau$ / ps	99.6	87.0
$V_{H_2O}$ / Å <sup>3</sup>	460.5	402.4
$n_{H_2O}$ / Å <sup>3</sup>	3.1	2.7
$V_{sol}$ / Å <sup>3</sup>	5.9	-
<b>D2</b>		
$\tau$ / ps	510.5	-
$V_{H_2O}$ / Å <sup>3</sup>	2361.1	-
$n_{H_2O}$ / Å <sup>3</sup>	16.1	-
$V_{sol}$ / Å <sup>3</sup>	30.0	-
<b>D3 and CD</b>		
$\tau$ / ps	2201.9	87.0
$V_{H_2O}$ / Å <sup>3</sup>	10184.1	-
$n_{H_2O}$ / Å <sup>3</sup>	69.3	-
$V_{sol}$ / Å <sup>3</sup>	129.3	193.5

for the  $\text{Na}_2\text{S}_2\text{O}_3\cdot 32.7\text{H}_2\text{O}$  spectrum and the  $\text{Na}_2\text{S}_2\text{O}_3\cdot 5\text{H}_2\text{O}$  spectrum at 75 °C, again strengthening the assignment to clusters and fully solvated ions.

## 6.4. Conclusions

With the presented data it is difficult to be certain whether the SED relation is applicable or not. This can be verified by comparing the concentration or temperature-dependent slopes of the rotational relaxation times and the viscosity. However, additional data would need to be taken with smaller temperature or concentration steps. As the rotational relaxation is difficult to separate from other contributions at a water to thiosulfate ratio of 1:33, higher ratios of thiosulfate would be necessary for this. The concentration dependence would not only help to judge the validity of SED in the system, but also help identify differences in the behaviour of a supersaturated solution. For the supersaturated solution, the temperature range would be restricted to between 25 °C and 50 °C in sodium thiosulfate pentahydrate, making temperature steps of 5 °C or even 2 °C necessary. This range is based on the 8 ns maximum delay time of our instruments, which allows measuring frequencies down to 125 MHz. Considering that at 25 °C the sodium thiosulfate pentahydrate rotational relaxation looks to be cut off around the peak maximum with a low-frequency limit of 500 MHz, it is unlikely that the rotational relaxation could be adequately captured at lower temperatures even with a 125 MHz limit. Further information could be gleaned by improving the data treatment. First off, subtracting spectral contributions of water and therefore reducing the OKE spectra to the pure thiosulfate contributions would reduce the number of variables in the system. Considering the magnitude of the water contributions, however, this would be a small improvement. A more important step is to include the time domain data into the fitting of the spectra. Due to the characteristic time scales and slopes associated with the relaxation processes, this would make it easier to separate the contributions of the  $\alpha$ - and  $\beta$ -relaxation.

All in all, the data are consistent with the presence of clusters if non-Newtonian effects are taken into account and therefore the viscosity of the surrounding water is used for the calculation. The strong increase in the macroscopic viscosity of the solution, which leads to very small volumes in the analysis of the data using the SED expression, can be understood as the result of jamming by the clusters. Then, distributions of increasingly large clusters can be seen at lower temperatures, which is equal to moving to higher supersaturation. While no direct rotational relaxation was observed for the monomers, it could easily be hidden

between the fastest  $\alpha$ -relaxational mode and the Cole-Cole function describing the  $\beta$ -relaxation. It is possible that the improvements to the data treatment discussed above can clarify this issue. The observed cluster sizes range from dimers and trimers to clusters of 73 ions, which have volumes in the nanometer range. The presence of small aggregates even in dilute solution is in accordance with the two observed librational modes in all spectra, which switch their relative amplitudes when going (distinctly) below supersaturated concentrations. In accordance with observations in eutectic salt solutions (see Chapter 5), which had more supporting data, the lower frequency librational mode is assigned to clusters and the higher frequency librational mode is assigned to fully solvated ions. The observed clusters are stable on a scale from hundreds of picoseconds to nanoseconds, which makes it debatable whether they fall under the strict definition of PNCs as outlined previously in Section 6.1. Nonetheless, they are long-lived clusters which are not nuclei, as evidenced by the solution not crystallising. This is not due to lack of observation time, as similar solutions were found to crystallise (see Section 6.3.1). Therefore, long-lived clusters with a wide distribution of sizes were observed spectroscopically in supersaturated sodium thiosulfate solutions.



# Appendices



## A. Ionic liquids

Table A.1.: Averaged and total scans per IL.

IL	scans averaged	scans total
Tetrabutylammonium chloride	101	157
Tetrabutylammonium bromide	114	162
Tributylmethylammonium chloride	53	68
Tributylmethylammonium bromide	45	78
Tributylammonium chloride	220	256
Tributylammonium bromide	94	153

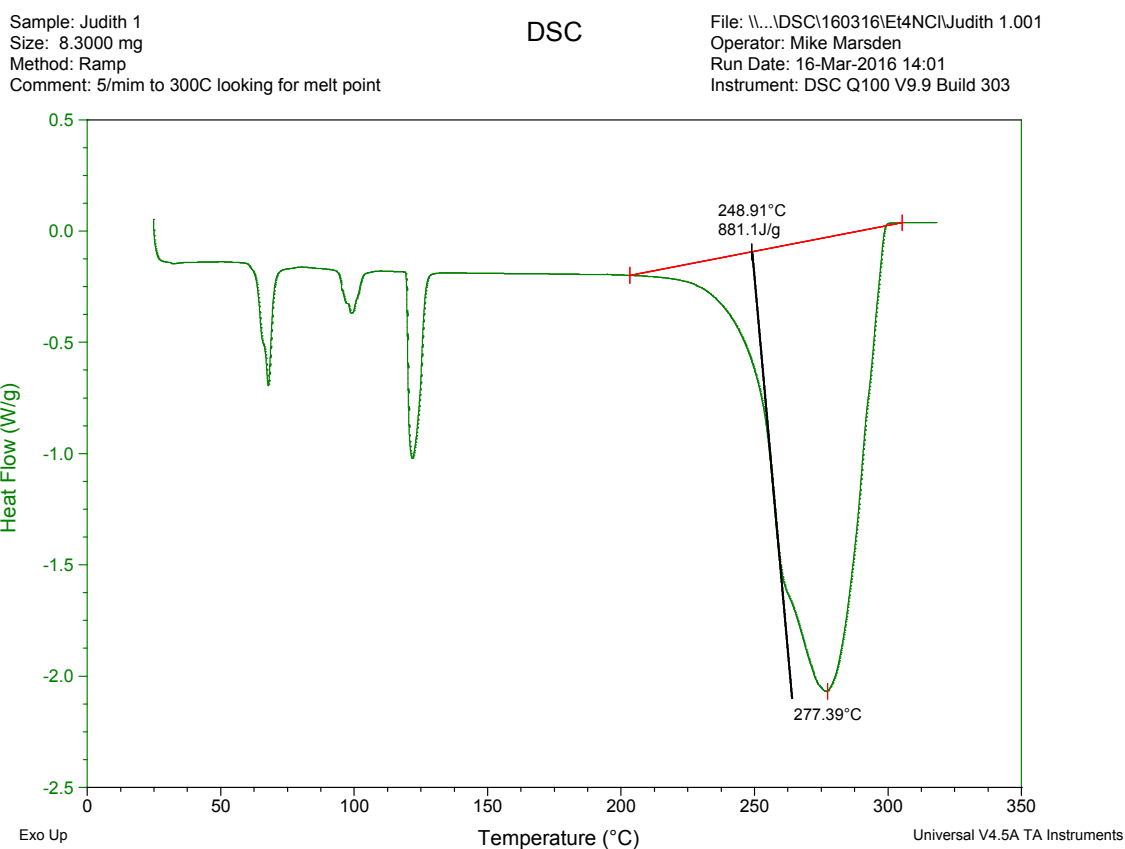


Figure A.1.: DSC measurement of tetraethylammonium chloride.

## A.1. Synthesis

**Tributylammonium bromide:** Following the procedure of Hojo et al.,<sup>[235]</sup> 1 equivalent of a 10 vol-% aqueous solution of hydrogen bromide (48% w/w, Lancaster) in methanol ( $\geq 99.7\%$ , Sigma-Aldrich) was added under stirring to 1 equivalent of tributylamine ( $\geq 99.5\%$ , Sigma-Aldrich) at room temperature and kept stirring for 30 minutes. The excess solvent was evaporated to dryness at below 50 °C in a rotary evaporator with a saturated aqueous potassium carbonate trap, which gave a yellow salt. This was recrystallized from hot methanol, filtered and then washed with cold diethyl ether ( $\geq 99.8\%$ , Sigma-Aldrich), giving a pale yellow solid. The yield was 88% and the purity was determined by <sup>1</sup>H-NMR to be  $\geq 95\%$ .

<sup>1</sup>H-NMR (400 MHz, DMSO-*d*<sub>6</sub>)  $\delta$  8.99 (1 H, br s), 3.03 (6 H, dt, *J* = 12.1 Hz, 4.8 Hz), 1.63 - 1.55 (6 H, m), 1.32 (6 H, tq, *J* = 7.4 Hz, 7.4 Hz), 0.92 (9 H, t, *J* = 7.3 Hz)

HRMS (ESI) exact mass calculated for C<sub>12</sub>H<sub>28</sub>N [M]<sup>+</sup> *m/z* 186.2216, found *m/z* 186.2213. Microanalysis calculated for C<sub>12</sub>H<sub>28</sub>NBr: C, 54.13; H, 10.60; N, 5.26. Found: C, 54.16; H, 10.65; N, 5.32.

**Tributylammonium chloride:** Following the procedure of Fumino et al.,<sup>[63]</sup> 1 M hydrogen chloride in diethyl ether (Sigma Aldrich) was added to tributylamine ( $\geq 99.5\%$ , Sigma Aldrich) while cooling to 0 °C. After maintaining for 30 min at 0 °C, volatile components were removed by rotary evaporation, affording the ammonium chloride salt in quantitative yield. The purity was determined by <sup>1</sup>H-NMR to be  $\geq 95\%$ .

<sup>1</sup>H-NMR (500 MHz, DMSO-*d*<sub>6</sub>)  $\delta$  10.70 (1 H, br s), 2.96 (6 H, dt, *J* = 12.4 Hz, 4.8 Hz), 1.67 - 1.60 (6 H, m), 1.30 (6 H, tq, *J* = 7.5 Hz, 7.5 Hz), 0.90 (9 H, t, *J* = 7.4 Hz)

HRMS (ESI) exact mass calculated for C<sub>12</sub>H<sub>28</sub>N [M]<sup>+</sup> *m/z* 186.2216, found *m/z* 186.2213. Microanalysis calculated for C<sub>12</sub>H<sub>28</sub>NCl: C, 64.98; H, 12.72; N, 6.31. Found: C, 64.49; H, 12.67; N, 6.44.

**Tetraethylammonium chloride:** The white crystalline salt tetraethylammonium chloride was prepared by the reaction of triethylamine with chloroethane in a pressure vessel at 70 °C overnight (the synthesis was adapted from the synthesis of 1-ethyl-3-methylimidazolium chloride).<sup>[236]</sup>

**Triethylammonium chloride:** The white crystalline salt tetraethylammonium chloride was prepared by the reaction of diethylamine with chloroethane in a pressure vessel at 70 °C overnight (the synthesis was adapted from the synthesis of 1-ethyl-3-methylimidazolium chloride).<sup>[236]</sup>

**Triethylmethylammonium chloride:** The white crystalline salt triethylmethylammonium chloride was successfully prepared by the reaction of triethylamine with chloromethane in a pressure vessel at 70 °C overnight (the synthesis was adapted from the synthesis of 1-ethyl-3-methylimidazolium chloride).<sup>[236]</sup>

## A.2. Time domain data

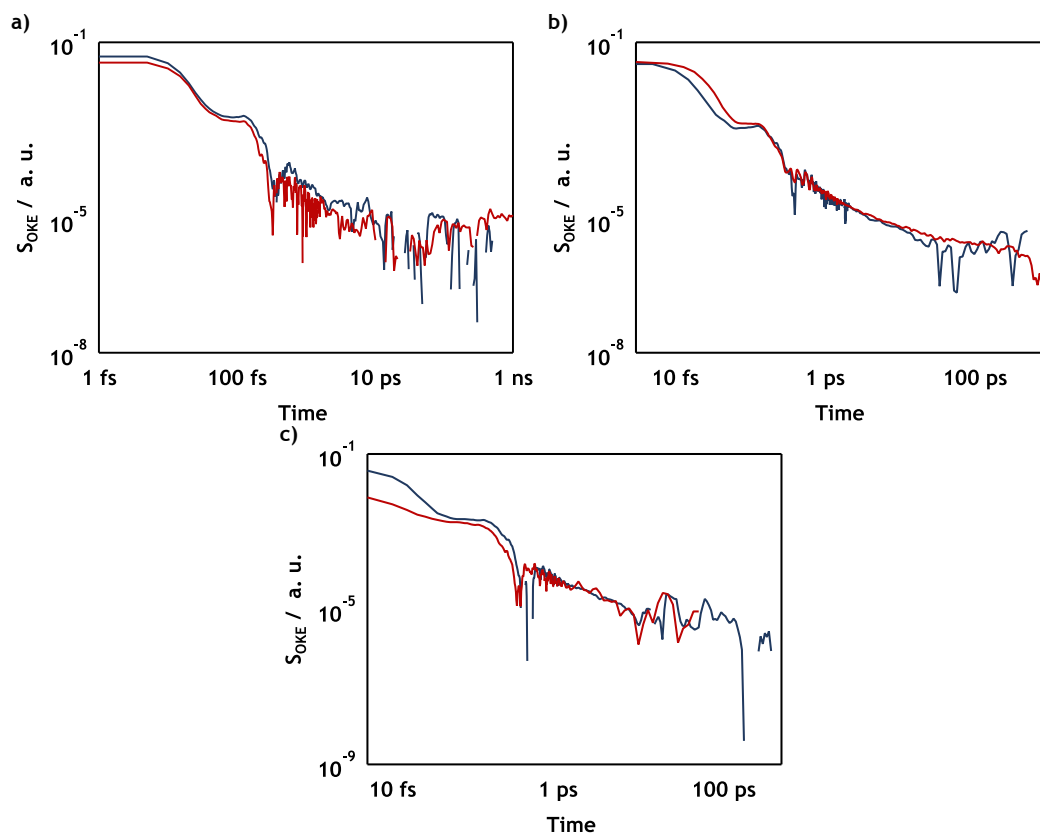


**Figure A.2.:** OKE time domain data on a log-log scale. Shown are a) tetrabutylammonium, b) tributylmethylammonium and c) tributylammonium chloride (red) and bromide (blue).



## B. Eutectic salt solutions

### B.1. Fit parameters

Table B.1.: Linear fit parameters for the temperature dependence of the LiSCN:5.8H<sub>2</sub>O OKE S population fraction.

Mode	Population <sub>0</sub> / %	Slope
S	0.20 ± 0.05	0.00027 ± 0.0002

Table B.2.: Linear fit parameters for the temperature dependence of the LiSCN:5.8H<sub>2</sub>O OKE frequencies. The main band of the librations was averaged over M1, M2 and M3, weighted by their population fraction at the temperature.

Mode	f <sub>0</sub> / THz	Slope
M1, M2, M3 average	2.56 ± 0.09	-0.0039 ± 0.0004
S	4.61 ± 0.08	-0.0025 ± 0.0004

Table B.3.: OKE fit parameters for the LiSCN:12H<sub>2</sub>O solution.

	A / a.u.	ω <sub>0</sub> / THz	γ / THz		
<b>Anti-symmetrised Gaussians</b>					
M1	0.39	1.29	1.26		
S	0.20	3.04	2.70		
<b>Havriliak-Negami</b>					
	A / a.u.	τ / ps	Γ <sub>Rise</sub> / THz	α	β
β	0.44	2.67	1.20	1.00	1.00
α	6.68	67.80	0.15	1.00	0.22



## B.2. Time domain data

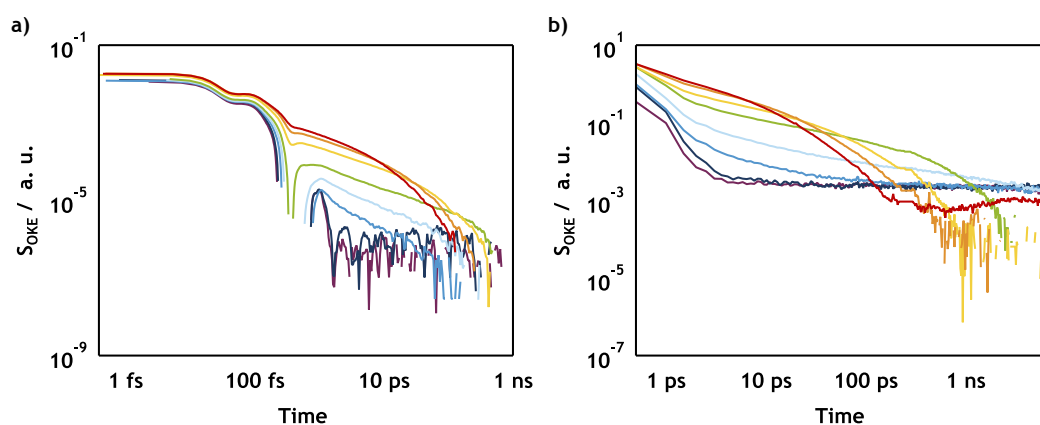


Figure B.1.: Temperature-dependent OKE time domain data of LiSCN:5.8H<sub>2</sub>O on a log-log scale. Shown are the a) high time-resolution and b) long delay measurements between 90 and 300 K (purple to red).

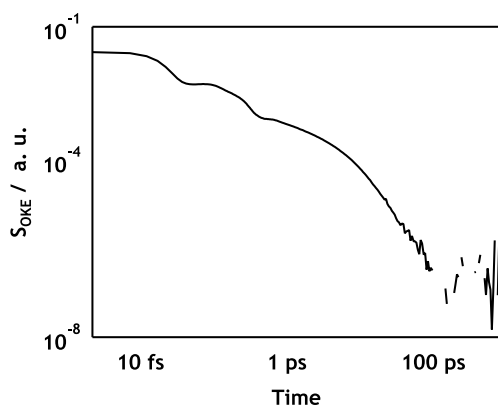


Figure B.2.: OKE time domain data of LiSCN:12H<sub>2</sub>O on a log-log scale.



## C. Supersaturated sodium thiosulfate solutions

### C.1. Crystal structures

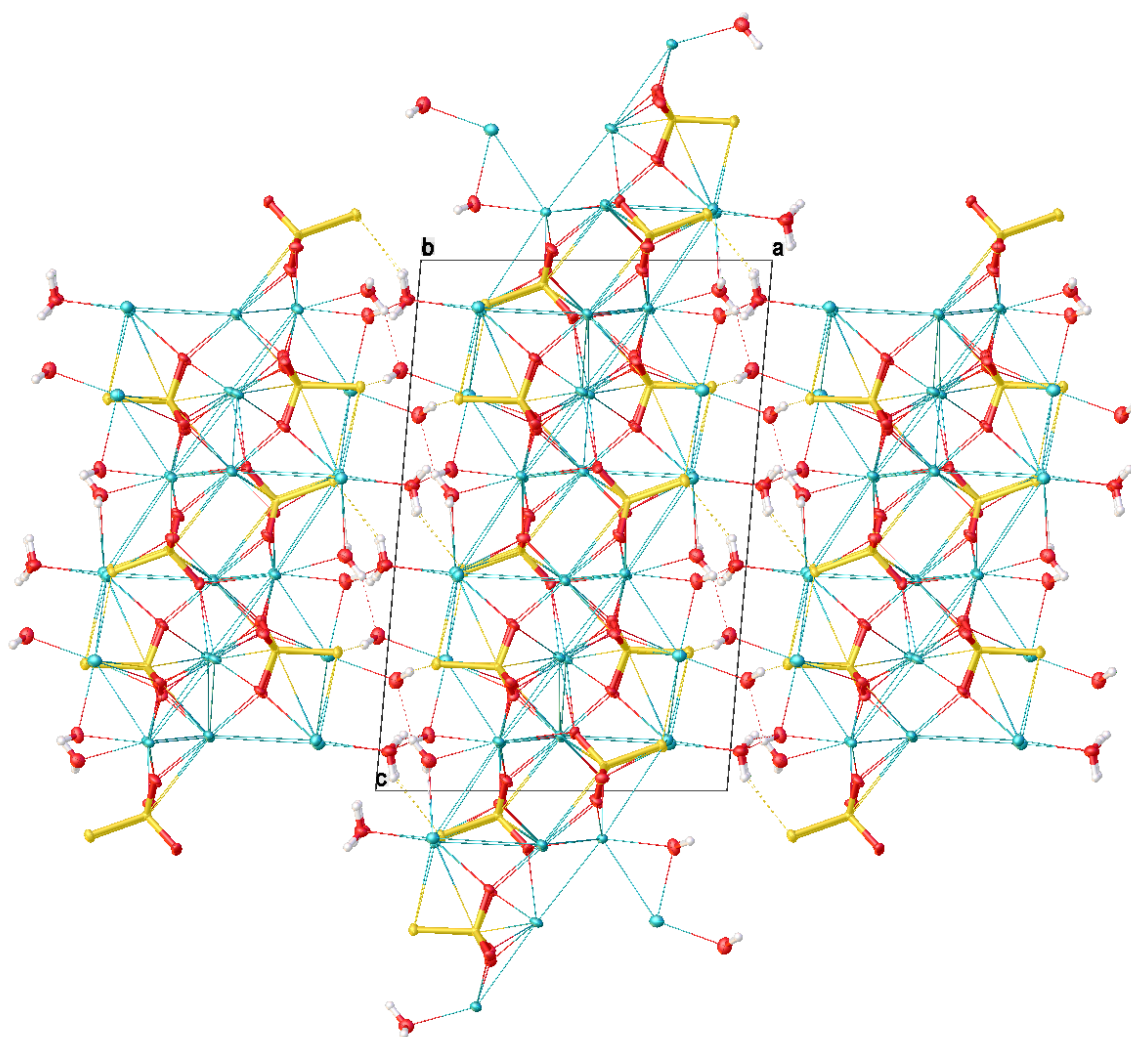
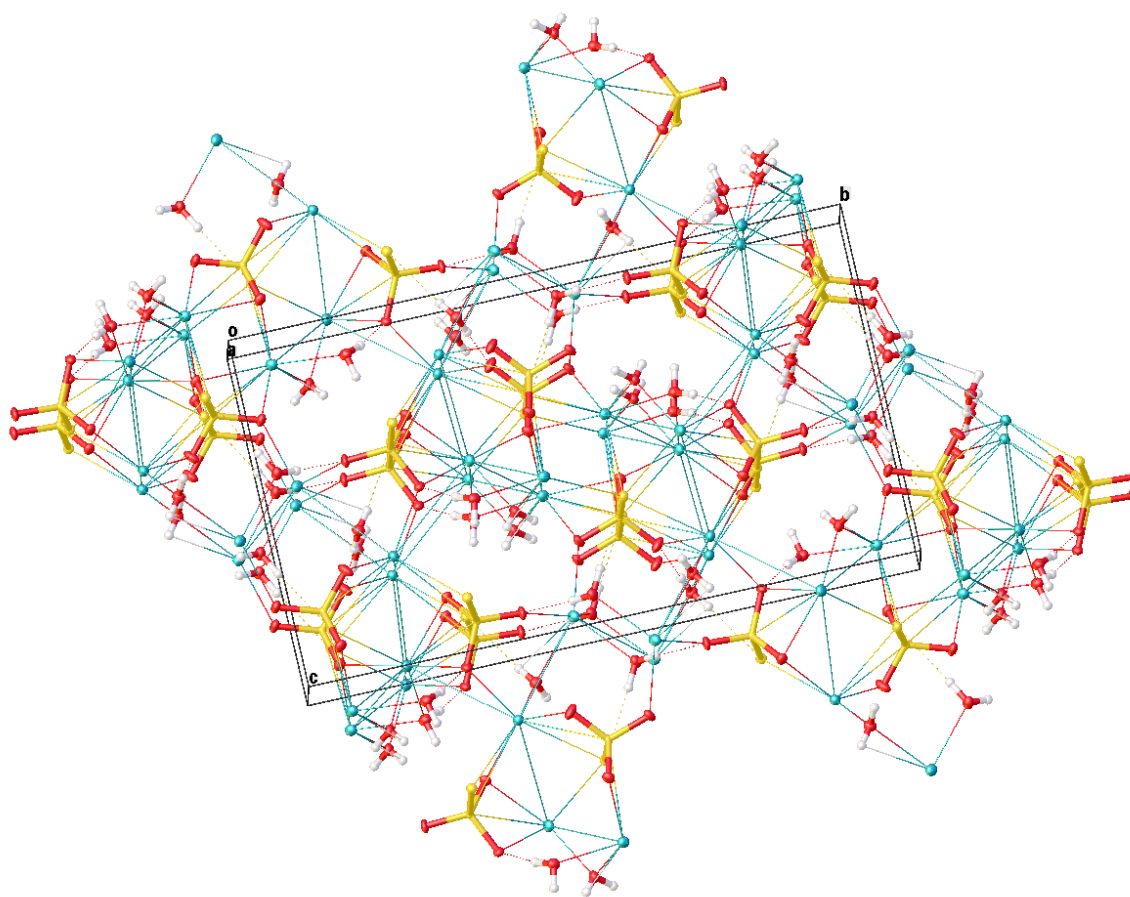


Figure C.1.: Crystal structure for the  $\text{Na}_2\text{S}_2\text{O}_3 \cdot 1.25\text{H}_2\text{O}$  monoclinic prisms. The colours are white for hydrogen, red for oxygen, yellow for sulfur and cyan for sodium.



**Figure C.2.:** Crystal structure for the  $\text{Na}_2\text{S}_2\text{O}_3 \cdot 2\text{H}_2\text{O}$  monoclinic rods. The colours are white for hydrogen, red for oxygen, yellow for sulfur and cyan for sodium.

## C.2. Fit parameters

Table C.1.: Temperature dependent fit for the OKE spectra of  $\text{Na}_2\text{S}_2\text{O}_3 \cdot 32.7\text{H}_2\text{O}$ .

	$A$ / a.u.	$\omega_0$ / THz	$\gamma$ / THz			
<b>Gaussians</b>						
$\text{TA}_{\text{H}_2\text{O}}$	0.057	0.76	1.74			
$\text{LA}_{\text{H}_2\text{O}}$	0.051	4.77	3.03			
<b>G1</b>	0.082	1.30	1.38			
<b>G2</b>	0.10	3.34	3.74			
<b>Brownians</b>						
$\text{lib}_{\text{H}_2\text{O}}$	0.047	12.57	6.81			
$\text{rock}_{\text{S-O-S}}$	0.021	10.24	0.85			
$\text{stretch}_{\text{S-S}}$	0.012	13.43	0.42			
$\text{bend}_{\text{S-O,as}}$	0.0043	16.24	0.66			

	$A$ / a.u.	$\tau$ / ps	$\Gamma_{\text{Rise}}$ / THz	$\Gamma_{\text{Decay}}$ / THz	$\alpha$	$\beta$
<b>Havriliak-Negami</b>						
$\text{CC}_{\text{H}_2\text{O}}$	0.086	0.7	10.0	0.0	0.94	1
<b>CC</b>	0.65	9.3	1	0.03	0.65	1
<b>CD</b>	0.48	87.0	0.5	0.0	1	0.67

Table C.2.: Temperature dependent fit for the OKE spectra of  $\text{Na}_2\text{S}_2\text{O}_3 \cdot 5\text{H}_2\text{O}$ . Shown are the parameters for the anti-symmetrised Gaussian and Brownian oscillator functions.

	-25 °C	0 °C	25 °C	50 °C	75 °C
<b>Gaussians</b>					
<b>G1</b>					
$A$ / a.u.	0.26	0.19	0.35	0.33	0.29
$\omega_0$ / THz	1.95	1.78	1.65	1.59	1.51
$\gamma$ / THz	1.35	1.34	1.41	1.45	1.43
<b>G2</b>					
$A$ / a.u.	0.13	0.16	0.28	0.26	0.33
$\omega_0$ / THz	4.45	3.96	3.61	3.52	3.44
$\gamma$ / THz	1.88	3.07	3.02	2.99	3.48
<b>Brownians</b>					
<b>rock<sub>s-o-s</sub></b>					
$A$ / a.u.	0.025	0.038	0.051	0.047	0.080
$\omega_0$ / THz	10.24	10.24	10.24	10.24	10.24
$\gamma$ / THz	0.37	0.54	0.37	0.37	0.76
<b>stretch<sub>s-s</sub></b>					
$A$ / a.u.	0.035	0.038	0.060	0.054	0.056
$\omega_0$ / THz	13.43	13.43	13.43	13.43	13.43
$\gamma$ / THz	0.30	0.035	0.30	0.30	0.36
<b>bend<sub>s-o,as</sub></b>					
$A$ / a.u.	0.0070	0.011	0.015	0.014	0.016
$\omega_0$ / THz	16.24	16.24	16.24	16.24	16.24
$\gamma$ / THz	0.47	0.64	0.47	0.47	0.58

**Table C.3.:** Temperature dependent fit for the OKE spectra of  $\text{Na}_2\text{S}_2\text{O}_3 \cdot 5\text{H}_2\text{O}$ . Shown are the parameters for the Havriliak-Negami functions.

	-25 °C	0 °C	25 °C	50 °C	75 °C
<b>CC</b>					
$A$ / a.u.	1.12	0.45	1.09	1.20	1.57
$\tau$ / ps	$44.1 \times 10^3$	27.2	20.9	10.2	10.1
$\Gamma_{\text{Rise}}$ / THz	1.0	1.0	1.0	1.0	1.0
$\Gamma_{\text{Decay}}$ / THz	0.0	0.0005	0.02	0.03	0.03
$\alpha$	0.28	0.42	0.67	0.70	0.66
$\beta$	1	1	1	1	1
<b>D1</b>					
$A$ / a.u.	-	-	0.48	0.53	0.59
$\tau$ / ps	-	-	99.6	45.4	25.4
$\Gamma_{\text{Rise}}$ / THz	-	-	0.1	0.1	0.1
$\Gamma_{\text{Decay}}$ / THz	-	-	0.0	0.0	0.0
$\alpha$	-	-	1	1	1
$\beta$	-	-	1	1	1
<b>D2</b>					
$A$ / a.u.	-	1.32	1.06	1.24	-
$\tau$ / ps	-	5101.6	510.5	210.0	-
$\Gamma_{\text{Rise}}$ / THz	-	0.1	0.1	0.1	-
$\Gamma_{\text{Decay}}$ / THz	-	0.0	0.0	0.0	-
$\alpha$	-	1	1	1	-
$\beta$	-	0.56	1	1	-
<b>D3</b>					
$A$ / a.u.	-	-	1.90	1.67	2.16
$\tau$ / ps	-	-	2201.9	704.7	206.7
$\Gamma_{\text{Rise}}$ / THz	-	-	0.1	0.1	0.1
$\Gamma_{\text{Decay}}$ / THz	-	-	0.0	0.0	0.0
$\alpha$	-	-	1	1	1
$\beta$	-	-	1	1	1

### C.3. Time domain data

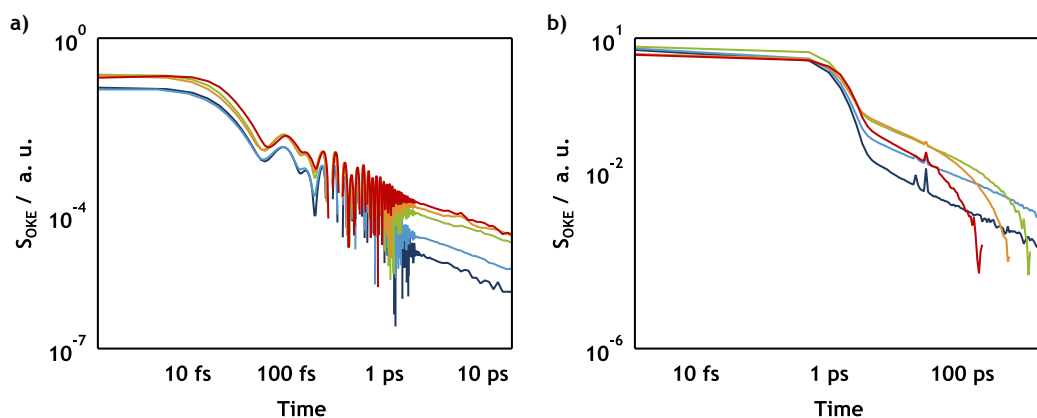


Figure C.3.: Temperature-dependent OKE time domain data of  $\text{Na}_2\text{S}_2\text{O}_3:5\text{H}_2\text{O}$  on a log-log scale. Shown are the a) high time-resolution and b) long delay measurements at  $-25\text{ }^\circ\text{C}$  (dark blue),  $0\text{ }^\circ\text{C}$  (light blue),  $25\text{ }^\circ\text{C}$  (green),  $50\text{ }^\circ\text{C}$  (orange) and  $75\text{ }^\circ\text{C}$  (red).

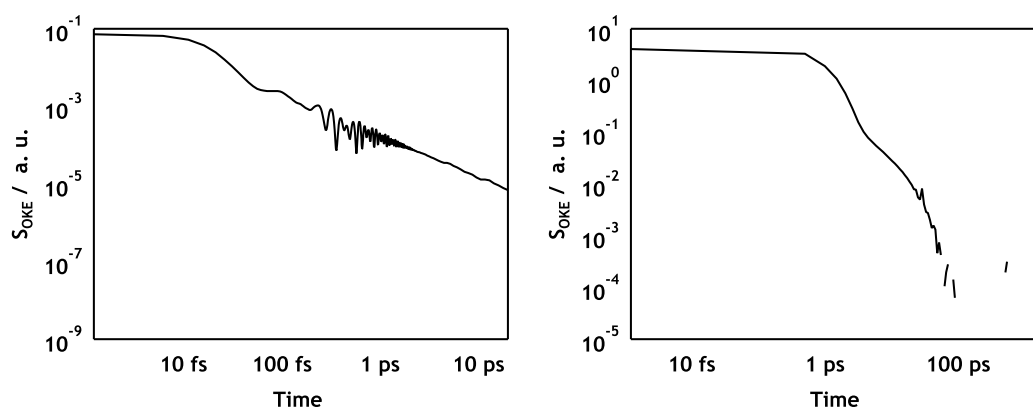


Figure C.4.: Temperature-dependent OKE time domain data of  $\text{Na}_2\text{S}_2\text{O}_3:32.7\text{H}_2\text{O}$  on a log-log scale. Shown are the a) high time-resolution and b) long delay measurements at  $25\text{ }^\circ\text{C}$ .

## D. Water model

The water model<sup>[12]</sup> used in Chapters 5 and 6 was described by

$$S(\omega, T) = w * (ASG_{TA}(\omega, T) + ASG_{LA}(\omega, T) + B_L(\omega) + H_{\alpha,1}(\omega, T)) \quad (D.1)$$

with  $w$  the weight fraction of water and  $T$  the temperature in K.  $ASG_{TA}$ ,  $ASG_{LA}$ ,  $B_L$  as well as  $H_{\alpha,1}$  are fit functions for OKE spectra as described in Section 3.2.  $ASG_{TA}$  and  $ASG_{LA}$  model the TA and LA phonon modes of water while  $B_L$  models the librational mode and  $H_{\alpha,1}$  the  $\beta$ -relaxation.

**Table D.1.:** Parameters for the OKE water model.  $ASG_{TA}$  and  $ASG_{LA}$  are the anti-symmetrised Gaussian functions used to model the TA and LA modes of water.  $BO_L$  is the Brownian oscillator function used to model the libration of water and  $H_{\alpha,1}$  is the Cole-Cole function used to model the translational relaxation.  $T$  is the temperature in K.

$ASG_{TA}$	
$A$ / a.u.	$-0.00040021 * T + 0.19160499$
$\omega_0$ / THz	$0.00075089309 * T + .53811094443$
$\gamma$ / THz	$0.00054012797 * T + 1.58205066089$
$ASG_{LA}$	
$A$ / a.u.	$-0.00021445 * T + 0.12822384$
$\omega_0$ / THz	$-0.00741815273 * T + 6.98590754919$
$\gamma$ / THz	$0.00209423323 * T + 2.40851739305$
$BO_L$	
$A$ / a.u.	0.06
$\omega_0$ / THz	12.5749
$\gamma$ / THz	6.8052
$H_{\alpha,1}$	
$A$ / a.u.	$0.00022993 * T + 0.04045736$
$\tau$ / ps	$103.64949140 * e^{-0.01689466 * T}$
$\alpha$	0.924
$beta$	1.000



## References

- [1] Becker, R.; Döring, W. *Ann. Phys.* **1935**, *24*, 719.
- [2] Volmer, M.; Weber, A. *Z. Phys. Chem.* **1926**, *119*, 277.
- [3] Farkas, L. *Z. Phys. Chem.* **1927**, *125*, 236.
- [4] Gibbs, J. W. *Trans. Conn. Acad. Arts Sci.* **1876**, *3*, 108.
- [5] Jones, R. A. L. *Soft Condensed Matter*; Oxford University Press: Oxford, 2002.
- [6] Atkins, P.; de Paula, J. *Physical Chemistry*, 9th ed.; Oxford University Press: Oxford, 2010.
- [7] Ohsaku, M.; Shiro, Y.; Murata, H. *Bull. Chem. Soc. Jpn.* **1972**, *45*, 954.
- [8] Lin-Vien, D.; Colthup, N. B.; Fateley, W. G.; Grasselli, J. G. *The Handbook of Infrared and Raman Characteristic Frequencies of Organic Molecules*; Academic Press: San Diego, 1991.
- [9] Hunt, N. T.; Jaye, A. A.; Meech, S. R. *Phys. Chem. Chem. Phys.* **2007**, *9*, 2167.
- [10] Turton, D. A.; Wynne, K. *J. Phys. Chem. B* **2014**, *118*, 4600.
- [11] Srivastava, G. P. *The Physics of Phonons*; Hilger: Bristol, 1990.
- [12] González-Jiménez, M.; Ramakrishnan, G.; Harwood, T.; Laphorn, A.; Kelly, S.; Ellis, E.; Wynne, K. *Nat. Commun.* **2016**, *7*, 11799.
- [13] Kossevich, A. M. *The Crystal Lattice: Phonons, Solitons, Dislocations*; WILEY-VCH Verlag GmbH: Weinheim, 1999.
- [14] Freemantle, M. *An Introduction to Ionic Liquids*; The Royal Society of Chemistry: Cambridge, 2009.

- [15] Plechkova, N. V.; Seddon, K. R. *Chem. Soc. Rev.* **2008**, *37*, 123.
- [16] Seddon, K. R.; Stark, A.; Torres, M.-J. *Pure Appl. Chem.* **2000**, *72*, 2275.
- [17] Coker, T. G.; Ambrose, J.; Janz, G. J. *J. Am. Chem. Soc.* **1970**, *92*, 5293.
- [18] Burns, J. A.; Verrall, R. E. *Thermochim. Acta* **1974**, *9*, 277.
- [19] Shim, J. J.; Kim, D.; Choon, S. R. *Bull. Korean Chem. Soc.* **2006**, *27*, 744.
- [20] McMichael, K. D.; Clement, R. A. *J. Org. Chem.* **1961**, *26*, 620.
- [21] Stern, H.; Bufalini, B. Y. J. *J. Am. Chem. Soc.* **1961**, *1*, 4362.
- [22] Elias, H.; Strecker, H. *Chem. Ber.* **1966**, *99*, 1019.
- [23] Holbrey, J. D.; Rogers, R. D. In *Ionic Liquids in Synthesis*, 2nd ed.; Wasserscheid, P., Welton, T., Eds.; Wiley-VCH: Weinheim, 2008.
- [24] Earle, M. J.; Esperanca, J. M. S. S.; Gilea, M. A.; Canongia Lopes, J. N.; Rebelo, L. P. N.; Magee, J. W.; Seddon, K. R.; Widegren, J. A. *Nature* **2006**, *439*, 831.
- [25] Walden, P. *Bull. Acad. Imper. Sci. St. Petersburg.* **1914**, *8*, 405.
- [26] Seddon, K. R. *J. Chem. Technol. Biotechnol.* **1997**, *68*, 351.
- [27] Freemantle, M. *Chem. Eng. News Arch.* **1998**, *76*, 32.
- [28] Matthias, M.; Klemens, M.; Klaus, H.; Ralf, N.; Michael, B.; Wolfgang, S.; Veit, S.; Miguel, F.; Oliver, H.; Michael, B. Method for the separation of acids from chemical reaction mixtures by means of ionic fluids. 2003.
- [29] Bukowski, M.; Endres, F.; Hempelmann, R.; Natter, H. Procedure for the electrochemical deposition of metals, alloys and semiconductors from ionic liquids and low melting salt mixtures. 2002.
- [30] Tempel, D. J.; Henderson, P. B.; Brzozowski, J. R.; Pearlstein, R.; Garg, D. Ionic liquid based mixtures for gas storage and delivery. 2006.
- [31] Tempel, D. J.; Henderson, P. B.; Brzozowski, J. R. Ionic liquid based mixtures for gas storage and delivery. 2006.

- [32] Adler, R.; Mayer, H. Procedure for lubricating and/or cooling a compressor by using ionic liquids. 2006.
- [33] Greaves, T. L.; Drummond, C. J. *Chem. Rev.* **2008**, *108*, 206.
- [34] Hallett, J. P.; Welton, T. *Chem. Rev.* **2011**, *111*, 3508.
- [35] Pârvulescu, V. I.; Hardacre, C. *Chem. Rev.* **2007**, *107*, 2615.
- [36] Angell, C. A.; Byrne, N.; Belieres, J. P. *Acc. Chem. Res.* **2007**, *40*, 1228.
- [37] Armand, M.; Endres, F.; MacFarlane, D. R.; Ohno, H.; Scrosati, B. *Nat. Mater.* **2009**, *8*, 621.
- [38] MacFarlane, D. R.; Tachikawa, N.; Forsyth, M.; Pringle, J. M.; Howlett, P. C.; Elliott, G. D.; Davis, J. H.; Watanabe, M.; Simon, P.; Angell, C. A. *Energy Environ. Sci.* **2014**, *7*, 232.
- [39] Zhang, S.; Ueno, K.; Dokko, K.; Watanabe, M. *Adv. Energy Mater.* **2015**, *5*, 1.
- [40] Hayes, R.; Warr, G. G.; Atkin, R. *Chem. Rev.* **2015**, *115*, 6357.
- [41] Zhang, S.; Zhang, Q.; Zhang, Y.; Chen, Z.; Watanabe, M.; Deng, Y. *Prog. Mater. Sci.* **2016**, *77*, 80.
- [42] Bernal, J. D. *Proc. R. Soc. London. Ser. A. Math. Phys. Sci.* **1964**, *280*, 299.
- [43] Headen, T. F.; Howard, C. A.; Skipper, N. T.; Wilkinson, M. A.; Bowron, D. T.; Soper, A. K. *J. Am. Chem. Soc.* **2010**, *132*, 5735.
- [44] Head-Gordon, T.; Hura, G. *Chem. Rev.* **2002**, *102*, 2651.
- [45] Paesani, F.; Voth, G. A. *J. Phys. Chem. B* **2009**, *113*, 5702.
- [46] Weingärtner, H. *Angew. Chem. Int. Ed* **2008**, *47*, 654.
- [47] Weingärtner, H. *Curr. Opin. Colloid Interface Sci.* **2013**, *18*, 183.
- [48] Daguenet, C.; Dyson, P. J.; Krossing, I.; Oleinikova, A.; Slattery, J.; Wakai, C.; Weingärtner, H. *J. Phys. Chem. B* **2006**, *110*, 12682.

- [49] Weingärtner, H.; Sasisanker, P.; Daguene, C.; Dyson, P. J.; Krossing, I.; Slattery, J. M.; Schubert, T. *J. Phys. Chem. B* **2007**, *111*, 4775.
- [50] Turton, D. A.; Sonnleitner, T.; Ortner, A.; Walther, M.; Hefter, G.; Seddon, K. R.; Stana, S.; Plechkova, N. V.; Buchner, R.; Wynne, K. *Faraday Discuss.* **2012**, *154*, 145.
- [51] Sonnleitner, T.; Turton, D. A.; Waselikowski, S.; Hunger, J.; Stoppa, A.; Walther, M.; Wynne, K.; Buchner, R. *J. Mol. Liq.* **2014**, *192*, 19.
- [52] Sonnleitner, T.; Turton, D. A.; Hefter, G.; Ortner, A.; Waselikowski, S.; Walther, M.; Wynne, K.; Buchner, R. *J. Phys. Chem. B* **2015**, *119*, 8826.
- [53] Zhao, W.; Leroy, F.; Heggen, B.; Zahn, S.; Kirchner, B.; Balasubramanian, S.; Müller-Plathe, F. *J. Am. Chem. Soc.* **2009**, *131*, 15825.
- [54] Kohagen, M.; Brehm, M.; Thar, J.; Zhao, W.; Müller-Plathe, F.; Kirchner, B. *J. Phys. Chem. B* **2011**, *115*, 693.
- [55] Leal, J. P.; Esperança, J. M. S. S.; Minas, M. E.; Lopes, J. N. C.; Rebelo, L. P. N.; Seddon, K. R. *J. Phys. Chem. A* **2007**, *111*, 6176.
- [56] Gozzo, F. C.; Santos, L. S.; Augusti, R.; Consorti, C. S.; Dupont, J.; Eberlin, M. N. *Chem. - A Eur. J.* **2004**, *10*, 6187.
- [57] Dorbritz, S.; Ruth, W.; Kragl, U. *Adv. Synth. Catal.* **2005**, *347*, 1273.
- [58] Bini, R.; Bortolini, O.; Chiappe, C.; Pieraccini, D.; Siciliano, T. *J. Phys. Chem. B* **2007**, *111*, 598.
- [59] Ludwig, R. *J. Phys. Chem. B* **2009**, *113*, 15419.
- [60] Fumino, K.; Wulf, A.; Ludwig, R. *Angew. Chem. Int. Ed.* **2009**, *48*, 3184.
- [61] Roth, C.; Peppel, T.; Fumino, K.; Köckerling, M.; Ludwig, R. *Angew. Chem. Int. Ed.* **2010**, *49*, 10221.
- [62] Fumino, K.; Peppel, T.; Geppert-Rybczynska, M.; Zaitsau, D. H.; Lehmann, J. K.; Verevkin, S. P.; Kockerling, M.; Ludwig, R. *Phys. Chem. Chem. Phys.* **2011**, *13*, 14064.
- [63] Fumino, K.; Reichert, E.; Wittler, K.; Hempelmann, R.; Ludwig, R. *Angew. Chem. Int. Ed.* **2012**, *51*, 6236.

- [64] Fumino, K.; Fossog, V.; Wittler, K.; Hempelmann, R.; Ludwig, R. *Angew. Chem. Int. Ed.* **2013**, *52*, 2368.
- [65] Bodo, E.; Mangialardo, S.; Ramondo, F.; Ceccacci, F.; Postorino, P. *J. Phys. Chem. B* **2012**, *116*, 13878.
- [66] Fannin, A. A.; King, L. A.; Levisky, J. A.; Wilkes, J. S. *J. Phys. Chem.* **1984**, *88*, 2609.
- [67] Wilkes, J. S.; Hussey, C. L.; Sanders, J. R. *Polyhedron* **1986**, *5*, 1567.
- [68] Hussey, C. L.; Sun, I.; Strubinger, S. K. D.; Barnard, P. A. *J. Electrochem. Soc.* **1990**, *137*, 2515.
- [69] Noda, A.; Hayamizu, K.; Watanabe, M. *J. Phys. Chem. B* **2001**, *105*, 4603.
- [70] Shimizu, K.; Pádua, A. A.; Canongia Lopes, J. N. *J. Phys. Chem. B* **2010**, *114*, 15635.
- [71] Shimizu, K.; Costa Gomes, M. F.; Pádua, A. A.; Rebelo, L. P.; Canongia Lopes, J. N. *Theochem* **2010**, *946*, 70.
- [72] Hardacre, C.; Holbrey, J. D.; McMath, S. E. J.; Bowron, D. T.; Soper, A. K. *J. Chem. Phys.* **2002**, *118*, 273.
- [73] Hardacre, C.; Holbrey, J. D.; Nieuwenhuyzen, M.; Youngs, T. G. A. *Acc. Chem. Res.* **2007**, *40*, 1146.
- [74] Hardacre, C.; Holbrey, J. D.; Mullan, C. L.; Youngs, T. G. A.; Bowron, D. T. *J. Chem. Phys.* **2010**, *133*, 74510.
- [75] Hayes, R.; Imberti, S.; Warr, G. G.; Atkin, R. *J. Phys. Chem. C* **2014**, *118*, 13998.
- [76] Triolo, A.; Russina, O.; Fazio, B.; Appetecchi, G. B.; Carewska, M.; Passerini, S. *J. Chem. Phys.* **2009**, *130*, 164521.
- [77] Russina, O.; Triolo, A.; Gontrani, L.; Caminiti, R.; Xiao, D.; Hines Jr, L. G.; Bartsch, R. A.; Quitevis, E. L.; Pleckhova, N.; Seddon, K. R. *J. Phys. Condens. Matter* **2009**, *21*, 424121.
- [78] Pott, T.; Meleard, P. *Phys. Chem. Chem. Phys.* **2009**, *11*, 5469.

- [79] Santos, C. S.; Annapureddy, H. V. R.; Murthy, N. S.; Kashyap, H. K.; Castner, E. W.; Margulis, C. J. *J. Chem. Phys.* **2011**, *134*, 064501.
- [80] Urahata, S. M.; Ribeiro, M. C. C. *J. Chem. Phys.* **2004**, *120*, 1855.
- [81] Wang, Y.; Voth, G. A. *J. Am. Chem. Soc.* **2005**, *127*, 12192.
- [82] Wang, Y.; Voth, G. A. *J. Phys. Chem. B* **2006**, *110*, 18601.
- [83] Lima, T. A.; Paschoal, V. H.; Faria, L. F. O.; Ribeiro, M. C. C.; Giles, C. J. *Chem. Phys.* **2016**, *144*, 224504.
- [84] Angell, C. A.; Ansari, Y.; Zhao, Z. *Faraday Discuss.* **2012**, *154*, 9.
- [85] Kerr, J. *Philos. Mag.* **1875**, *50*, 337.
- [86] Kerr, J. *Philos. Mag.* **1875**, *50*, 446.
- [87] Pockels, F. C. A. *Abh. Königl. Ges. Wiss. Göttingen* **1894**, *39*, 1.
- [88] Mayer, G.; Gires, F. C. *R. Acad. Sci.* **1964**, *258*, 2039.
- [89] Maker, P. D.; Terhune, R. W.; Savage, C. M. *Phys. Rev. Lett.* **1964**, *12*, 507.
- [90] Righini, R. *Science* **1993**, *262*, 1386.
- [91] Smith, N. A.; Meech, S. R. *Int. Rev. Phys. Chem.* **2002**, *21*, 75.
- [92] Gauglitz, G., Moore, D. S., Eds. *Handbook of Spectroscopy*, 2nd ed.; Wiley-VCH Verlag GmbH: Weinheim, 2014.
- [93] Larkin, P. B. *Infrared and Raman Spectroscopy*; Elsevier: Oxford, 2011.
- [94] Levine, I. N. *Molecular Spectroscopy*; John Wiley & Sons, Inc.: New York, 1975.
- [95] Ball, D. W. *Field Guide to Spectroscopy*; SPIE Press: Bellingham, Washington, 2006.
- [96] Röntgen, W. C. *Sonderabdruck aus den Sitzungsberichten der Würzburg. Phys. Gesellschaft*; Stahel'sche K. Hof- und Universitätsbuch- und Kunsthandlung: Würzburg, 1895.
- [97] Stribeck, N. *X-ray Scattering of Soft Matter*; Springer-Verlag: Berlin, 2007.

- [98] Sivia, D. *Elementary Scattering Theory*; Oxford University Press: Oxford, 2011.
- [99] Hecht, J. *Understanding Lasers : An Entry-Level Guide*, 2nd ed.; IEEE Press: New York, 1994.
- [100] Reid, G. D.; Wynne, K. In *Encyclopedia of Analytical Chemistry*; Meyers, R. A., Ed.; John Wiley & Sons Ltd: Chichester, 2000.
- [101] Turton, D. A.; Senn, H. M.; Harwood, T.; Laphorn, A. J.; Ellis, E. M.; Wynne, K. *Nat. Commun.* **2014**, *5*, 3999.
- [102] *Mathematica* 11. 2017.
- [103] Barbara, P. F.; Jarzeba, W. *Advances in Photochemistry*; John Wiley & Sons, Inc., 1990.
- [104] Kinoshita, S.; Kai, Y.; Ariyoshi, T.; Shimada, Y. *Int. J. Mod. Phys. B* **1996**, *10*, 1229.
- [105] Cho, M.; Du, M.; Scherer, N. F.; Fleming, G. R.; Mukamel, S. *J. Chem. Phys.* **1993**, *99*, 2410.
- [106] Giraud, G.; Wynne, K. *J. Chem. Phys.* **2003**, *119*, 11753.
- [107] McMorrow, D. *Opt. Commun.* **1991**, *86*, 236.
- [108] Nymand, T. M.; Rønne, C.; Keiding, S. R. *J. Chem. Phys.* **2001**, *114*, 5246.
- [109] Berne, B. J.; Harp, G. D. In *Advances in Chemical Physics*; Prigogine, I., Rice, S. A., Eds.; John Wiley & Sons, Inc.: Hoboken, NJ, 1970; Vol. 17.
- [110] Kindt, J. T.; Schmuttenmaer, C. A. *J. Chem. Phys.* **1997**, *106*, 4389.
- [111] Turton, D. A.; Wynne, K. *J. Chem. Phys.* **2008**, *128*, 154516.
- [112] McMorrow, D.; Lotshaw, W. T. *Chem. Phys. Lett.* **1993**, *201*, 369.
- [113] Bouzón Capelo, S.; Méndez-Morales, T.; Carrete, J.; López Lago, E.; Vila, J.; Cabeza, O.; Rodríguez, J. R.; Turmine, M.; Varela, L. M. *J. Phys. Chem. B* **2012**, *116*, 11302.
- [114] Govinda, V.; Vasantha, T.; Khan, I.; Venkatesu, P. *Ind. Eng. Chem. Res.* **2015**, *54*, 9013.

- [115] Xu, Y.; Chen, B.; Qian, W.; Li, H. *J. Chem. Thermodyn.* **2013**, *58*, 449.
- [116] Birch, J. R.; Nicol, E. A. *Infrared Phys.* **1984**, *24*, 573.
- [117] Salzer, H. E. *Math. Tables Other Aids to Comput.* **1951**, *5*, 67.
- [118] Smiglak, M.; Pringle, J.; Lu, X.; Han, L.; Zhang, S.; Gao, H.; MacFarlane, D.; Rogers, R. *Chem. Commun.* **2014**, *50*, 9228.
- [119] Buffeteau, T.; Grondin, J.; Danten, Y.; Lassègues, J. C. *J. Phys. Chem. B* **2010**, *114*, 7587.
- [120] Grondin, J.; Lassègues, J. C.; Cavagnat, D.; Buffeteau, T.; Johansson, P.; Holomb, R. *J. Raman Spectrosc.* **2011**, *42*, 733.
- [121] Wulf, A.; Fumino, K.; Ludwig, R. *Angew. Chem. Int. Ed.* **2010**, *49*, 449.
- [122] Yamada, T.; Tominari, Y.; Tanaka, S.; Mizuno, M. *J. Phys. Chem. B* **2015**, *119*, 15696.
- [123] Xiao, D.; Rajian, J. R.; Cady, A.; Li, S.; Bartsch, R. A.; Quitevis, E. L. *J. Phys. Chem. B* **2007**, *111*, 4669.
- [124] Turton, D. A.; Hunger, J.; Stoppa, A.; Hefter, G.; Thoman, A.; Walther, M.; Buchner, R.; Wynne, K. *J. Am. Chem. Soc.* **2009**, *131*, 11140.
- [125] Xiao, D.; Hines, L. G.; Holtz, M. W.; Song, K.; Bartsch, R. A.; Quitevis, E. L. *Chem. Phys. Lett.* **2010**, *497*, 37.
- [126] Shiota, H.; Kakinuma, S. *J. Phys. Chem. B* **2015**, *119*, 9835.
- [127] Castner, E. W.; Wishart, J. F. *J. Chem. Phys.* **2010**, *132*, 120901.
- [128] Fumino, K.; Reimann, S.; Ludwig, R. *Phys. Chem. Chem. Phys.* **2014**, *16*, 21903.
- [129] Turton, D. A.; Wynne, K. *J. Chem. Phys.* **2009**, *131*, 201101.
- [130] Turton, D. A.; Hunger, J.; Hefter, G.; Buchner, R.; Wynne, K. *J. Chem. Phys.* **2008**, *128*, 161102.
- [131] Reichenbach, J.; Ruddell, S. A.; González-Jiménez, M.; Lemes, J.; Turton, D. A.; France, D. J.; Wynne, K. *J. Am. Chem. Soc.* **2017**, *139*, 7160.

- [132] Kobler, H.; Munz, R.; Al Gasser, G.; Simchen, G. *Justus Liebigs Ann. Chem.* **1978**, 1937.
- [133] Grovenstein, J., E.; Blanchard, J., E. P.; Gordon, D. A.; Stevenson, R. W. *J. Am. Chem. Soc.* **1959**, *81*, 4842.
- [134] Frisch, M. J.; Trucks, G. W.; Schlegel, H. B.; Scuseria, G. E.; Robb, M. A.; Cheeseman, J. R.; Scalmani, G.; Barone, V.; Mennucci, B.; Petersson, G. A.; Nakatsuji, H.; Caricato, M.; Li, X.; Hratchian, H. P.; Izmaylov, A. F.; Bloino, J.; Zheng, G.; Sonnenberg, J. L.; Hada, M.; Ehara, M.; Toyota, K.; Fukuda, R.; Hasegawa, J.; Ishida, M.; Nakajima, T.; Honda, Y.; Kitao, O.; Nakai, H.; Vreven, T.; J. A. Montgomery, J.; Peralta, J. E.; Ogliaro, F.; Bearpark, M.; Heyd, J. J.; Brothers, E.; Kudin, K. N.; Staroverov, V. N.; Keith, T.; Kobayashi, R.; Normand, J.; Raghavachari, K.; Rendell, A.; Burant, J. C.; Iyengar, S. S.; Tomasi, J.; Cossi, M.; Rega, N.; Millam, J. M.; Klene, M.; Knox, J. E.; Cross, J. B.; Bakken, V.; Adamo, C.; Jaramillo, J.; Gomperts, R.; Stratmann, R. E.; Yazyev, O.; Austin, A. J.; Cammi, R.; Pomelli, C.; Ochterski, J. W.; Martin, R. L.; Morokuma, K.; Zakrzewski, V. G.; Voth, G. A.; Salvador, P.; Dannenberg, J. J.; Dapprich, S.; Daniels, A. D.; Farkas, O.; Foresman, J. B.; Ortiz, J. V.; Cioslowski, J.; Fox, D. J. *Gaussian 09*, Revision D.01. 2013.
- [135] *OPUS*. 2012.
- [136] *LabVIEW 2011 SP1*. 2012.
- [137] Anderson, H. L. *A Physicist's Desk Reference*, 2nd ed.; American Institute of Physics: New York, 1989; p 202.
- [138] Barron, L. D. *Molecular Light Scattering and Optical Activity*, 2nd ed.; Cambridge University Press: Cambridge, 2009.
- [139] Lide, D. R., Haynes, W. M., Eds. *CRC Handbook of Chemistry and Physics*, 90th ed.; CRC Press/Taylor and Francis: Boca Raton, FL, 2009.
- [140] Bender, J. S.; Coasne, B.; Fourkas, J. T. *J. Phys. Chem. B* **2015**, *119*, 9345.
- [141] Murphy, W. F. *J. Chem. Phys.* **1977**, *67*, 5877.
- [142] Fecko, C. J.; Eaves, J. D.; Tokmakoff, A. *J. Chem. Phys.* **2002**, *117*, 1139.

- [143] Li, H.; Zhao, G.; Liu, F.; Zhang, S. *J. Chem. Eng. Data* **2013**, *58*, 1505.
- [144] Kittel, C. *Introduction to Solid State Physics*, 8th ed.; John Wiley & Sons, Inc.: Hoboken, NJ, 2005.
- [145] Mondal, A.; Balasubramanian, S. *J. Phys. Chem. A* **2015**, *119*, 1994.
- [146] Fumino, K.; Ludwig, R. *J. Mol. Liq.* **2014**, *192*, 94.
- [147] Wendler, K.; Brehm, M.; Malberg, F.; Kirchner, B.; Delle Site, L. *J. Chem. Theory Comput.* **2012**, *8*, 1570.
- [148] Speedy, R. J.; Angell, C. A. *J. Chem. Phys.* **1976**, *65*, 851.
- [149] Angell, C. A.; Sichina, W. J.; Oguni, M. *J. Phys. Chem.* **1982**, *86*, 998.
- [150] Huang, C.; Weiss, T. M.; Nordlund, D.; Wikfeldt, K. T.; Pettersson, L. G. M.; Nilsson, A. *J. Chem. Phys.* **2010**, *133*, 134504.
- [151] Mason, B. J. *Adv. Phys.* **1958**, *7*, 221.
- [152] Pettersson, L. G. M.; Henchman, R. H.; Nilsson, A. *Chem. Rev.* **2016**, *116*, 7459.
- [153] Gallo, P.; Amann-Winkel, K.; Angell, C. A.; Anisimov, M. A.; Caupin, F.; Chakravarty, C.; Lascaris, E.; Loerting, T.; Panagiotopoulos, A. Z.; Russo, J.; Sellberg, J. A.; Stanley, H. E.; Tanaka, H.; Vega, C.; Xu, L.; Pettersson, L. G. M. *Chem. Rev.* **2016**, *116*, 7463.
- [154] Speedy, R. J. *J. Phys. Chem.* **1982**, *86*, 982.
- [155] Poole, P. H.; Sciortino, F.; Essmann, U.; Stanley, H. E. *Nature* **1992**, *360*, 324.
- [156] Poole, P. H.; Sciortino, F.; Grande, T.; Stanley, H. E.; Angell, C. A. *Phys. Rev. Lett.* **1994**, *73*, 1632.
- [157] Sastry, S.; Debenedetti, P. G.; Sciortino, F.; Stanley, H. E. *Phys. Rev. E* **1996**, *53*, 6144.
- [158] Xu, L.; Kumar, P.; Buldyrev, S. V.; Chen, S.-H.; Poole, P. H.; Sciortino, F.; Stanley, H. E. *Proc. Natl. Acad. Sci. U.S.A.* **2005**, *102*, 16558.
- [159] Sivakumar, T. C.; Rice, S. A. *J. Chem. Phys.* **1978**, *69*, 3468.

- [160] Mishima, O.; Calvert, L. D.; Whalley, E. *Nature* **1984**, *310*, 393.
- [161] Mishima, O.; Calvert, L. D.; Whalley, E. *Nature* **1985**, *314*, 76.
- [162] Bellissent-Funel, M.-C.; Bosio, L.; Hallbrucker, A.; Mayer, E.; Sridi-Dorbez, R. *J. Chem. Phys.* **1992**, *97*, 1282.
- [163] Bellissent-Funel, M.-C.; Bosio, L. *J. Chem. Phys.* **1995**, *102*, 3727.
- [164] Mishima, O.; Stanley, H. E. *Nature* **1998**, *392*, 164.
- [165] Bellissent-Funel, M.-C. *Eur. Lett.* **1998**, *42*, 161.
- [166] Soper, A. K.; Ricci, M. A. *Phys. Rev. Lett.* **2000**, *84*, 2881.
- [167] Maruyama, S.; Wakabayashi, K.; Oguni, M. *Am. Inst. Phys. Conf. Proc.* **2003**, *708*, 675.
- [168] Sciortino, F.; La Nave, E.; Tartaglia, P. *Phys. Rev. Lett.* **2003**, *91*, 155701.
- [169] Fuentevilla, D. A.; Anisimov, M. A. *Phys. Rev. Lett.* **2006**, *97*, 195702.
- [170] Bertrand, C. E.; Anisimov, M. A. *J. Phys. Chem. B* **2011**, *115*, 14099.
- [171] Amann-Winkel, K.; Bellissent-Funel, M.-C.; Bove, L. E.; Loerting, T.; Nilsson, A.; Paciaroni, A.; Schlesinger, D.; Skinner, L. *Chem. Rev.* **2016**, *116*, 7570.
- [172] Perakis, F.; Marco, L. D.; Shalit, A.; Tang, F.; Kann, Z. R.; Kühne, T. D.; Torre, R.; Bonn, M.; Nagata, Y. *Chem. Rev.* **2016**, *116*, 7590.
- [173] Mishima, O. *Phys. Rev. Lett.* **2000**, *85*, 334.
- [174] Finney, J. L.; Bowron, D. T.; Soper, A. K.; Loerting, T.; Mayer, E.; Hallbrucker, A. *Phys. Rev. Lett.* **2002**, *89*, 205503.
- [175] Sellberg, J. A.; Huang, C.; McQueen, T. A.; Loh, N. D.; Laksmono, H.; Schlesinger, D.; Sierra, R. G.; Nordlund, D.; Hampton, C. Y.; Starodub, D.; DePonte, D. P.; Beye, M.; Chen, C.; Martin, A. V.; Barty, A.; Wikfeldt, K. T.; Weiss, T. M.; Caronna, C.; Feldkamp, J.; Skinner, L. B.; Seibert, M. M.; Messerschmidt, M.; Williams, G. J.; Boutet, S.; Pettersson, L. G. M.; Bogan, M. J.; Nilsson, A. *Nature* **2014**, *509*, 381.
- [176] Huang, C.; Wikfeldt, K. T.; Tokushima, T.; Nordlund, D.; Harada, Y.;

Bergmann, U.; Niebuhr, M.; Weiss, T. M.; Horikawa, Y.; Leetmaa, M.; Ljungberg, M. P.; Takahashi, O.; Lenz, A.; Ojamäe, L.; Lyubartsev, A. P.; Shin, S.; Pettersson, L. G. M.; Nilsson, A. *Proc. Natl. Acad. Sci. U.S.A.* **2009**, *106*, 15214.

- [177] Taschin, A.; Bartolini, P.; Eramo, R.; Righini, R.; Torre, R. *Nat. Commun.* **2013**, *4*, 2401.
- [178] Mishima, O. *J. Chem. Phys.* **2005**, *123*, 154506.
- [179] Mishima, O. *J. Chem. Phys.* **2007**, *126*, 244507.
- [180] Fuentevilla, D. A.; Anisimov, M. A. *Phys. Rev. Lett.* **2007**, *98*, 149904.
- [181] Suzuki, Y.; Mishima, O. *Phys. Rev. Lett.* **2000**, *85*, 1322.
- [182] Suzuki, Y.; Mishima, O. *J. Chem. Phys.* **2013**, *138*, 084507.
- [183] Le, L.; Molinero, V. *J. Phys. Chem. A* **2011**, *115*, 5900.
- [184] Yamanaka, K.; Yamagami, M.; Takamuku, T.; Yamaguchi, T.; Wakita, H. *J. Phys. Chem.* **1993**, *97*, 10835.
- [185] Yamaguchi, T.; Yamagami, M.; Wakita, H.; Soper, A. K. *Stud. Phys. Theor. Chem.* **1995**, *83*, 91.
- [186] Turton, D. A.; Corsaro, C.; Martin, D. F.; Mallamace, F.; Wynne, K. *Phys. Chem. Chem. Phys.* **2012**, *14*, 8067.
- [187] Omta, A. W.; Kropman, M. F.; Woutersen, S.; Bakker, H. J. *Science* **2003**, *301*, 347.
- [188] Murata, K.-I.; Tanaka, H. *Nat. Mater.* **2012**, *11*, 436.
- [189] Suzuki, Y.; Mishima, O. *J. Chem. Phys.* **2014**, *141*, 094505.
- [190] Popov, I.; Greenbaum, A.; Sokolov, A. P.; Feldman, Y. *Phys. Chem. Chem. Phys.* **2015**, *17*, 18063.
- [191] Bruijn, J. R.; Van Der Loop, T. H.; Woutersen, S. *J. Phys. Chem. Lett.* **2016**, *7*, 795.
- [192] Zhao, Z.; Angell, C. A. *Angew. Chem. Int. Ed.* **2016**, *55*, 2474.

- [193] Woutersen, S.; Hilbers, M.; Zhao, Z.; Angell, C. A. <http://arxiv.org/abs/1605.08985> **2016**, 1.
- [194] Schultz, P. W.; Leroi, G. E.; Popov, A. I. *J. Am. Chem. Soc.* **1996**, *118*, 10617.
- [195] Schimmel, F. A. *J. Chem. Eng. Data* **1960**, *5*, 519.
- [196] Monnin, C.; Dubois, M.; Papaiconomou, N.; Simonin, J.-P. *J. Chem. Eng. Data* **2002**, *47*, 1331.
- [197] Fritzsche, R.; Brady, O.; Adair, E.; Wright, J. A.; Pickett, C. J.; Hunt, N. T. *J. Phys. Chem. Lett.* **2016**, *7*, 2838.
- [198] Basham, M.; Filik, J.; Wharmby, M. T.; Chang, P. C. Y.; El Kassaby, B.; Gerring, M.; Aishima, J.; Levik, K.; Pulford, B. C. A.; Sikharulidze, I.; Sneddon, D.; Webber, M.; Dhesi, S. S.; Maccherozzi, F.; Svensson, O.; Brockhauser, S.; Náray, G.; Ashton, A. W. *J. Synchrotron Radiat.* **2015**, *22*, 853.
- [199] *Igor Pro 7*. 2017.
- [200] Tassaing, T.; Danten, Y.; Besnard, M. *J. Mol. Liq.* **2002**, *101*, 149.
- [201] Czurlok, D.; Gleim, J.; Lindner, J.; Vo, P. *J. Phys. Chem. Lett.* **2014**, *5*, 3373.
- [202] Gafurov, M. M.; Aliev, A. R.; Akhmedov, I. R. *Spectrochim. Acta Mol. Biomol. Spectrosc.* **2002**, *58*, 2683.
- [203] Kobayashi, M.; Tanaka, H. *Phys. Rev. Lett.* **2011**, *106*, 125703.
- [204] Li, M.; Owrutsky, J.; Sarisky, M.; Culver, J. P.; Yodh, A.; Hochstrasser, R. M. *J. Chem. Phys.* **1993**, *98*, 5499.
- [205] Zhong, Q.; Baronavski, A. P.; Owrutsky, J. C. *J. Chem. Phys.* **2003**, *119*, 9171.
- [206] Lenchenkov, V.; She, C.; Lian, T. *J. Phys. Chem. B* **2006**, *110*, 19990.
- [207] Oh, K. I.; Choi, J. H.; Lee, J. H.; Han, J. B.; Lee, H.; Cho, M. *J. Chem. Phys.* **2008**, *128*, 154504.
- [208] Park, S.; Ji, M.; Gaffney, K. J. *J. Phys. Chem. B* **2010**, *114*, 6693.

- [209] Choi, J. H.; Kim, H.; Kim, S.; Lim, S.; Chon, B.; Cho, M. *J. Chem. Phys.* **2015**, *142*, 204102.
- [210] Angell, C. A.; Bressel, R. D. *J. Phys. Chem.* **1972**, *76*, 3244.
- [211] Kleis, S. J.; Sanchez, L. A. *Sol. Energy* **1990**, *45*, 201.
- [212] Jal, J. F.; Soper, A. K.; Carmona, P.; Dupuy, J. *J. Phys. Condens. Matter* **1991**, *3*, 551.
- [213] Bauer, J.; Spanton, S.; Henry, R.; Quick, J.; Dziki, W.; Porter, W.; Morris, J. *Pharm. Res.* **2001**, *18*, 859.
- [214] Baumgartner, J.; Dey, A.; Bomans, P. H. H.; Le Coadou, C.; Fratzl, P.; Sommerdijk, N. A. J. M.; Faivre, D. *Nat. Mater.* **2013**, *12*, 310.
- [215] Pouget, E. M.; Bomans, P. H. H.; Goos, J. A. C. M.; Frederik, P. M.; de With, G.; Sommerdijk, N. A. J. M. *Science* **2009**, *323*, 1455.
- [216] Van Driessche, A. E. S.; Benning, L. G.; Rodriguez-Blanco, J. D.; Osorio, M.; Bots, P.; García-Ruiz, J. M. *Science* **2012**, *336*, 69.
- [217] Gebauer, D.; Völkel, A.; Cölfen, H.; Volkel, A.; Colfen, H. *Science* **2008**, *322*, 1819.
- [218] Jawor-Baczynska, A.; Moore, B. D.; Lee, H. S.; McCormick, A. V.; Sefcik, J. *Faraday Discuss.* **2013**, *167*, 425.
- [219] De Yoreo, J. *Nat. Mater.* **2013**, *12*, 284.
- [220] Gebauer, D.; Cölfen, H. *Nano Today* **2011**, *6*, 564.
- [221] Gebauer, D.; Kellermeier, M.; Gale, J. D.; Bergström, L.; Cölfen, H. *Chem. Soc. Rev.* **2014**, *43*, 2348.
- [222] Navrotsky, A. *Proc. Natl. Acad. Sci. U.S.A.* **2004**, *101*, 12096.
- [223] Turton, D. A.; Hunger, J.; Stoppa, A.; Thoman, A.; Candelaresi, M.; Hefter, G.; Walther, M.; Buchner, R.; Wynne, K. *J. Mol. Liq.* **2011**, *159*, 2.
- [224] Turton, D. A.; Martin, D. F.; Wynne, K. *Phys. Chem. Chem. Phys.* **2010**, *12*, 4191.

- [225] Young, S. W.; Mitchell, J. P. *J. Am. Chem. Soc.* **1904**, *26*, 1389.
- [226] Chan, E. J.; Skelton, B. W.; White, A. H. *Z. Anorg. Allg. Chem.* **2008**, *634*, 2825.
- [227] von Siebert, H. *Z. Anorg. Allg. Chem.* **1954**, *275*, 225.
- [228] Haigh, J. A.; Hendra, P. J.; Rowlands, A. J.; Degen, I. A.; Newman, G. A. *Spectrochim. Acta* **1993**, *49A*, 723.
- [229] Mahiuddin, S.; Ismail, K. *Fluid Phase Equilib.* **1996**, *123*, 231.
- [230] Moynihan, C. T. *J. Phys. Chem.* **1966**, *70*, 3399.
- [231] Bhattacharjee, C.; Ismail, S.; Ismail, K. *J. Chem. Eng. Data* **1986**, *31*, 117.
- [232] Turton, D. A.; Corsaro, C.; Candelaresi, M.; Brownlie, A.; Seddon, K. R.; Mallamace, F.; Wynne, K. *Faraday Discuss.* **2011**, *150*, 493.
- [233] Watanabe, K.; Tanaka, H. *Phys. Rev. Lett.* **2008**, *100*, 158002.
- [234] Li, Z. *Phys. Rev. E* **2009**, *80*, 61204.
- [235] Hojo, M.; Takiguchi, T.; Hagiwara, M.; Nagai, H.; Imai, Y. *J. Phys. Chem.* **1989**, *93*, 955.
- [236] Wilkes, J. S.; Levisky, J. A.; Wilson, R. A.; Hussey, C. L. *Inorg. Chem.* **1982**, *21*, 1263.